

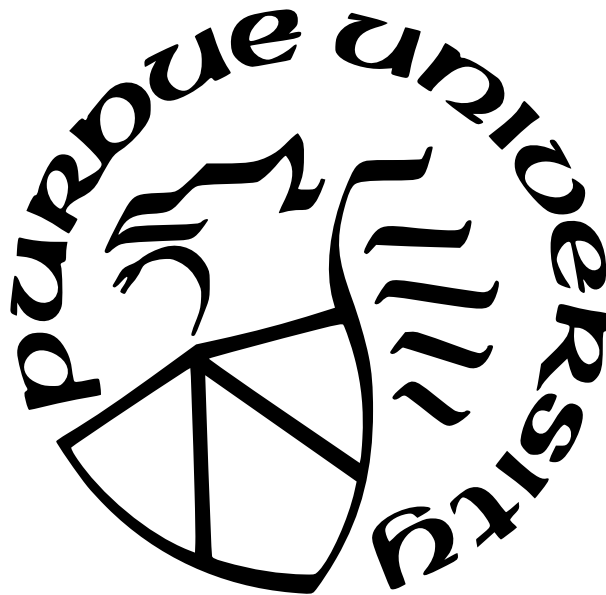
# PIEZOELECTRIC TRANSDUCTION OF SILICON NITRIDE PHOTONIC SYSTEM

by  
Hao Tian

A Dissertation

*Submitted to the Faculty of Purdue University  
In Partial Fulfillment of the Requirements for the degree of*

Doctor of Philosophy



School of Electrical and Computer Engineering

West Lafayette, Indiana

May 2022

**THE PURDUE UNIVERSITY GRADUATE SCHOOL  
STATEMENT OF COMMITTEE APPROVAL**

**Dr. Sunil A. Bhave, Chair**

Elmore Family School of Electrical and Computer Engineering

**Dr. Andrew M. Weiner**

Elmore Family School of Electrical and Computer Engineering

**Dr. Peter Bermel**

Elmore Family School of Electrical and Computer Engineering

**Dr. Chen-Lung Hung**

Department of Physics and Astronomy

**Approved by:**

Dr. Dimitrios Peroulis



## ACKNOWLEDGMENTS

I would like to firstly thank my Ph.D. advisor, Prof. Sunil A. Bhave, for his significant advising about the device design, fabrication, testing of optomechanical devices, and any problems met in the research. He can always bring up new ideas and inspire you deeply into the topic. He fully supports me with research funding and encourages me to try different methods. He provides me with lots of resources such as the collaboration with excellent people all over the world, attending international conferences.

I would also thank my committee members, Prof. Andrew M. Weiner, Prof. Peter Bermel, and Prof. Chen-Lung Hung, for providing valuable suggestions on my study and research at Purdue. I can still remember the precious time I spent in Prof. Weiner's class on Ultra-fast optics. Many of the course materials were well designed and helped a lot during my research, such as spectrum analysis, laser physics, and optical nonlinearity. I especially want to thank Prof. Weiner for supporting experiments in their lab and borrowed me their equipments, and thank Dr. Daniel E Leaird for organizing the experiments. Prof. Bermel has been my Master degree advisor. I cherish his guidance during the early stage of my research, where I learnt how to design an experiment, analyze the data, and present the work scientifically. He helped me grow up from beginner to be able to conduct research independently.

I'd like to thank my colleagues from the OxideMEMS and HybridMEMS groups, especially Dr. Bin Dong and Dr. Mert Torunbalci, Dr. Ben Yu, Dr. Yanbo He for their help on fabrication, device characterization, and valuable discussions. I really enjoy the past five years spent with you in daily life, in the lab and cleanroom. Your mental support encourages me to keep trying and not give up when I stuck in the research.

I would also give my great appreciation to our collaborators from Prof. Tobias Kippenberg's group in EPFL for fabricating and testing the high performance photonic devices. Prof. Kippenberg has been one of the experts in optomechanics and  $\text{Si}_3\text{N}_4$  photonics. His full support keeps each of the research project going efficiently and smoothly. He can always come up with genius ideas that bring the project into next level. Dr. Junqiu Liu has been one of the experts in nano-fabrication, who continuously provides us with high quality  $\text{Si}_3\text{N}_4$

photonic wafers. His believe in me encouraged me to keep working even though the first several runs of the devices were failed, and only after two years we finally got the device working. I want to thank Anat Siddharth, Dr. Rui Ning Wang, Terence Blésin, Dr. Jijun He, Dr. Grigory Lihachev, Dr. Johann Riemensberger, Dr. Wenle Weng for their testing of the optical devices and valuable discussion in each group meeting we had on Wednesday. I really expected and enjoyed each Wednesday meeting where we shared ideas and discussed the progresses we made.

I would like to thank Prof. Matteo Rinaldi's group from Northeastern University for providing us the high quality Sc doped AlN thin films for testing its piezoelectric tuning of the optical microring resonators. I want to thank William Zhu and Michele Pirro for depositing the AlScN thin films.

I would like to thank our staff and engineers of our Birck Nanotechnology Center for their support of keeping the cleanroom and labs running efficiently. I want to thank Joon Park and Bill Rowe for fixing issues every time I met with the photolithography, thank Jeremiah Shepard and Francis Manfred for maintaining the etching tools, thank Dave Lubelski and Dan Hosler for training me on the deposition tools, thank Mary Jo and Kyle Corwin for sending and receiving packages which connects us with other groups.

I would like to thank all the funding agencies, especially the NSF Quantum Information Science and Engineering Network (QISE-NET) program which supports the research studies of graduate students and get connected with other researchers in the field of quantum technology. I would also thank the OEM Group (now with Plasma therm) for providing high quality AlN thin films for fabricating piezoelectric actuators, thank Radiant Technologies for providing high performance PZT actuators, thank Prof. Matteo Rinaldi for providing AlScN thin films.

I would like to finally give my thank to my family for supporting me during the hard time of the Ph.D. studies, for encouraging me to explore the unknowns and keep curiosity, and always staying with me and giving me the courage to overcome all the obstacles.

# TABLE OF CONTENTS

LIST OF TABLES . . . . .	10
LIST OF FIGURES . . . . .	11
LIST OF SYMBOLS . . . . .	29
ABBREVIATIONS . . . . .	32
ABSTRACT . . . . .	35
1 INTRODUCTION . . . . .	37
1.1 Background . . . . .	37
1.2 Piezoelectric tuning of a $\text{Si}_3\text{N}_4$ microring resonator . . . . .	42
1.2.1 Optical waveguide and ring resonator . . . . .	42
1.2.2 Piezoelectric effect . . . . .	45
1.2.3 Photoelastic and moving boundary effects . . . . .	46
1.3 Organization of the thesis . . . . .	50
2 UNRELEASED PIEZOELECTRIC ACTUATION . . . . .	53
2.1 AlN actuator piezoelectric tuning . . . . .	53
2.1.1 Design of the AlN actuator . . . . .	53
2.1.2 Fabrication flow . . . . .	57
2.1.3 DC tuning of the optical resonance . . . . .	59
2.1.4 Optimization of the waveguide placement . . . . .	62
2.1.5 Characterization of the tuning speed . . . . .	66

2.1.6	Strategies to improve the tuning speed . . . . .	73
2.2	HBAR acousto-optic modulation . . . . .	76
2.2.1	HBAR AOM of Disk actuator . . . . .	76
2.2.2	Analysis of mechanical dispersion . . . . .	79
2.2.3	HBAR AOM of Donut actuator . . . . .	82
2.2.4	Electromechanical cross-talk between adjacent actuators . . . . .	83
2.2.5	Strategy for mitigating HBAR resonances . . . . .	85
2.3	AlScN actuator piezoelectric tuning . . . . .	88
2.4	PZT actuator piezoelectric tuning . . . . .	89
2.4.1	DC tuning with PZT actuator . . . . .	89
2.4.2	Co-integration with a thermal heater . . . . .	92
2.4.3	Characterization of the tuning speed . . . . .	94
2.4.4	HBAR AOM of the PZT actuator . . . . .	96
2.5	Summary . . . . .	97
3	PIEZOELECTRIC CONTROL OF SOLITON MICROCOMBS . . . . .	100
3.1	Optical Kerr frequency comb . . . . .	100
3.2	Voltage controlled soliton states . . . . .	104
3.3	HBAR induced PDH error signal . . . . .	106
3.4	Stabilization of the Kerr frequency comb . . . . .	108
3.5	Summary . . . . .	110

4	RELEASED PIEZOELECTRIC ACTUATION . . . . .	111
4.1	Design of the released piezoelectric actuator . . . . .	111
4.2	Fabrication processes . . . . .	116
4.3	DC optical resonance tuning . . . . .	117
4.4	Tuning dynamics and speed . . . . .	121
4.5	GHz acousto-optic modulation via bulk acoustic resonance . . . . .	125
4.6	Released HBAR with AlScN actuator . . . . .	130
4.7	Summary . . . . .	131
5	MAGNETIC-FREE SILICON NITRIDE INTEGRATED OPTICAL ISOLATOR	134
5.1	Background . . . . .	134
5.2	Design of the integrated optical isolator . . . . .	135
5.2.1	Working principle and design . . . . .	135
5.2.2	Theoretical analysis via the coupled mode theory . . . . .	137
5.2.3	Numerical simulation of the spatio-temporal modulation . . . . .	142
5.2.4	Device fabrication and characterization . . . . .	143
5.3	Characterization of the on-chip optical isolation . . . . .	149
5.3.1	Measurement set-up for the isolator . . . . .	149
5.3.2	Dependency on the RF phases . . . . .	150
5.3.3	Dependency on the RF power . . . . .	154
5.3.4	Detuning of the optical mode spacing . . . . .	159

5.3.5	Comparison with the Floquet analysis . . . . .	161
5.3.6	Time domain optical isolation . . . . .	162
5.3.7	Dependency on the optical power . . . . .	162
5.3.8	Results of the over-coupled device . . . . .	163
5.4	Frequency shifter and polarization rotator . . . . .	165
5.5	Comparison with the state of the art . . . . .	169
5.6	Summary . . . . .	172
5.6.1	Outlook on future applications and improvements . . . . .	172
6	QUANTUM MICROWAVE TO OPTICAL CONVERTER . . . . .	176
6.1	Introduction . . . . .	176
6.2	Theoretical analysis with Coupled Mode Theory . . . . .	179
6.2.1	Relation between $\eta$ and optomechanical $S_{21}$ . . . . .	183
6.2.2	Derivation of $V_\pi$ from $S_{21}$ . . . . .	186
6.2.3	Efficiency of the isolator device . . . . .	186
6.3	Device design . . . . .	187
6.4	Experimental realization with 22 $\mu\text{m}$ radius device . . . . .	193
6.4.1	Challenge 1: releasing of the chip edge . . . . .	194
6.4.2	Challenge 2: nonuniform releasing of the actuator . . . . .	194
6.4.3	Challenge 3: non-ideal optical modes . . . . .	195
6.4.4	Challenge 4: undesired HBAR beneath the signal pad . . . . .	196

6.5	Estimation of efficiency $\eta$ and $g_0$ . . . . .	197
6.6	Summary . . . . .	199
7	OUTLOOK . . . . .	201
7.1	Hybrid integrated quantum systems . . . . .	201
7.1.1	Piezoelectric programmable photonic circuits . . . . .	206
7.1.2	Photonic synthetic dimension enabled by HBAR AOM . . . . .	207
7.1.3	Classical readout and control of superconducting qubit . . . . .	210
	REFERENCES . . . . .	213
A	ANALYTIC ANALYSIS OF ELECTRO-OPTOMECHANICAL RESPONSE . . .	241
A.1	Electromechanical model of HBAR mode . . . . .	241
A.2	Electromechanical $S_{11}$ reflection parameter . . . . .	246
A.3	Mechanical dispersion analysis . . . . .	247
A.4	Electromechanical coupling and acousto-optic overlap . . . . .	251
B	DESIGNING THE OPTICAL WAVEGUIDE FOR TE-TM MODE COUPLING	254
B.1	Design of quasi-square optical waveguide . . . . .	254
B.2	Calibration of the azimuthal order difference $\Delta m$ . . . . .	256
	VITA . . . . .	258
	LIST OF PUBLICATIONS . . . . .	259

## LIST OF TABLES

2.1	Comparison of the piezoelectric tuning with different design parameters for both AlN, AlScN, and PZT actuators. . . . .	97
2.2	Comparison with the piezoelectric tuning demonstrated in the literature. All the works here are unreleased structure, and the optical waveguide is made from $\text{Si}_3\text{N}_4$ . MZI: Mach-Zehnder interferometer. The FSR for each optical ring is as labeled. $V_\pi \cdot L$ has unit of V·cm, and is estimated from the resonance tuning for the microring structure. The last three rows compare with thermo-optic tuning. WG: waveguide. . . . .	99
4.1	Comparison of the piezoelectric tuning with different design parameters. . . . .	131
4.2	Comparison with the piezoelectric tuning demonstrated in the literature. All the works here are released structure, and the optical waveguide is made from $\text{Si}_3\text{N}_4$ . The FSR for each optical ring is as labeled. $V_\pi \cdot L$ has unit of V·cm, and is estimated from the resonance tuning for the microring structure. BW: bandwidth, which is also the frequency of the fundamental mechanical mode. . . . .	132
5.1	Fitting parameters of the MBVD model of HBAR at 2.958 GHz. . . . .	148
5.2	Comparison of optical non-reciprocal devices realized using different schemes: MO (magneto-optic), NL (nonlinear optics), OM (optomechanical), SBS (stimulated Brillouin scattering), SM (synthetic magnetic field), and ST (spatio-temporal modulation). IL: Insertion loss. The three devices with 950, 850, and 600 nm gaps shown in this work are listed separately. A commercial bulk optical isolator is listed for comparison. <i>a</i> : Non-reciprocal sideband modulation. <i>b</i> : Optical pump power. . . . .	171
6.1	Comparison with experimental demonstrations of microwave to optical converters in the literature using electro-optic (EO) or piezo-optomechanical (OM) methods. Note the “isolator” device is the same device presented in the last chapter and driven with a single optical mode. The proposed device is with two optical modes. . . . .	192
6.2	Summary of the parameters for the isolator device, current first-generation 22 $\mu\text{m}$ -radius device, and projected future goals. . . . .	199
A.1	Material properties of each layer employed in the analytic model . . . . .	246
A.2	Effective cavity length at different resonant conditions. The effective boundary condition at each interface is compared. . . . .	250



## LIST OF FIGURES

1.1	Schematics of stress-optical tuning. (a) A piezoelectric actuator is placed on top of an optical waveguide (blue). Upon external electric signal, the piezoelectric film will deform and generate stress distribution crossing the waveguide (red dashed lines). The boundary of the waveguide will displace (dark blue dashed lines) and thus change the shape of the waveguide. (b) Released structure where the substrate is removed to suspend the actuator for larger mechanical deformation. . . . .	39
1.2	Comparison of AOM between Surface and Bulk acoustic waves. Typical AOM via surface acoustic wave where the optical waveguide is formed by either (a) etching trenches into the piezoelectric film or (b) embedding the waveguide near surface. The surface acoustic wave (violet curve) is excited by interdigital electrode fingers (orange). (c) AOM via bulk acoustic waves proposed in this work, which is excited vertically towards the substrate by piezoelectric actuator. . . . .	41
1.3	(a) Cross-section of an optical waveguide. (b) Electric field distribution for TE and TM optical modes. The white arrows denote the direction of electric field. (c) Top view of an optical microring resonator. (d) Transmission spectrum of a typical optical resonator. The dashed curve shows the shifting of the optical resonances under piezoelectric tuning. . . . .	43
2.1	Schematics for the designed devices with (a) Disk shape and (b) Donut shape actuators with silicon nitride ring resonator (blue) having different relative positions. (c) and (d) are the cross-sections for Disk and Donut devices along black dashed lines in (a) and (b), respectively. (e), (f) COMSOL simulation of horizontal stress distribution around optical waveguide under +60 V DC biasing for Disk and Donut devices, respectively. The overlaid gray arrows denote the local mechanical displacement with the biggest arrow scaling as 1 nm. Reprinted from Ref. [12]. . . . .	54
2.2	Static stress distribution in $z$ and $\phi$ directions. (a) and (b) show the numerical simulation of vertical $z$ stress distribution under +60 V DC biasing for the Disk and Donut devices, respectively. Both of them show extensional stress around the waveguide. (c) and (d) are out of plane (tangential to the optical ring) stress distributions for Disk and Donut devices. They present different sign inside the waveguide, since the optical ring of the Disk device expands while the Donut device squeezes. Reprinted from Ref. [12]. . . . .	55
2.3	Fabrication flow for the unreleased AlN piezoelectric actuator. . . . .	56
2.4	(a) Optical microscope image and (b) false color SEM around Disk actuator corner as labeled in white dashed box in (a) for Disk device. (c) Optical microscope image and (d) false color SEM around actuator corner for Donut device. Reprinted from Ref. [12]. . . . .	57

2.5	(a) Transmission spectrum of one resonance of TE and TM polarization mode for Disk device under +60 V (blue), 0 V (black), and -60 V (red). The x axis represents wavelength shifts relative to resonant wavelength $\lambda_0$ ( $\sim 1550$ nm) of each mode. The tuning direction reverses for opposite voltages, demonstrating bi-directional tuning. (b) Dependence of resonant wavelength detune on voltages. Experimental results (squares) show high linearity for both TE (pink) and TM (cyan) modes, with $R^2 > 99\%$ linear fitting (straight lines). (c) Influence of piezoelectric actuation on the optical quality factor Q for TE and TM modes, which verifies that the actuation will not influence the optical Q. Reprinted from Ref. [12]. . . . .	58
2.6	(a) Transmission spectrum of one resonance of TE and TM polarization mode for Donut device under +60 V (blue), 0 V (black), and -60 V (red). (b) Dependence of resonant wavelength detune on voltages. Experimental results (squares) show high linearity for both TE (pink) and TM (cyan) modes, with $R^2 > 99\%$ linear fitting (straight lines). (c) Influence of piezoelectric actuation on the optical quality factor Q for TE and TM modes. Reprinted from Ref. [12]. . . . .	59
2.7	Current-Voltage relation for the capacitor-like AlN actuator. Black square is the experimental results, which the red dashed line is the linear fitting. . . .	60
2.8	(a) Resonance shift versus applied voltage in forward and backward directions, showing the small hysteresis. V incr. / decr.: voltage increase / decrease; meas.: measured data. (b) Resonance shift for TE resonances in the wavelength range from 1500 nm to 1630 nm, when the applied voltage changes from -100 V to +150 V. The wavelength-dependent tuning results from a 5.3 MHz change of the FSR due to the piezoelectric actuation. Reprinted from Ref. [121]. . . . .	61
2.9	(a) COMSOL simulation of the tuning efficiency for Disk device under different relative shift between the waveguide and the top electrode's outer edge. The definition of the shift is as shown in the inset and the arrow denotes the positive shift direction. Both TE (red) and TM (blue) modes are shown. (b) Distribution stress of $\sigma_r$ for different shifts from left to the right as labeled in (a). . . . .	63
2.10	Examples of fabricated Disk devices with -8 $\mu\text{m}$ (left), 0 $\mu\text{m}$ (middle), and 8 $\mu\text{m}$ shift. The blue dashed curve illustrates the position of the microring resonator. . . . .	64
2.11	Experimentally measured tuning efficiency for (a) Disk and (b) Donut actuators. Both TE (red) and TM (blue) modes are measured. . . . .	64
2.12	Optical resonance tuning of TE (upper) and TM (lower) modes for (a) Disk and (b) Donut device with optimal shift under $\pm 60$ V. . . . .	65

2.13	(a) Image of measurement setup. The chip with devices of different sizes is shown in the middle. (b) Tuning efficiency of TE (red) and TM (blue) modes for devices with different radius and thus FSR. (Courtesy of Anat Siddharth)	66
2.14	Time domain response (black) to a large-signal input square wave (red) with 20 V $V_{pp}$ . The repetition rate is increased from 100 kHz to 1 MHz (left to right). The duty cycle of the square wave is 50%. . . . .	67
2.15	Fast Fourier Transform (FFT) of the 1 MHz repetition rate input and output square waves in Fig. 2.14. The position and frequency of each acoustic resonance is as labeled. . . . .	67
2.16	(a) Time domain response (orange) to a small-signal square wave (gray) with 2 V $V_{pp}$ , 1 MHz repetition rate, and a 50% duty cycle. (b) Time domain response to short pulses with 20 V $V_{pp}$ , 5 MHz repetition rate, and a 20 ns pulse width, demonstrating ultra-fast (sub-ns) tuning speed. The inset shows the normalized cross-correlation (black) between input and output signals and the auto-correlation (red) of the input signal. The right Y axis in (a), (b) denotes the resonant wavelength shifting relative to 0 V voltage, according to a linear tuning of -0.2 pm/V. Reprinted from Ref. [12]. . . . .	68
2.17	6 GHz square wave driving at the frequency where mechanical resonances disappear due to low mechanical Q. The electrical signal (gray) is measured by an oscilloscope (Tektronix DSA8200) after 20 dB attenuation of the original signal. The optical output shows clear oscillations with a frequency equal to the driving field, illustrating GHz level piezoelectric actuation. Reprinted from Ref. [12]. . . . .	69
2.18	(a) Schematic of the setup for measuring electromechanical and optomechanical response. ECDL: external cavity diode laser, PC: polarization controller, DUT: device under test, PD: photo-diode, VNA: vector network analyzer. (b) Electromechanical $S_{11}$ and (c) optomechanical $S_{21}$ spectrum response of the piezoelectric transduction from 300 kHz to 100 MHz. The position and frequency of each acoustic resonance is as labeled. . . . .	71
2.19	(a) Schematic of the device cross-section. (b) Numerical simulation of one of the HBAR modes around 82 MHz, showing the vertical $z$ displacement. Acoustic standing wave is formed over the whole substrate. The mode is axisymmetric around the vertical dashed line. . . . .	72
2.20	(a) Optomechanical $S_{21}$ response at low frequency. The frequency is plotted in log scale. (b) Simulation of typical mechanical modes of the entire photonic chip, including flexural mode at 480 kHz, face-shear mode at 665 kHz, and Lamé mode at 755 kHz. . . . .	73

2.21	Optomechanical $S_{21}$ responses of Disk actuator with single actuation (gray), dual actuators with differential drive for a square $\text{Si}_3\text{N}_4$ chip (green), an apodized chip (red), and an apodized chip on a carbon tape (blue). Inset: numerical simulation of three mechanical modes of the square $S_{21}$ chip and the apodized chip (1.69 MHz). Photo of the apodized chip with the dual-actuator configuration. Experimental schematic for differential driving of dual actuators. (Courtesy of Anat Siddharth) . . . . .	74
2.22	Hybrid nanophotonic high-overtone bulk acoustic resonator (HBAR) platform. 3D schematic illustrating excitation of bulk acoustic wave resonances via a macroscopic piezoelectric actuator, which transmit vertically into the stack and form acoustic standing waves inside the various acoustic Fabry-Pérot cavities. The resonance enhanced mechanical stress changes the waveguide's effective index via the stress-optical effect, and thereby modulate the output optical intensity. Reprinted from Ref. [12]. . . . .	75
2.23	Microwave frequency electro-acousto-optic modulation. (a) Electromechanical $S_{11}$ spectrum from 1 to 6 GHz. A range of equidistant bulk acoustic resonances is found to exist over a broad frequency range. The inset schematic illustrates the acoustic wave reflection at interfaces. (b), (c) Optomechanical $S_{21}$ responses of TE and TM modes demonstrate acousto-optic modulation covering multiple octave-spanning microwave frequencies. Due to different optical mode shapes (insets in (b) and (c)) and thus acousto-optic mode overlap, TE and TM modes show dissimilar $S_{21}$ spectra. (d), (e) The zoom-in of $S_{11}$ , and TE mode's $S_{21}$ within the window (green shaded area in (b)) around 2 GHz. (f) The zoom-in of TM mode's $S_{21}$ around 4 GHz in (c). The resonances distribute evenly with an FSR of 17.5 MHz. Reprinted from Ref. [12]. . . . .	77
2.24	(a) Numerical simulation of vertical stress $\sigma_z$ distribution for one typical acoustic resonant mode at 2.041 GHz under 1 V driving field, with a zoom-in around the optical waveguide (red box in (a)) shown in (b). At GHz frequencies, the acoustic wavelength is similar in scale to optical wavelength and waveguide structure. Reprinted from Ref. [12]. . . . .	78

2.25	Mechanical dispersion analysis of HBAR modes. (a) Calculated and (b) measured $S_{11}$ spectrum showing good agreement between the electromechanical model and experiment. Each green dashed line denotes the location of a resonance from the $\text{SiO}_2$ cavity. The inset in (b) illustrates the coupling between Si, $\text{SiO}_2$ , and AlN cavities. (c) The measured (circle) and calculated (solid line) frequency difference between each pair of adjacent Si resonances, showing a periodic variation of local FSR around an average value of 17.5 MHz. Note that the maxima of FSR align with green dashed lines where the $\text{SiO}_2$ resonances are located. (d) Measured (circle) and calculated (solid line) higher order dispersion represented by the frequency deviation from an equidistant frequency grid (with average FSR = 17.515 MHz), referencing to mode $\nu_0$ (= 3.0145 GHz, labeled as yellow dot). $\mu$ is the mode number difference relative to the mode at 3.0145 GHz. . . . .	80
2.26	The same $S_{11}$ and $S_{21}$ measurements on the Donut device in GHz range. (a) Electromechanical $S_{11}$ spectrum from 1 to 6 GHz. Optomechanical $S_{21}$ responses of (b) TE and (c) TM modes demonstrate effective stress-optical modulation spanning a broad range of microwave frequencies. The Donut device shows similar results as reported for the Disk device in the main text. (d) and (e) show the zoom-in of $S_{11}$ and $S_{21}$ responses of TE mode within the window (green shaded area) around 2 GHz in (b), while (f) shows the zoom-in of TM mode's $S_{21}$ response around 4 GHz in (c). Reprinted from Ref. [12]. . .	81
2.27	(a) Numerical simulation of $\sigma_z$ distribution for one typical acoustic resonant mode at 2.125 GHz, with a zoom-in around the optical waveguide (red box) shown in (b). Reprinted from Ref. [12]. . . . .	83
2.28	Demonstration of low electromechanical cross-talk between adjacent actuators. (a) Optical microscope image of the device with three closely placed actuators. (b) (top) Two port electromechanical $S_{21}$ measurement by driving actuator 1 and sensing from actuator 2 as labeled in (a). (bottom) $S_{11}$ reflection for device 1. The cross-talk between the two devices is as low as -60 dB which guarantees compact integration. (c) Zoom-in of the measured $S_{21}$ and $S_{11}$ responses in the green shaded region in (b). Reprinted from Ref. [12]. . .	84
2.29	Fabrication flow for removing HBAR resonances by roughing the backside surface of the Si substrate and pasting a layer of polyurethane (PU) epoxy mixed with 3 $\mu\text{m}$ nickle powder. . . . .	84
2.30	(a) Cross-section of the device after roughing and then pasting polyurethane (PU) epoxy (mixed with 3 $\mu\text{m}$ Nickle powders) on the backside of the Si substrate. (b) $S_{11}$ and (c) $S_{21}$ of the TM mode from 1 to 10 GHz after damping acoustic resonances. The VNA responses become smoother with only wide range envelope variation. Enabled only by AlN fundamental and second harmonic resonances (green shaded regions), broadband modulation can be achieved with 3 dB bandwidth of 250 MHz for each. Reprinted from Ref. [12]. . . . .	85

2.31	$S_{11}$ (top) and $S_{21}$ (bottom) of the TM mode from 20 MHz to 1GHz after damping acoustic resonances. The frequency is in log scale. . . . .	86
2.32	(a) Optical image for an AlScN actuator on an optical microring resonator with 200 GHz FSR. (b) Cross-section of the device with 500 nm AlScN thin film. (c) SEM image of one AlScN actuator. . . . .	87
2.33	(a) Optical image for devices with different sizes. The FSR of each optical ring resonator is as labeled. (b) The tuning efficiency for each device with different FSR. All the devices are with the 8 $\mu\text{m}$ shift, except for the 25 GHz FSR device which has 10 $\mu\text{m}$ shift. . . . .	88
2.34	(a) Optical image for a PZT actuator on an optical microring resonator with 100 GHz FSR. The dashed blue circle indicates the optical microring. (b) False color SEM of the PZT actuator in (a). (c) False-colored SEM image of the cross-section, showing the PZT actuator integrated on the $\text{Si}_3\text{N}_4$ photonic circuit. The piezoelectric actuator is composed of Pt (yellow), PZT (green) layers on top of the $\text{Si}_3\text{N}_4$ waveguide (blue) buried in $\text{SiO}_2$ cladding. . . . .	89
2.35	(a) PZT piezoelectric tuning of a 100 GHz FSR optical resonator. The tuning of the resonance under 5 V before (yellow) and after (blue) electrical poling the PZT film are shown. (b) The shift of the optical resonance as the voltage increases (red) and decreases (blue), showing slight hysteresis. . . . .	90
2.36	(a) Optical image of one photonic chip with different sizes of devices. The FSR of each type of device is as labeled. (b) The resonance tuning for devices with different sizes as the voltage is increased. (c) The tuning efficiency for devices with different FSR. . . . .	91
2.37	(a) Top: Optical image of the PZT chip containing 30 GHz and 100 GHz FSR devices. Bottom: optical image of the PZT actuator co-integrated with a heater surrounding the optical ring. The zoom-in in the red dashed box is shown on the right. The optical waveguide is right beneath the edge of the top metal as indicated by the blue dashed line. (b) Tuning of the optical resonance for 30 GHz (top) and 100 GHz (bottom) FSR devices under different voltages. . . . .	92
2.38	Thermal-optical tuning of the the optical resonance for (a) 100 GHz and (b) 30 GHz FSR devices. Over one FSR tuning can be achieved when voltage is larger than 13 V for both of them. The lower panel shows the electrical power and current under each voltage. The gray dashed line indicates the FSR for each device. . . . .	93
2.39	Time domain modulation of the light output for (a) 100 GHz and (b) 30 GHz FSR devices. The top and middle rows are square waves with 100 kHz and 500 kHz repetition rate, respectively. The bottom row is under electrical pulse with 0.5 $\mu\text{s}$ pulse width. The $V_{\text{pp}}$ of the the square waves and pulse is 1 V only. . . . .	94

2.40	Zoom-in of the ringing down tail of the time domain switching under 100 kHz square wave for the 100 GHz (black dots) and 30 GHz (blue dots) devices in Fig. 2.39. The decay is fitted exponentially for 100 GHz (red line) and 30 GHz (red dashed line) to extract the time constant as labeled. The capacitance is measured as shown in the inset. . . . .	95
2.41	(a) Electromechanical $S_{11}$ (top) and optomechanical $S_{21}$ (bottom) responses over a wide frequency range. (b) Zoom-in of $S_{11}$ (top) and $S_{21}$ (bottom) from 0.5 to 2 GHz, showing HBAR resonances of the PZT actuator. . . . .	96
3.1	Schematics for the optical frequency comb in the time domain (a) and the frequency domain (b). The carrier-envelope offset phase $\phi_{\text{CEO}}$ is defined as the phase difference between the peak of envelope and the closest peak of carrier. The discrete frequencies distribute evenly with interval $f_{\text{rep}}$ , and the offset frequency is $f_{\text{CEO}}$ . . . . .	101
3.2	Principle of the Kerr comb. The comb is firstly generated by the degenerate FWM process which converts two pump photons into evenly distributed sidebands. As the power from pump is distributed to sideband, the FWM is dominated by the non-degenerated version which generates new sidebands and forces even frequency distribution. . . . .	102
3.3	(a) Schematic of the AlN actuator on top of a $\text{Si}_3\text{N}_4$ microring resonator. CW light (green) is coupled into the resonator which generates dissipative solitons (red pulses) at the output. The modulation signal applied to the AlN actuator induces bulk acoustic waves (purple waves), which transduces the modulation to all the comb lines of the generated soliton pulses (spectrum at bottom right). (b) Optical image showing the $\text{Si}_3\text{N}_4$ microresonator (red dashed line) with a disk-shape AlN actuator. (c) False-colour SEM image of the sample cross-section, showing Al (yellow), AlN (green), Mo (red), $\text{Si}_3\text{N}_4$ (blue) and the optical TE mode (rainbow). The inset shows the schematic of the cross-section. Reprinted from Ref. [121]. . . . .	104
3.4	(a) Experimental set-up for comb generation and control. OSC, oscilloscope; FBG, fibre Bragg grating; OSA, optical spectrum analyser; PD, photodiode; EOM, electro-optic modulator; VNA: vector network analyzer. (b) A typical soliton step of millisecond length. (c) Optical spectrum for frequency comb at different states under different voltages. PC: primary comb; MI: modulation instability; MS: multi-soliton. (d) Resonance detuning measured by VNA. The cavity resonance is initially 1 GHz smaller than the laser frequency, and is then tuned to the laser and generates different comb states. (e) Optical spectrum for single soliton states with different bandwidth when varying the voltage. (f) Cavity and soliton resonance detuning in the soliton state with different voltages. SS: single soliton. Reprinted from Ref. [121]. . . . .	105



3.5	(a) Experimental set-up for On-chip generation of PDH error signals using the HBAR modes induced by AlN actuation. LPF: low-pass filter; Amp.: RF power amplifier. PDH error signal (blue) modulated at (b) 78.67 MHz and (c) 114.1 MHz HBAR modes. The optical resonance is shown as the orange curves. $\Delta f$ is the relative detune between the laser and the optical resonance. Reprinted from Ref. [121]. . . . .	107
3.6	Stabilization of the frequency comb over a long period of time. (a) Experimental setup for locking the resonance to the laser and maintaining the soliton detuning. OSC: oscilloscope; BPF: bandpass filter; FBG: fiber Bragg grating. (b) Soliton stabilization over 5 hours. Three selected comb lines are shown here with stability over 5 h. Reprinted from Ref. [121]. . . . .	108
3.7	Stabilization of the repetition rate of the soliton. (a) Experimental setup used to lock the microcomb to an electro-optic (EO) comb, and characterize the in-loop phase noise of the beatnote signal between line no. -1 of the microcomb and line no. -13 of the EO comb. DSO, digital storage oscilloscope; MZM, Mach-Zehnder modulator; EOM, electro-optic modulator; ESA, electrical spectrum analyzer; PNA, phase noise analyser. (b) Schematic of soliton repetition rate stabilization using an EO comb with 14.6974 GHz line spacing. Line no. -1 of the microcomb and line no. -13 of the EO comb are locked and referenced to a 60.0 MHz signal. (c) Measured beat-note signal of line no. -1 of the microcomb and line no. -13 of the EO comb, in the cases of locked and free-running (unlocked) states. Resolution bandwidth (RBW) is 1 kHz. (d) Measured phase noise of the beat signal in the locked (blue) and free-running states (red), in comparison to the 60.0 MHz reference signal (black). The locking bandwidth of the AlN actuator is 0.6 MHz. Reprinted from Ref. [121].	109
4.1	Schematics of cross-section of the devices with different relative positions of Si <sub>3</sub> N <sub>4</sub> ring resonator for (a) 6 $\mu\text{m}$ from tip edge, (b) 12 $\mu\text{m}$ from tip edge, and (c) right at the anchor. The thickness of each layer is labeled in each figure, while the dimensions of the waveguide is $1.8 \times 0.8 \mu\text{m}^2$ . The relative position of rotational axis of the device is shown as in (a), and the cylindrical coordinate is employed. AlN sandwiched between Al and Mo serves as piezoelectric actuator which will bend the membrane when we apply voltage. (d-f) shows the FEM simulation of r direction displacement (top) and horizontal stress distribution (bottom) around the waveguide for (a-c), respectively. As positive 60 V is applied, the membrane will bend downwards, and tune the resonant wavelength by shrinking the ring mechanically and perturbing the refractive index through the stress-optical effect. . . . .	112



4.2	(a) Optical microscope of Device Edge 2. (b) Zoom-in optical microscope images around waveguide coupling region for Device Edge 1 (top) and Device Edge 2 (bottom), which corresponds to the white dashed rectangle in (a). The relative position of ring resonator inside membrane is clearly shown. (c) and (d) illustrate the optical microscope image of the whole device and zoom-in near waveguide coupling region (white dashed region in (c)) for Device Anchor, respectively. (e) and (f) show the false color SEM near red dashed rectangle in (a) and (c) respectively. Yellow region is top Al electrode with AlN (green) beneath it. Red is for released SiO <sub>2</sub> membrane while blue is Si substrate. . . . .	113
4.3	(a) COMSOL simulation of total displacement distribution of device Edge 2 under 60 V DC voltage. COMSOL optical mode simulation for (b) TE (upper) and TM (lower) modes respectively. . . . .	114
4.4	Schematics of fabrication flow for the released piezoelectric actuator. (a) Cross-section of the device after fabrication of the Si <sub>3</sub> N <sub>4</sub> ring resonator using the Damascene process. (b) Mo and AlN are RIE etched to define the shape of the actuator. (c) Etching the bottom Mo metal. (d) Release holes are defined by deep RIE etching of SiO <sub>2</sub> and Si, followed by (e) isotropic dry etching of the Si substrate. (f) The wafer is finally mechanically polished to be diced into small chips. . . . .	115
4.5	SEM image of the Si substrate of the device Anchor after vertical DRIE (white arrows) and Si lateral etching (red arrows). . . . .	116
4.6	(a-c) DC tuning spectrum for TE (upper) and TM (lower) modes under 0 V (gray), 60 V (red), and -60 V (blue) for device Edge 1, Edge 2, and Anchor respectively. The x axis for each spectrum is relative to the center wavelength of each mode, with $\lambda_0$ for Edge 1 TE mode 1548.4 nm and TM mode 1548.8 nm, and for Edge 2 TE mode 1549.6 nm and TM mode 1548.8 nm, and for Anchor TE mode 1549.1 nm and TM mode 1549.7 nm. All devices and modes show red detune (increasing resonant wavelength) for positive voltage and blue detune (decreasing resonant wavelength) under negative voltage, but with different tuning efficiency. (d-f) Dependence of the resonant wavelength tuning $\Delta\lambda$ on DC voltage for devices Edge 1, Edge 2, and Anchor, respectively. Orange (purple) dots and lines are experiment points and linear fitting for TE (TM) mode, respectively. The tuning is highly linear ( $R^2 > 99\%$ ) and has positive slope with voltage, showing bidirectional tuning. (g-i) Dependence of the optical quality factor Q on voltages for TE (orange) and TM (purple) modes. TE modes show higher Q than TM mode in all cases. . . . .	118

4.7	Time domain intensity modulation of device Edge 1 under triangle waves with (a) 10 kHz and (b) 100 kHz, as well as under square waves with 10 kHz (c) and 100 kHz (d). The top part (black) of each figure is the input RF signal while the lower part (red) is the output optical modulation. (e) Optomechanical $S_{21}$ response to the input RF modulation, showing mechanical resonance at 1.36 MHz with 190 mechanical Q. (f) COMSOL simulation of the fundamental mechanical mode at 1.36 MHz. . . . .	120
4.8	Time domain intensity modulation of device Edge 2 under triangle waves with (a) 10 kHz and (b) 100 kHz, as well as under square waves with 10 kHz (c) and 100 kHz (d). The top part (black) of each figure is the input RF signal while the lower part (red) is the output optical modulation. (e) Optomechanical $S_{21}$ response to the input RF modulation, showing mechanical resonance at 1.2 MHz with 312 mechanical Q. (f) COMSOL simulation of fundamental mechanical mode at 1.2 MHz. . . . .	122
4.9	Time domain intensity modulation of device Anchor under triangle waves with (a) 10 kHz and (b) 100 kHz, as well as under square waves with 10 kHz (c) and 100 kHz (d). The top part (black) of each figure is the input RF signal while the lower part (red) is the output optical modulation. (e) Optomechanical $S_{21}$ response to the input RF modulation, showing four closely located modes around 1.35 MHz. (f) COMSOL simulation of the four mechanical modes as labeled in (e). . . . .	123
4.10	(a) Measured spectrum of the displacement at the tip of the cantilever using Laser Doppler Vibrometer (LDV). (b) Measured mechanical displacement distribution for each mode as labeled in (a). The COMSOL simulation is shown in the lower panel which matches well with the measurement. . . . .	124
4.11	(a) Electromechanical $S_{11}$ spectrum from 1 to 10 GHz with the mode order labeled for each visible acoustic resonance in oxide cavity. The inset shows the zoom-in of the green shaded region. (b) Calculated electromechanical coupling efficiency $k_{t,eff}^2$ for each HBAR mode (black square). The $k_{t,eff}^2$ of unreleased HBAR (red curve) is plotted for comparison. (c) Numerical simulation of the vertical stress distribution $\sigma_z$ for typical modes. The mode order is as labeled in (a). The mode is axisymmetric which revolves around the vertical dashed line. Reprinted from Ref. [16]. . . . .	126
4.12	Acousto-optic modulation response $S_{21}$ for TE (upper) and TM (lower) modes from 1 to 10 GHz. Periodic resonances can be observed corresponds to each of the dip from $S_{11}$ . The orders for the resonances at high frequencies that can hardly be distinguished in $S_{11}$ are as labeled. The $S_{21}$ for unreleased devices for TE (purple) and TM (red) modes are overlapped for comparison. . . . .	127
4.13	(a) Electromechanical $S_{11}$ and (b) optomechanical $S_{21}$ at the microwave X-band. The HBAR mode from 18 to 20 order can be clearly seen. The definition of different microwave bands is indicated at top. . . . .	128

- 4.14 (a) Optical image of the fabrication released AlScN HBAR actuators. (b) Zoom-in SEM around the two actuators. (c) Electromechanical  $S_{11}$  and (d) admittance  $Y_{11}$  of one actuator. Inset in (d) shows the fitting of  $Y_{11}$  using the Modified Butterworth-Van Dyke model (MBVD, red line). . . . . 131
- 5.1 (a) Schematic and device rendering. Three discrete AlN piezoelectric actuators are equidistantly integrated on top of a  $\text{Si}_3\text{N}_4$  microring resonator (blue solid). Upon coherent driving these actuators with fixed relative phases  $(\phi_1, \phi_2, \phi_3) = (0^\circ, 120^\circ, 240^\circ)$ , a rotating acoustic wave (black arrow) is generated that spatio-temporally modulates the two co-propagating optical modes (red and green arrows), leading to indirect interband transition in only one direction where the phase matching condition is fulfilled. (b) Frequency domain representation illustrating the indirect interband transition. When the two optical modes,  $a$  and  $b$ , are spaced by the resonant frequency  $\Omega_m$  of the mechanical mode  $c$ , scattering among modes  $a$  and  $b$  happens with a scattering rate of  $g = g_0\sqrt{n_c}$  under a microwave drive at  $\Omega_m$ . (c) Schematic of  $\omega - k$  space showing the energy ( $\Delta\omega_{ba} = \Omega_m$ ) and momentum ( $\Delta k_{ba} = -k_m$ ) conservations. Interband transition that couples the two optical modes with the acoustic wave is only allowed in the direction where phase matching condition is fulfilled, giving rise to transparency on resonance in this direction (“forward”, as shown in **a**) and extinction in the other direction (“backward”). Reprinted from Ref. [169]. . . . . 136
- 5.2 (a) Schematic for the coupling between the two optical modes and the mechanical mode. The system is pumped by the external microwave drive which couples strongly the two optical modes. (b) Energy level for the three wave mixing process. The microwave stimulates the energy exchange between the two optical modes.  $\kappa_{a,i}$ ,  $\kappa_{b,i}$ , and  $\kappa_{c,i}$  are the intrinsic losses for the two optical modes and the mechanical mode. . . . . 138
- 5.3 (a) 2D Schematic of the simulated optical ring resonator. The refractive index of three regions are modulated as labeled by the red area. The relative phases of the modulation between the adjacent area can be controlled in the simulation. Electric field ( $E_z$ , out of plane) distribution of (b) optical mode  $a$  and (c) mode  $b$ .  $m$  is the azimuthal order for each mode. (d) Optical transmission of mode  $a$  in the forward (red) and backward (blue) directions. Electric field ( $E_z$ , out of plane) distribution under reversed phases: (e)  $(\phi_{21}, \phi_{31}) = (120^\circ, -120^\circ)$  (perfect phase matching) and (f)  $(\phi_{21}, \phi_{31}) = (-120^\circ, 120^\circ)$  (largest phase mismatch). The input light wavelength is at the resonant wavelength of mode  $a$  ( $\lambda_a = 1502.8$  nm). As we change the rotation direction of the modulation wave, the light changes from (e) transmission to (f) isolation. Reprinted from Ref. [169]. . . . . 141

5.4	(a) Transmission spectra of mode $a$ and (b) converted sideband in mode $b$ under 2D sweep of the relative phase $\phi_{21}$ and $\phi_{31}$ . Each column corresponds to the spectrum under the same phase $\phi_{31}$ and has a spectra span of (1.5027 nm, 1.5031nm). The spectra in Fig. 5.3(d) are the slices as labeled by the black dashed lines in (a). Reprinted from Ref. [169]. . . . .	143
5.5	(a) False-colored top-view SEM image of the fabricated device. Inset: False-colored SEM image of the sample cross-section, showing the vertical structure of the piezoelectric actuator and quasi-square $\text{Si}_3\text{N}_4$ photonic waveguide. (b) Optical microscope image highlighting the bus-microring coupling section, the released $\text{SiO}_2$ area, and the relative positions of $\text{Si}_3\text{N}_4$ waveguides (blue line) and two AlN actuators. (c) FEM numerical simulations of the vertical stress $\sigma_z$ distribution of a typical HBAR mode at 2.9 GHz, which is conducted along the cross-section indicated by the red dashed line in (b). Insets: the optical profiles of the $\text{TE}_{00}$ and $\text{TM}_{00}$ modes of the quasi-square $\text{Si}_3\text{N}_4$ waveguide. White arrows mark the optical polarization directions. (d) Optical transmission spectrum showing a pair of $\text{TE}_{00}$ and $\text{TM}_{00}$ modes with around 3 GHz frequency spacing. The x-axis is frequency-calibrated relative to the center frequency of the $\text{TE}_{00}$ mode around 1546 nm. Inset shows the relative position of the two modes in the $\omega - k$ space. Reprinted from Ref. [169]. . . . .	144
5.6	From top to bottom are microwave reflection $S_{11}$ , and optomechanical response $S_{21}$ of the actuator 1, 2, 3 (labeled in Fig. 5.5(a)), respectively. Red arrow marks the mechanical mode at 2.958 GHz that is used in the experiment. Reprinted from Ref. [169]. . . . .	146
5.7	(a) Schematic of equivalent electrical circuit model representing one HBAR mode. (b) Upper panel: electro-mechanical $S_{11}$ around the HBAR mode used in the experiment in the main text. Lower panel: Calculated admittance (blue) and MBVD fitting (red). Reprinted from Ref. [169]. . . . .	147
5.8	(a) Optical microscope image of the device. Three actuators are as labeled. (b) Electro-mechanical $S_{11}$ (purple), electrical cross-talk between actuators 2 and 1 $S_{21}$ (pink), and 3 and 1 $S_{31}$ (yellow). The noise floor with probes lifted (gray) is shown for reference. Reprinted from Ref. [169]. . . . .	148
5.9	(a) Experimental setup. Three RF signals are amplified and applied to the AlN actuators with phases controlled individually. An optical switch is used to control the direction of input TE light (red arrows). The output TE light (red arrows) and the generated TM sideband (green arrows) are spatially separated and detected. The white arrow on the device denotes the clockwise rotation of the RF drive in the forward direction. Amp: RF amplifier. ECDL: external-cavity diode laser. FPC: fiber polarization controller. F-PBS: fiber polarization beam splitter. PD: photodetector. (b) Optical transmission spectra with $(\phi_{21}, \phi_{31}) = (120^\circ, -120^\circ)$ (perfect phase matching, red) and $(\phi_{21}, \phi_{31}) = (-120^\circ, 120^\circ)$ (largest phase mismatch, gray). Reprinted from Ref. [169]. . . . .	150

- 5.10 (a) Optical transmission and (b) converted sideband under phase sweep of signals 2 and 3 relative to signal 1, i.e. sweeping  $\phi_{21}$  and  $\phi_{31}$ . Each column is an experimentally measured spectrum under the same  $\phi_{31}$  with spectral span of  $\pm 16$  pm relative to the center wavelength  $\lambda_0$  (1542.6 nm) of the TE<sub>00</sub> mode. Both **b** and **c** are normalized to the input TE light power on chip. The spectra in Fig. 5.9(b) are the slices as labeled by the black dashed lines in (a). Reprinted from Ref. [169]. . . . . 151
- 5.11 (a) From top to bottom are microwave reflection  $S_{11}$ , optomechanical response  $S_{21}$  of the three actuators 1, 2, and 3, respectively. Red arrows mark the mechanical mode at 3.833 GHz that is used in the experiment. (b) Normalized optical transmission of the TE<sub>00</sub> mode under 2D sweep of phases of signals 2 and 3 relative to signal 1, i.e. sweeping  $\phi_{21}$  and  $\phi_{31}$ . Each column is the measured spectrum under the same  $\phi_{31}$  with spectral span of  $\pm 24$  pm relative to the center wavelength  $\lambda_0$  (1553 nm) of the TE<sub>00</sub> mode. (c) Optical transmission spectra along black dashed lines in (b) with reversed phases:  $(\phi_{21}, \phi_{31}) = (120^\circ, -120^\circ)$  (purple, perfect phase matching) and  $(\phi_{21}, \phi_{31}) = (-120^\circ, 120^\circ)$  (green, largest phase mismatch). Reprinted from Ref. [169]. . . 153
- 5.12 (a) Optical transmission spectra of the TE light in the forward (red solid) and backward (gray solid) directions, with increasing RF power from 15 to 20 dBm.  $\Delta\lambda$  is the wavelength detuning of the input laser relative to the TE<sub>00</sub> mode  $\Delta\lambda = \lambda_L - \lambda_{\text{TE},0}$ , with  $\lambda_{\text{TE},0} = 1544.1$  nm. (b) Generated light of the anti-Stokes TM sideband in the forward direction, normalized by the input TE light power. The RF power increase is the same as (a). The anti-Stokes sideband is blue-shifted relative to the input laser by the modulation frequency 2.968 GHz ( $\sim 24$  pm,  $\lambda_{\text{TM}} - \lambda_{\text{TE},0} = \Delta\lambda - 24$ ). The fitted transmission using Coupled Mode Theory (CMT, blue dashed) is also shown in (a) and (b). (c) Conversion efficiency of the TM sideband at  $\Delta\lambda = 0$  and (d) Scattering rate  $g$  as a function of RF power. Experimental data (squares) are grouped as low RF power (red) and high RF power (blue), fitted individually with CMT (solid lines) with different microwave drive to mechanical resonance detuning  $\Delta\Omega = \Omega_d - \Omega_m$ . Horizontal gray dashed line in (d) marks the value of  $g/2\pi \sim 460$  MHz when cooperativity  $C = 1$ . Vertical red and blue dashed lines in (c) and (d) mark the maximum conversion at each detuning. The error bars of each data point represent the standard deviation (SD) from 5 individual measurements. The dependence of isolation on RF power is shown in (c) with experimental data (brown circle) and exponential fitting (brown solid line). Reprinted from Ref. [169]. . . . . 155
- 5.13 (a) Scattering rate  $g$  at different RF power. Green squares are fine sweep between 17 to 18 dBm with 0.1 dBm step. Red and purple squares correspond to the same data in the main text. (b) Electro-mechanical  $S_{11}$  under different RF power around the HBAR mode used in the main text. The resonances of SiO<sub>2</sub> and Si HBARs are as labeled. Reprinted from Ref. [169]. . . . . 157

5.14	(a) Optical microscope image of the device undergoes 30 dBm RF power. Black line denotes the edge of the SiO <sub>2</sub> undercut. Blue lines outlines the Si <sub>3</sub> N <sub>4</sub> microring waveguide and dummy waveguides. (b) SEM image showing the corrugated surface of the Al top electrode. (c) Zoom-in SEM of the region in the red dashed box in (b). Reprinted from Ref. [169]. . . . .	158
5.15	Top panel: Optical transmission spectra in the forward (red) and backward (gray) directions, with increasing center wavelength (left to right). The mode spacing ( $\Delta\omega_{ba}$ ) changes correspondingly due to the different FSRs of the TE <sub>00</sub> and TM <sub>00</sub> modes. Insets show the relative positions of the two modes in the $\omega - k$ space (not to scale). Bottom panel: spectra of isolation ratios varying with the center wavelength. Reprinted from Ref. [169]. . . . .	159
5.16	Comparison of one typical experimental result (the 18 dBm RF power case in Fig. 5.12(a)) with the temporal coupled mode theory based on the Floquet analysis from Ref. [51]. Here the backward direction transmission can also be predicted which shows good agreement with the experiment. . . . .	160
5.17	(a) Transmission of optical pulse trains in the forward (red) and backward (gray) directions for 100 ns (top panel) and 10 ns (bottom panel) pulse width. The power is normalized to the maximum power of the forward pulse in each case. (b) The isolation ratio decreases with narrower pulse width due to the finite photon lifetime ( $\sim 1.5$ ns) in the optical cavity. Experimental data (circle) are fitted with an exponential function (solid line). Reprinted from Ref. [169]. . . . .	161
5.18	Measured data (blue circle) showing that the isolation remains nearly constant around 9 dB (red dashed line) over 30 dB dynamic range of the optical input power. Reprinted from Ref. [169]. . . . .	163
5.19	(a) Normalized optical transmission in the phase-mismatched case (red) and phase-matched cases with increasing RF power applied on each actuator (green, yellow, blue). (b) Conversion to the TM mode under each setting in (a). (c) Isolation ratio by taking difference between the phase-matched case under 28 dBm (blue) and mismatched case (red) in (a). Reprinted from Ref. [169]. . .	164
5.20	(a) Schematic showing encoding information (logical $ 0\rangle$ and $ 1\rangle$ ) in different frequencies of the optical modes ( $\omega_0$ and $\omega_1$ ). Representations of (b) SWAP operation and (c) beam-splitter operation in analogy of a Mach-Zehnder interferometer in space. (d) Cascading of multiple microrings for compact integration. . . . .	166
5.21	(a) Transmission spectrum for TE (red) and TM (green) modes under 10 dBm RF power applied to each actuator. x-axis the the relative detuning of the input laser to the resonance of TE mode. (b) Optical spectrum of the output light when RF power is off (red dashed line) and when RF power is on (solid line). Part of the energy is converted to the TM light (green) with shorter wavelength. The inset shows the beam-splitter operation diagram. . . . .	167



5.22	(a) Optical spectrum in log scale when RF power is on (green) and off (red) for fixed input laser frequency at the resonance of the TE mode. (b) Same optical spectrum as in (a) in linear scale. The inset shows the SWAP operation diagram. . . . .	168
5.23	Transmission spectrum for TE (red) and TM (green) light when input light is aligned with the TM mode (upper) and TM mode (lower), which demonstrates the bi-directional conversion between TE and TM modes. . . . .	169
5.24	Comparison of insertion loss and isolation among several experimental realizations of optical isolators. These devices are classified by the level of integration into monolithic (green), and non-monolithic (red). Devices relying on magneto-optic material (blue) is separately listed while others are all magnetic-free. The three devices with 950, 850, and 600 nm gaps shown in this work are listed separately as solid green squares. The references are as labeled. Reprinted from Ref. [169]. . . . .	170
6.1	(a) Schematic showing the coupling between the mechanical mode and two optical modes. The vibration of mechanical resonator scatters pump light in mode $a$ ( $\omega_a$ ) into higher frequency mode $b$ ( $\omega_b$ ). The inset shows the quantum picture of the process where an incoming phonon scatters one pump photon into higher frequency signal photon. (b) Schematic for the triple-mode optomechanical system, where the TE mode is pumped which couples the mechanical and TM modes. . . . .	179
6.2	(a) Schematics showing the cascaded coupling efficiencies that determine overall system efficiency, including input coupling efficiency from microwave channel to mechanical cavity $\eta_{\text{ex,m}}$ , intra-cavity conversion efficiency from mechanical phonon to photon $\eta_{\text{in}}$ , and output coupling efficiency from optical cavity to fiber $\eta_{\text{ex,opt}}$ . (b) The dependence of internal efficiency on enhanced cooperativity $C$ . . . . .	182
6.3	(a) Electromechanical $S_{11}$ and (b) optomechanical $S_{21}$ of one actuator of the isolator device. The red arrow denotes the mode that is analyzed. . . . .	187
6.4	(a) Schematic showing the proposed piezo-optomechanical quantum converter. By driving the piezoelectric actuator with microwave signal, the input pump light is scattered to output signal photon with high quantum efficiency. (b) Cross-section along the black dashed line in (a). . . . .	188
6.5	(a) Vertical stress distribution of one typical HBAR mode at 4.4 GHz. (b) Electric field distribution of TE and TM modes with close frequency spacing. The white arrows denote the magnitude and direction of the electric field. . . . .	189

6.6	(a) Dependence of the required pump optical power to achieve $C = 1$ (left Y axis) and total optical Q (right Y axis) on external coupling strength for fixed $g_0 = 1$ kHz. Three different intrinsic Q are chosen that are experimentally realizable. M is short for Million. (b) Dependence of the required pump power on the optomechanical coupling strength $g_0$ under critical coupling regime for three different optical Q. The green dashed line show the power level of 1 mW and red dashed line shows the position of 1 kHz $g_0/2\pi$ as estimated in simulation. . . . .	190
6.7	2D contour plot of the required pump power for various optical Q and $g_0$ under critical coupling. The mechanical loss rate is assumed to be 1 MHz. The red (yellow) star indicates the proposed (current measured) device parameters. .	191
6.8	(a) Optical microscope image of the fabricated device with two AlN actuators fabricated on the same $\text{Si}_3\text{N}_4$ microring resonator with 22 $\mu\text{m}$ radius (THz FSR). (b) Zoom-in SEM of the device in the red dashed box in (a). (c) Optical image of the chip edge. The inset shows the pre-off of the Si at the chip edge to compensate for the etching during release in the future. (d) Zoom-in SEM of the chip edge after the breaking of the suspended oxide membrane. . . .	193
6.9	(a) Nonuniform releasing of the optical microring resonator with $\text{XeF}_2$ . (b) Releasing of the oxide membrane with $\text{SF}_6$ which generates a uniform circle.	195
6.10	Optical transmission spectrum for different devices. The red dashed line is the Lorentz fitting with linewidth of 137 MHz, which indicates an optical Q of 1.4 Million. . . . .	196
6.11	(a) Optical transmission spectrum of the TE mode. It is fitted with the Lorentz function (red dashed line), with linewidth of 153 MHz. (b) Electromechanical $S_{11}$ and optomechanical $S_{21}$ measured on one actuator. . . . .	197
6.12	(a) Electromechanical $S_{11}$ of one actuator. (b) Electromechanical $S_{21}$ between the two actuators to measure the cross-talk between them. . . . .	198
7.1	Diagram illustrating the interaction scheme between photon, phonon, and superconducting (SC) qubit. Piezoelectric material is the core for realization of this hybrid quantum system. . . . .	202
7.2	The coupling between optical, mechanical, and SC qubit devices with different structures has been studied and demonstrated. The black link shows the demonstrations from the literature. The red link is the work of this thesis. The red dashed link hasn't been achieved yet. . . . .	203
7.3	Layout for future hybrid quantum system that leverages different modules from photonic, phononic, and superconducting circuits. The function, material, devices, and structure for each module are listed. The optical input/output (I/O) ports serves to communicate the quantum information. . . . .	204



7.4	Schematic of a proposed fully packaged hybrid quantum chip. The SC qubit is protected from the stray light from the photonic circuits. . . . .	205
7.5	(a) Schematic for a programmable photonic circuits made from a mesh of Mach-Zehnder Interferometers (MZI). (b) Example of one MZI where the optical phases of the top and bottom arms will be actuated for controlling the path of photons. . . . .	206
7.6	Top: The coupling between optical mode with its adjacent mode (red), the next-nearest neighbour (green), and the next-next-nearest neighbour (yellow). Bottom: equivalent synthetic frequency lattices in 1D, 2D, and 3D. The black dot indicates one photon. . . . .	208
7.7	Schematic showing the multiplex of microwave tones for the control of multiple qubits with the same device. The spacing between the two optical modes are engineered by the FSR difference between them, where each pair can be coupled to HBAR modes with equidistant spacing. Each RF tone can be addressed to each qubit by flux tuning the qubit transition frequency. . . .	211
A.1	Model of acoustic wave propagation in a non-piezoelectric material. (a) Acoustic wave propagates in forward and backward directions in a layer of non-piezoelectric material. The layer thickness is $d$ with two boundaries located at $z_1$ and $z_2$ . The wave distribution is solely determined by the boundary conditions of force $F$ and velocity $v$ . (b) Equivalent circuit model describing acoustic wave transmission. (c) The two boundaries can be correlated by a transfer matrix $M$ which is a function of the acoustic impedance and the propagation length. Reprinted from Ref. [12]. . . . .	242
A.2	Model of acoustic wave propagation in a piezoelectric material. (a) Equivalent circuit Mason model that describes the excitation and propagation of acoustic waves in the piezoelectric layer. The three resistors represent the propagation of acoustic waves, while the transformer represents energy conversion between electrical and mechanical domain. (c) Three ports representation of the piezoelectric actuator. Reprinted from Ref. [12]. . . . .	244
A.3	Electromechanical model of the actual device in this work. (a) Vertical stacking structure of the whole device. (b) Equivalent circuit model by connecting adjacent layers. The end ports are shorted as required by the free boundary condition. (c) Transfer matrix chain that connects each interface. The input impedance at each port can be correlated and calculated by the multiplication of matrices in between. Reprinted from Ref. [12]. . . . .	245
A.4	Measured (a) and calculated (b) $S_{11}$ reflection parameter, showing much similarity in terms of varied envelope and its period. Reprinted from Ref. [12]. .	247

A.5	Four different regions are labeled by number in the order from top to bottom corresponding to Table A.2. The green dashed lines denote the FSR of each region and the corresponding effective length $d_{\text{eff}}$ is labeled on the right. The bottom insets show the schematics of the acoustic stress wave distribution for each region, illustrating the locations of interfaces relative to the stress wave. Reprinted from Ref. [12]. . . . .	249
A.6	(a) Measured $S_{11}$ response (top) and calculated effective electromechanical coupling coefficient $k_{\text{t,eff}}^2$ (bottom). The coupling reaches a maximum value of 0.15% around 4.3 GHz. (b-c) Measured $S_{21}$ response of the TE and TM mode (top) and corresponding normalized product of acousto-optic overlap and $k_{\text{t,eff}}^2$ (bottom). When the node of the acoustic stress wave is located at the center of the waveguide, the acousto-optic overlap integral $\Gamma$ becomes zero and thus causes notches in the $S_{21}$ response. Reprinted from Ref. [12]. . . . .	252
B.1	(a) Schematic of optical waveguide cross-section with $\text{Si}_3\text{N}_4$ (blue) fully embedded in isotropic $\text{SiO}_2$ cladding. The definition of height $h$ , bottom width $w_b$ , and sidewall angle $\theta$ are as labeled. (b) False colored SEM showing the cross-section of the fabricated optical waveguide. The sidewall angles are as labeled. (c) Simulations suggests that the required $h$ and $w_b$ combination produces close $\text{TE}_{00}$ and $\text{TM}_{00}$ modes around 1550 nm with $\Delta m = 1$ (red), $\Delta m = 4$ (green), $\Delta m = 5$ (purple). Different sidewall angles are studied and labeled. The blue shaded area indicates the variation of waveguide height in the fabrication. Reprinted from Ref. [169]. . . . .	255
B.2	(a) Measured $\text{TE}_{00}$ and $\text{TM}_{00}$ mode anti-crossing around 1540 nm. The wavelength $\lambda_0$ is the center wavelength between $\text{TE}_{00}$ and $\text{TM}_{00}$ . (b) Simulated height $h$ that generates close $\text{TE}_{00}$ and $\text{TM}_{00}$ modes, and (c) corresponding FSR difference $\Delta\text{FSR}$ for different sidewall angles and $\Delta m$ . The variation of width $w_b$ is included as lower (810 nm) and higher (830 nm) bounds of each $\Delta m$ plot. The blue shaded areas are experimental variations. Reprinted from Ref. [169]. . . . .	256

## LIST OF SYMBOLS

$r$	radius of the optical microring
$\lambda_0$	optical resonant wavelength in the vacuum
$n_{\text{eff}}$	effective refractive index of the optical waveguide
$n$	effective refractive index of the optical material
$m$	azimuthal order of the optical mode
$c$	velocity of light in the vacuum
$\omega_0$	resonant angular frequency of the optical mode
$\hat{a}$	intra-cavity optical field amplitude
$\kappa$	total loss of the optical mode
$\kappa_i$	intrinsic loss of the optical mode
$\kappa_{\text{ex}}$	external coupling loss of the optical mode
$\hat{a}_{\text{in}}$	amplitude of input optical field
$\hat{a}_{\text{out}}$	amplitude of output optical field of mode $a$
$\Delta$	relative detune between the laser and the resonant frequency of the optical mode
$\varepsilon$	mechanical strain
$\sigma$	mechanical stress
$D$	electric displacement
$E$	electric field
$S_{IJ}$	compliance coefficient
$d_{iJ}$	piezoelectric coefficient
$\epsilon_{ij}$	permittivity of dielectric
$p_{ij}$	strain-optic coefficient
$C_i$	stress-optic coefficient
$E_{\text{mod}}$	Young's modulus
$G$	shear modulus
$\nu$	Poisson ratio
$\epsilon_0$	vacuum permittivity
$\mathbf{Q}$	mechanical displacement

$x_{\text{ZPF}}$	zero-point fluctuation of the mechanical mode
$m_{\text{eff}}$	effective mass of the mechanical resonator
$\Omega_{\text{m}}$	resonant frequency of the mechanical resonator
$\rho$	density of the material
$g_0$	single photon optomechanical coupling rate
$g$	enhanced optomechanical coupling rate
$\tau_{ph}$	intra-cavity photon lifetime
$f_{\text{rep}}$	repetition rate
$f_{\text{CEO}}$	carrier-envelope offset frequency
$S_{11}$	electromechanical response
$S_{21}$	optomechanical response
$v_g$	group velocity of light
$v_{ph}$	phase velocity of light
$k_{\text{t,eff}}^2$	electromechanical coupling efficiency
$\eta$	quantum conversion efficiency
$I$	optical pump power
$R_{\text{PD}}$	responsivity of the photo-detector
$\Gamma$	total loss of the mechanical resonator
$\Gamma_{\text{ex}}$	external coupling loss of the mechanical mode
$C_0$	single-photon cooperativity
$C$	enhanced cooperativity
$\Delta\omega_{ba}$	angular frequency difference between optical modes $a$ and $b$
$k_m$	wavenumber of the mechanical mode
$\Delta k_{ba}$	wavenumber difference between optical modes $a$ and $b$
$\Delta m_{ba}$	azimuthal order difference between optical modes $a$ and $b$
$H_I$	interaction Hamiltonian of the system
$\hbar$	reduced Planck constant
$\Omega_d$	microwave drive angular frequency
$P_{\text{in}}$	input microwave power

$P_{\text{in,opt}}$	input optical pump power
$\bar{n}$	average intra-cavity photon/phonon number
$\omega_L$	angular frequency of input laser
$T$	transmission of light
$R_m$	motional resistance of the mechanical mode
$L_m$	motional inductance of the mechanical mode
$C_m$	motional capacitance of the mechanical mode
$Z$	impedance
$Y$	admittance
$\Delta\lambda$	wavelength detuning of the input laser relative to the optical mode
$J$	modulation-induced coupling strength between optical modes
$k_B$	Boltzmann constant
$\eta_{\text{ex,m}}$	coupling efficiency from microwave channel the mechanical cavity
$\eta_{\text{ex,opt}}$	coupling efficiency from the optical cavity to the bus waveguide
$A_0$	magnitude of the intra-cavity optical field of the carrier
$A_+$	magnitude of the intra-cavity optical field of the anti-Stokes sideband
$A_{0,\text{out}}$	output electric field magnitude of the carrier
$A_{+,\text{out}}$	output electric field magnitude of the anti-Stokes sideband
$A_{\text{in}}$	electric field magnitude of the input pump light
$B$	magnitude of the intra-cavity acoustic field
$U$	output microwave voltage of the photodetector
$P_{\text{out},m}$	output microwave power of the photodetector
$P_{0,\text{out}}$	output optical power of the carrier
$P_{+,\text{out}}$	output optical power of the anti-Stokes sideband
$V_\pi$	applied voltage that induces $\pi$ phase shift of the optical field in the microring
$\Omega_R$	Rabi oscillation frequency

## ABBREVIATIONS

AlN	Aluminum Nitride
AlScN	Scandium doped AlN
LiNbO <sub>3</sub>	Lithium Niobate
Si <sub>3</sub> N <sub>4</sub>	Silicon Nitride
PZT	Lead Zirconate Titanate
GaP	Gallium Phosphide
GaAs	Gallium Arsenide
AOM	Acousto-optic Modulation
EOM	Electro-optic Modulation
EO	Electro-optical
HBAR	High overtone Bulk Acoustic wave Resonances
BAW	Bulk Acoustic Waves
SAW	Surface Acoustic Waves
SC	Superconducting
OMC	Optomechanical Crystal
ECDL	External Cavity Diode Laser
EDFA	Erbium-Doped Fiber Amplifier
ESA	Electrical Spectrum Analyzer
FPC	Fiber Polarization Controller
PBS	Polarization Beam Splitter
DUT	Device Under Test
OSA	Optical Spectrum Analyser
OSC	Oscilloscope
PD	Photo-Diode
VNA	Vector Network Analyzer
RIE	Reactive Ion Etching
DRIE	Deep Reactive Ion Etching
CMP	Chemical Mechanical Polishing

CMT	Coupled Mode Theory
CW	Clockwise
CCW	Counter-clockwise
EIT	Electromagnetic Induced Transparency
OMIT	Optomechanically Induced Transparency
DC	Direct Current
RF	Radiofrequency
PIC	Photonic Integrated Circuits
OFC	Optical Frequency Comb
DKS	Dissipative Kerr Soliton
PE	Photoelastic
MB	Moving Boundary
MEMS	Micro-Electro-Mechanical System
LiDAR	Light Detection and Ranging
IDT	Interdigital transducer
TIR	Total Internal Reflection
TE	Transverse Electric
TM	Transverse Magnetic
FSR	Free Spectrum Range
GVD	Group Velocity Dispersion
FEM	Finite Element Method
ZPF	Zero Point Fluctuation
PDH	Pound–Drever–Hall
LPCVD	Low Pressure Chemical Vapor Deposition
PVD	Physical Vapor Deposition
SEM	Scanning Electron Microscopy
SNR	Signal to Noise Ratio
FFT	Fast Fourier Transform
FMCW	Frequency Modulated Continuous Wave

MZI	Mach-Zehnder interferometer
CEO	Carrier-Envelope Offset
FWM	Four Wave Mixing
CMOS	Complementary Metal-Oxide Semiconductor
MI	Modulation Instability
MS	Multi-Soliton
PID	Proportional–Integral–Derivative
BPF	Band-pass Filter
FBG	Fiber Bragg Grating
LDV	Laser Doppler Vibrometer
MBVD	Modified Butterworth-Van Dyke model
Ce:YIG	Cerium-substituted Yttrium Iron Garnet
SBS	Stimulated Brillouin Scattering
RWA	Rotating-Wave Approximation
FDFD	Finite Difference Frequency Domain
PLD	Pulsed Laser Deposition
IL	Insertion Loss
WGM	Whispering Gallery Modes
QKD	Quantum Key Distribution
QRAM	Quantum Random Access Memory
cQAD	circuit Quantum Acousto-Dynamic
TLS	Two-Level-System
ONN	Optical Neural Networks



## ABSTRACT

Integrated photonics has provided an elegant way to bring the table-top bulky optical systems from the research lab to our daily life, thanks to its compact size, robustness, and low power consumption. Over the past decade, Silicon Nitride ( $\text{Si}_3\text{N}_4$ ) photonics has become a leading material platform, benefiting from its record-low loss, large Kerr nonlinearity, and compatibility with the foundry process. However, the lack of electro-optical effect makes it challenging to actively tune the  $\text{Si}_3\text{N}_4$  photonic circuits for advanced applications, such as LiDAR, spectroscopy, and microwave photonics. During my Ph.D. research, I have developed a new platform of piezoelectric control of  $\text{Si}_3\text{N}_4$  photonics through stress-optical effect. By integrating an Aluminum Nitride (AlN) piezoelectric actuator, I demonstrated the tuning of a  $\text{Si}_3\text{N}_4$  optical microring resonator at sub-microsecond speed with nano-Watt power consumption. Microwave frequency (GHz) acousto-optic modulation (AOM) is realized by exciting high-overtone bulk acoustic wave resonant modes (HBAR), which are tightly confined in an acoustic Fabry-Pérot cavity. Maximum of 9.2 GHz modulation is achieved which falls into the microwave X-band. Both released and unreleased mechanical structures are thoroughly studied, aiming at high efficiency, low-cost, and robustness.

The applications of the Piezo-on-Photonic platform are extensively explored in the quasi-DC and high frequency regimes. By working as a stress-optical tuner at low frequency, it allows us to actively tune a Kerr frequency comb into different states, and stabilize it over several hours, which can serve as the light source for the next-generation chip-based LiDAR engine. On the other hand, the GHz frequency AOM has helped me demonstrate a magnetic-free integrated optical isolator through spatio-temporal modulation. Three AlN HBAR actuators are integrated closely on the same  $\text{Si}_3\text{N}_4$  microring resonator, which generate an effective rotating acoustic wave and break the transmission reciprocity of the light. A maximum of 10 dB isolation is achieved under 300 mW total radiofrequency power, with minimum insertion loss of 0.1 dB. Finally, the application of the same technique in quantum microwave to optical converter is theoretically analyzed, showing potential for building future quantum networks. The initial experimental attempt and outlook for future improvements are discussed. In conclusion, this thesis investigated a novel Piezo-on-Photonic platform for

flexible and efficient control of the  $\text{Si}_3\text{N}_4$  photonic system, and its applications in a wide variety of advanced devices are demonstrated, with the potential of being key building blocks for future optical systems on-chip.

# 1. INTRODUCTION

## 1.1 Background

Integrated photonics [1], [2] has enabled chip-scale optical systems with compact sizes, portable weight, and low power consumption, which have been translated from table-top research setups to commercial products. With the advancement of nano-fabrication technology, there have been major achievements in integrated semiconductor lasers [3]–[8], modulators [9]–[16], photodetectors [17], [18], as well as ultralow-loss PICs [19]–[26]. Importantly, the nonlinearities of ultralow-loss Photonic Integrated Circuits (PICs) have been explored and harnessed [27], [28], giving rise to nonlinear photonics such as optical frequency comb (OFC) generation [29]. Formed in Kerr-nonlinear optical microresonators, dissipative Kerr soliton (DKS) microcombs [28]–[30] constitute miniaturized, coherent, broadband OFCs with repetition rates in the millimeter-wave to microwave domain, and are amenable to heterogeneous integration with III-V/Si lasers [7], [31]–[33].

Major progress has been made in the past decade in developing various platforms [34], including Si<sub>3</sub>N<sub>4</sub> [22]–[25], LiNbO<sub>3</sub> [19], [35]–[37], AlN [38], [39] and AlGaAs [21], [40]. Among the materials developed thus far for integrated nonlinear photonics, Si<sub>3</sub>N<sub>4</sub> has attracted intense efforts due to its wide transparency window from the mid-ultraviolet (400 nm) to mid-infrared, ultra-low linear losses, absence of two photon absorption in the telecommunication band, space-compatibility [41], large Kerr nonlinearity ( $\chi^{(3)}$ ), and wide geometric flexibility for waveguide dispersion engineering [28]. Silicon Nitride has been the material of choice for soliton microcomb generation [42], and supercontinuum generation [28], optical filters [43], gyroscopes [44], and optical interconnects [45]. Recent advances of Si<sub>3</sub>N<sub>4</sub>-based dissipative Kerr soliton microcombs, have included octave-spanning comb spectra [46], [47], ultra-low initiation power [31], [32], [48], and microcomb repetition rates in the microwave domain [49]. Integrated Si<sub>3</sub>N<sub>4</sub> soliton microcombs which are fully frequency-stabilized and operated with low electrical power would enable chip-based optical [50] and microwave [49] frequency synthesizers with ultrahigh frequency precision and a compact form factor. Meanwhile, high- $Q$  Si<sub>3</sub>N<sub>4</sub> microresonators have also been used recently to create ultralow-noise semiconductor lasers [5], [7] whose performance is on par with advanced fiber lasers.

Reliable and fast resonance tuning of  $\text{Si}_3\text{N}_4$  microring resonators is becoming an important asset and requirement for a number of applications in integrated nonlinear photonics. For example, high bandwidth tuning allows microcomb repetition rate stabilization [50], resonance tuning for tunable filters, and compensating fabrication errors. Likewise, recently emerged platforms such as spatio-temporal modulation based optical non-reciprocity [51] and topological optical band structures in synthetic frequency dimension [52]–[54] both require GHz speed modulation within optical micro-resonators, which poses stringent requirements on the cross-talk and size.

However, due to the inversion symmetry, and thus the lack of  $\chi^{(2)}$  nonlinearity, it is difficult to electrically modulate the refractive index of  $\text{Si}_3\text{N}_4$ . Traditionally, the thermo-optical effect is employed to fulfill the tuning requirement [55]–[59] which, presents low tuning speed ( $\sim 1$  ms), high power consumption ( $\sim 1$  mW), and large thermal cross-talk. These drawbacks make it incompatible with large-scale integration and cryogenic applications [60]. Although hybrid integration with various electro-optical materials, e.g., graphene [61], lead zirconate titanate (PZT) [62], lithium niobate ( $\text{LiNbO}_3$ ) [63], and monolayer  $\text{WS}_2$  [64] has made significant progresses, there are still remaining challenges related to CMOS-compatibility, fabrication complexity, optical losses, and dispersion engineering. To fully utilize the maturity and advantages of  $\text{Si}_3\text{N}_4$  photonics, new tuning mechanisms which retain the original optical properties are needed.

The stress-optical effect, discovered over a hundred years ago, has recently gained attention for its role in the modulation of  $\text{Si}_3\text{N}_4$  waveguides and microring resonators both theoretically [65], [66] and experimentally [67]–[73], thanks to the advances in Micro-Electro-Mechanical Systems (MEMS) [74], [75]. By either piezoelectrically [71], [72] or electrostatically [76], [77] applying an external force to the optical waveguide, the deformation of the mechanical structure changes the effective refractive index of the waveguide by generating stresses and modifying the shape of the waveguide (see Fig. 1.1(a)). While the former is the so-called **photoelastic** [65] effect, the latter is the well-known **moving boundary** [78] effect. While electrostatic method has been successfully applied for mechanically tunable photonic waveguides and resonators (e.g., directional coupler [79], optical switches [80], [81], phase shifter [82]), there remains challenges that need to be addressed in the future. For

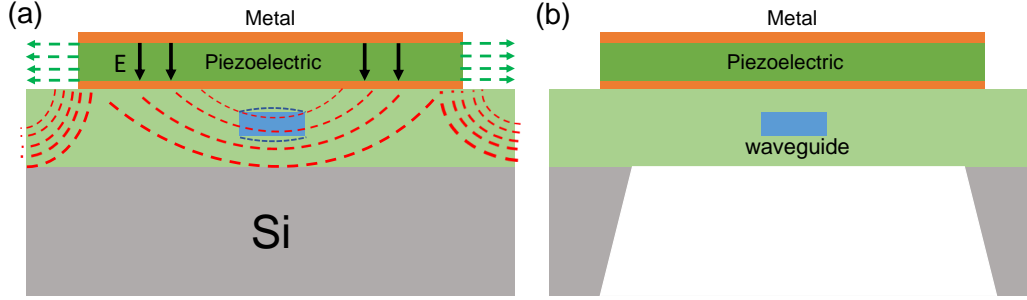


**Figure 1.1.** Schematics of stress-optical tuning. (a) A piezoelectric actuator is placed on top of an optical waveguide (blue). Upon external electric signal, the piezoelectric film will deform and generate stress distribution crossing the waveguide (red dashed lines). The boundary of the waveguide will displace (dark blue dashed lines) and thus change the shape of the waveguide. (b) Released structure where the substrate is removed to suspend the actuator for larger mechanical deformation.

example, the optical waveguides have to be suspended which may compromise its robustness and large-scale integration. Also, the air-cladded waveguide would present higher optical losses, subjecting to the scattering from particles in the air. The piezoelectric method would circumvent these problems by fully cladding the waveguide in dielectric material, and the stresses are generated by deforming the piezoelectric material upon applying electric field. Thus, this thesis mainly focuses on the piezoelectric actuation of integrated photonic devices.

The piezoelectric controlled photonic devices can be categorized in terms of piezoelectric material, whether the mechanical structure is released, and the frequency range the device is working at. Both of these aspects will be studied thoroughly in this thesis in the following chapters. Two main piezoelectric materials that are widely used in the literature are **Aluminum Nitride (AlN)** and **Lead Zirconate Titanate (PZT)**. They both have their own pros and cons. While PZT shows  $>20$  times larger piezoelectric coefficient, AlN advances in better linearity, smaller dielectric constant (thus smaller capacitance and shorter charge-discharge time), and zero hysteresis (PZT has ferroelectricity). Therefore, the right material should be chosen depending on specific application requirements. Compared with the thermal-optical tuning, they both show much less power consumption (sub- $\mu\text{W}$ ) and faster actuation speed ( $\mu\text{s}$ ), which makes the piezoelectric tuning suitable for large-scale, cryogenic, fast reconfigurable applications, such as high-refresh-rate LiDAR source [83], pro-

grammable photonic circuits [73], and integrated tunable laser [84]. To further increase the tuning efficiency, the mechanical structure that hosts the photonic waveguides can be suspended to have larger deformation (see Fig. 1.1(b)). This is the so-called “released” structure where the device is released from the substrate. However, released structure usually presents low mechanical resonant frequencies from kHz to MHz, which ultimately limits the tuning speed and requires extra cares for damping the mechanical ringing.

Besides quasi-DC operation (DC-MHz), when driving at microwave frequencies (GHz), sub-micron wavelength acoustic waves are excited which enable efficient acousto-optic modulation (AOM). AOM is conventionally widely adopted in laser systems, spectroscopy, and atomic physics because of its flexibility in controlling the light direction, intensity, and frequency precisely. However, traditional AOMs are realized by making interdigital transducer (IDT) on bulky piezoelectric crystal (e.g., fused silica,  $\text{LiNbO}_3$ , chalcogenide glasses) and works mainly for free space light, which consumes a lot of electrical power (few Watts), and limits the maximum working frequency to 100 MHz. It is only within most recent decade that the integration of AOM into chip scale has been successfully demonstrated, extending the modulation frequency beyond 10 GHz [14], [85]–[91]. Most of these demonstrations excite the **Surface Acoustic Wave (SAW)** by fabricating co-planar IDT electrodes with sub-micron interdigital fingers’ width, thanks to the advances in nano-fabrication technologies. Since the acoustic waves transmit along the surface, to have efficient optical modulation, the optical waveguides have to be brought towards the surface of the substrate by either directly etching trenches on the surface of the piezoelectric film [14], or burying the waveguide within sub-micron away from the top surface of the cladding [92] (see Fig. 1.2(a-b)). These would inevitably scatter light into the environment and increase the optical loss.

In this thesis, I proposed and demonstrated a new way of acousto-optic modulation by exciting **High Overtone Bulk Acoustic Waves Resonances (HBAR)** (see Fig. 1.2(c)). Although HBAR has been ubiquitously deployed in modern wireless systems for high quality filters [93], [94] and oscillators [95], [96], and coupled with quantum systems such the superconducting qubit [97]–[99] and the Nitrogen Vacancy center [100], [101], it is the first time for it to couple with an integrated photonic device. Different from SAW, Bulk Acoustic Waves (BAW) transmit vertically into the substrate and perpendicular to

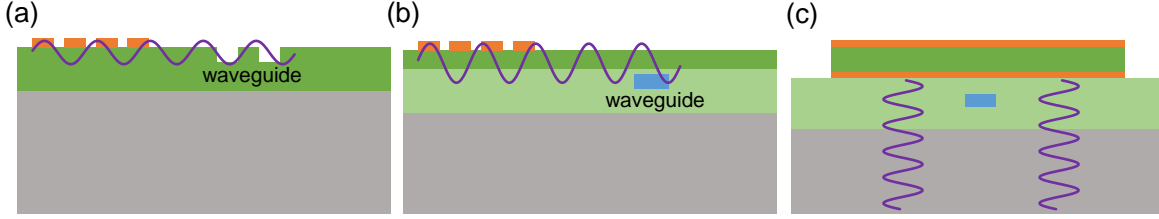


**Figure 1.2.** Comparison of AOM between Surface and Bulk acoustic waves. Typical AOM via surface acoustic wave where the optical waveguide is formed by either (a) etching trenches into the piezoelectric film or (b) embedding the waveguide near surface. The surface acoustic wave (violet curve) is excited by interdigital electrode fingers (orange). (c) AOM via bulk acoustic waves proposed in this work, which is excited vertically towards the substrate by piezoelectric actuator.

optical paths. An acoustic Fabry-Pérot cavity is naturally formed by the top and bottom surfaces of the substrate, which confines tightly the acoustic energy and forms a rich family of acoustic resonant modes. The coupling between vertical acoustic waves and in-plane optical circuits makes it possible for independent optimization of the actuator and optical components. Thus, waveguides can be fully cladded for preserving high quality factor and desirable frequency dispersion. Furthermore, the high lateral acoustic mode confinement enables low cross-talk and compact integration.

Therefore, the simple but efficient Piezo-on-Photonics stress-optical platform demonstrated in this work, either working as quasi-static tuner or GHz frequency optical modulator, would find widespread applications in  $\text{Si}_3\text{N}_4$  microwave photonics [102], such as the repetition rate stabilization and tuning of soliton microcombs via injection-locking [103], on-chip optomechanical frequency comb generation [104], and comb-assisted microwave photonic filters [105]. Specifically, I will show later the application in the piezoelectric control of Kerr micro-comb generated in the  $\text{Si}_3\text{N}_4$  microring resonator. Also, the GHz frequency AOM is used to demonstrate a fully electrically controlled, magnetic-free optical isolator integrated on chip. The application of AOM in quantum microwave to optical conversion is theoretically studied and the first experimental realization will be discussed.

## 1.2 Piezoelectric tuning of a $\text{Si}_3\text{N}_4$ microring resonator

This section gives a brief overview of the working principle and theoretical treatment of the piezoelectric actuation on a  $\text{Si}_3\text{N}_4$  microring resonator demonstrated in this work. The cross-section of the typical device structure is as shown in Fig. 1.1(a), where a thin film of piezoelectric material is sandwiched between top and bottom metal electrodes and placed directly on top of the optical waveguide. By applying external electric field, the piezoelectric film will expand or squeeze, which generates stress and strain around the optical waveguide and changes the materials' refractive index through stress-optical effects. In the following, detailed description of each component will be given and the basic concepts will be reviewed in order to be prepared for the experimental results in the following chapters.

### 1.2.1 Optical waveguide and ring resonator

The main principle of an optical waveguide is based on the well-known Total Internal Reflection (TIR) where light will get fully reflected when it's injected from high refractive index to low index material and the incident angle is bigger than Brewster's angle. In such way, light will be guided in a channel formed by a waveguide core with high refractive index that is surrounded by the waveguide cladding with low refractive index, as shown in Fig. 1.3(a). Since the  $\text{Si}_3\text{N}_4$ 's index  $n = 2$  is bigger than  $\text{SiO}_2$  whose index is 1.44, light will be confined inside the  $\text{Si}_3\text{N}_4$  waveguide and transmit with ultra-low loss (1 dB/m [24]). Different optical modes can be supported in the same waveguide by solving the eigenmode of the Maxwell equations. In this work, I mainly focus on the fundamental Transverse Electric (TE) and Transverse Magnetic (TM) modes with different optical polarization. As shown in Fig. 1.3(b), while the direction of TE's electric field is parallel to the surface of the substrate, that of the TM mode is vertical.

As shown in Fig. 1.3(c), an optical ring resonator consists of a straight bus waveguide and an adjacent microring. Light is injected from one port of the bus waveguide and evanescently coupled into the optical microring through the narrowest region between the bus and the ring. The coupling gap can be controlled by the design during fabrication. The narrower the gap, the stronger the external coupling rate  $\kappa_{\text{ex}}$  from the bus to the ring. As light is injected



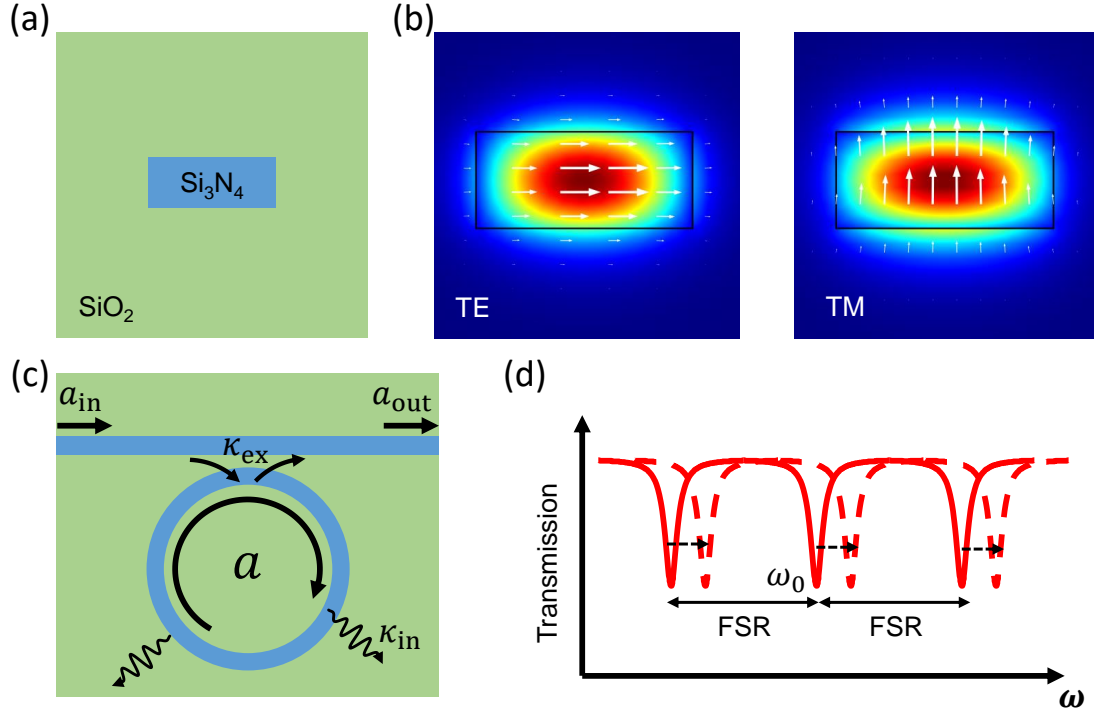


**Figure 1.3.** (a) Cross-section of an optical waveguide. (b) Electric field distribution for TE and TM optical modes. The white arrows denote the direction of electric field. (c) Top view of an optical microring resonator. (d) Transmission spectrum of a typical optical resonator. The dashed curve shows the shifting of the optical resonances under piezoelectric tuning.

into the ring, constructive interference will largely enhance the light intensity if perimeter of the ring is an integer number of the optical wavelength, the so-called resonant condition:

$$2\pi r = m\lambda_0/n_{\text{eff}} \quad (1.1)$$

where  $r$  is the radius of the ring,  $\lambda_0$  is the optical wavelength in vacuum,  $n_{\text{eff}}$  is the effective refractive index of the optical waveguide,  $m = 1, 2, 3, \dots$  is an integer number. Equation 1.1 can be expressed in terms of optical angular frequency  $\omega_0$  as:

$$\omega_0 = \frac{mc}{rn_{\text{eff}}} \quad (1.2)$$

where  $c$  is the velocity of light in the vacuum. The application of stress and strain to the waveguide will both alter the radius  $r$  and the effective refractive index  $n_{\text{eff}}$ . By taking differential on both side of Eq. 1.2, the perturbation on the resonant angular frequency  $\omega_0$  can be found as:

$$\frac{\Delta\omega_0}{\omega_0} = -\frac{\Delta n_{\text{eff}}}{n_{\text{eff}}} - \frac{\Delta r}{r} \quad (1.3)$$

where the relative change of the resonant angular frequency is the sum of the relative change of the index and radius, and the minus sign means they change in different directions. Equation 1.3 shows intuitively the basic effects of piezoelectric tuning on the optical microring resonator. More rigorous analysis that incorporates the perturbation theory will be given in the following sections.

From Eq. 1.2, it can be found that for each integer  $m$  there exists an optical resonance, and they are equally spaced with the spacing defined as the Free Spectrum Range (FSR), as shown in Fig. 1.3(d). We should note that because of the material and geometric dispersion,  $n_{\text{eff}}$  is a function of frequency, so FSR is only locally equidistant, and related with higher order dispersion such as group velocity dispersion (GVD). Following the Coupled Mode Theory (CMT) [106], the dynamic equation of light in an optical cavity can be described as:

$$\frac{d}{dt}\hat{a} = -(\text{i}\Delta + \frac{\kappa}{2})\hat{a} + \sqrt{\kappa_{\text{ex}}}\hat{a}_{\text{in}} \quad (1.4)$$

$$\hat{a}_{\text{out}} = \hat{a}_{\text{in}} - \sqrt{\kappa_{\text{ex}}}\hat{a} \quad (1.5)$$

where  $\Delta = \omega_0 - \omega_l$  is the relative detune between the laser and the optical resonant angular frequency.  $\hat{a}$  is the intra-cavity optical field amplitude which is normalized such that  $\|\hat{a}\|^2$  is the intra-cavity photon number.  $\|\hat{a}_{\text{in}}\|^2$  is the input photon flux  $P/\hbar\omega_l$  where  $P$  is the optical power.  $\kappa$  is the total loss of the optical cavity which is the sum of the intrinsic loss  $\kappa_i$  of the cavity and the external coupling rate  $\kappa_{\text{ex}}$ . At steady state, the intra-cavity optical field and the output optical amplitude can be found as:

$$\hat{a} = \frac{\sqrt{\kappa_{\text{ex}}}\hat{a}_{\text{in}}}{\text{i}\Delta + \frac{\kappa}{2}} \quad (1.6)$$

$$\hat{a}_{\text{out}} = \frac{\text{i}\Delta + \frac{\kappa}{2} - \kappa_{\text{ex}}}{\text{i}\Delta + \frac{\kappa}{2}}\hat{a}_{\text{in}} \quad (1.7)$$

The optical power transmission can thus be calculated as:

$$T = \left\| \frac{\hat{a}_{\text{out}}}{\hat{a}_{\text{in}}} \right\|^2 = \frac{\Delta^2 + (\frac{\kappa}{2} - \kappa_{\text{ex}})^2}{\Delta^2 + \frac{\kappa^2}{4}} \quad (1.8)$$

This is the traditional expression for an optical resonance with Lorentz shape. When  $\kappa_{\text{ex}} = \kappa_i = \kappa/2$ , the optical ring is critically coupled to the bus waveguide such that the transmission at the resonant frequency ( $\Delta = 0$ ) is 0. Besides, depending on the relative size of the external and intrinsic losses, the optical resonance can be classified into under-coupled ( $\kappa_{\text{ex}} < \kappa_i$ ) and over-coupled ( $\kappa_{\text{ex}} > \kappa_i$ ) regimes. Depending on specific applications, these working regimes can be controlled by adjusting the coupling gap in the design and fabrication.

### 1.2.2 Piezoelectric effect

The piezoelectric effect is an effect where charges can be generated and accumulated at the surface of the material upon external pressure. It can happen on certain crystalline material with no inversion symmetry, such as PZT, AlN, LiNbO<sub>3</sub>. The inverse effect is often true where stress and strain can be built as external electric field is applied across the material. The direct and inverse piezoelectric effect can be mathematically described by relating the electric field to the strain of the material:

$$\varepsilon_I = \sum_{J=1}^6 S_{IJ} \sigma_J + \sum_{j=1}^3 d_{Ij}^t E_j \quad (1.9)$$

$$D_i = \sum_{J=1}^6 d_{iJ} \sigma_J + \sum_{j=1}^3 \epsilon_{ij} E_j \quad (1.10)$$

where  $\varepsilon$  and  $\sigma$  are the strain and stress,  $D$  and  $E$  are the electric displacement and electric field.  $S_{IJ}$  is the compliance coefficient that describes the microscopic Hooke's law in linear elastic material.  $\epsilon_{ij}$  is the permittivity of dielectric.  $d_{iJ}$  is the piezoelectric coefficient in the unit of C/N (which is also equal to m/V). Note the piezoelectric coefficient is often quoted as  $e_{ijk}$  which relates the strain to the electric displacement in the unit of C/m<sup>2</sup>. The subscript indices represent different components of each physical quantity. The capital indices  $I, J$  are for stress and strain which range from 1 to 6 to take into account the normal

and shear components with the conventional notation that:  $1 \rightarrow xx, 2 \rightarrow yy, 3 \rightarrow zz, 4 \rightarrow yz, 5 \rightarrow xz, 6 \rightarrow xy$ . The indices  $i, j$  are for electric field and displacement, and each has three components:  $1 \rightarrow x, 2 \rightarrow y, 3 \rightarrow z$ . Note that due to the symmetry,  $d_{Ij}^t = d_{jI}$ .

The piezoelectric coefficient is related with the crystal structure of each piezoelectric material. Although  $d_{iJ}$  has 18 components, due to the symmetry of the crystal, only few are non-zero. For the piezoelectric materials explored in this thesis, including AlN and PZT, the prominent components are  $d_{31}$  (relating electric field in  $z$  to strain in  $x$ ) and  $d_{33}$  (relating electric field in  $z$  to strain in  $z$ ). For AlN,  $d_{31} = -2$  pm/V and  $d_{33} = 3.9$  pm/V. On the other hand, PZT shows much higher piezoelectric coefficient  $d_{31} \approx -150$  pm/V and  $d_{33} \approx 100$  pm/V. The application for both of them in piezoelectric tuning of optical microring resonator will be fully studied in the next chapter.

### 1.2.3 Photoelastic and moving boundary effects

The application of external electric field to the piezoelectric actuator will generate stress and strain surrounding the optical waveguide, and change the optical resonant frequency by either modifying the refractive index or deforming the radius of the optical ring (see Eq. 1.3). There are mainly two effects, **photoelastic** and **moving boundary**, that should be taken into account to describe the interaction between light and mechanical structures (acoustic waves), which are widely adopted in fields like cavity optomechanics [107], stimulated Brillouin scattering [108], and acousto-optic modulation (AOM) [14], [15], and are applicable in a wide frequency range from Direct Current (DC) to Radio-frequency (RF). While the photoelastic and moving boundary describe the action of mechanics on the light, the inverse effects where the photon generates optical forces on the mechanical structures will also take place, which correspond to the electrostrictive and radiation pressure forces [109], respectively.

The photoelastic effect is the change of the refractive index  $n$  (also the permittivity  $\epsilon$ ) of an optical material under stress and strain [65], [110]. In general, the permittivity is a rank-2 tensor which contains 6 independent components due to the symmetry [65]:

$$\epsilon = \begin{pmatrix} n_1^2 & n_6^2 & n_5^2 \\ n_6^2 & n_2^2 & n_4^2 \\ n_5^2 & n_4^2 & n_3^2 \end{pmatrix} \quad (1.11)$$

where  $n_{1-6}$  is the refractive index that relates electric fields in different directions, and the subscripts follow the same convention as the last section. The relative change of refractive index under strain is conventionally described by the strain-optic coefficient  $p_{ij}$  as:

$$\Delta \frac{1}{n_i^2} = \sum_{j=1}^6 p_{ij} \epsilon_j \quad (1.12)$$

For most of the optical material used in this work, which are amorphous  $\text{SiO}_2$  and amorphous  $\text{Si}_3\text{N}_4$ , the strain-optic coefficients have only two independent components due to the symmetry of the material as the following [65]:

$$\Delta \begin{pmatrix} 1/n_1^2 \\ 1/n_2^2 \\ 1/n_3^2 \\ 1/n_4^2 \\ 1/n_5^2 \\ 1/n_6^2 \end{pmatrix} = \begin{pmatrix} p_{11} & p_{12} & p_{12} & 0 & 0 & 0 \\ p_{12} & p_{11} & p_{12} & 0 & 0 & 0 \\ p_{12} & p_{12} & p_{11} & 0 & 0 & 0 \\ 0 & 0 & 0 & p_{44} & 0 & 0 \\ 0 & 0 & 0 & 0 & p_{44} & 0 \\ 0 & 0 & 0 & 0 & 0 & p_{44} \end{pmatrix} \begin{pmatrix} \epsilon_1 \\ \epsilon_2 \\ \epsilon_3 \\ \epsilon_4 \\ \epsilon_5 \\ \epsilon_6 \end{pmatrix} \quad (1.13)$$

where  $p_{44} = (p_{11} - p_{12})/2$ . For  $\text{SiO}_2$ ,  $p_{11} = 0.121$  and  $p_{12} = 0.27$  [65]. As there is no direct measurement of the strain-optic coefficient of  $\text{Si}_3\text{N}_4$  from the literature, it is inferred from relevant experiments that  $p_{11} = 0.239$  [111] and  $p_{12} = 0.047$  [112].

The stress-optic coefficient  $C_i$  is also often referred in the literature which directly relates the change of index with the stress  $\sigma$  as [65]:

$$\begin{pmatrix} n_1 \\ n_2 \\ n_3 \\ n_4 \\ n_5 \\ n_6 \end{pmatrix} = \begin{pmatrix} n_0 \\ n_0 \\ n_0 \\ 0 \\ 0 \\ 0 \end{pmatrix} - \begin{pmatrix} C_1 & C_2 & C_2 & 0 & 0 & 0 \\ C_2 & C_1 & C_2 & 0 & 0 & 0 \\ C_2 & C_2 & C_1 & 0 & 0 & 0 \\ 0 & 0 & 0 & C_3 & 0 & 0 \\ 0 & 0 & 0 & 0 & C_3 & 0 \\ 0 & 0 & 0 & 0 & 0 & C_3 \end{pmatrix} \begin{pmatrix} \sigma_1 \\ \sigma_2 \\ \sigma_3 \\ \sigma_4 \\ \sigma_5 \\ \sigma_6 \end{pmatrix} \quad (1.14)$$

where  $n_0$  is the original refractive index of the optical materials used in this work which are isotropic. It can be intuitively seen that  $C_1$  relates the index and stress in the same direction, while  $C_2$  relates that in orthogonal direction. The stress-optic coefficient  $C_i$  can be calculated from the strain-optic coefficient  $p_{ij}$  through [65]:

$$C_1 = n_0^3 \frac{p_{11} - 2\nu p_{12}}{2E_{\text{mod}}} \quad (1.15)$$

$$C_2 = n_0^3 \frac{p_{12} - \nu(p_{11} + p_{12})}{2E_{\text{mod}}} \quad (1.16)$$

$$C_3 = n_0^3 \frac{p_{44}}{2G} \quad (1.17)$$

where  $E_{\text{mod}}$ ,  $G$ ,  $\nu$  are Young's modulus, shear modulus, and Poisson ratio, respectively. From the expressions, we can see  $p_{ij}$  and  $C_i$  are correlated through the mechanical properties of the material, that govern the relation between the stress and strain.

Now that we know how the stress modifies the refractive index, we can next calculate the change of the effective refractive of the optical waveguide, and thus the optical resonant frequency by the Bethe-Schwinger perturbation theory [15], [108], [113]:

$$\Delta n_{\text{eff,PE}} = \frac{n_{\text{eff}}}{2} \frac{\iiint \mathbf{E}^* \cdot \Delta \epsilon \cdot \mathbf{E} dV}{\iiint \mathbf{E}^* \epsilon \mathbf{E} dV} \quad (1.18)$$

where the numerator is the perturbation of the electromagnetic energy in the optical cavity, and the denominator is the total energy of the optical mode. The volume integral is over the

whole region where the electromagnetic field resides.  $\Delta\epsilon$  is a rank-2 tensor and the integrand in the numerator can be expanded as [15]:

$$\mathbf{E}^* \cdot \Delta\epsilon \cdot \mathbf{E} = -\epsilon_0 n^4 \begin{pmatrix} E_1^* & E_2^* & E_3^* \end{pmatrix} \begin{pmatrix} \Delta\frac{1}{n_1^2} & \Delta\frac{1}{n_6^2} & \Delta\frac{1}{n_5^2} \\ \Delta\frac{1}{n_6^2} & \Delta\frac{1}{n_2^2} & \Delta\frac{1}{n_4^2} \\ \Delta\frac{1}{n_5^2} & \Delta\frac{1}{n_4^2} & \Delta\frac{1}{n_3^2} \end{pmatrix} \begin{pmatrix} E_1^* \\ E_2^* \\ E_3^* \end{pmatrix} \quad (1.19)$$

where  $\epsilon_0$  is the vacuum permittivity. The  $\Delta(1/n_i^2)$  can be directly calculated from the strain-optic relation in Eq. 1.13. From Eqs 1.18-1.19, we can estimate the change of the refractive index of the optical waveguide by simulating the optical and strain field distribution using Finite Element Method (FEM) such as multiphysics software COMSOL.

Due to the large contrast between the refractive index of the waveguide core and the cladding material, the abrupt displacement of the waveguide's boundary will modify the overall effective refractive index of the waveguide, which is the so-called moving boundary effect. It will play an important role when the shape of the waveguide deforms under external mechanical strain. Rigorous derivation of the relation between the index and the boundary displacement can be found in Ref [78], and the main result is summarized as below [15], [113]:

$$\Delta n_{\text{eff,MB}} = \frac{n_{\text{eff}}}{2} \frac{\iint (\mathbf{Q} \cdot \hat{\mathbf{n}}) (\Delta\epsilon E_{\parallel}^2 - \Delta\epsilon^{-1} D_{\perp}^2) dS}{\iiint \mathbf{E}^* \epsilon \mathbf{E} dV} \quad (1.20)$$

where  $\mathbf{Q}$  is the mechanical displacement of the boundary, and  $\hat{\mathbf{n}}$  is the normal vector of the boundary facing outward. So the dot product of  $\mathbf{Q} \cdot \hat{\mathbf{n}}$  picks the component of  $\mathbf{Q}$  normal to the boundary.  $E_{\parallel}$  only takes the component parallel to the boundary, and  $D_{\perp}$  is the perpendicular component.  $\Delta\epsilon = \epsilon_{\text{core}} - \epsilon_{\text{cladding}}$  and  $\Delta\epsilon^{-1} = \epsilon_{\text{core}}^{-1} - \epsilon_{\text{cladding}}^{-1}$  are the difference of permittivity and inverse of permittivity between the waveguide core and cladding materials. The surface integral in the numerator is taken over all the surfaces of the waveguide.

The tuning of the resonant frequency of the optical resonator can be inferred by substituting the photoelastic effect (Eq. 1.18) and the moving boundary effect (Eq. 1.20) into Eq. 1.3:

$$\Delta\omega_0 = -\omega_0 \frac{\Delta n_{\text{eff,PE}} + \Delta n_{\text{eff,MB}}}{n_{\text{eff}}} \quad (1.21)$$

The above equations will be useful for simulating the tuning of the optical resonance upon quasi-DC voltages applied to the actuator. At the microwave frequency AOM, it is widely adopted to describe the interaction between photon and phonon quantum mechanically by using the single photon-phonon optomechanical coupling rate  $g_0$ , which can be calculated by normalizing Eq. 1.21 using the Zero Point Fluctuation (ZPF) of the mechanical motion as:

$$g_0 = \Delta\omega_0 \frac{x_{\text{ZPF}}}{\max\{Q\}} \quad (1.22)$$

$$x_{\text{ZPF}} = \sqrt{\frac{\hbar}{2m_{\text{eff}}\Omega_{\text{m}}}} \quad (1.23)$$

$$m_{\text{eff}} = \frac{\iiint \rho Q^2 dV}{\max\{Q^2\}} \quad (1.24)$$

where  $x_{\text{ZPF}}$ ,  $m_{\text{eff}}$  and  $\Omega_{\text{m}}$  are the zero-point motion, effective mass, and resonant frequency of the mechanical resonator, respectively.  $\rho$  is the material's density, and  $\max\{Q\}$  and  $\max\{Q^2\}$  are the maximum displacement and its square over the whole mechanical mode. Intuitively,  $g_0$  measures the scattering rate between a single photon and phonon in an optomechanical cavity, and is related with the overlap between the optical and mechanical modes. It can be experimentally calibrated by optomechanically measuring the thermal Brownian noise of the mechanical resonator [114]. From the expressions, we can also see the larger the mechanical mass  $m_{\text{eff}}$  and frequency  $\Omega_{\text{m}}$ , the smaller the  $x_{\text{ZPF}}$ , and thus smaller coupling rate. In the case where large  $g_0$  is preferred, we would want to tightly confine the mechanical mode in a small volume.

### 1.3 Organization of the thesis

This thesis will cover the piezoelectric tuning of a  $\text{Si}_3\text{N}_4$  microring resonator with released and unreleased structures. The applications in the quasi-DC and RF frequencies will be discussed, and the demonstrations in fast actuation of the Kerr frequency comb, integrated optical isolator, and quantum microwave to optical conversion will be presented in the following chapters.



In Chapter 2, the quasi-DC tuning of a microring resonator in an unreleased structure will be studied, and the tuning will be characterized from different aspects including the actuator shape, relative position between the actuator and the optical waveguide, tuning efficiency, tuning speed, and the electrical power consumption. Different piezoelectric materials, AlN, AlScN, and PZT, will be explored and compared. By exciting HBAR modes at the microwave frequency, efficient AOM will be demonstrated. The mechanical dispersion of the HBAR modes will be analyzed via an established electromechanical analytic model.

In Chapter 3, the application of the unreleased actuator in the piezoelectric tuning of a Kerr frequency comb will be presented. Dissipative Kerr soliton is initiated by tuning the resonance of the optical resonator to a fixed-frequency laser. The soliton repetition rate is stabilized with a locking bandwidth of 0.6 MHz and maintained over 6 hours. The HBAR is demonstrated to generate an on-chip Pound–Drever–Hall (PDH) error signal which can be used to lock the laser frequency to the resonance of a stabilized optical cavity in a reliable way.

In Chapter 4, I removed the Si substrate to create a released structure with suspended SiO<sub>2</sub> membrane, in an attempt to increase the tuning efficiency. The relative position of the optical microring inside the membrane is studied, indicating the tuning is dominated by the stress-optical effect. The optical resonance is tuned by 25 pm upon applying 60 V to the top electrode with a 1 nA current draw, demonstrating ultra-low DC power consumption (2.4 pW/MHz). Sub- $\mu$ s tuning speed is achieved which is ultimately limited by the fundamental mechanical mode of the released cantilever around 1.3 MHz. Microwave frequency modulation (up to 9 GHz) is achieved by exciting bulk acoustic waves which are confined tightly in released SiO<sub>2</sub> thin film. The modulation efficiency is increased by over 100 times compared with unreleased devices. The excitation of released HBAR modes with the AlScN actuator will also be presented.

In Chapter 5, I demonstrated a magnetic-free optical isolator based on aluminum nitride (AlN) piezoelectric modulators monolithically integrated on low-loss Si<sub>3</sub>N<sub>4</sub> PIC. The transmission reciprocity is broken by spatio-temporal modulation of a Si<sub>3</sub>N<sub>4</sub> microring resonator with three AlN bulk acoustic wave resonators that are driven with a rotational phase. This design creates an effective rotating acoustic wave that allows indirect interband transition

in only one direction among a pair of strongly coupled optical modes. Maximum of 10 dB isolation is achieved under 300 mW total RF power applied to three actuators, with minimum insertion loss of 0.1 dB. An isolation bandwidth of 700 MHz is obtained, determined by the optical resonance linewidth. The isolation remains constant over nearly 30 dB dynamic range of optical input power, showing excellent optical linearity. I also demonstrated an integrated non-reciprocal optical frequency shifter by coupling TE and TM modes. the device is at the same time a polarization rotator. 50% conversion efficiency between TE and TM optical modes is achieved, with 15 dB suppression of carrier frequency and 12 dB sideband asymmetry.

In Chapter 6, the released HBAR AOM is proposed to realize the quantum microwave to optical conversion. A quantum model is established to describe the conversion process and estimate the conversion efficiency. Different device parameters are investigated aiming at the highest efficiency with reasonable amount of pump optical power. It is encouraging to find out that the converter and isolator share the same triple-mode operation. In the isolator, microwave serves as the pump to couple TE and TM optical modes. However, in the converter, TE is pumped to couple the mechanical mode with the TM optical mode, which swaps the quantum information. The first generation of device is fabricated and the preliminary measurement will be presented. Future improvements of the efficiency will be discussed.

In Chapter 7, I will conclude the thesis by the outlook for the Piezo-on-Photonics platform in future prospective applications enabled by the technique. Specifically, I will envision the apply of the platform in building a hybrid integrated quantum system where mechanics couples or mediates the coupling between distinct quantum objects (e.g., superconducting qubits, photons, spins), with application scenarios being discussed in piezoelectric programmable photonic circuits, photonic synthetic dimension, and classical readout and control of superconducting qubit.

## 2. UNRELEASED PIEZOELECTRIC ACTUATION

### 2.1 AlN actuator piezoelectric tuning

#### 2.1.1 Design of the AlN actuator

As a well-known piezoelectric thin film, AlN is utilized to form the piezoelectric actuator which generates stress around  $\text{Si}_3\text{N}_4$  waveguides. When an electric field is applied across the AlN film, the film is deformed and generates stress and stress gradient in the layers beneath. Two designs are considered in this work as shown in Fig. 2.1(a-b). First, a disk-shape actuator is placed directly on top of the  $\text{Si}_3\text{N}_4$  ring resonator, as shown in Fig. 2.1(a), which is referred as **Disk** device in following sections. Since the stress mainly originates from the corner of the actuator, the microring resonator is positioned at the outer edge of the disk actuator. Under positive DC biasing on top electrode (while bottom electrode is always grounded), the AlN film expands and pushes the ring outwards (i.e. expanding in Fig. 2.1(e)). Intuitively, the other design is to use donut-shape actuator which squeezes the microring resonator if it is placed at the inner edge of the actuator, as shown in Fig. 2.1(b), which is referred as **Donut** device in subsequent sections. These two designs will show different stress distribution and static resonance tuning as demonstrated later. Additionally, the areas around the bus-waveguide-to-microring-resonator coupling regions are opened to prevent any actuation-induced perturbation of light coupling.

The cross-sections with more structure details are illustrated in Fig. 2.1(c-d). To apply vertical electric field, AlN film of  $1\ \mu\text{m}$  thickness is sandwiched between top Aluminum (100 nm) and bottom Molybdenum (100 nm) metal layers. The  $\text{Si}_3\text{N}_4$  waveguides are fabricated using either a subtractive process [22], [115] or a photonic Damascene process [116]–[118], which have 800 nm height and  $1.8\ \mu\text{m}$  width and are fully buried in a  $6\text{-}\mu\text{m}$ -thick  $\text{SiO}_2$  cladding (with  $3\ \mu\text{m}$   $\text{SiO}_2$  from the Mo layer to prevent metal absorption). The entire device sits on a  $230\text{-}\mu\text{m}$ -thick Si substrate. The radius of the microring resonator is  $118\ \mu\text{m}$ . The ring is placed  $3\ \mu\text{m}$  within the edge of Disk actuator and  $5\ \mu\text{m}$  for the Donut actuator.

The static mechanical simulation is conducted using finite element method (COMSOL) as shown in Fig. 2.1(e-f), in which +60 V DC biasing is applied on top Al layer while bottom Mo layer is grounded (same in the following experiments). In this case, negative electric field

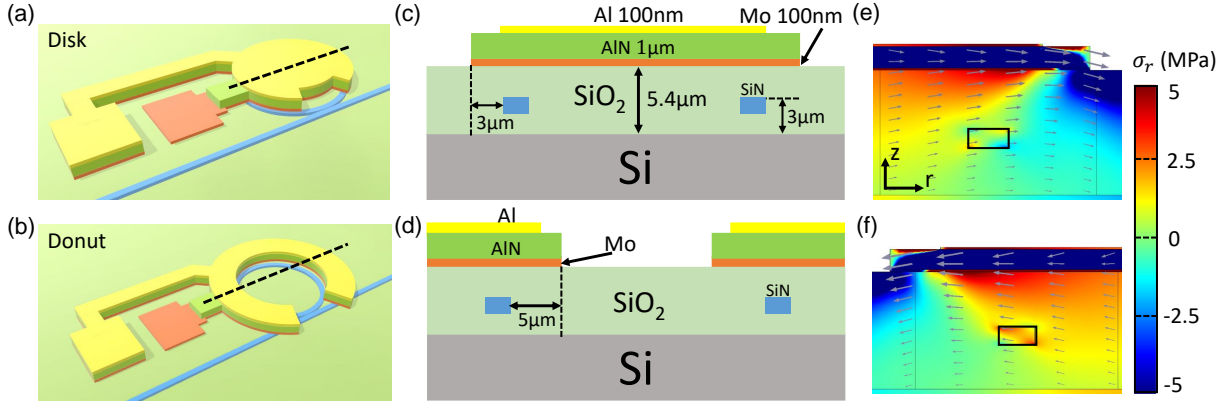


**Figure 2.1.** Schematics for the designed devices with (a) Disk shape and (b) Donut shape actuators with silicon nitride ring resonator (blue) having different relative positions. (c) and (d) are the cross-sections for Disk and Donut devices along black dashed lines in (a) and (b), respectively. (e), (f) COMSOL simulation of horizontal stress distribution around optical waveguide under +60 V DC biasing for Disk and Donut devices, respectively. The overlaid gray arrows denote the local mechanical displacement with the biggest arrow scaling as 1 nm. Reprinted from Ref. [12].

$E_z$  forms (points downwards) across the AlN thin film, and due to the positive piezoelectric coefficient  $e_{33}$  ( $1.55 \text{ C/m}^2$ ), the AlN film will be squeezed in the  $z$ -direction and expand horizontally (positive Poisson ratio). Fig. 2.1(e) illustrates the horizontal stress distribution and the mechanical displacement around the optical waveguide at the upper right corner of Fig. 2.1(c). As AlN expands, starting from the corner, the stress splits into two parts: extensional stress under the actuator and compressing stress at outside, and the mechanical displacement orients mainly horizontally and points outside the actuator. Similar results can be drawn for Donut device as in Fig. 2.1(f). Depending on the position of the waveguide, it experiences extension, compression, or the interplay between these two. For the Disk device, the horizontal stress inside the waveguide is a mixture of extension and compression, while for the Donut device, it is mainly extension. Additionally, when applying negative voltages, AlN actuator changes from expanding (horizontally) to shrinking, so that all the stresses in the above analysis change sign. In this way, bi-directional tuning can be achieved by reversing the applied voltage's sign, as demonstrated in the following sections.

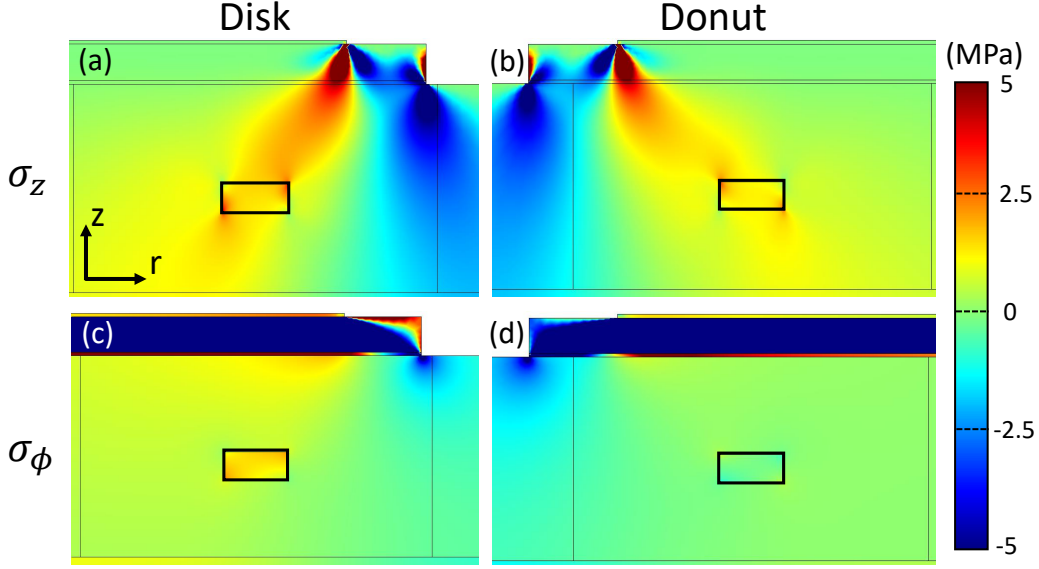


**Figure 2.2.** Static stress distribution in  $z$  and  $\phi$  directions. (a) and (b) show the numerical simulation of vertical  $z$  stress distribution under +60 V DC biasing for the Disk and Donut devices, respectively. Both of them show extensional stress around the waveguide. (c) and (d) are out of plane (tangential to the optical ring) stress distributions for Disk and Donut devices. They present different sign inside the waveguide, since the optical ring of the Disk device expands while the Donut device squeezes. Reprinted from Ref. [12].

Besides the dominant horizontal stress, stresses in other directions will also affect the modulation on the refractive index. As shown in Fig. 2.2(a) and (b), originating from the corner of top metal,  $\sigma_z$  exhibits two main lobes with different signs. Inside the actuator, the waveguides in both cases experience extensional stress around 2 MPa. Under positive biasing, the ring of the Disk device will be pushed outwards as the actuator expands, which builds up extensional stress in the waveguide as in Fig. 2.2(c). On the other hand, at the inner edge of the Donut actuator, the optical ring is squeezed, generating compressing stress [Fig. 2.2(d)]. Since shear stress is found to play a less role compared with normal stress[65], it is not taken into account in this study. Additionally, when applying negative voltages, the AlN actuator changes from expanding (horizontally) to shrinking, so that all the stresses in the above analysis change sign. In this way, bi-directional tuning can be achieved by reversing the applied voltage's sign, as demonstrated in the following section.

The presence of stress will change the refractive index of optical material, and affect differently for light with different polarization, causing so-called birefringence. Numerically, they are correlated by stress-optical coefficients by [65]:

$$n_r = n_0 - C_1\sigma_r - C_2(\sigma_\phi + \sigma_z) \quad (2.1)$$

$$n_\phi = n_0 - C_1\sigma_\phi - C_2(\sigma_z + \sigma_r) \quad (2.2)$$

$$n_z = n_0 - C_1\sigma_z - C_2(\sigma_r + \sigma_\phi) \quad (2.3)$$

where,  $n_0$  is the original refractive index of the material,  $C_1$  relates refractive index and stress that are in the same direction while  $C_2$  relates the two that are orthogonal. These equations are applicable to isotropic material such as amorphous  $\text{Si}_3\text{N}_4$  from low-pressure chemical vapor deposition (LPCVD) used in this work. The lack of the stress-optical coefficient for  $\text{Si}_3\text{N}_4$  in the literature makes it difficult to predict precisely the response of the optical ring resonator. However, it would be possible to extract the coefficients by comparing experimental tuning of optical ring resonator with simulation, which is under investigation.

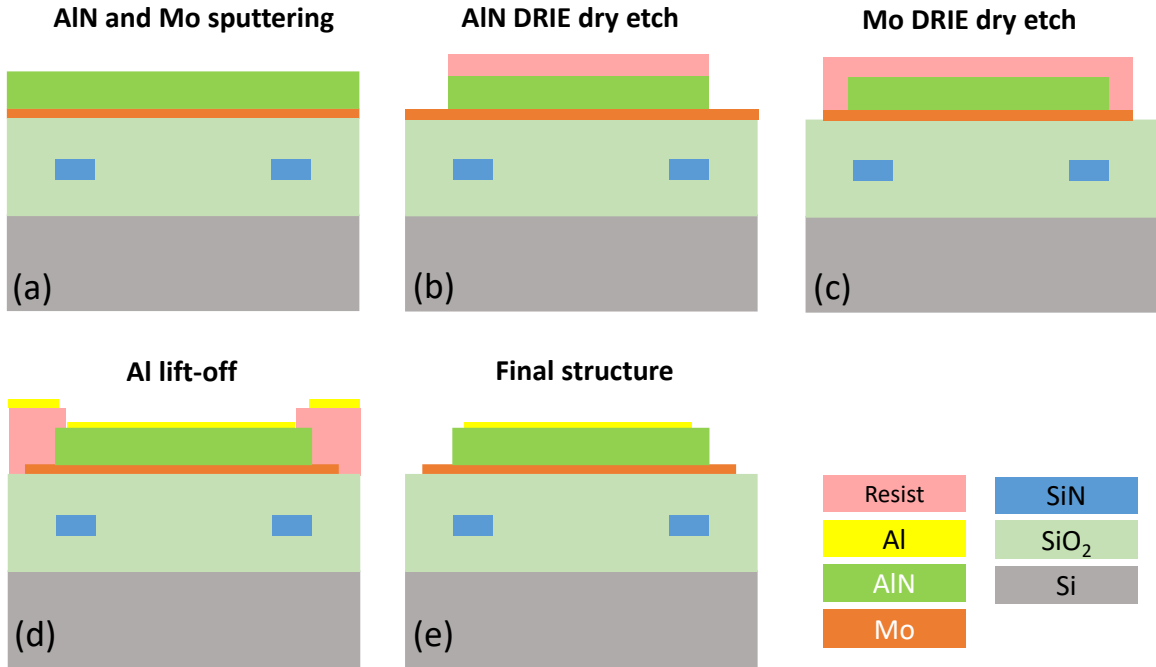


**Figure 2.3.** Fabrication flow for the unreleased AlN piezoelectric actuator.

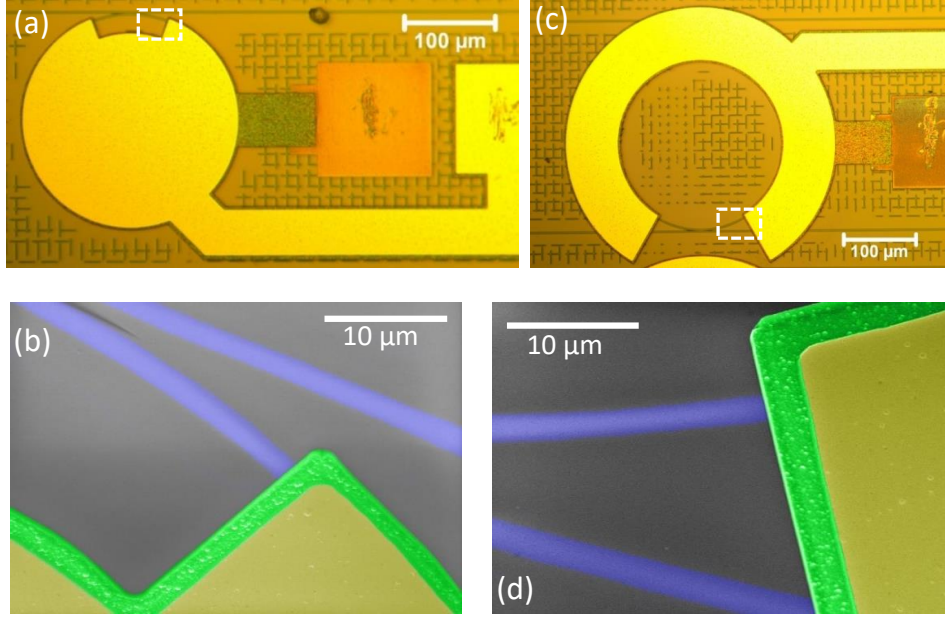


**Figure 2.4.** (a) Optical microscope image and (b) false color SEM around Disk actuator corner as labeled in white dashed box in (a) for Disk device. (c) Optical microscope image and (d) false color SEM around actuator corner for Donut device. Reprinted from Ref. [12].

### 2.1.2 Fabrication flow

The fabrication of the high performance  $\text{Si}_3\text{N}_4$  photonic circuits using the photonic Damascene process can be found in Ref [116]–[118]. The AlN piezoelectric actuators are directly fabricated on top of the  $\text{Si}_3\text{N}_4$  microring resonator separated by the  $\text{SiO}_2$  cladding for preserving the low loss of the optical waveguide. The fabrication flow is as shown in Fig. 2.3. 100 nm Mo and 1  $\mu\text{m}$  polycrystalline AlN films are sputtered on the  $\text{SiO}_2$  substrate through the foundry service (OEM Group). The AlN disk (or donut) is patterned by photoresist (SPR 220-4.5), and dry etched using  $\text{Cl}_2$  and  $\text{BCl}_3$  in a Panasonic E620 Etcher [119]. The dry etching of the bottom electrode (Mo) is performed using  $\text{Cl}_2$  and  $\text{O}_2$  in the same Panasonic E620 Etcher. Finally, the top 100 nm of Al is evaporated by a PVD E-beam evaporator, and patterned using a standard lift-off process.

The whole wafer is finally diced into individual chips by deep reactive ion etching (RIE) followed by a backside mechanical polishing of the Si substrate. This enables smooth chip facets for efficient coupling of light from lensed fiber to inverse waveguide taper at the edge. This three-mask photolithography fabrication leads to a low cost and high fabrication tolerance. The final fabricated devices are shown in Fig. 2.4(a,c) for the two designs. In Fig. 2.4(b,d), false color SEMs that are zoomed-in around actuator corners show the relative position between the optical microring resonator (blue) and the AlN actuator (green).

The above fabrication flow is for our first generation device with Al top metal. In our second generation, the top metal is replaced by Mo which is sputtered following the AlN in the same vacuum sputtering chamber. This will reduce the required masks to two, where the top metal can be etched using the same mask as AlN in the same time. This will further lower the fabrication cost for large volume production.

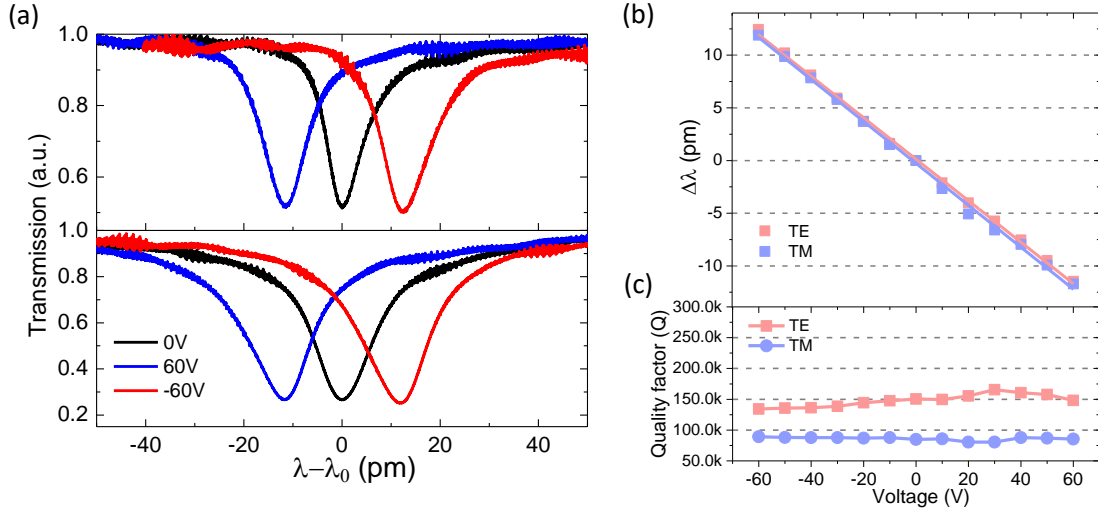


**Figure 2.5.** (a) Transmission spectrum of one resonance of TE and TM polarization mode for Disk device under +60 V (blue), 0 V (black), and -60 V (red). The x axis represents wavelength shifts relative to resonant wavelength  $\lambda_0$  ( $\sim 1550$  nm) of each mode. The tuning direction reverses for opposite voltages, demonstrating bi-directional tuning. (b) Dependence of resonant wavelength detune on voltages. Experimental results (squares) show high linearity for both TE (pink) and TM (cyan) modes, with  $R^2 > 99\%$  linear fitting (straight lines). (c) Influence of piezoelectric actuation on the optical quality factor Q for TE and TM modes, which verifies that the actuation will not influence the optical Q. Reprinted from Ref. [12].



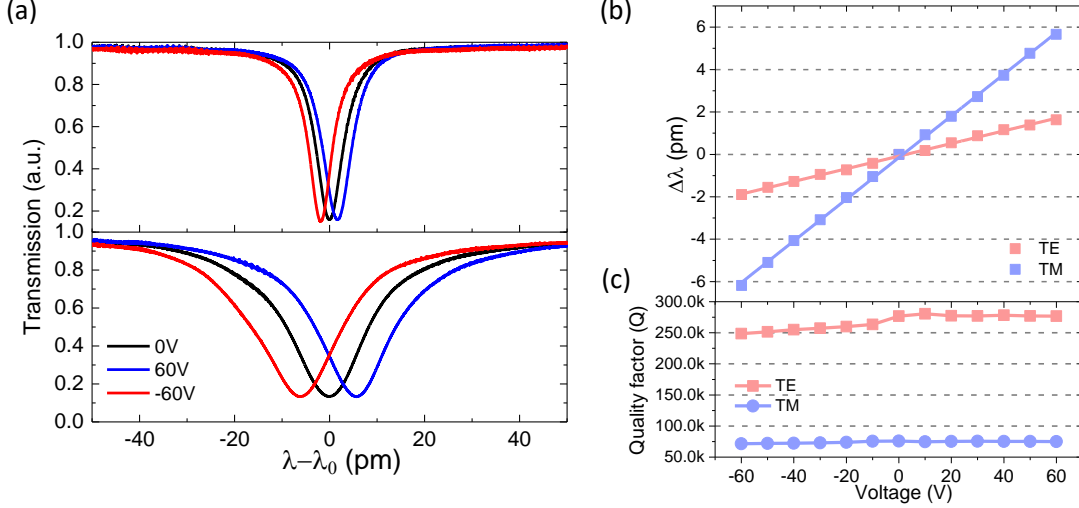


**Figure 2.6.** (a) Transmission spectrum of one resonance of TE and TM polarization mode for Donut device under +60 V (blue), 0 V (black), and -60 V (red). (b) Dependence of resonant wavelength detune on voltages. Experimental results (squares) show high linearity for both TE (pink) and TM (cyan) modes, with  $R^2 > 99\%$  linear fitting (straight lines). (c) Influence of piezoelectric actuation on the optical quality factor  $Q$  for TE and TM modes. Reprinted from Ref. [12].

### 2.1.3 DC tuning of the optical resonance

Working as a  $\text{Si}_3\text{N}_4$  ring resonator tuner, the static optical resonance tuning is performed by applying DC biasing. Fig. 2.5(a) shows the transmission spectrum of one resonance under different voltages for both TE and TM modes of the Disk device. One can see that as we apply a positive 60 V, the resonance shifts to shorter wavelength (blue curve) relative to the original resonance (black curve), and the tuning changes direction after reversing the voltage (red curve), demonstrating bi-directional tuning ability. Also, it can be observed that the resonance dip only shifts horizontally with little changes of vertical depth, since the waveguide coupling region is unaffected by the opening section of the actuator. The dependence of resonant wavelength on voltages is summarized in Fig. 2.5(b), showing high linearity. Both TE and TM modes demonstrate similar tuning performances with nearly -12 pm under positive 60 V, with tuning efficiency of -0.2 pm/V. As 1 GHz frequency difference equals to 8 pm wavelength change for infrared light, the tuning efficiency is also equivalent to

25 MHz/V for the tuning of the resonant frequency. The tuning range at 60 V is on a similar order or larger than the linewidth of the high-optical-Q resonances, which is applicable for  $\text{Si}_3\text{N}_4$  microcomb applications such as Kerr comb generation and stabilization.

Interestingly, due to different relative positions of the ring resonator, the Donut device shows opposite behaviour: the resonant wavelength increases for positive voltages and vice versa, as can be seen in Fig. 2.6(a, b). Here, the slope of tuning with respect to voltage changes from negative to positive. On the other hand, it shows much smaller tuning range with 5.66 pm for the TM mode and 1.63 pm for the TE mode under +60 V, with efficiency of 0.094 pm/V (-11.8 MHz/V) and 0.027 pm/V (-3.4 MHz/V), respectively. The different tuning range of two orthogonal polarization modes, TE and TM, demonstrates tunable birefringence in an otherwise isotropic material by controlling the stress, which can be utilized for the polarization control [120] or tuning the mode spacing and coupling between a pair of TE and TM modes in a microring resonator.

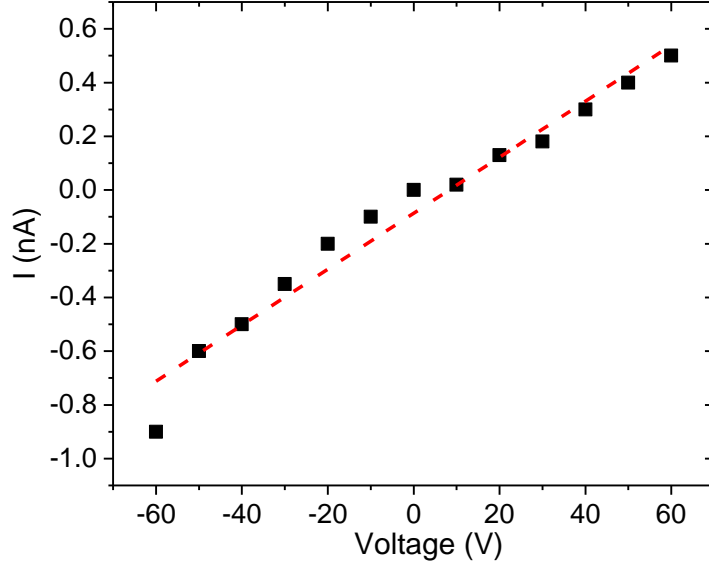


**Figure 2.7.** Current-Voltage relation for the capacitor-like AlN actuator. Black square is the experimental results, which the red dashed line is the linear fitting.

The effect of mechanical actuation on the optical Q is plotted in Fig. 2.5(c) and Fig. 2.6(c), which is found to be insignificant. The TE mode shows much higher Q than the TM

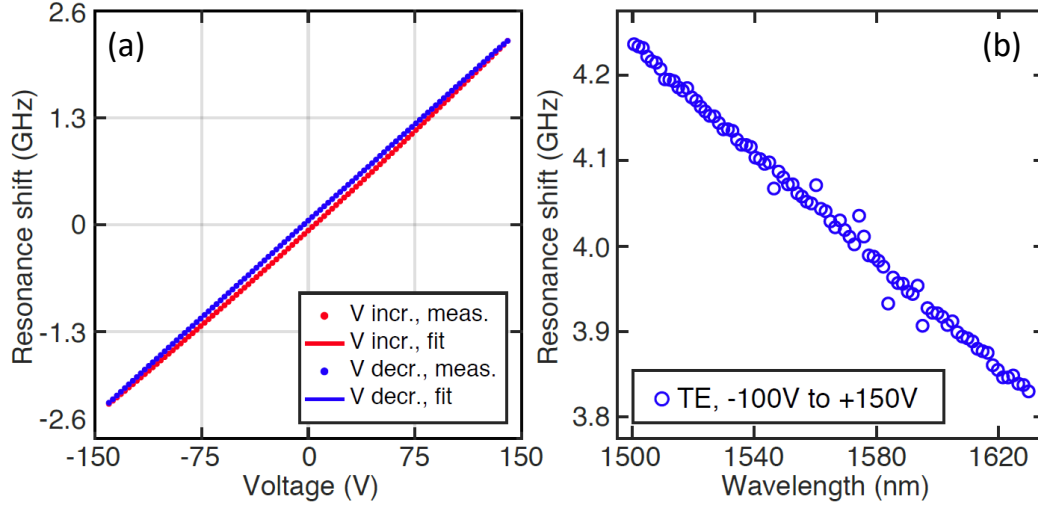


**Figure 2.8.** (a) Resonance shift versus applied voltage in forward and backward directions, showing the small hysteresis. V incr. / decr.: voltage increase / decrease; meas.: measured data. (b) Resonance shift for TE resonances in the wavelength range from 1500 nm to 1630 nm, when the applied voltage changes from -100 V to +150 V. The wavelength-dependent tuning results from a 5.3 MHz change of the FSR due to the piezoelectric actuation. Reprinted from Ref. [121].

mode, since the TM mode extends further in the vertical direction which is prone to the absorption of the bottom metal. Additionally, as shown in Fig. 2.7, the DC current drawing from the actuator is monitored while tuning, which keeps below 1 nA at 60V. The power consumption is at the level of 5 nW/pm, making it possible for large scale integration and cryogenic applications.

As shown in Fig. 2.8(a), a small hysteresis is observed when the voltage is swept between  $\pm 140$  V back and forth. While polycrystalline AlN is non-ferroelectric, such hysteresis is commonly caused by the trapped charges accumulated at AlN interfaces or combined with bulk defects [122]. Figure 2.8(b) shows the frequency tuning for TE resonances ranging from 1500nm to 1630 nm, calibrated using the frequency-comb assisted diode laser spec-

troscopy [48]. The wavelength-dependent total tuning results from a 5.3 MHz change of the microresonator's FSR (191.0 GHz), which can be inferred from Eq. 1.2:

$$\frac{\Delta\text{FSR}}{\text{FSR}} \sim \frac{\Delta\omega_0}{\omega_0} \quad (2.4)$$

where the relative change of the FSR is on the similar order with that of the resonant frequency. The nearly linear change of the tuning with wavelength in Fig. 2.8(b) shows that there is no observable change of the dispersion (where the  $\Delta\text{FSR}$  varies with wavelength). While the capability of controlling the dispersion could find application in versatile programming of the frequency comb's spectrum [61], the linear tuning of the FSR is preferred in stabilization of the frequency comb [123].

#### 2.1.4 Optimization of the waveguide placement

In this section, the relative position between the waveguide and the edge of the actuator is studied to optimize the tuning efficiency. The tuning efficiency under different relative shifts between them are simulated as shown in Fig. 2.9(a) and the examples of stress distribution are shown in Fig. 2.9(b). Note that in the simulation and the experiments below, the radius (thus the position of the waveguide) is fixed, and the radius (thus the edge) of the actuator is varied. It can be seen from the stress distribution that as the waveguide moves from outside of the actuator to inside, the stress on the waveguide changes from negative (compression) to positive (extension). When the waveguide is right beneath the top metal's edge, the waveguide is near the transition region between compression and extension stress, and the average stress on the waveguide is zero. This will lead to a relatively small tuning efficiency.

For positive shift where the waveguide is well beneath the actuator, the tuning efficiency gradually increases and saturates as the waveguide moves in. Maximum of 40 MHz/V can be achieved. The fact that the tuning is not sensitive to the shift allows for more tolerance in fabrication misalignment. On the other hand, for negative shift, the negative stress changes the tuning direction. As there is a negative stress 'hot-spot' region right outside of the AlN edge's corner, the tuning efficiency experiences a maximum value around -6  $\mu\text{m}$  shift, which shows -80 MHz/V. However, as will be seen in the following experimental results, this 'hot-

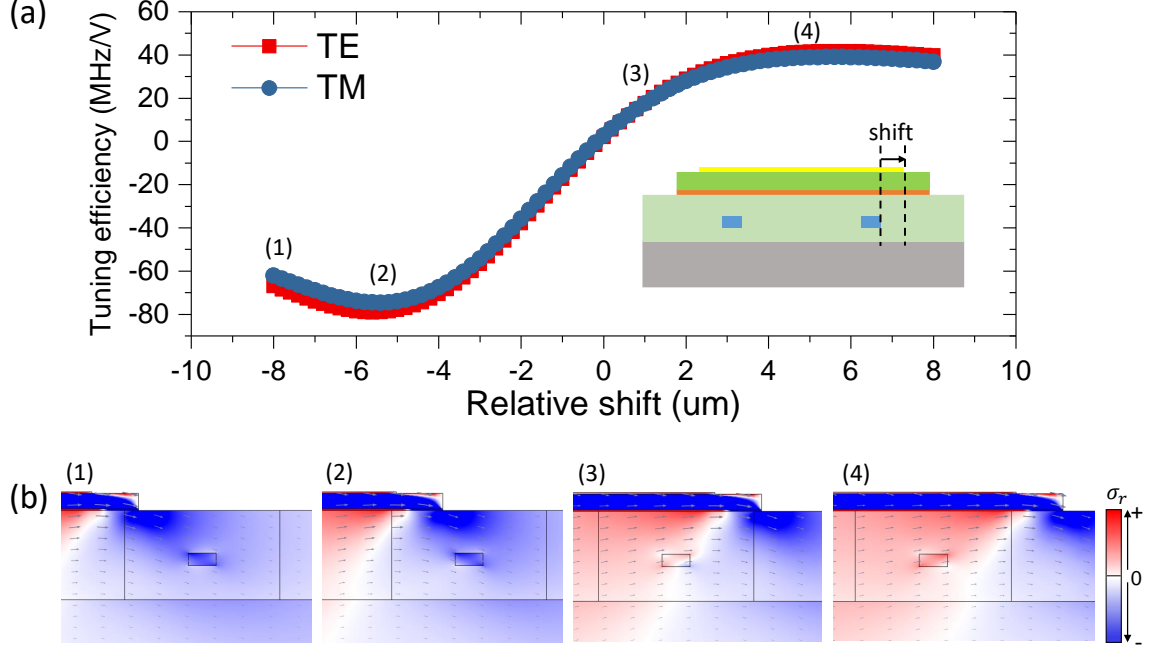


**Figure 2.9.** (a) COMSOL simulation of the tuning efficiency for Disk device under different relative shift between the waveguide and the top electrode's outer edge. The definition of the shift is as shown in the inset and the arrow denotes the positive shift direction. Both TE (red) and TM (blue) modes are shown. (b) Distribution stress of  $\sigma_r$  for different shifts from left to the right as labeled in (a).

spot' is not observed and the tuning remains positive even for negative shift. More careful studies would be needed in the future for explaining this discrepancy.

Experimentally, I designed actuators with different sizes while the radius of the  $\text{Si}_3\text{N}_4$  microring is kept as  $118 \mu\text{m}$ . The relative shift is swept from  $-8 \mu\text{m}$  to  $+8 \mu\text{m}$  in  $2 \mu\text{m}$  step. Examples of the fabricated devices are as shown in Fig 2.10, where the relative position between the waveguide and the actuator edge can be seen. The experimentally measured tuning efficiency for Disk and Donut actuators are shown in Fig. 2.11(a) and (b), respectively. For Disk actuator, the tuning increases for TE mode and keeps nearly constant for TM mode as the shift changes from negative to positive, which is different than the simulation. Maximum of  $32 \text{ MHz/V}$  is achieved for  $+8 \mu\text{m}$ , which means  $6 \text{ GHz}$  resonance scanning can be realized under  $\pm 100 \text{ V}$ . On the other hand, TM mode keeps  $20 \text{ MHz/V}$  irrespective of the shift.

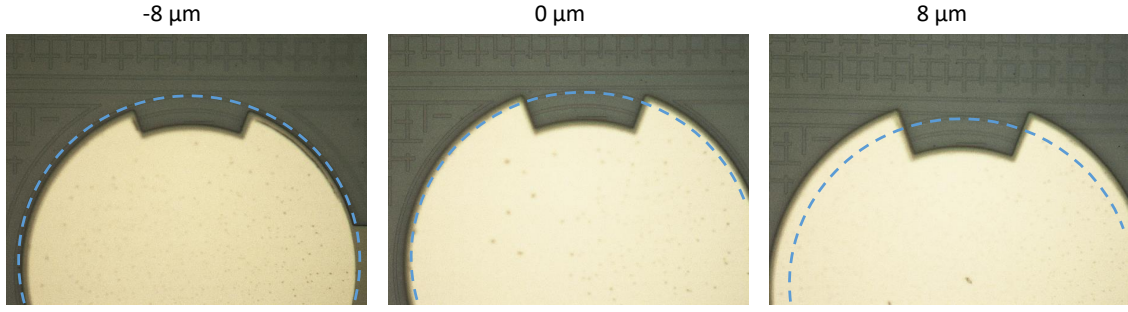


**Figure 2.10.** Examples of fabricated Disk devices with  $-8 \mu\text{m}$  (left),  $0 \mu\text{m}$  (middle), and  $8 \mu\text{m}$  shift. The blue dashed curve illustrates the position of the microring resonator.

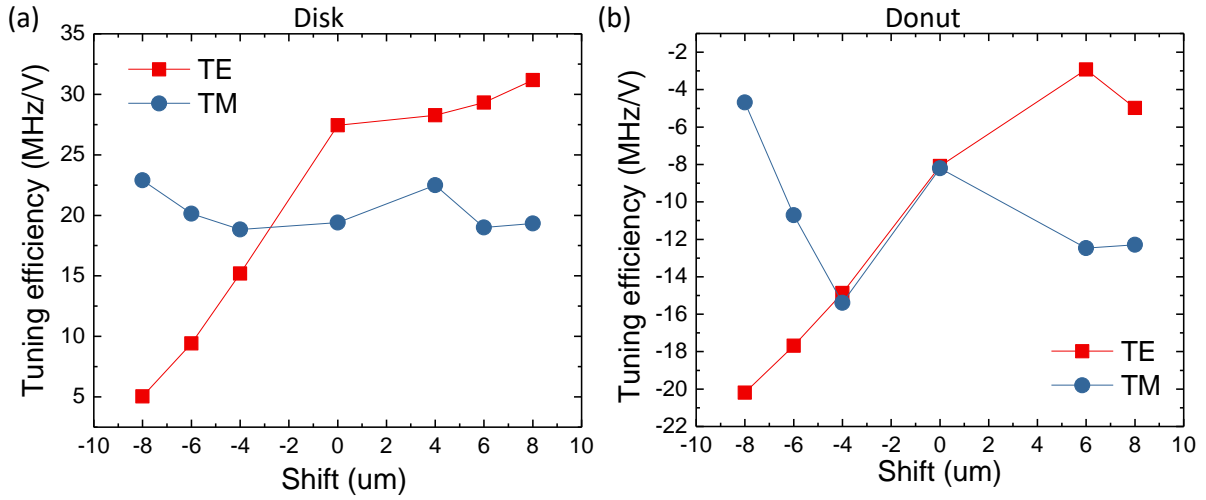


**Figure 2.11.** Experimentally measured tuning efficiency for (a) Disk and (b) Donut actuators. Both TE (red) and TM (blue) modes are measured.

For Donut actuator, the tuning changes to negative sign and reaches maximum tuning for negative shift. Similarly, TM mode is less sensitive to the shift than TE mode. Overall, Donut actuator shows smaller tuning than Disk, since Donut has more freely moving boundaries which releases the stress constrain. Examples of the resonance tuning for TE and TM modes are shown in Fig. 2.12 for both Disk and Donut devices. These devices exhibit larger optical Q than the device in Fig. 2.5 - 2.6, as they are fabricated using the optimized photonic Damascene process [118]. Because of the improved optical Q, the resonance can be clearly resolved under 60 V applied, and the tuning can be achieved an order of magnitude larger

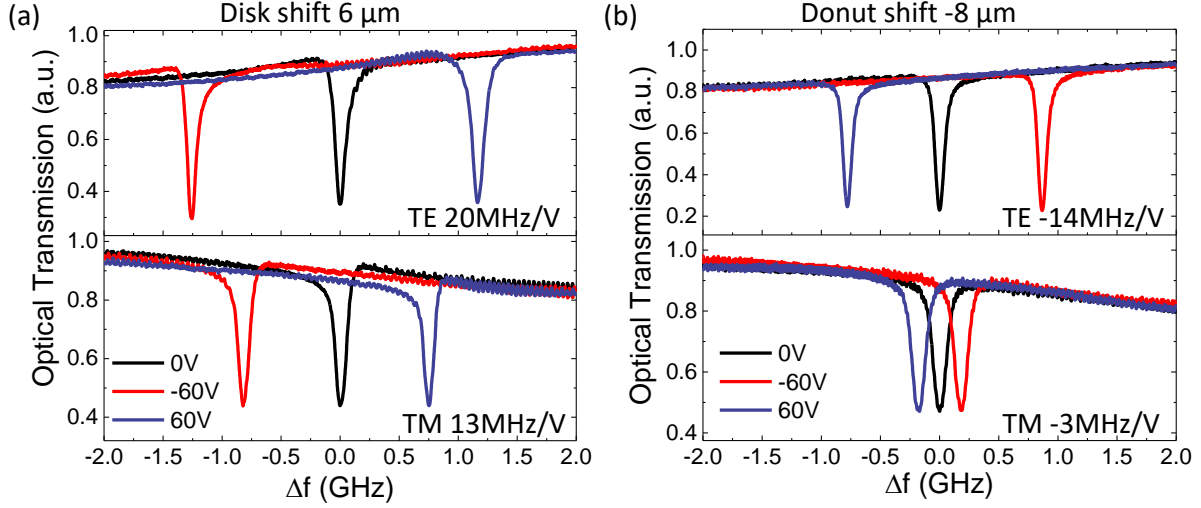


**Figure 2.12.** Optical resonance tuning of TE (upper) and TM (lower) modes for (a) Disk and (b) Donut device with optimal shift under  $\pm 60$  V.

than the optical resonance linewidth. But also note that these devices show smaller tuning than that in Fig. 2.11 probably because of the variation in fabrication or the measurement uncertainty.

Disk devices with different radius (and thus FSR) are fabricated and measured in Fig. 2.13. The optical image shows the measurement setup where the chip with different devices can be seen in the middle. Lensed optical fibers come from left and right to coupling laser in and out. The DC needle probes are landed from the top to apply voltages to the actuator. From Eq. 1.2,  $\text{FSR} = c/rn_{\text{eff}}$ , where FSR is inversely proportional to the radius of the microring resonator. For 40 GHz FSR microring, the radius is  $575 \mu\text{m}$ , whereas for 400 GHz, the radius is  $57.5 \mu\text{m}$ . From Fig. 2.13(b), the tuning efficiency increases for both TE and TM modes as the radius decreases (FSR increases). This is expected from Eq. 1.3 where as  $r$  decreases, the relative change of radius  $\Delta r/r$  increases since  $\Delta r$  is more related with local stress and is independent of  $r$ .

In summary, Disk actuator prefers placing the waveguide beneath the Disk, while Donut has larger tuning when the waveguide is outside of the actuator. Disk usually shows larger tuning than Donut. TE mode is more sensitive to the shift than the TM mode. The discrepancy between the experiment and the simulation probably comes from the built-in stress in

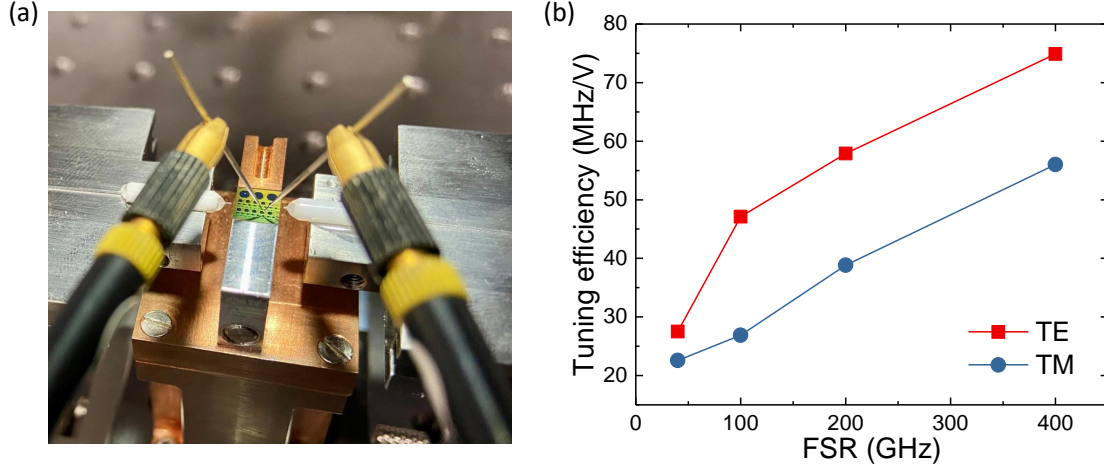


**Figure 2.13.** (a) Image of measurement setup. The chip with devices of different sizes is shown in the middle. (b) Tuning efficiency of TE (red) and TM (blue) modes for devices with different radius and thus FSR. (Courtesy of Anat Siddharth)

the  $\text{SiO}_2$  and  $\text{Si}_3\text{N}_4$  film that is not taken into account in the simulation. Also, the indirectly inferred photoelastic coefficient of  $\text{Si}_3\text{N}_4$  will require further experimental investigation in the future.

### 2.1.5 Characterization of the tuning speed

In this section, the tuning speed of the actuator is characterized in both time and frequency domain. In most applications, it is required There are mainly three limiting factors including RC transition time, photon lifetime, and mechanical response. Due to the small area of the device and small dielectric constant of AlN, the capacitor is estimated to be 10 pF which guarantees fast electrical response of  $\sim 10$  ps. The cavity photon lifetime in our case can be estimated by  $\tau_{ph} = \lambda Q / 2\pi c$  [124], which is  $\sim 0.1$  ns. The high acoustic wave velocity in  $\text{SiO}_2$  (5900 m/s) helps fast ( $\sim 0.5$  ns) stress field build up around the waveguide. Based on these observations, ultra-fast sub-nanosecond dynamic response can be expected, which is several orders of magnitude larger than current thermal tuning [57].

To demonstrate the high speed switching, time domain dynamic response of the output light intensity is recorded while applying modulating signals and biasing the laser at the slope



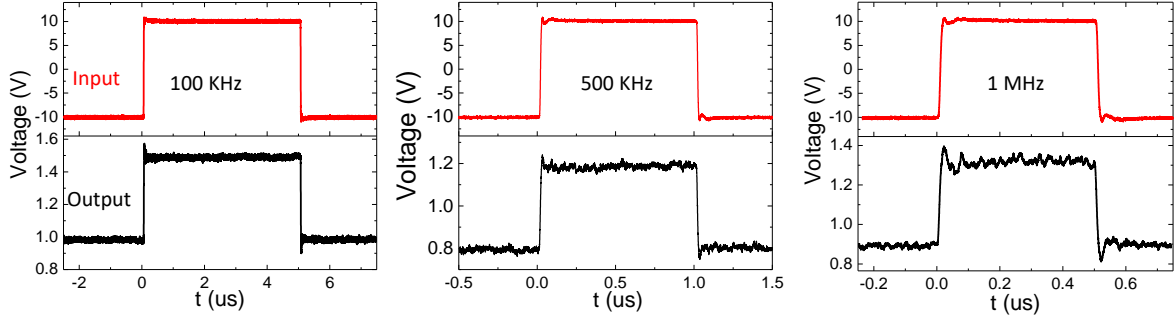


**Figure 2.14.** Time domain response (black) to a large-signal input square wave (red) with 20 V  $V_{pp}$ . The repetition rate is increased from 100 kHz to 1 MHz (left to right). The duty cycle of the square wave is 50%.

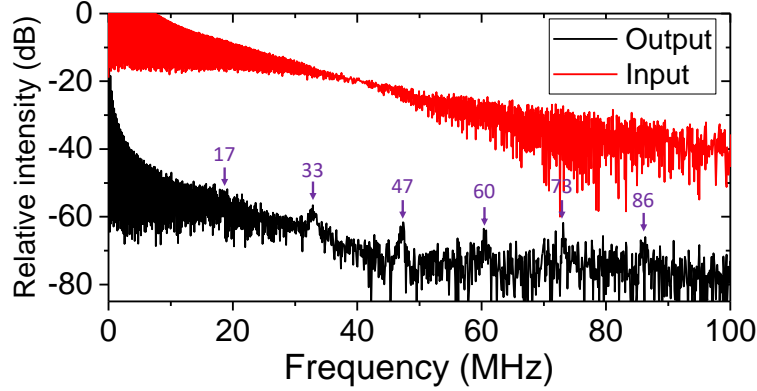


**Figure 2.15.** Fast Fourier Transform (FFT) of the 1 MHz repetition rate input and output square waves in Fig. 2.14. The position and frequency of each acoustic resonance is as labeled.

of the optical resonance. As shown in Fig. 2.14, square waves with 20 V  $V_{pp}$  are applied to the actuator with different repetition rates. The output shows sharp switching between the two voltage levels with high signal to noise ratio (SNR). From the 1 MHz result, it can be seen the device instantaneously responds to the input signal with speed much faster than 0.1  $\mu$ s. However, it is observed that there exist sharp spikes at tuning edges when switching from one voltage state to the other, irrespective of the repetition rate. Although the actuator is unreleased, they are from the acoustic resonances excited in the bulk substrate and the mechanical vibration of the entire chip which is  $5 \times 5$  mm<sup>2</sup>.

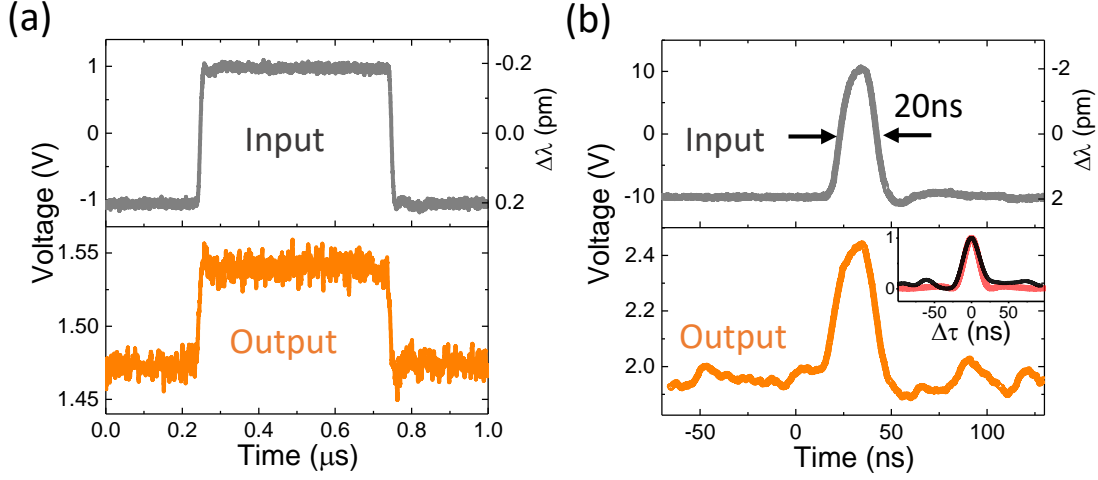


**Figure 2.16.** (a) Time domain response (orange) to a small-signal square wave (gray) with 2 V  $V_{pp}$ , 1 MHz repetition rate, and a 50% duty cycle. (b) Time domain response to short pulses with 20 V  $V_{pp}$ , 5 MHz repetition rate, and a 20 ns pulse width, demonstrating ultra-fast (sub-ns) tuning speed. The inset shows the normalized cross-correlation (black) between input and output signals and the auto-correlation (red) of the input signal. The right Y axis in (a), (b) denotes the resonant wavelength shifting relative to 0 V voltage, according to a linear tuning of -0.2 pm/V. Reprinted from Ref. [12].

To see it more clearly, Fast Fourier Transforms (FFT) of both the input and output time domain response of the 1 MHz square waves are conducted as shown in Fig. 2.15. Compared with the input signal, the output light modulation presents resonant peaks as labeled by the purple arrows. As will be shown in more details in the next section, these resonances are from the High-overtone Bulk Acoustic Resonances (HBAR) formed in the Si substrate. As we drive the actuator, vibration of the AlN actuator will launch an acoustic wave vertically into the substrate, which will be trapped in an acoustic Fabry-Pérot cavity formed by the top and bottom surfaces of the entire chip. With 17 MHz resonance being the first order mode, an equidistantly spaced higher order harmonics can be found that are nearly integer number of the fundamental mode. These resonances will add extra unnecessary noise to the light modulation and compromise the linearity of the actuator's response which is especially important in long distance ( $>100$  m) detection of LiDAR [84].

Next, the ability of the piezoelectric transduction is pushed towards small signal and higher speed. A small-signal ( $V_{pp} = 2$  V) square wave (1 MHz) is firstly applied in Fig.

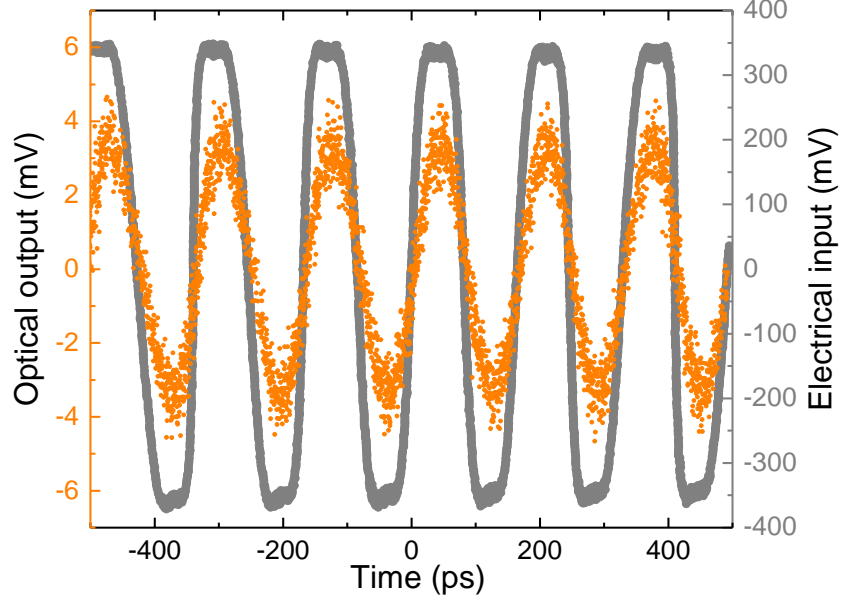


**Figure 2.17.** 6 GHz square wave driving at the frequency where mechanical resonances disappear due to low mechanical  $Q$ . The electrical signal (gray) is measured by an oscilloscope (Tektronix DSA8200) after 20 dB attenuation of the original signal. The optical output shows clear oscillations with a frequency equal to the driving field, illustrating GHz level piezoelectric actuation. Reprinted from Ref. [12].

2.16(a), and the transmitted light intensity modulation is measured. Although with only 0.4 pm relative resonant wavelength shifting, the output signal shows clear separation between the two switching states which is larger than the noise level. Periodic (5 MHz) short pulses with 20 ns pulse widths are also applied as seen in Fig. 2.16(b). To quantitatively show the similarity between input and output signals, the normalized cross-correlation between them is calculated as shown in the inset of Fig. 2.16(b). Indeed, the similarity between the auto-correlation (red) of the input signal itself and the cross-correlation (black) demonstrates ultra-fast actuation beyond the nanosecond.

Despite the high actuation speed, the existence of HBAR modes prevents digital modulation at repetition rates beyond 1 GHz, where a flat and broadband response is usually required as in traditional optical communication. In this sense, pre-conditioning of the input signal or data post-processing is necessary to eliminate the distortion from mechanical resonances. However, due to the constant  $f \cdot Q$  product in a general mechanical resonant systems,

the acoustic resonances at high frequency gradually disappear due to low mechanical  $Q$ . If we apply an ultra-high repetition rate ( $f_{\text{rep}}$ ) signal in the mechanical resonance damping-out region, we can still retrieve a clear output, getting rid of resonance induced signal distortion. This is demonstrated in Fig. 2.17, where a 6 GHz square wave (gray curve) is applied using a programmable pattern generator (Tektronix PPG1251), and amplified by an optical modulator driver (WJ communication SA1137-2) to  $V_{\text{pp}}$  of 7 V. The output optical modulation (orange) shows distinguishable oscillation at the same repetition rate, which suggests that the piezoelectric actuator itself can perform ultra-fast actuation, despite the fact that broad-band modulation is mostly limited by acoustic resonances. Because of the lower responsivity to higher harmonic Fourier components (e.g., 12 GHz, 24 GHz) of the input square wave, the output behaves more like a 6 GHz sinusoidal wave.

For an ideal high speed tuning of the optical resonator, it is required the actuator keeps flat response from DC up to an high frequency (which is dependent on specific application). The frequency response of the actuator is directly measured by the setup shown in Fig. 2.18(a). Both the electromechanical  $S_{11}$  and optomechanical  $S_{21}$  spectrum responses are measured. The  $S_{11}$  is the reflection of the electrical energy from the actuator which is measured using port 1 of the network analyzer (Agilent E8364B), where the electrical signal (-5 dBm) is applied to the actuator through an RF GS probe (GGB 40A-GS-150). As shown in Fig. 2.18(b), the mechanical resonances can be found from the dips where the electrical energy is converted to the acoustic energy into the device. Ideally,  $S_{11}$  should be smaller than 0 dB which means there is no gain in the system. However, there are several spikes that are above 0, which is mainly due to the difficulty in calibration in low frequencies of the VNA. Also, note that the scale of  $S_{11}$  is small on the order of 0.1 dB.

For the optomechanical  $S_{21}$  measurement, around 100  $\mu\text{W}$  continuous wave light from a diode laser (Velocity Tunable Laser 6328) is edge-coupled to the device using a lensed fiber via inverse taper. A -5 dBm RF electrical signal is applied from port 1 of the network analyzer to drive the piezoelectric actuator and the light intensity modulation is detected by a 12 GHz photodiode (New Focus 1544), which is sent back to port 2 of the network analyzer. A series of periodic HBAR modes can be clearly observed which aligns with the dips in  $S_{11}$ . Also, these resonances match with the FFT spectrum in Fig. 2.15, and the slightly higher

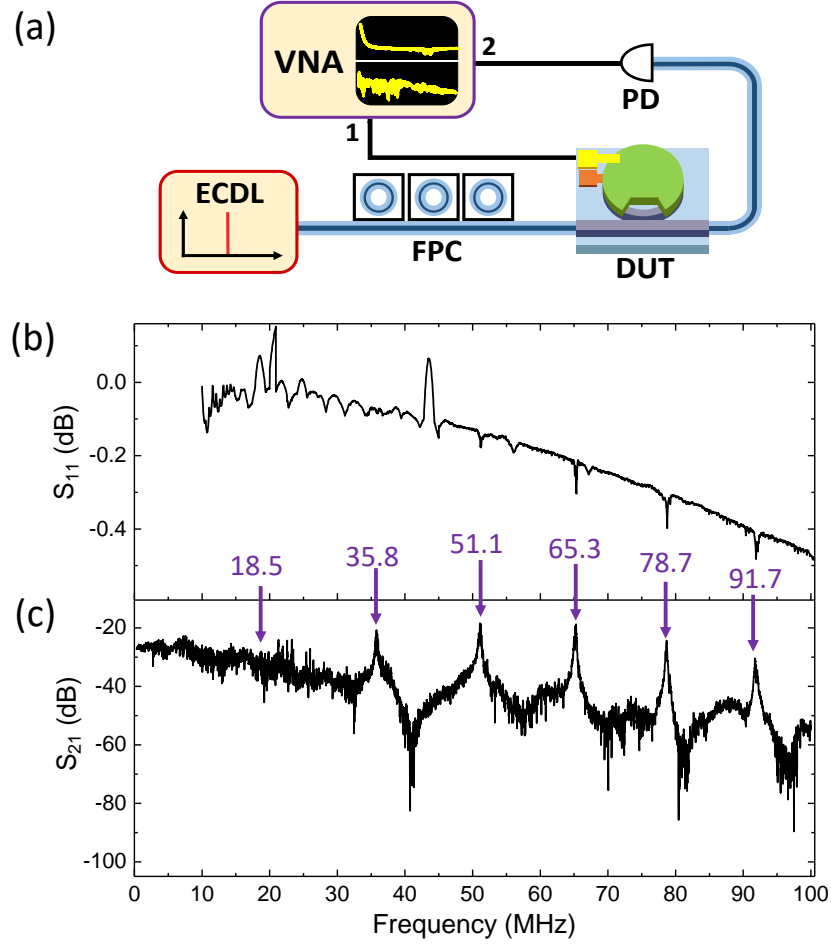


**Figure 2.18.** (a) Schematic of the setup for measuring electromechanical and optomechanical response. ECDL: external cavity diode laser, PC: polarization controller, DUT: device under test, PD: photo-diode, VNA: vector network analyzer. (b) Electromechanical  $S_{11}$  and (c) optomechanical  $S_{21}$  spectrum response of the piezoelectric transduction from 300 kHz to 100 MHz. The position and frequency of each acoustic resonance is as labeled.

frequency is because of the variation of the Si substrate's thickness from each fabrication run. One of the typical HBAR mode is simulated in Fig. 2.19(b), showing the distribution of vertical mechanical displacement. It can be seen the mode distributes over the whole substrate, and the acoustic wavelength is on the order of 100  $\mu\text{m}$  at MHz frequencies which is excited by AlN actuator with only 1  $\mu\text{m}$ .

Due to the high optical  $Q$  ( $\sim 1$  Million), the HBAR resonances (except for the fundamental harmonic at 18.5 MHz) in  $S_{21}$  show over 20 dB contrast in SNR, and the resonance and anti-

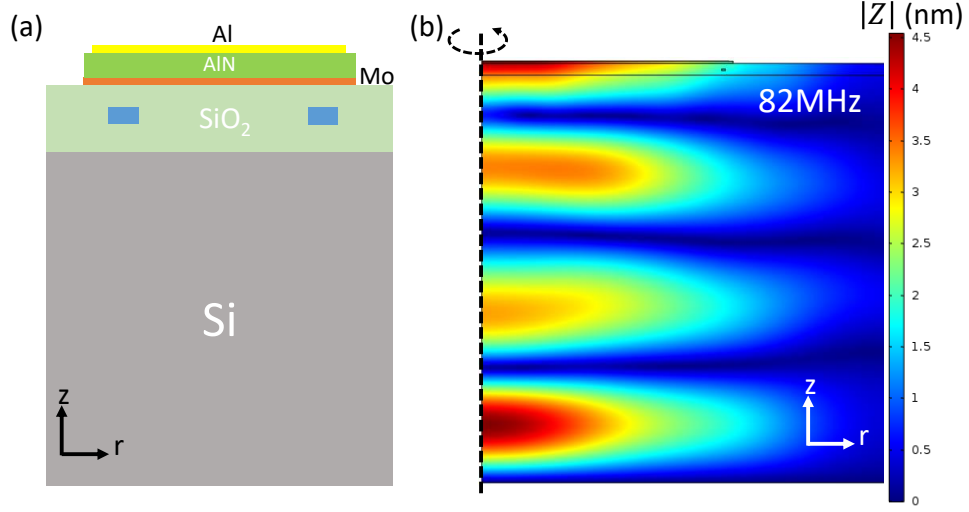


**Figure 2.19.** (a) Schematic of the device cross-section. (b) Numerical simulation of one of the HBAR modes around 82 MHz, showing the vertical  $z$  displacement. Acoustic standing wave is formed over the whole substrate. The mode is axisymmetric around the vertical dashed line.

resonance which are typical for a mechanical resonance can be clearly resolved. This is in contrast to the electrical  $S_{11}$  measurement where resonances are smaller 0.1 dB. The high sensitivity of the optical readout on the one hand can be used for optomechanical sensors. On the other hand, all the unwanted mechanical vibration can be picked which would add extra noise to the output optical signal and compromise the linearity of the piezoelectric actuation at high speed.

Not only the HBAR modes at 10s of MHz, the bulk modes of the chip at lower frequency (100s kHz) are also coupled to the output of the light modulation, as shown in Fig. 2.20(a). A very rich family of mode can be found. As hundreds of mechanical modes can be supported by the chip, it is challenging to identify each resonance and match with the simulation. The simulations of typical mechanical modes of the chip are shown in Fig. 2.20(b), which include the flexural mode, Lamé mode, and face-shear mode [125]. While the vibration of the flexural mode is mainly out of plane, that of the Lamé and face-shear mode is in plane. These mechanical modes of the chip needs to be eliminated in order to have a flat response up to 10 MHz, as will be shown in the next section.

### 2.1.6 Strategies to improve the tuning speed

As illustrated in the last section, the high density of mechanical modes at MHz frequency severely limits the linear response of the actuator. We investigate here different strategies to suppress the mechanical modes of the chip and the combination of them results in flat response up to 10 MHz. At low frequency, the actuator is relatively small compared with the wavelength of the acoustic wave, so it can be treated as a point source that locally emits acoustic waves. As inspired by Ref [126] where the flexural modes of a nanomechanical membrane are suppressed by the far field destructive interference between elastic waves, we mitigated the flexural mode of the chip by differential driving of two adjacent actuators. As shown in the optical image of the insets in Fig. 2.21, an auxiliary disk actuator is placed

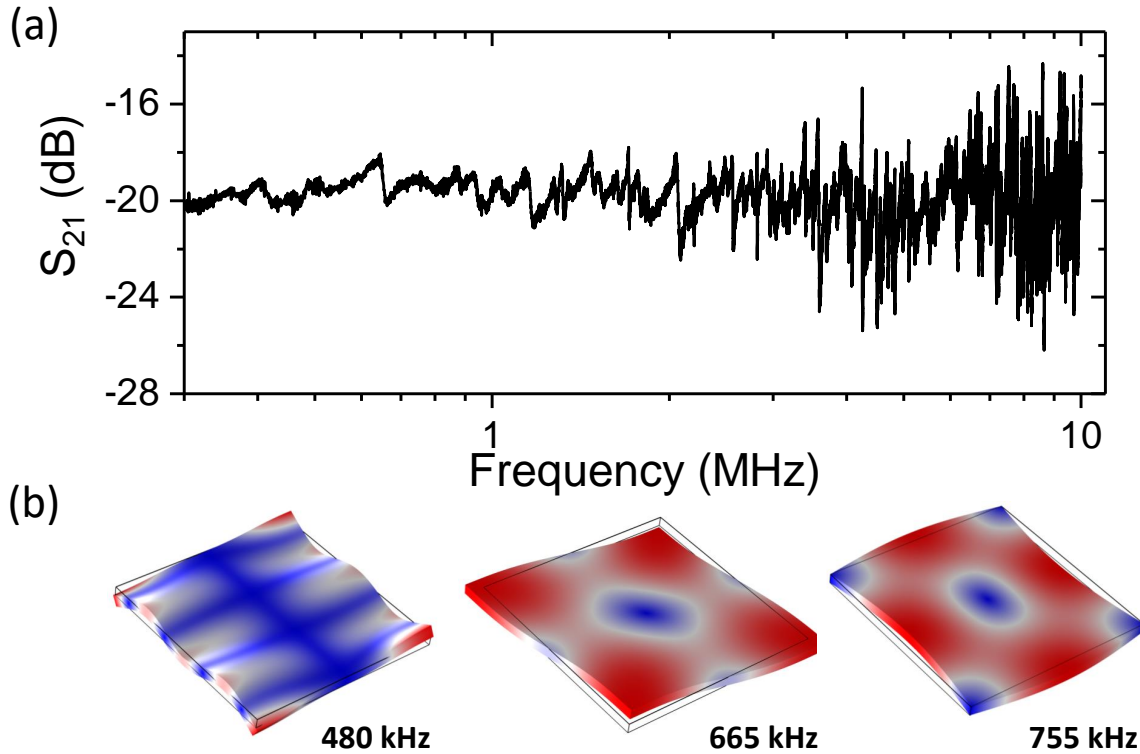


**Figure 2.20.** (a) Optomechanical  $S_{21}$  response at low frequency. The frequency is plotted in log scale. (b) Simulation of typical mechanical modes of the entire photonic chip, including flexural mode at 480 kHz, face-shear mode at 665 kHz, and Lamé mode at 755 kHz.

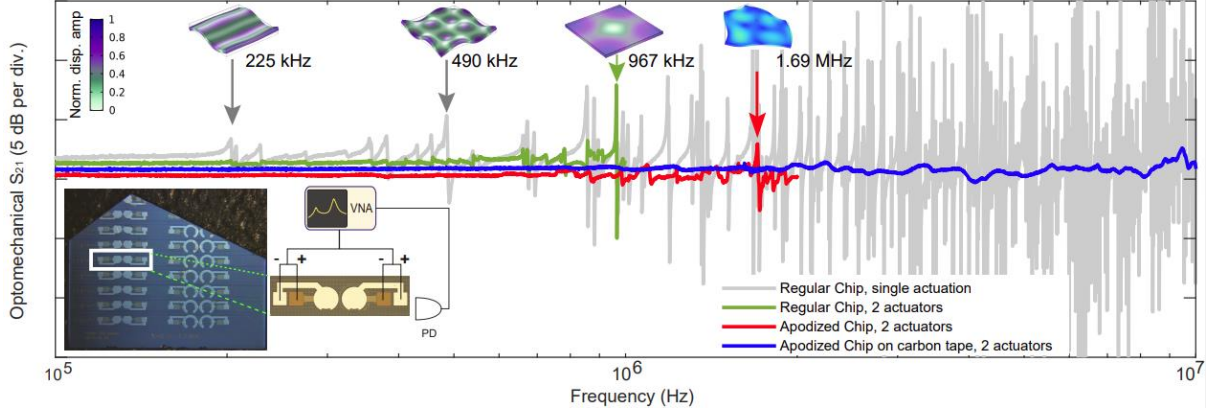


**Figure 2.21.** Optomechanical  $S_{21}$  responses of Disk actuator with single actuation (gray), dual actuators with differential drive for a square  $\text{Si}_3\text{N}_4$  chip (green), an apodized chip (red), and an apodized chip on a carbon tape (blue). Inset: numerical simulation of three mechanical modes of the square  $S_{21}$  chip and the apodized chip (1.69 MHz). Photo of the apodized chip with the dual-actuator configuration. Experimental schematic for differential driving of dual actuators. (Courtesy of Anat Siddharth)

adjacent to the actuator that is on the optical microring resonator. By driving them with the same signal but with  $\pi$  phase difference, the excitation of mechanical resonances can be effectively suppressed as shown in Fig. 2.21 green curve. However, it is mostly effective for modes below 1 MHz where most flexural modes reside. The in plane shear modes are still significant as illustrated by the 967 KHz resonance in Fig. 2.21.

To further suppress the in plane acoustic waves, the entire chip is apodized into a polygon with non-parallel edges to suppress the reflection and thus resonant of in plane elastic waves. The lower left optical image in Fig. 2.21 shows one of the apodized photonic chip where the top two corners are intentionally cut to reduce parallel faces. This strategy extends the flatness of the response further to beyond 1 MHz as shown by the red curve in Fig. 2.21. However, since we have to couple light in and out through the left and right edges of the chip, they are still parallel. One of the mechanical mode of the apodized chip is shown as the 1.69 MHz mode in Fig. 2.21. Finally, we further flatten the actuation response by attaching the apodized chip on a piece of carbon tape and then differentially driving the actuators. In such a way, both the flexural and the bulk mechanical modes are damped, and



a flat response can be achieved up to 10 MHz with variation smaller than 1 dB, as shown in the blue curve of Fig. 2.21. This flat response will improve the linearity of piezoelectric actuation for integrated tunable laser, and frequency modulated continuous wave (FMCW) LiDAR where any nonlinearity will reduce the SNR as light travels over long distance ( $>100$  m) [84]. While these strategies are effective for mechanical modes of the chip, the HBAR modes at 10s of MHz that inherently reside in the substrate will require extra solutions, as will be discussed in the next section.

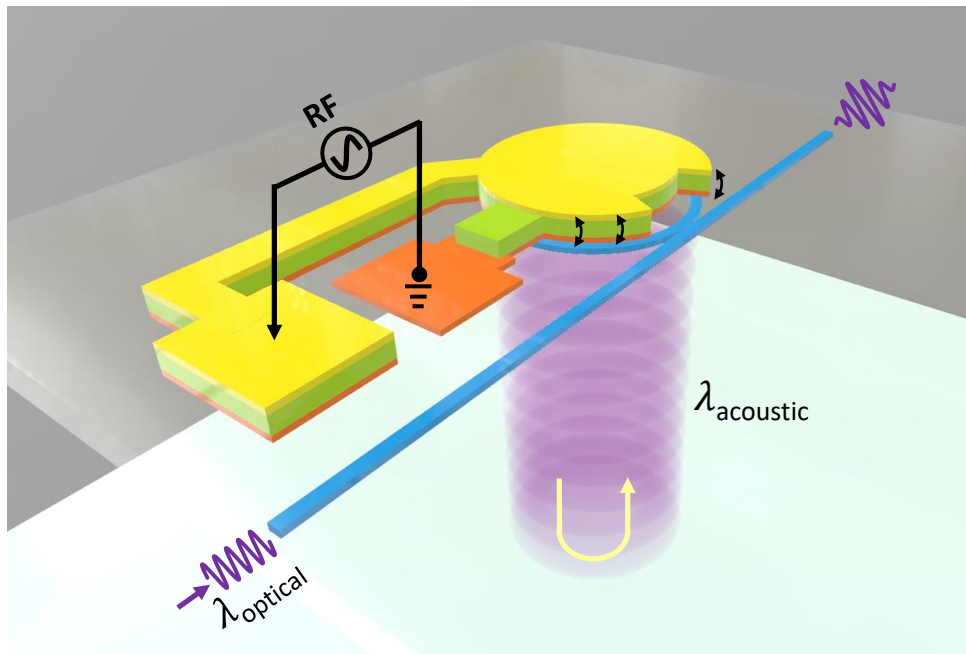


**Figure 2.22.** Hybrid nanophotonic high-overtone bulk acoustic resonator (HBAR) platform. 3D schematic illustrating excitation of bulk acoustic wave resonances via a macroscopic piezoelectric actuator, which transmit vertically into the stack and form acoustic standing waves inside the various acoustic Fabry-Pérot cavities. The resonance enhanced mechanical stress changes the waveguide’s effective index via the stress-optical effect, and thereby modulate the output optical intensity. Reprinted from Ref. [12].

## 2.2 HBAR acousto-optic modulation

### 2.2.1 HBAR AOM of Disk actuator

As illustrated in previous section, as we switch fast, there form spikes at the edges. After careful frequency analysis, we found these are caused by the mechanical ringing from a rich family of High-overtone Bulk Acoustic wave Resonances (known as HBAR modes), as illustrated in Fig. 2.22. As we drive the actuator harmonically, vibration of the AlN disk will launch an acoustic wave vertically into the substrate. Since the bottom surface of the substrate is smooth and flat, the acoustic wave will be reflected and subsequently bounce back and forth between the top and bottom surfaces. Working as an acoustic Fabry-Pérot cavity, the counter-propagating acoustic waves will constructively interfere when the cavity length is an integer number of the acoustic wavelength, with acoustic energy trapped inside the cavity. These bulk acoustic standing waves will enhance the stress field around optical waveguides and modulate the effective index through stress-optical effect [65].

Experimentally, the electromechanical reflection parameter  $S_{11}$  is first measured as shown in Fig. 2.23(a). A series of resonance dips is found to evenly distribute over multiple octaves in the microwave regime. A zoom-in of the spectrum is illustrated in Fig. 2.23(d) which highlights the resonance shape, linewidth ( $\sim 3$  MHz), and acoustic free spectral range (FSR) of around 17.5 MHz. The narrow linewidth demonstrates high mechanical Q ( $\sim 1000$ ) which is mainly limited by the intrinsic acoustic loss in the substrate and the scattering at interfaces.

It is interesting to note that the envelope of these sharp resonances varies slowly and smoothly with a period of  $\sim 490$  MHz. This is caused by the resonance inside the  $5.4 \mu\text{m}$   $\text{SiO}_2$  cladding layer, which stems from acoustic wave reflections at the Si- $\text{SiO}_2$  interface due to an acoustic impedance mismatch. The position of  $\text{SiO}_2$  resonance is located at the node of the envelope, whereas anti-resonance is located at the anti-node. Intuitively speaking, at the anti-resonance of the  $\text{SiO}_2$  layer, it works as an acoustic anti-reflection coating such that more acoustic energy will transmit into the Si substrate, which has larger acoustic impedance, and thus better electromechanical conversion. When the acoustic half wavelength matches the  $1 \mu\text{m}$  AlN thickness, the AlN layer reaches its fundamental resonance mode and becomes more efficient in excitation of acoustic waves around 4 – 4.3 GHz. It can be seen that, by optimizing

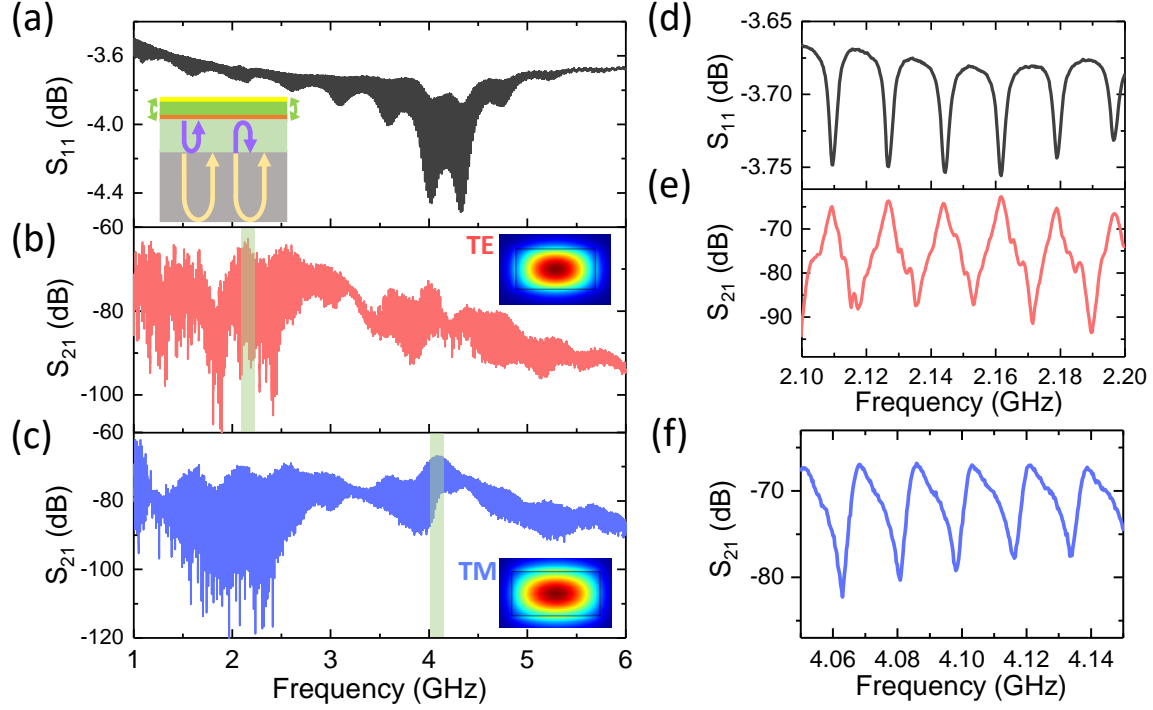


**Figure 2.23.** Microwave frequency electro-acousto-optic modulation. (a) Electromechanical  $S_{11}$  spectrum from 1 to 6 GHz. A range of equidistant bulk acoustic resonances is found to exist over a broad frequency range. The inset schematic illustrates the acoustic wave reflection at interfaces. (b), (c) Optomechanical  $S_{21}$  responses of TE and TM modes demonstrate acousto-optic modulation covering multiple octave-spanning microwave frequencies. Due to different optical mode shapes (insets in (b) and (c)) and thus acousto-optic mode overlap, TE and TM modes show dissimilar  $S_{21}$  spectra. (d), (e) The zoom-in of  $S_{11}$ , and TE mode's  $S_{21}$  within the window (green shaded area in (b)) around 2 GHz. (f) The zoom-in of TM mode's  $S_{21}$  around 4 GHz in (c). The resonances distribute evenly with an FSR of 17.5 MHz. Reprinted from Ref. [12].

AlN and SiO<sub>2</sub> thicknesses, the resonances of these two cavities can be misaligned to further improve acoustic wave excitation. Additionally, the coupling between the Si substrate cavity and the SiO<sub>2</sub> and AlN cavities causes periodic fluctuations of the FSR and higher order dispersion, as will be discussed later.

The acousto-optic modulation of the microring resonator can be characterized by an optomechanical  $S_{21}$  measurement as shown in Fig. 2.18(a), where by biasing the input laser ( $\sim 1550$  nm) at the slope of the optical resonance, its output intensity is modulated as we

launch a -5 dBm RF signal from port 1 of the VNA. The intensity modulation of the optical signal is measured using a photodiode and sent back to port 2 for the  $S_{21}$  measurement. Note that no optical and electrical amplifiers are employed in an effort to preserve direct electro-opto-mechanical transduction. The optomechanical  $S_{21}$  measurements are performed for both the transverse electric (TE) and transverse magnetic (TM) optical modes, as shown in Fig. 2.23(b) and (c) respectively.

As expected, a broad range of periodic peaks is observed which correspond to each HBAR mode in  $S_{11}$ . Due to the different optical mode profiles of the TE and TM modes (and thus acousto-optic mode overlaps) and optical Q factors, they respond differently, with the TE mode response strongest around 2 GHz and the TM mode responding most strongly around 4 GHz. Since the TE mode shows higher optical Q, it will enter the resolved sideband regime at frequencies far beyond its linewidth (1 – 2 GHz), where the modulation sidebands are suppressed when biasing at the resonance slope. The zoom-in of highlighted regions (green shaded areas) are as shown in Fig. 2.23(e) and (f), illustrating clear peaks with high contrast ( $>20$  dB) between resonance and anti-resonance.

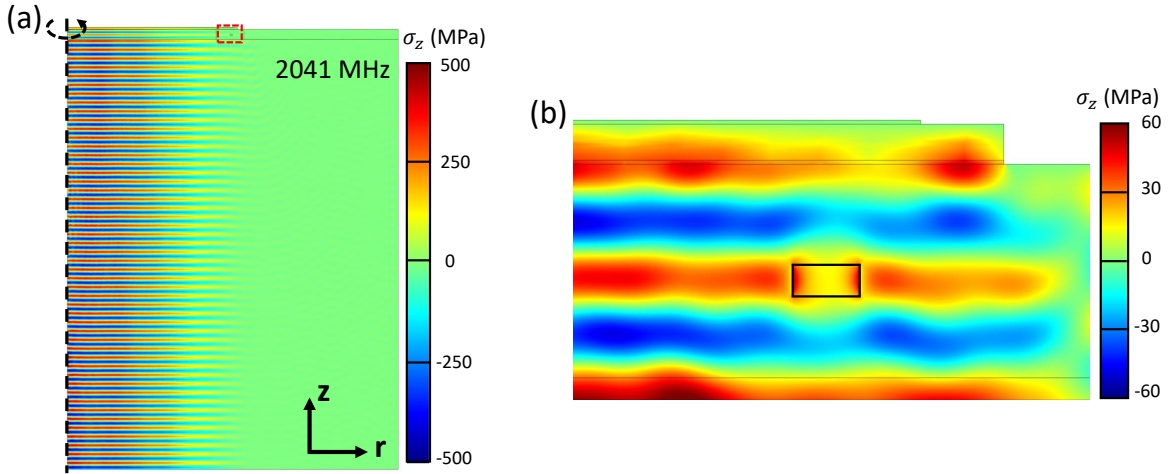


**Figure 2.24.** (a) Numerical simulation of vertical stress  $\sigma_z$  distribution for one typical acoustic resonant mode at 2.041 GHz under 1 V driving field, with a zoom-in around the optical waveguide (red box in (a)) shown in (b). At GHz frequencies, the acoustic wavelength is similar in scale to optical wavelength and waveguide structure. Reprinted from Ref. [12].

A numerical (COMSOL) simulation of one typical acoustic mode at 2.041 GHz is shown in Fig. 2.24(a), and a zoom-in around the optical waveguide is in Fig. 2.24(b). The acoustic standing wave distributes uniformly over the entire substrate, which indicates that the optical circuits can be buried deeply inside the SiO<sub>2</sub> cladding, free from the trade-off between actuation efficiency and absorption losses due to metal as found in traditional optical modulators. Also, an acoustic wavelength that is comparable to the optical wavelength and waveguide structure at microwave frequencies is achieved with macroscopic actuators. As is evident, the simplicity of our structure presents advantages such as simple fabrication, high fabrication tolerance, high rigidity, and high power handling. Additionally, it can be seen from Fig. 2.24(a) that the acoustic mode is largely confined beneath the actuator which guarantees low electromechanical cross-talk (-60 dB) between adjacent devices (see next section). These features may supplement conventional SAW based AOM for future microwave photonics applications with ultra-high optical Q, low cost, and dense integration.

### 2.2.2 Analysis of mechanical dispersion

An analytical electromechanical model is established to help us get deep understanding of the mechanical performance of the device (see Appendix A for details). The  $S_{11}$  response is first calculated as shown in Fig. 2.25(a), illustrating high accuracy of the model as compared to the experiment (Fig. 2.25(b)). As mentioned above, the coupling from SiO<sub>2</sub> and AlN cavities not only modulates the resonances' magnitude envelope, but also the dispersion of mechanical modes (deviation from equidistant spectrum). Fig. 2.25(c) clearly shows the variation of frequency difference (local FSR) between each pair of adjacent resonances. The local FSR varies nearly periodically around an average value of 17.5 MHz with the same period as the envelope in Fig. 2.25(b). By comparing Fig. 2.25(b) and (c), it can be found that at each node of the envelope, the FSR reaches maximum value, which means the spacing of Si resonances increases near the SiO<sub>2</sub> resonance. From the standpoint of the Si cavity, the variation of FSR can be understood intuitively that, the wave reflected back into the Si substrate from the Si-SiO<sub>2</sub> interface experiences varied phases relative to the SiO<sub>2</sub> resonance. For example, around SiO<sub>2</sub> resonance, the Si-SiO<sub>2</sub> interface locates at the node

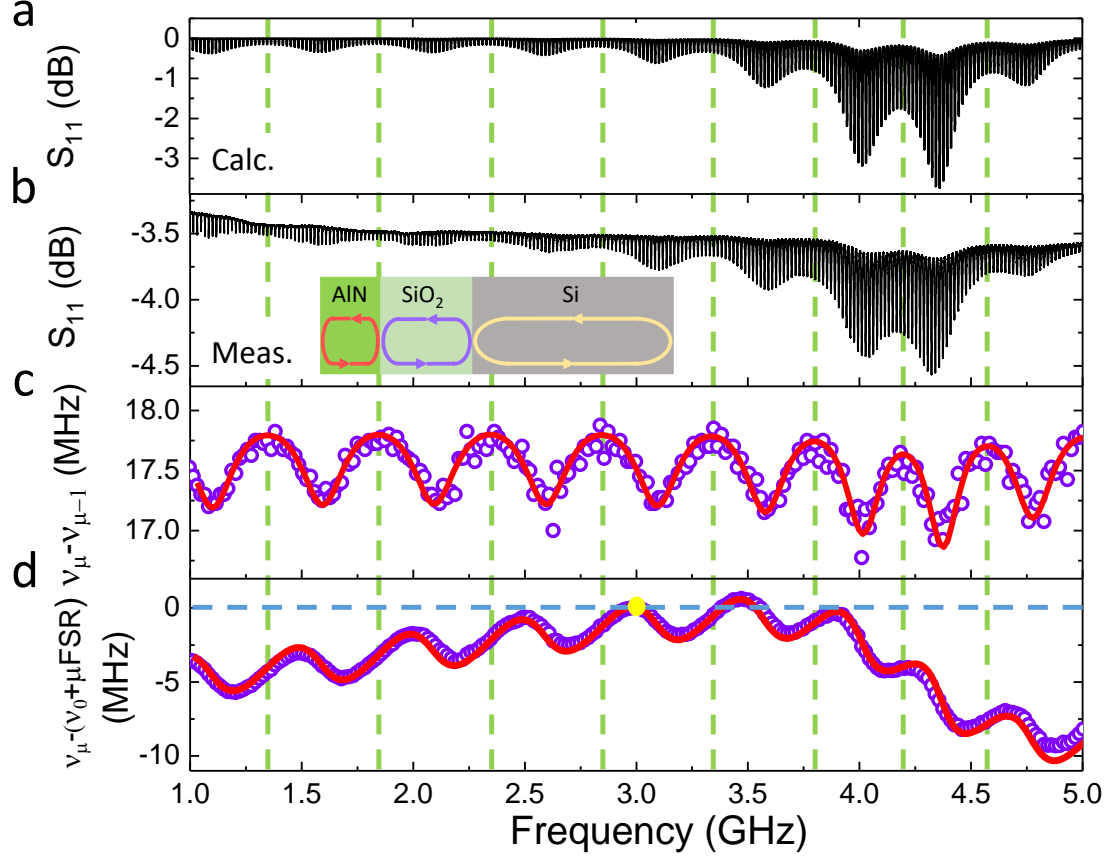


**Figure 2.25.** Mechanical dispersion analysis of HBAR modes. (a) Calculated and (b) measured  $S_{11}$  spectrum showing good agreement between the electromechanical model and experiment. Each green dashed line denotes the location of a resonance from the  $\text{SiO}_2$  cavity. The inset in (b) illustrates the coupling between Si,  $\text{SiO}_2$ , and AlN cavities. (c) The measured (circle) and calculated (solid line) frequency difference between each pair of adjacent Si resonances, showing a periodic variation of local FSR around an average value of 17.5 MHz. Note that the maxima of FSR align with green dashed lines where the  $\text{SiO}_2$  resonances are located. (d) Measured (circle) and calculated (solid line) higher order dispersion represented by the frequency deviation from an equidistant frequency grid (with average FSR = 17.515 MHz), referencing to mode  $\nu_0$  ( $= 3.0145$  GHz, labeled as yellow dot).  $\mu$  is the mode number difference relative to the mode at 3.0145 GHz.

of an acoustic stress wave with near-zero stress (maximum displacement), which presents a free boundary condition. Far beyond  $\text{SiO}_2$  resonances, the interface is at an anti-node corresponding to fixed boundary condition (zero displacement). These various boundary conditions each impose a particular phase for a given reflected wave, and thus change the effective cavity length of Si.

However, for the AlN and  $\text{SiO}_2$  cavities, the green dashed lines that denote the location of each  $\text{SiO}_2$  resonance bunch together around 4 GHz where the AlN cavity resonance is located. Also, it can be seen that the average FSR of acoustic modes decreases around the AlN resonance. Based on these observations and the fact that the acoustic impedance of  $\text{SiO}_2$  is smaller than Si and then AlN, we can conclude that, for two coupled acoustic cavities, the small cavity (e.g.,  $\text{SiO}_2$ ) with smaller acoustic impedance tends to decrease (increase) the effective cavity length (FSR) of the big cavity (e.g., Si) when it's on resonance compared

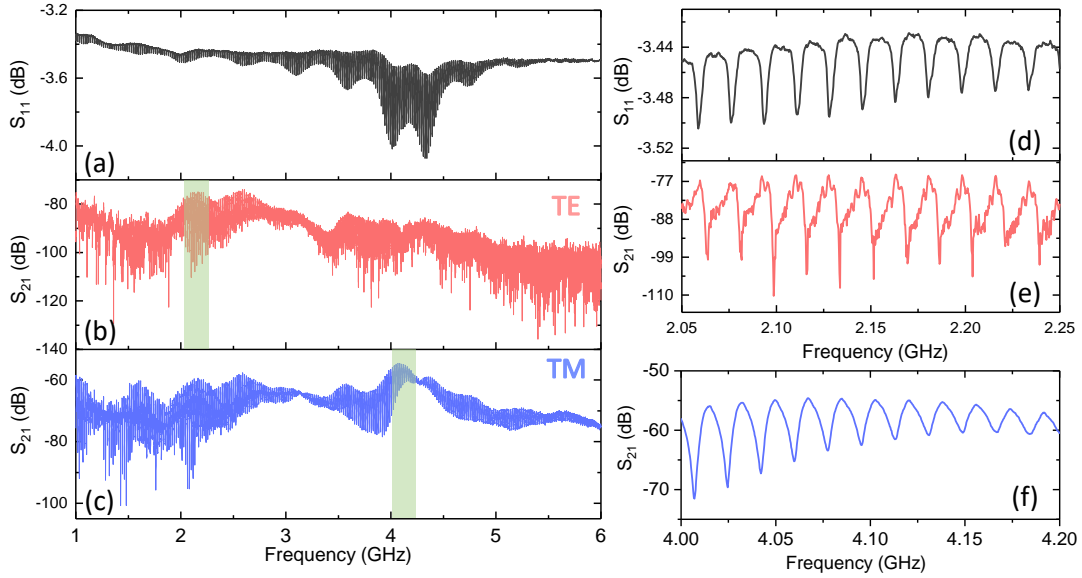


**Figure 2.26.** The same  $S_{11}$  and  $S_{21}$  measurements on the Donut device in GHz range. (a) Electromechanical  $S_{11}$  spectrum from 1 to 6 GHz. Optomechanical  $S_{21}$  responses of (b) TE and (c) TM modes demonstrate effective stress-optical modulation spanning a broad range of microwave frequencies. The Donut device shows similar results as reported for the Disk device in the main text. (d) and (e) show the zoom-in of  $S_{11}$  and  $S_{21}$  responses of TE mode within the window (green shaded area) around 2 GHz in (b), while (f) shows the zoom-in of TM mode's  $S_{21}$  response around 4 GHz in (c). Reprinted from Ref. [12].

to off resonance, and vice versa [127]. This is, to some extent, similar to coupled optical cavities by treating acoustic impedance as the effective refractive index.

The higher order dispersion is presented in Fig. 2.25(d), which shows the frequency deviation of each resonance from the ideally even distribution with reference to mode at 3.0145 GHz and period of 17.515 MHz. Mathematically, it can be interpreted as the integral of Fig. 2.25(c) (that is, the accumulation of FSR deviation relative to 17.515 MHz) with respect to the origin at 3.0145 GHz. The higher order dispersion also shows periodic variation caused by the coupling between the Si and SiO<sub>2</sub> cavities, which varies between normal and anomalous group velocity dispersion. The roll-off starting around 3.5 GHz is caused by reduced FSR due to coupling of the AlN cavity. This study of mechanical dispersion could benefit the growing field of mechanical dispersion engineering for future applications (e.g., mechanical solitons) and future devices by optimizing Si, SiO<sub>2</sub>, and AlN thicknesses or by choosing materials with different acoustic impedance [128]–[130]. In this sense, further theoretical and numerical studies are necessary for a more complete understanding of the acoustic wave propagation and mechanical cavity coupling in such a platform.

### 2.2.3 HBAR AOM of Donut actuator

The same measurements are also done for the Donut device, including  $S_{11}$  and  $S_{21}$  responses as shown in Fig. 2.26. No big differences can be found between the Disk and Donut devices in terms of mode distribution, envelope of resonances, and signal to noise ratio. This indicates that the HBAR mode distribution and optomechanical spectra are less related to the shape of the actuator, but more to the vertical stack. This relaxes the requirements on actuator shape and size, which lends itself with high design freedom and small footprint. In the zoom-in around 2 GHz in Fig. 2.26(e), there are multiple peaks inside each resonance due to existence of higher order acoustic modes.

Numerical simulations of one of the fundamental modes at 2.125 GHz is shown in Fig. 2.27(a), and the zoom-in around waveguide is in Fig. 2.27(b). From the mode distribution, we can see the acoustic wave is effectively excited and confined under the actuator vertically



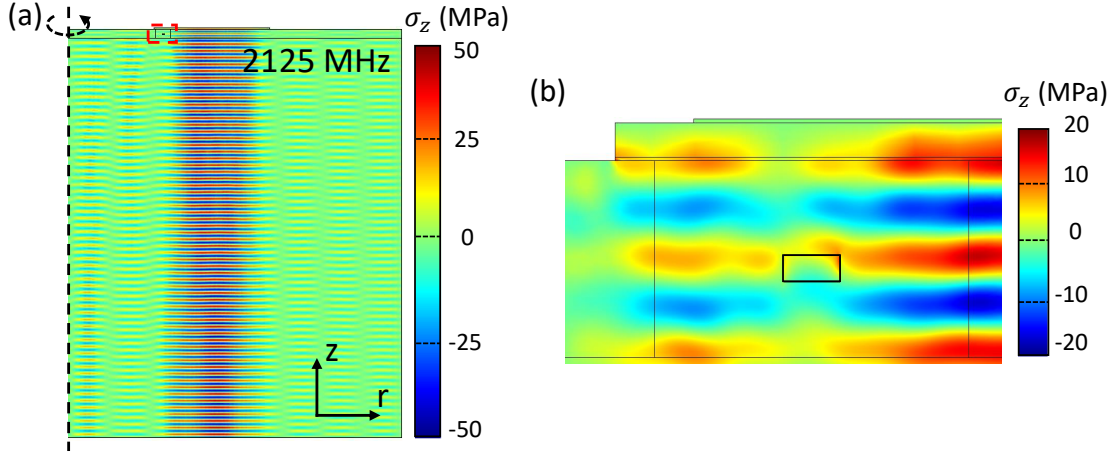


**Figure 2.27.** (a) Numerical simulation of  $\sigma_z$  distribution for one typical acoustic resonant mode at 2.125 GHz, with a zoom-in around the optical waveguide (red box) shown in (b). Reprinted from Ref. [12].

with little diffraction angle. The good mode confinement guarantees low cross-talk between closely placed actuators.

#### 2.2.4 Electromechanical cross-talk between adjacent actuators

As mentioned in the previous section, the high confinement of the acoustic mode beneath the actuator guarantees low cross-talk between adjacent actuators. To demonstrate this, three actuators are closely placed on the same optical ring resonator, which cover the whole ring in an interval of  $120^\circ$ , as shown in Fig. 2.28(a). The one port reflection parameter  $S_{11}$  of actuator 1 is first measured as illustrated in Fig. 2.28(b). The difference from the  $S_{11}$  shown in the main text is caused by the thicker Si substrate ( $500\ \mu\text{m}$ ) and thicker  $\text{SiO}_2$  cladding ( $7\ \mu\text{m}$ ). These lead to smaller FSR and period of the envelope.

More importantly, the cross-talk is measured by performing a two-port electromechanical  $S_{21}$  measurement, where we drive actuator 1 and sense the electrical signal out from the adjacent actuator 2. The cross-talk mainly comes from the leaking of acoustic waves from actuator 1 which can be sensed out by actuator 2 via the piezoelectric effect. The leakage of electric field will also be sensed by device 2 and cause cross-talk between electrical signals of device 1 and 2. As demonstrated in Fig. 2.28(b),  $S_{21}$  as low as -60 dB of cross-talk is

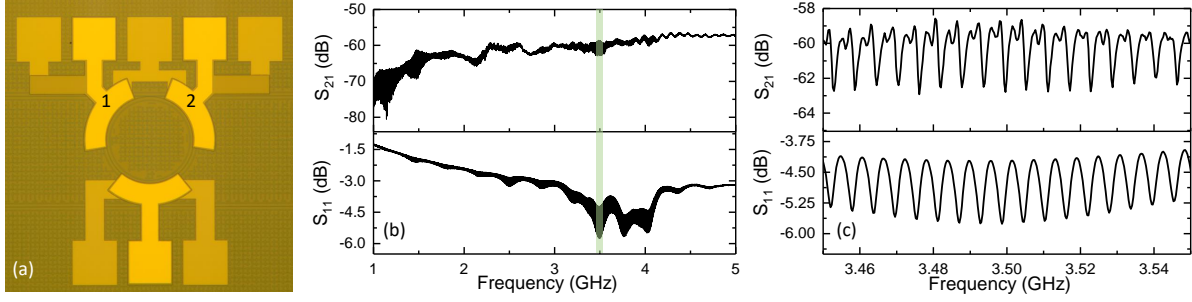


**Figure 2.28.** Demonstration of low electromechanical cross-talk between adjacent actuators. (a) Optical microscope image of the device with three closely placed actuators. (b) (top) Two port electromechanical  $S_{21}$  measurement by driving actuator 1 and sensing from actuator 2 as labeled in (a). (bottom)  $S_{11}$  reflection for device 1. The cross-talk between the two devices is as low as -60 dB which guarantees compact integration. (c) Zoom-in of the measured  $S_{21}$  and  $S_{11}$  responses in the green shaded region in (b). Reprinted from Ref. [12].

achieved, which illustrates the electrical and mechanical isolation between the two adjacent devices. This low cross-talk enables us to fabricate several actuators on the same optical ring, which may realize optical isolation through spatial-temporal modulation [51], [131]–[133], or dispersion engineering of  $\text{Si}_3\text{N}_4$  microring resonator [61] by engineering stress distribution.

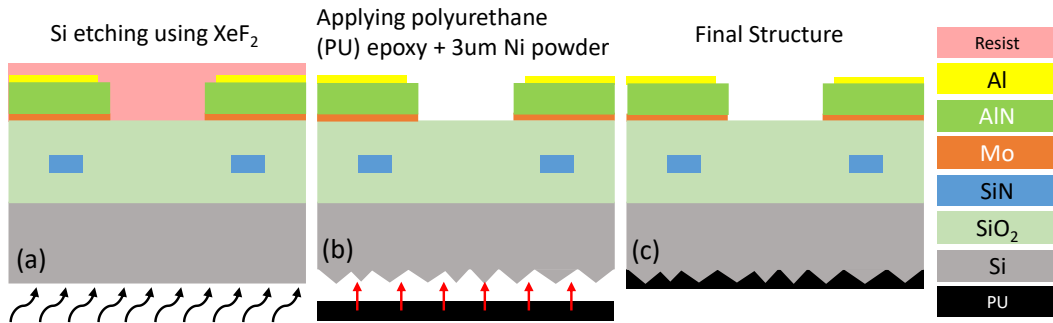


**Figure 2.29.** Fabrication flow for removing HBAR resonances by roughing the backside surface of the Si substrate and pasting a layer of polyurethane (PU) epoxy mixed with 3  $\mu\text{m}$  nickle powder.

### 2.2.5 Strategy for mitigating HBAR resonances

For applications where a broad bandwidth is required, the acoustic modes should be effectively damped or even eliminated. As shown in Fig. 2.29, to damp and eliminate the intrinsic bulk acoustic wave resonances, the backside surface of the Si substrate is first isotropically etched by  $\text{XeF}_2$  in a Xactix Xenon Difluoride E1 system, with the top surface protected by the photoresist AZ1518. The roughing will diffract acoustic waves to random directions and thus weaken constructive interference. Next, as suggested by previous work [134], a layer of polyurethane (PU) epoxy mixed with 3  $\mu\text{m}$  nickle powder is pasted at the bottom, which can damp acoustic vibration at the boundaries and absorb acoustic energy.

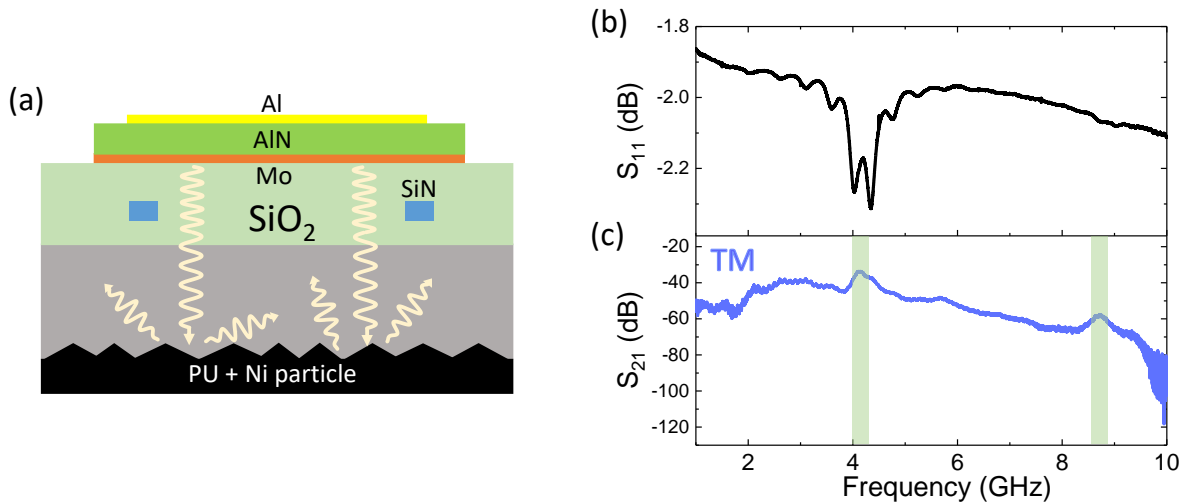


**Figure 2.30.** (a) Cross-section of the device after roughing and then pasting polyurethane (PU) epoxy (mixed with 3  $\mu\text{m}$  Nickle powders) on the backside of the Si substrate. (b)  $S_{11}$  and (c)  $S_{21}$  of the TM mode from 1 to 10 GHz after damping acoustic resonances. The VNA responses become smoother with only wide range envelope variation. Enabled only by AlN fundamental and second harmonic resonances (green shaded regions), broadband modulation can be achieved with 3 dB bandwidth of 250 MHz for each. Reprinted from Ref. [12].

After post-processing the fabricated device, its electromechanical and optomechanical performances are recorded in Fig. 2.30(b) and (c), respectively. To increase the signal to noise ratio of  $S_{21}$  at high frequencies, the RF signal from the VNA is amplified before being applied to the actuator. From the  $S_{11}$  response, one can see that nearly all resonances from the Si substrate cavity are diminished. However, the smoothly varying envelope from resonances in

SiO<sub>2</sub> and AlN cavities still exists, since they remain unaffected by the post-processes. The S<sub>21</sub> measurement also demonstrates the smoothing of the modulation spectrum, but with broad range variations. Some exceptionally small resonances are still visible below 2.5 GHz in S<sub>21</sub>, because the acoustic wavelength at low frequencies is comparable or larger than the Si roughing scale ( $\sim 5 \mu\text{m}$ ). It's worth noting here that the optical measurement is more sensitive than its electrical counterpart due to the high optical Q and its signal to noise ratio. The fast roll-off of S<sub>21</sub> starting around 9.5 GHz is mainly limited by the optical quality factor of the TM mode, and the actual acousto-optic interaction may potentially extend to frequencies beyond 10 GHz.

The fundamental resonance from the AlN thin film enhances the electromechanical conversion efficiency and thus optical modulation around 4.13 GHz, and thanks to its low mechanical Q, we observe broadband modulation with a 3 dB bandwidth of 250 MHz, as shown in Fig. 2.30(c). The second harmonic resonance of AlN cavity is also found in S<sub>21</sub> around 8.7 GHz, here with a 260 MHz bandwidth. These broad bands of modulation can potentially be used to connect superconducting circuits with optical interfaces for low-loss

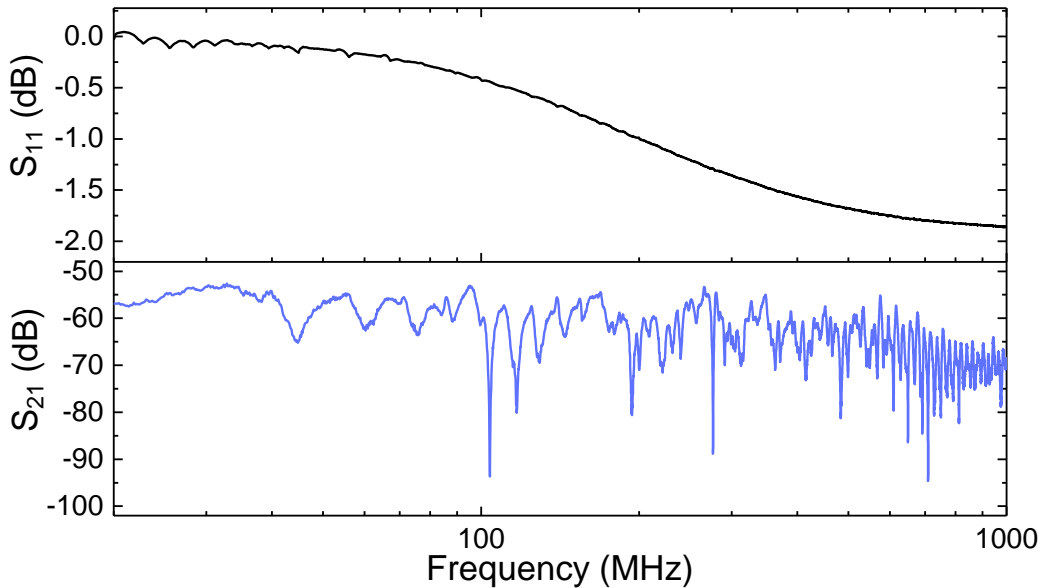


**Figure 2.31.** S<sub>11</sub> (top) and S<sub>21</sub> (bottom) of the TM mode from 20 MHz to 1GHz after damping acoustic resonances. The frequency is in log scale.

quantum information communication [74], [135]. Of note, the positions of these bands can be engineered by modifying the AlN and SiO<sub>2</sub> film thickness for specific applications.

However, the above solution is not effective for HBAR modes below 1 GHz. As shown in Fig. 2.31, the mechanical resonances are still significant at this frequency range, although they can be hardly seen from the electromechanical  $S_{11}$  response. In the future, dedicated design and patterning of the bottom surface of the substrate can be done for better suppression of acoustic resonances from Si cavity. For example, it was shown that deeply etched trenches from the Si substrate's backside can effectively scatter off the acoustic waves below 1 GHz [136]. Also, by having thinner Si substrate, we can push the fundamental Si HBAR resonance beyond 100 MHz. For example, 100 MHz HBAR fundamental mode corresponds to 42  $\mu\text{m}$  thick Si substrate. To further increase the modulation bandwidth above 1 GHz, more effort is needed to eliminate resonances from SiO<sub>2</sub> and AlN layers, which can be realized by matching mechanical impedance at interfaces, such as using an acoustic anti-reflection layer [137], or through phononic crystal band gap engineering to suppress undesired acoustic modes [138].

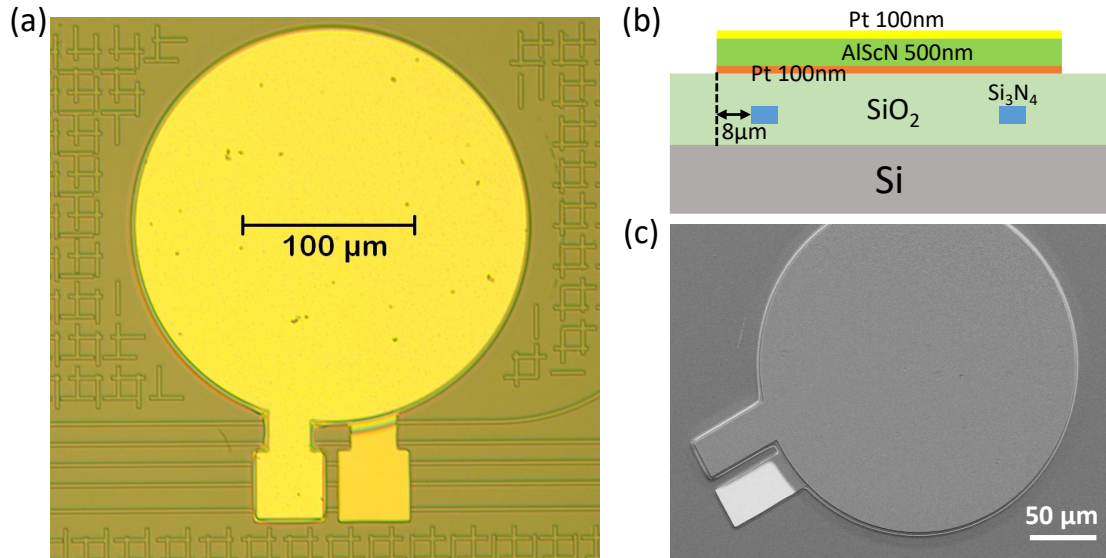


**Figure 2.32.** (a) Optical image for an AlScN actuator on an optical microring resonator with 200 GHz FSR. (b) Cross-section of the device with 500 nm AlScN thin film. (c) SEM image of one AlScN actuator.

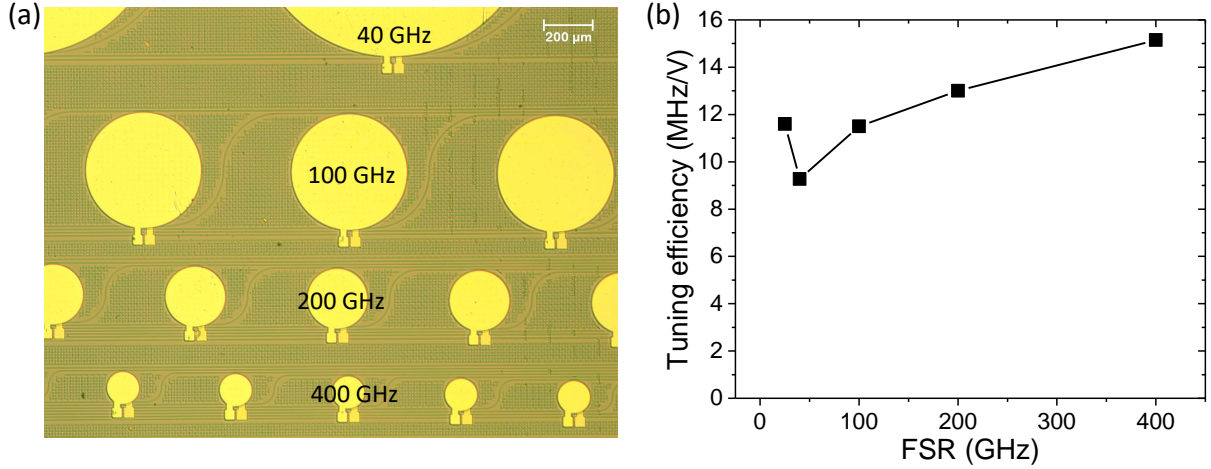


**Figure 2.33.** (a) Optical image for devices with different sizes. The FSR of each optical ring resonator is as labeled. (b) The tuning efficiency for each device with different FSR. All the devices are with the 8  $\mu\text{m}$  shift, except for the 25 GHz FSR device which has 10  $\mu\text{m}$  shift.

### 2.3 AlScN actuator piezoelectric tuning

It has been recently found out that by doping the AlN with Scandium (Sc), the piezoelectric coefficient can be increased by around 4 times [139]–[143]. The piezoelectric tuning of the optical microring resonator using the actuator made from AlScN is studied here. As shown in Fig. 2.32(b), a 500-nm AlScN thin film is sandwiched between top and bottom electrodes made of 100 nm Pt. They are all etched by the physical ion milling etching tool (AJA ICP Argon Ion Mill Etcher). For most devices, the waveguide is 8  $\mu\text{m}$  within the disk actuator based on the previous study on the position of the waveguide. The optical and SEM images of the fabricated AlScN actuator can be found in Fig. 2.32(a) and (c), respectively.

The tuning efficiency for devices with different sizes and thus different FSR is measured and shown in Fig. 2.33(b). Since the AlScN is also a ferroelectric material, a 40 V DC voltage is first applied to pole the polarization of the film in the same direction. Similar as the AlN actuator, the tuning efficiency increases as the FSR increases. However, note that all the devices have 8  $\mu\text{m}$  shift, except for the device with the lowest FSR (25 GHz) which has a 10  $\mu\text{m}$  shift. It deviates from the trend and shows higher efficiency, which indicates that by placing the waveguide further inside the actuator, we could further increase the



tuning in the future. The value of the tuning for each device is summarized in Table 2.1. By comparing with the AlN actuator, the AlScN actuator shows generally two times smaller tuning efficiency which doesn't reflect its 4 times higher piezoelectric coefficient. This is probably because of its much thinner thickness with 500 nm, which is the thickest that can be deposited currently. Further investigation in the future is needed to take full advantage of the higher piezoelectric response of the AlScN.

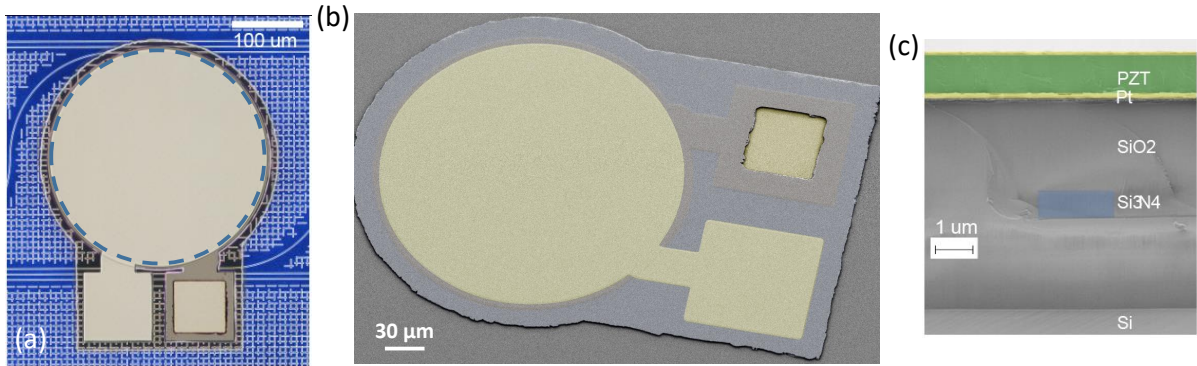


**Figure 2.34.** (a) Optical image for a PZT actuator on an optical microring resonator with 100 GHz FSR. The dashed blue circle indicates the optical microring. (b) False color SEM of the PZT actuator in (a). (c) False-colored SEM image of the cross-section, showing the PZT actuator integrated on the  $\text{Si}_3\text{N}_4$  photonic circuit. The piezoelectric actuator is composed of Pt (yellow), PZT (green) layers on top of the  $\text{Si}_3\text{N}_4$  waveguide (blue) buried in  $\text{SiO}_2$  cladding.

## 2.4 PZT actuator piezoelectric tuning

### 2.4.1 DC tuning with PZT actuator

PZT has been one of the well-known piezoelectric material and widely used not only in academic research and industry but also in our daily life such as microphone, acoustic guitar, and electric lighter in the kitchen, thanks to its large piezoelectric response. It presents a piezoelectric coefficient nearly 20 times larger than AlN with  $e_{33}$  of 23 C/m<sup>2</sup>. Here, PZT actuators are designed based on the experience gained from the results of AlN in the last section, and are fabricated by the foundry process from Radiant Technologies. The optical image of one of the typical actuator is shown in Fig. 2.34(a), which is placed on top of an

optical microring resonator with 100 GHz FSR. The optical waveguide is positioned  $8\ \mu\text{m}$  inside from the edge of the top metal. Since the PZT is optically transparent at visible light, the optical circuits beneath the PZT can be seen clearly. The PZT is sandwiched between top and bottom metal electrodes which are made both from 100 nm Platinum (Pt), as shown in Fig. 2.34(c). Different from previous AlN actuator, the bottom metal can be patterned before depositing the PZT, so the bottom metal below the top metal's signal pad can be removed to eliminate the capacitance from the signal pad. This is especially important for PZT as it has a relatively large permittivity. Any parasitic capacitance will increase the RC constant and reduce the response speed of the actuator.

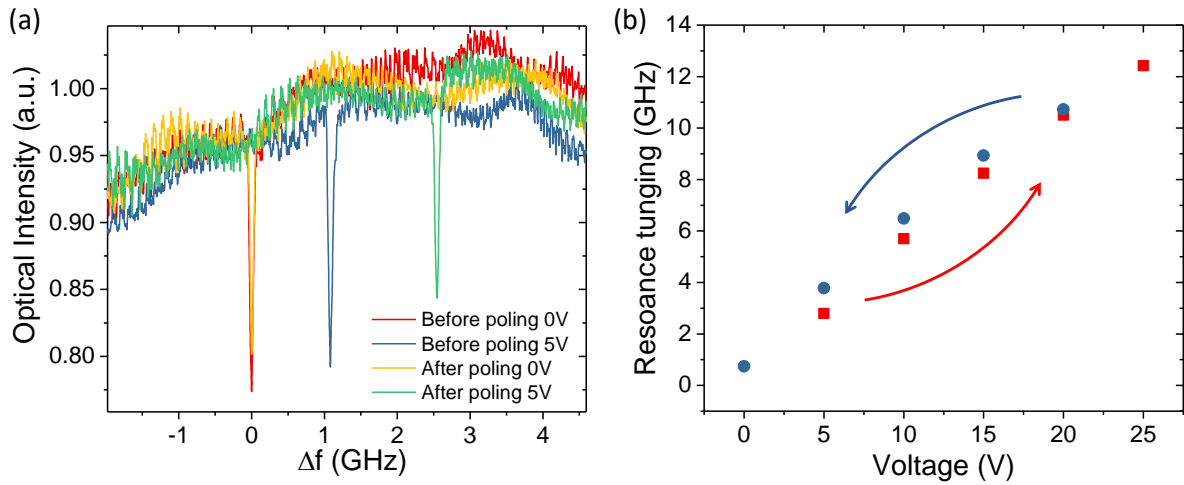


**Figure 2.35.** (a) PZT piezoelectric tuning of a 100 GHz FSR optical resonator. The tuning of the resonance under 5 V before (yellow) and after (blue) electrical poling the PZT film are shown. (b) The shift of the optical resonance as the voltage increases (red) and decreases (blue), showing slight hysteresis.

Since PZT is also ferroelectric, appropriate electrical poling of the film is necessary to align the polarization of each domain in the same direction, such that the piezoelectric effect can be maximized. This is verified by measuring the resonance tuning before and after poling the PZT, as shown in Fig. 2.35(a). The poling is conducted by applying 25 V DC voltage to the top metal while grounding the bottom metal and wait for at least 1 second. It can be seen, the poling doubles the tuning efficiency from 1 GHz to 2.5 GHz under 5 V. The tuning efficiency after poling is around 500 MHz/V which is ten times larger than the maximum



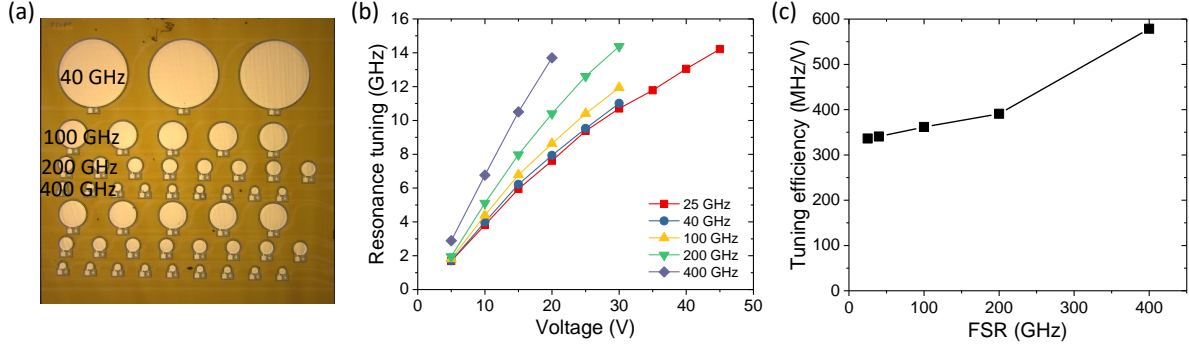


**Figure 2.36.** (a) Optical image of one photonic chip with different sizes of devices. The FSR of each type of device is as labeled. (b) The resonance tuning for devices with different sizes as the voltage is increased. (c) The tuning efficiency for devices with different FSR.

tuning efficiency for AlN actuators. In the following sections, the results are after poling by default. A slight hysteresis is observed as the voltage is swept back and forth as shown in Fig. 2.35(b). This is commonly observed for most ferroelectric material [144], which is mainly due to the change of polarization with the applied electric field. Despite of that, over 12 GHz of tuning is achieved under 25 V. To maintain the direction of the polarization of the film, only positive voltage is applied, and the application of negative voltage will reverse the polarization and compromise the poling. Thus, in real applications, a positive bias should be applied if bi-directional tuning is desired. Fortunately, the low leaky current of the PZT film ( $\sim 1$  nA) helps to remain low power consumption with tens of nW despite of the constantly applied DC bias.

The tuning for devices with different sizes are studied as shown in Fig. 2.36. It can be seen the tuning increases as the radius of the device decreases (FSR increases). All the devices achieve tuning larger than 10 GHz when the voltage is larger than 30 V. However, as the voltage further increases, the tuning tends to saturate due to the saturation of the polarization of PZT at high electric field. This leads to a nonlinear response for the large signal and long range tuning, which can be compensated with programmable input signal. It is noteworthy that over 500 MHz/V tuning can be achieved for 400 GHz FSR device, which is among the largest tuning efficiency for an unreleased structure up to date. It is also interesting to see that, for the 25 GHz FSR device ( $r = 900 \mu\text{m}$ ), tuning over half FSR

(= 12.5 GHz) is achieved for 40 V, which equals to  $\pi$  phase shift for the light in the ring. The figure of merit of the product  $V_\pi \cdot L = 22 \text{ V}\cdot\text{cm}$ , where  $V_\pi$  is the voltage that produces  $\pi$  phase shift of the light. Although this value is an order of magnitude larger than that for the state of the art electro-optic tuning using LiNbO<sub>3</sub> [10], the product that includes the loss  $V_\pi \cdot L \cdot \alpha = 0.2 \text{ V}\cdot\text{dB}$  is comparable, thanks to the ultra-low loss of the Si<sub>3</sub>N<sub>4</sub> waveguide (1 dB/m) [24].

#### 2.4.2 Co-integration with a thermal heater

Despite of the high tuning efficiency of the PZT actuator, sometimes the tuning of the optical resonator on the order of 100 GHz is required to compensate for the fabrication variation in more advanced applications, such as spectroscopy [59], FMCW LiDAR [83], and integrated tunable laser [84]. In that sense, a combination of the heater and the piezoelectric

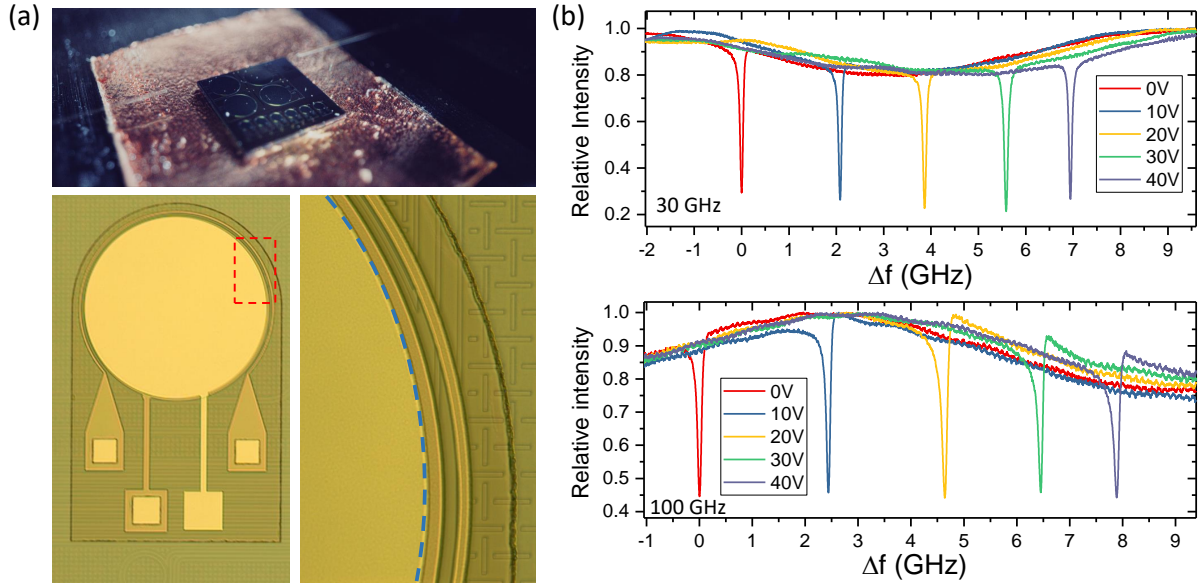


**Figure 2.37.** (a) Top: Optical image of the PZT chip containing 30 GHz and 100 GHz FSR devices. Bottom: optical image of the PZT actuator co-integrated with a heater surrounding the optical ring. The zoom-in in the red dashed box is shown on the right. The optical waveguide is right beneath the edge of the top metal as indicated by the blue dashed line. (b) Tuning of the optical resonance for 30 GHz (top) and 100 GHz (bottom) FSR devices under different voltages.

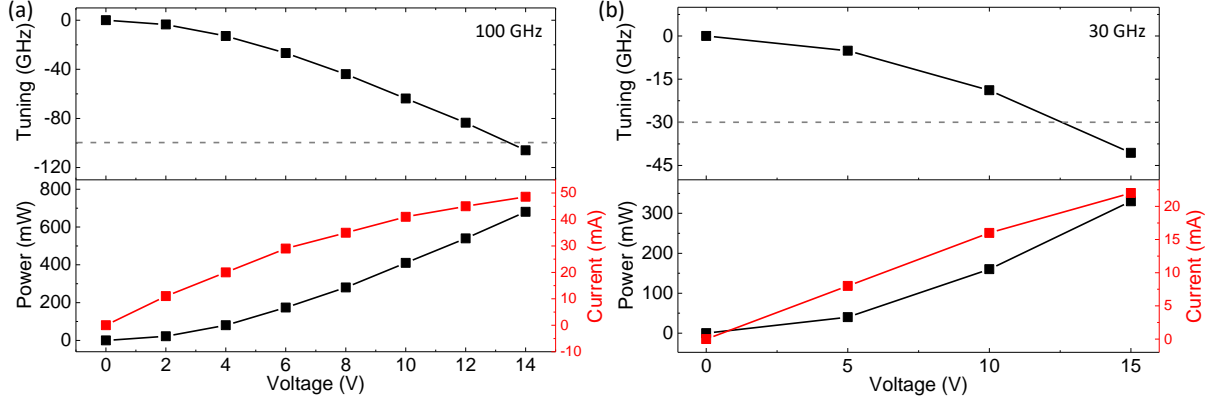


**Figure 2.38.** Thermal-optical tuning of the the optical resonance for (a) 100 GHz and (b) 30 GHz FSR devices. Over one FSR tuning can be achieved when voltage is larger than 13 V for both of them. The lower panel shows the electrical power and current under each voltage. The gray dashed line indicates the FSR for each device.

actuator could provide a way that supports both wide range and high speed tuning. In a new fabrication process, the PZT actuator is co-integrated with a heater as shown in Fig. 2.37(a). Since the heater has to be as close as possible to the waveguide to have effective local heating, we have to bring the waveguide to the edge of the actuator. This may compromise the piezoelectric tuning to some extent as illustrated in Fig. 2.37(b). The tuning efficiency decreases to 208 MHz/V and 243 MHz/V for 30 GHz and 100 GHz devices, respectively. However, tuning of 8 GHz can still be achieved under 40 V.

The resistance of the heater for 100 and 30 GHz devices are measured to be 182  $\Omega$  and 625  $\Omega$ , respectively. The thermal tuning for the two devices are illustrated in Fig. 2.38. Both of them can achieve over one FSR tuning when the voltage is larger than 13 V. As expected, the tuning is quadratic dependent on the voltage, the square of which is proportional to the heating power. Because of the smaller resistance of 100 GHz FSR device, it consumes higher current. While the 100 GHz FSR device consumes 680 mW to achieve one FSR tuning, the 30 GHz FSR device will take 250 mW. Different from the piezoelectric tuning, the thermal tuning can only red shift the wavelength (in other words, decreasing the frequency). It is also interesting to observe that the resistance slightly increases with the voltage probably because higher temperature increases the resistivity. From both the piezoelectric and thermal tuning,

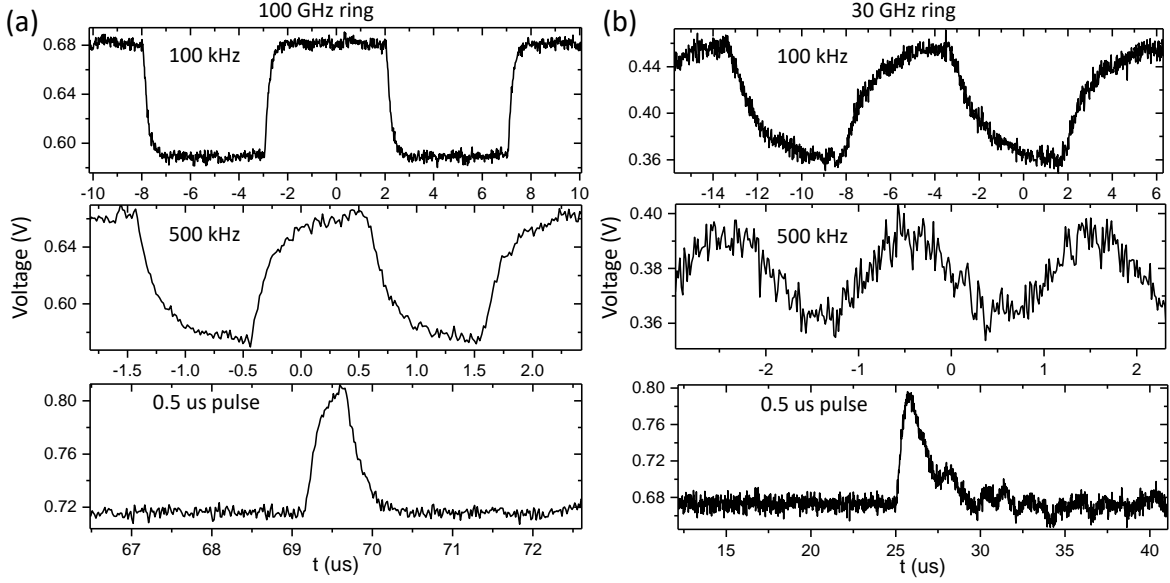


**Figure 2.39.** Time domain modulation of the light output for (a) 100 GHz and (b) 30 GHz FSR devices. The top and middle rows are square waves with 100 kHz and 500 kHz repetition rate, respectively. The bottom row is under electrical pulse with 0.5  $\mu$ s pulse width. The  $V_{pp}$  of the the square waves and pulse is 1 V only.

it can conclude that the combination of heater and piezoelectric actuator will provide a more flexible control of the photonic circuits and will find wide applications in the future.

### 2.4.3 Characterization of the tuning speed

The switching speed of the PZT actuator is characterized for the same 30 and 100 GHz FSR devices as in the last section, as shown in Fig. 2.39. A relatively long switching tail can be observed due to the large capacitance of the PZT actuator. Due to the large radius (700  $\mu$ m) of the 30 GHz ring, it shows even longer ringing down than the 100 GHz device with radius of 235  $\mu$ m. For 500 kHz rate, the 30 GHz device can hardly reproduce the input square wave due to the slow response. To find the factor that limits the speed, the ringing down is fitted with an exponent function as shown in Fig. 2.40. The time constant is found to be 1.4  $\mu$ s and 0.2  $\mu$ s for 30 GHz and 100 GHz device, respectively. The time of 30 GHz device is 7 times larger than the 100 GHz, which aligns with the ratio between the area of

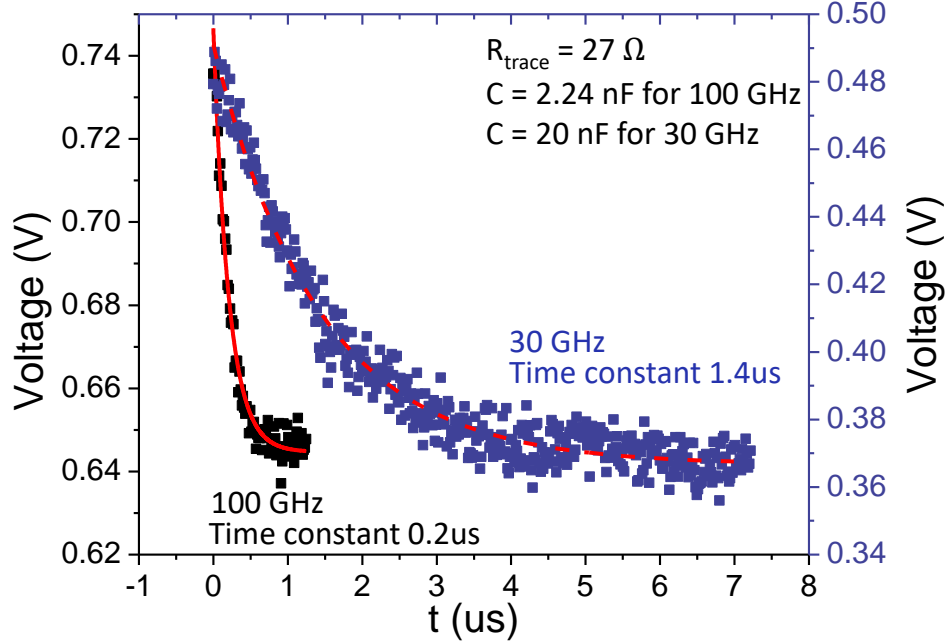


**Figure 2.40.** Zoom-in of the ringing down tail of the time domain switching under 100 kHz square wave for the 100 GHz (black dots) and 30 GHz (blue dots) devices in Fig. 2.39. The decay is fitted exponentially for 100 GHz (red line) and 30 GHz (red dashed line) to extract the time constant as labeled. The capacitance is measured as shown in the inset.

them. This indicates that the switching speed is mainly limited by the time it takes to charge and discharge the capacitance which is governed by the RC time constant. The capacitance is measured to be 2 nF for 100 GHz and 20 nF for 30 GHz device. The resistance is mainly from the long and narrow traces for the signal lines which is around  $27 \Omega$ .

In the future, the RC time can be reduced by making shorter and wider traces, and patterning the top metal by carving out the center area of the disk to reduce the capacitor area. In previous experiment, I found that Donut shaped actuator has smaller tuning efficiency than Disk, probably because of more degree of freedom of moving boundaries which release the concentration of the stress. If we only pattern the top electrode and leave the disk of the PZT, we may not compromise the tuning efficiency, which needs more investigation in the future.

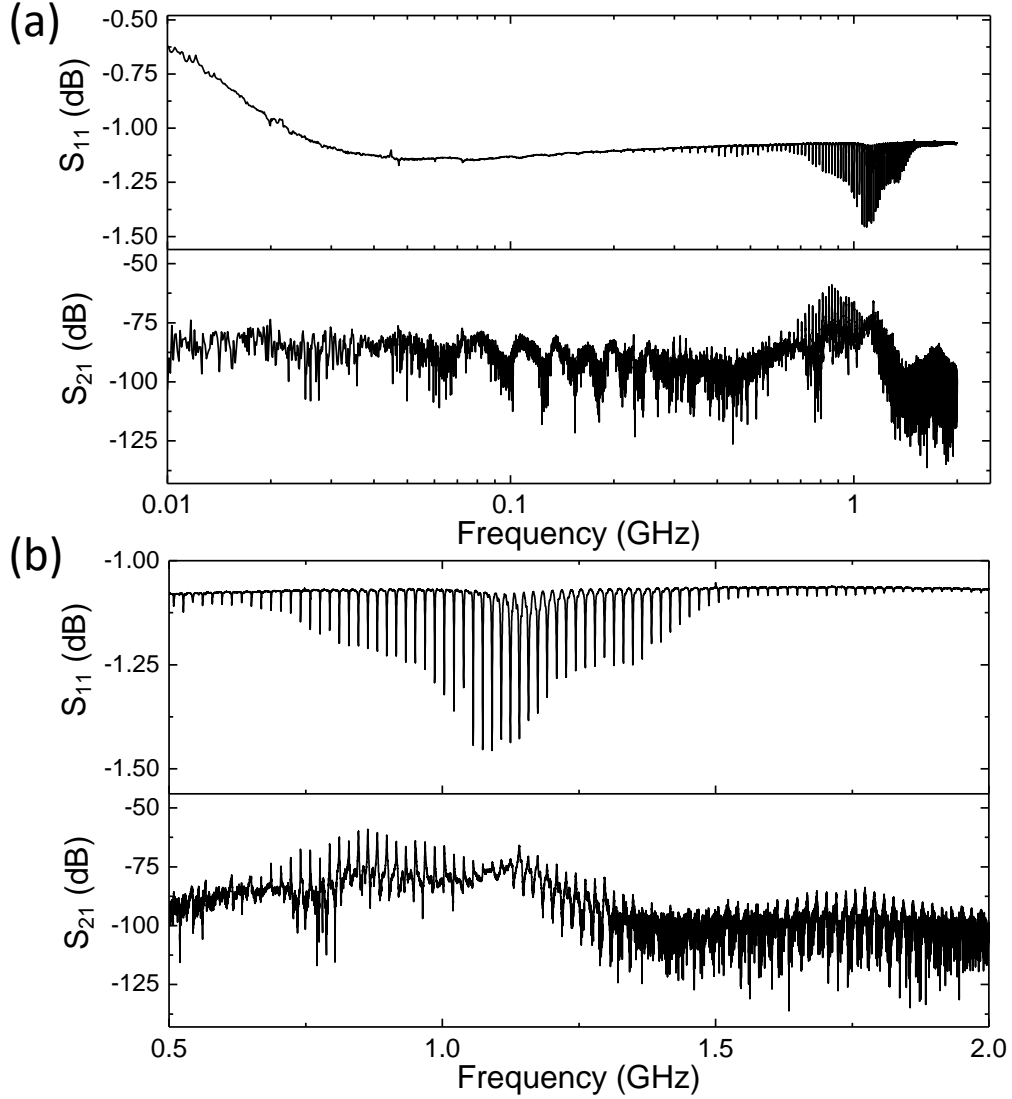


**Figure 2.41.** (a) Electromechanical  $S_{11}$  (top) and optomechanical  $S_{21}$  (bottom) responses over a wide frequency range. (b) Zoom-in of  $S_{11}$  (top) and  $S_{21}$  (bottom) from 0.5 to 2 GHz, showing HBAR resonances of the PZT actuator.

#### 2.4.4 HBAR AOM of the PZT actuator

The acousto-optic modulation can also be realized by driving the PZT actuator harmonically. The Electromechanical  $S_{11}$  (top) and optomechanical  $S_{21}$  (bottom) are measured accordingly as shown in Fig. 2.41. Despite of the large loss tangent of the PZT at RF frequencies, the HBAR modes can be seen clearly around 1 GHz both electrically and optically. However, beyond 2 GHz, the excitation of HBAR mode become less efficient. This is

**Table 2.1.** Comparison of the piezoelectric tuning with different design parameters for both AlN, AlScN, and PZT actuators.

Material	Shape	Shift	FSR (GHz)	Optical Mode	Tuning (MHz/V)
AlN	Disk	0 $\mu\text{m}$	200	TE	25
AlN	Disk	0 $\mu\text{m}$	200	TM	25
AlN	Donut	3 $\mu\text{m}$	200	TE	-3.4
AlN	Donut	3 $\mu\text{m}$	200	TM	-11.8
AlN	Disk	8 $\mu\text{m}$	200	TE	31
AlN	Disk	8 $\mu\text{m}$	200	TM	19
AlN	Donut	-8 $\mu\text{m}$	200	TE	-20
AlN	Donut	-8 $\mu\text{m}$	200	TM	-4.7
AlN	Disk	8 $\mu\text{m}$	400	TE	75
AlN	Disk	8 $\mu\text{m}$	400	TM	56
AlScN	Disk	10 $\mu\text{m}$	25	TE	11.6
AlScN	Disk	8 $\mu\text{m}$	40	TE	9.27
AlScN	Disk	8 $\mu\text{m}$	100	TE	11.5
AlScN	Disk	8 $\mu\text{m}$	200	TE	13
AlScN	Disk	8 $\mu\text{m}$	400	TE	15.15
PZT	Disk	0 $\mu\text{m}$	30	TE	208
PZT	Disk	0 $\mu\text{m}$	100	TE	243
PZT	Disk	8 $\mu\text{m}$	200	TE	391
PZT	Disk	8 $\mu\text{m}$	400	TE	578

mainly because the large parasitic capacitance shunts most of the microwave energy into the ground without being converted to mechanical vibration. Although the microwave frequency response of the PZT actuator is not as good as the AlN, the 1 GHz AOM allows locking of the optical resonance through the Pound–Drever–Hall (PDH) technique [121], [145]. Therefore, the technique developed here enables multi-functional control of the photonic circuits from wide range tuning (heater) to ultra-fast agitation and GHz modulation using the PZT piezoelectric transduction.

## 2.5 Summary

In summary, the piezoelectric tuning of the  $\text{Si}_3\text{N}_4$  microring resonator is demonstrated by designing and fabricating both AlN, AlScN, and PZT actuators on an unreleased substrate. The performance of the tuning for AlN and PZT actuators with different design parameters is summarized in Table 2.1. Several design rules can be summarized as followings:

- Disk actuator shows larger tuning rate than Donut actuator
- TE mode generally has higher tuning than TM mode
- Disk actuator prefers positive shift while Donut actuator prefers negative shift
- Optical ring with larger FSR (smaller radius) has higher tuning rate
- PZT has much higher tuning efficiency than AlN, although AlN advances in linearity, negligible hysteresis, bi-directional tuning, and higher actuation bandwidth

The comparison of the AlN, AlScN, and PZT piezoelectric tuning with other similar works in the literature is summarized in Table 2.2. It can be seen the PZT actuator in this work shows the most efficient optical resonance tuning with estimated  $V_\pi \cdot L$  of 12.5 V·cm. The power consumption of 1.7 pW per MHz resonance tuning is among the lowest in the literature. Also, the tuning speed on the order of sub- $\mu$ s is much faster than other works, which is ultimately limited by the bulk mechanical modes of the photonic chip. In the lower rows of Table 2.2, it is compared with thermal tuning in the literature. As expected, thermal tuning shows three orders of magnitude larger tuning range at the expense of three orders of magnitude larger power consumption and lower response speed. Therefore, while heater is suitable for coarse tuning, piezoelectric actuator can be used for fast fine tuning, as demonstrated in the last section.

Besides quasi-DC tuning, I also demonstrated microwave frequency acousto-optic modulation of the  $\text{Si}_3\text{N}_4$  microring resonator by exciting HBAR modes using both the AlN and PZT actuators. Upon electrical signals, bulk acoustic waves (BAW) are excited, transmitting vertically towards the optical resonator which modulates the refractive index through the stress-optical effect. The flat top and bottom surfaces of the photonic chip naturally form an acoustic Fabry–Pérot cavity, which supports a series of evenly distributed resonances covering multiple octaves from 1 to 6 GHz. I further developed the electromechanical model for precisely predicting the frequency and dispersion of mechanical resonances, which allows engineering the mode spacing. The advantages of HBAR based AOM over traditional surface acoustic waves include:



**Table 2.2.** Comparison with the piezoelectric tuning demonstrated in the literature. All the works here are unreleased structure, and the optical waveguide is made from  $\text{Si}_3\text{N}_4$ . MZI: Mach-Zehnder interferometer. The FSR for each optical ring is as labeled.  $V_\pi \cdot L$  has unit of V·cm, and is estimated from the resonance tuning for the microring structure. The last three rows compare with thermo-optic tuning. WG: waveguide.

Ref.	Piezo	Structure	Tuning (MHz/V)	$V_\pi \cdot L$	Speed	Power
[67]	PZT	MZI		12.5	$0.25 \mu\text{s}$	300 nW
[68]	PZT	MZI		50	$100 \mu\text{s}$	$1 \mu\text{W}$
[70]	PZT	MZI		16	$0.85 \mu\text{s}$	$0.1\text{-}1 \mu\text{W}$
[69]	PZT	Ring (48GHz)	160	55		38 pW/MHz
This work	PZT	Ring (25GHz)	336	20	$1 \mu\text{s}$	3 pW/MHz
This work	PZT	Ring (200GHz)	400	18	$0.1 \mu\text{s}$	2.5 pW/MHz
This work	PZT	Ring (400GHz)	578	12.5	$0.1 \mu\text{s}$	1.7 pW/MHz
This work	AlN	Ring (200GHz)	58	124	$0.1 \mu\text{s}$	18 pW/MHz
This work	AlScN	Ring (200GHz)	13	553	$0.1 \mu\text{s}$	77 pW/MHz
Thermal	WG	Structure	Tuning		Speed	Power
[55]	Si	Ring (800GHz)	300 GHz/mW		$170 \mu\text{s}$	3 nW/MHz
[56]	$\text{Si}_3\text{N}_4$	Ring (231GHz)	0.1 GHz/mW		$710 \mu\text{s}$	$10 \mu\text{W/MHz}$
[58]	$\text{Si}_3\text{N}_4$	Disk	1.8 GHz/mW		$30 \mu\text{s}$	$0.5 \mu\text{W/MHz}$

- The HBAR explores the design of freedom in the vertical direction, allowing compact integration.
- $\text{Si}_3\text{N}_4$  waveguides can be cladded with thick oxide for preserving high quality factor and dispersion.
- The tight vertical confinement enables a close arrangement of multiple actuators with low cross-talk.
- The mechanical frequency is dictated solely by the thicknesses of each layer. The lateral dimensions can be photolithograph defined, allowing large volume production with little frequency variation.

Therefore, the marriage between HBAR and  $\text{Si}_3\text{N}_4$  integrated circuits, which are key techniques in each's field, will open up a new avenue for MEMS-enabled photonic devices in the future.

### 3. PIEZOELECTRIC CONTROL OF SOLITON MICROCOMBS

In this chapter, the application of the piezoelectric control of the optical microring resonator has been demonstrated in tuning of the generated Kerr frequency comb from the  $\text{Si}_3\text{N}_4$  microring. After briefly introducing the frequency comb, the piezoelectric tuning of the comb into different states will be shown. The actuation and stabilization of the comb will also be discussed.

#### 3.1 Optical Kerr frequency comb

Frequency comb, since its invention, has boosted a wide variety of applications, such as frequency metrology [146], atomic clock [123], spectroscopy [147], and signal synthesis [50], since stabilized frequency comb shows ultrahigh frequency accuracy and stability [148]. In frequency domain, frequency comb consists of discrete, evenly spaced sharp lines, as shown in Fig. 3.1(b). If there is a coherent relative phase among these comb lines, they will form pulses with periodic envelope in the time domain, superimposed with fast oscillating optical carrier, as shown in Fig. 3.1(a). The envelope in the time and frequency domain satisfy Fourier transform with each other. Therefore, the frequency spacing is equal to the pulse repetition rate, which is the inverse of pulse period  $f_{\text{rep}} = 1/T$ . One important parameter of frequency comb is the so called carrier-envelope offset phase  $\phi_{\text{CEO}}$ , which is the phase difference between the peak of envelope and the closest peak of carrier. Due to the dispersion in the cavity in practical application, the group velocity  $v_g$  of the envelope usually is smaller than the phase velocity  $v_{ph}$  of the carrier. Therefore, the  $\phi_{\text{CEO}}$  varies from pulse to pulse in a step of  $\Delta\phi_{\text{CEO}}$  [148]:

$$\Delta\phi_{\text{CEO}} = \left( \frac{1}{v_g} - \frac{1}{v_{ph}} \right) l_c \omega_c \text{mod}(2\pi) \quad (3.1)$$

where  $l_c$  is the length of the optical cavity,  $\omega_c$  is the angular frequency of the optical carrier. Due to the evolution of carrier-envelope phase, there is an absolute offset of the comb in frequency domain,  $f_{\text{CEO}} = f_{\text{rep}} \Delta\phi_{\text{CEO}} / 2\pi$ . The absolute frequency of each comb line can then be found as:

$$f_n = f_{\text{CEO}} + n f_{\text{rep}} \quad (3.2)$$

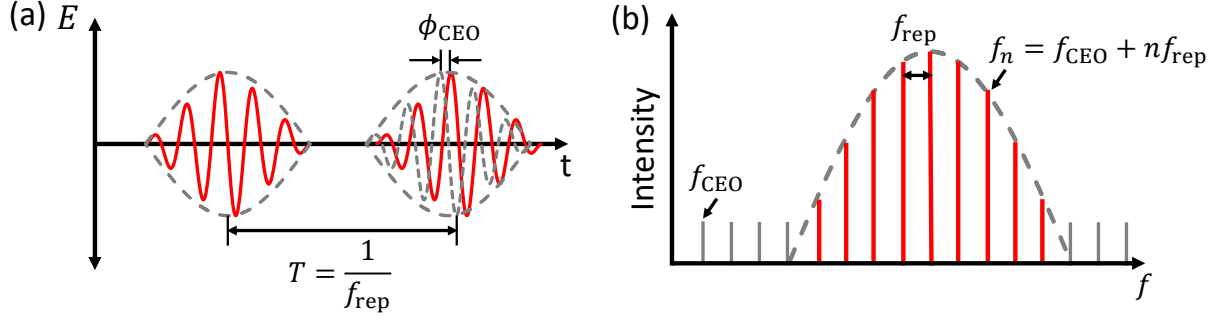


**Figure 3.1.** Schematics for the optical frequency comb in the time domain (a) and the frequency domain (b). The carrier-envelope offset phase  $\phi_{\text{CEO}}$  is defined as the phase difference between the peak of envelope and the closest peak of carrier. The discrete frequencies distribute evenly with interval  $f_{\text{rep}}$ , and the offset frequency is  $f_{\text{CEO}}$ .

A frequency comb can be fully stabilized by measuring and stabilizing the frequency spacing  $f_{\text{rep}}$  and the overall offset  $f_{\text{CEO}}$ . The  $f_{\text{rep}}$  can be either measured directly by fast photodetectors for low repetition rate (10s of GHz) frequency comb, or by beating with another comb with known repetition rate for comb THz rate. Measuring the  $f_{\text{CEO}}$  is more difficult to implement experimentally, since it is hidden as phase information. One commonly used technique is self-referencing  $f - 2f$  technique [50], which utilizes octave spanning frequency comb (maximum frequency is two times bigger than the lowest frequency) and second harmonic generation [148]. The main principle is as follows: if the frequency comb is doubled by a second harmonic crystal, the comb line with index  $n$  will have close frequency with the frequency component with index  $2n$  of the original comb. The frequency difference between them is precisely the  $f_{\text{CEO}}$ :

$$2f_n - f_{2n} = 2(nf_{\text{rep}} + f_{\text{CEO}}) - (2nf_{\text{rep}} + f_{\text{CEO}}) = f_{\text{CEO}} \quad (3.3)$$

This can be easily implemented by doing the heterodyne measurement in RF domain, which provides a high precision.

The frequency comb is conventionally generated by an ultrafast mode-locked laser, such as the Kerr lens mode-locked (KLM) Ti:sapphire laser [148]. Over the past decade, frequency comb has been realized on chip utilizing the optical Kerr nonlinearity, the so called Kerr comb

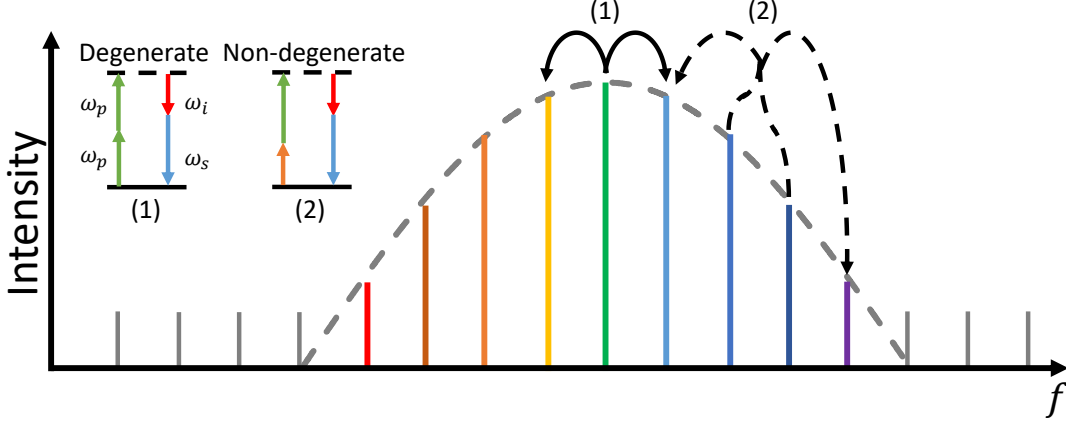


**Figure 3.2.** Principle of the Kerr comb. The comb is firstly generated by the degenerate FWM process which converts two pump photons into evenly distributed sidebands. As the power from pump is distributed to sideband, the FWM is dominated by the non-degenerated version which generates new sidebands and forces even frequency distribution.

[29], [42], [149]. With the help of parametric four wave mixing (FWM) in dielectric material [150], Kerr comb has been demonstrated over broad bandwidth in infrared region. The main advantages of these combs over conventional ultrafast lasers are the GHz to THz repetition rate and the compact size.

As shown in Fig. 3.2, the parametric process is initially dominated by the degenerate FWM, where two input pump photons  $\omega_p$  annihilate and generate a higher frequency signal photon  $\omega_s$ , and a frequency downshifted photon idler photon  $\omega_i$ . The energy conservation law requires that the signal and idler photons equally distribute on the two sides of the pump. Also, the degenerate FWM will be highly enhanced if the frequencies coincide with the resonant mode of the an optical cavity. Since the mode frequency spacing of cavity (FSR) is nearly evenly distributed (regardless of dispersion of cavity), this also guarantees even distribution with respect to the pump. As more sidebands generated, and the power of them grows, the non-degenerate FWM dominates. In this case, two photons with different frequencies can interact and generate new frequencies. Through these cascaded FWM processes, frequencies with evenly distributed spacing are generated, which form a frequency comb. The bandwidth of the final spectrum will be limited by dispersion inside resonator

and the transparent bandwidth of material, while the first factor is the mainly bottleneck in practice [151].

Many materials have been demonstrated experimentally to generate frequency comb efficiently, such as silica [149],  $\text{Si}_3\text{N}_4$  [152],  $\text{CaF}_2$  [153],  $\text{AlN}$  [38], and  $\text{AlGaAs}$  [21], [40], to name a few. Kerr comb is first demonstrated on a silica toroidal microresonator (75  $\mu\text{m}$  diameter), which high quality factor ( $>10^8$ ), tight mode confinement, and large repetition rate ( $\sim 1$  THz) [149]. All these features make it possess low threshold power, which is 60 mW. Because of the intrinsic dispersion compensation, the generated frequency comb covers a large spectrum bandwidth of 490 nm. Another widely used material and structure is the  $\text{Si}_3\text{N}_4$  microring resonator studied in this work. Its high third order nonlinearity ( $2.5 \times 10^{-15} \text{ cm}^2/\text{W}$ , an order of magnitude higher than silica,  $\text{CaF}_2$ ) makes it possible to serve as good frequency comb generator with low pump power. The advantages of this  $\text{Si}_3\text{N}_4$  microring resonator Kerr comb include CMOS compatibility and planar integration, which allows it to be integrated together with other optical components like waveguides, light source, photodetector, and with thermal heater and piezoelectric actuator demonstrated in this work.

High-speed actuation of laser frequency [154] is critical in applications using lasers and frequency combs [148], and is a prerequisite for phase locking, frequency stabilization and stability transfer among optical carriers. For example, locking combs to microwave standards is key to optical frequency synthesis [155]. Phase-locking of combs to stable reference cavities is also central for low-noise microwave generation via optical frequency division [156]. Optical clocks require frequency combs to be locked to atomic transitions [157], and higher-bandwidth actuators are needed to keep pace with the improvement in clock fractional uncertainty [158]. Frequency combs based on mode-locked lasers have established elaborate techniques for wideband frequency actuation, typically realized using bulk phase or amplitude modulators within the laser cavity. In contrast, measurement-based high-speed feedback stabilization of chip-based microcombs is currently only achieved with off-chip bulk modulators that actuate the pump laser. Therefore, high-speed actuators on-chip are highly desirable for integrated soliton microcombs, where the demonstrated piezoelectric actuation can play an important role.

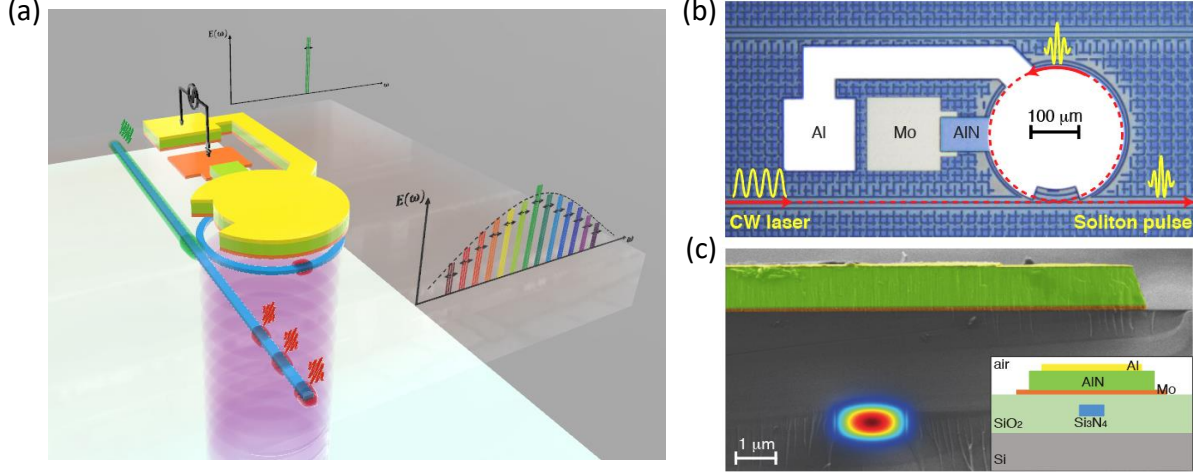


**Figure 3.3.** (a) Schematic of the AlN actuator on top of a Si<sub>3</sub>N<sub>4</sub> microring resonator. CW light (green) is coupled into the resonator which generates dissipative solitons (red pulses) at the output. The modulation signal applied to the AlN actuator induces bulk acoustic waves (purple waves), which transduces the modulation to all the comb lines of the generated soliton pulses (spectrum at bottom right). (b) Optical image showing the Si<sub>3</sub>N<sub>4</sub> microresonator (red dashed line) with a disk-shape AlN actuator. (c) False-colour SEM image of the sample cross-section, showing Al (yellow), AlN (green), Mo (red), Si<sub>3</sub>N<sub>4</sub> (blue) and the optical TE mode (rainbow). The inset shows the schematic of the cross-section. Reprinted from Ref. [121].

### 3.2 Voltage controlled soliton states

As shown in Fig. 3.3, a Disk AlN actuator is placed on top of a Si<sub>3</sub>N<sub>4</sub> microring resonator with radius of 118  $\mu\text{m}$  and FSR of 191 GHz. The Si<sub>3</sub>N<sub>4</sub> is fully buried by the SiO<sub>2</sub> cladding to preserve the low loss of the Si<sub>3</sub>N<sub>4</sub> waveguide which leads to a measured intrinsic quality factor,  $Q_0 > 15 \times 10^6$ . This is identical to that of bare microresonators without AlN [24], demonstrating that the monolithically integrated AlN actuators are compatible with the ultralow-loss Si<sub>3</sub>N<sub>4</sub> photonic circuits. Also, the dispersion is preserved which is essential for the Kerr soliton generation [121].

The Kerr frequency comb is generated using the setup shown in Fig. 3.4(a). A 15 mW CW laser is butt coupled into the the microring resonator with a 60% coupling efficiency per chip facet. The laser frequency is fixed which is 1 GHz larger (blue detune) than the optical resonance. By applying positive voltage to the AlN actuator, the soliton is initiated by tuning

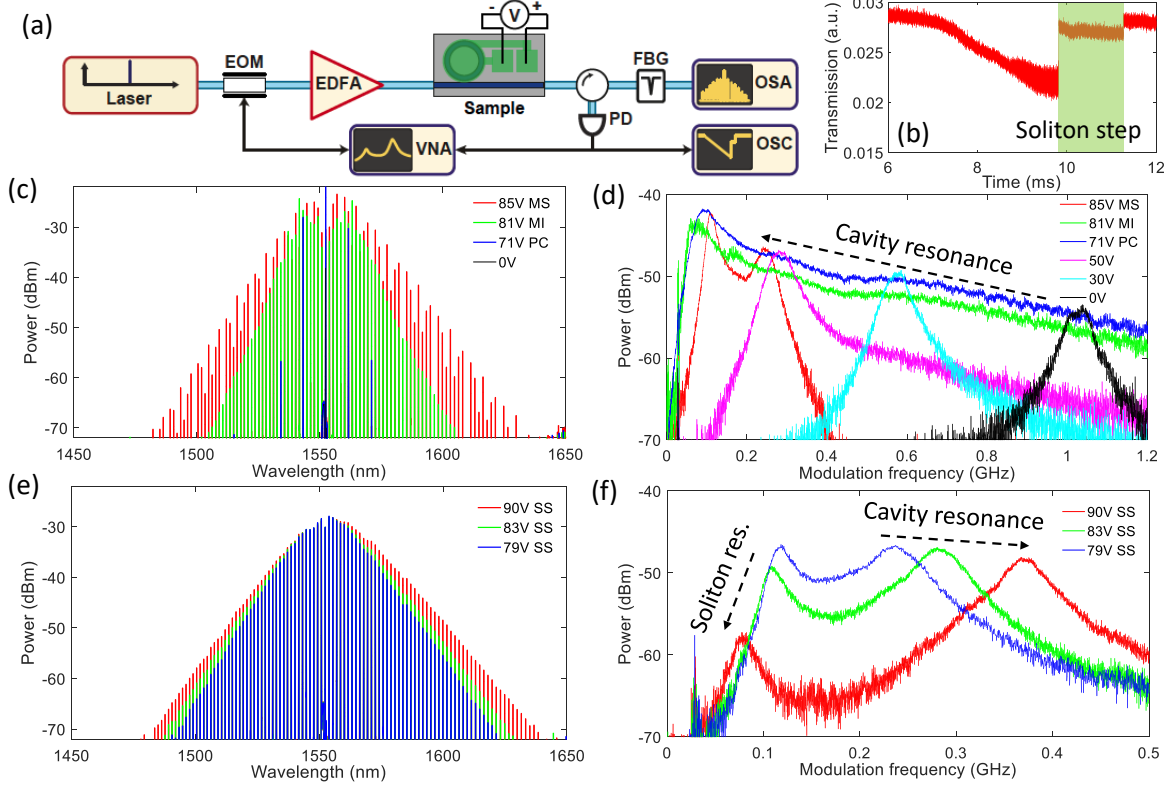


**Figure 3.4.** (a) Experimental set-up for comb generation and control. OSC, oscilloscope; FBG, fibre Bragg grating; OSA, optical spectrum analyser; PD, photodiode; EOM, electro-optic modulator; VNA: vector network analyzer. (b) A typical soliton step of millisecond length. (c) Optical spectrum for frequency comb at different states under different voltages. PC: primary comb; MI: modulation instability; MS: multi-soliton. (d) Resonance detuning measured by VNA. The cavity resonance is initially 1 GHz smaller than the laser frequency, and is then tuned to the laser and generates different comb states. (e) Optical spectrum for single soliton states with different bandwidth when varying the voltage. (f) Cavity and soliton resonance detuning in the soliton state with different voltages. SS: single soliton. Reprinted from Ref. [121].

the resonance to the laser [30], [57]. A typical soliton step of millisecond duration is shown in Fig. 3.4(b). Though not required for soliton initiation, we monitor the resonance–laser detuning using an electro-optic modulator (EOM) and a vector network analyser (VNA) [159]. As the voltage is increased, the detuning between the laser and resonance decreases as can be seen from the black (0 V), cyan (30 V), and pink (50 V) in Fig. 3.4(d). As more laser is pumped into the resonance at 71 V, the primary comb is generated with the spacing of several FSR as illustrated by the blue curve in 3.4(c-d). Subsequently, the comb enters

into the modulation instability at 81 V (green) and multi-soliton state to 85 V (red). As the comb is in the soliton state, the VNA trace shows double peaks with the lower frequency being the soliton resonance and the higher frequency for the cavity resonance (red curve in Fig. 3.4(d)).

Next, the AlN voltage is reduced such that the backward tuning enables switching [159] to the single soliton state at 79 V (blue in Fig. 3.4(e-f)). The voltage is increased again (90 V) to increase the soliton bandwidth. Figure 3.4(e) shows different soliton states with different applied voltages. From Fig. 3.4(f), while the cavity detuning increases with the voltage, the soliton resonance remains close to the laser. These results demonstrate that the soliton can be initiated by solely tuning the optical resonance with fixed-frequency laser which usually shows lower linewidth and noise than the tunable laser. Also, the frequency comb can be programmed in situ into different states by adjusting the voltage applied to the actuator. Therefore, the voltage-controlled AlN actuator can be used to implement feedback and to eliminate the detuning drift for long-term soliton stabilization as demonstrated later.

### 3.3 HBAR induced PDH error signal

The Pound–Drever–Hall (PDH) technique [160] has long been widely used to lock the laser frequency to the resonance of a stabilized optical cavity in a reliable way. Compared with the locking to the slope of the resonance, it elegantly decouples the fluctuation of the frequency and intensity of the laser, and the locking bandwidth is not limited to the cavity’s linewidth which is usually small for stabilized, high finesse optical cavity. It is a combination of heterodyne and homodyne detection in optical and RF domain, respectively. As shown in the setup of Fig. 3.5(a), the optical resonator is modulated which generates modulation sidebands around the input laser. Depending on the relative detune between the laser and the optical resonance, the sidebands will carry different relative phases, and show either constructive or destructive interference at the photodetector. The beatnote between the sidebands and the laser will have the same frequency as the modulation signal  $f_{\text{mod}}$ , which can be sampled by mixing them with the original local oscillator using an RF mixer. This RF homodyne detection will generate a DC signal which can be selected by a low pass filter,



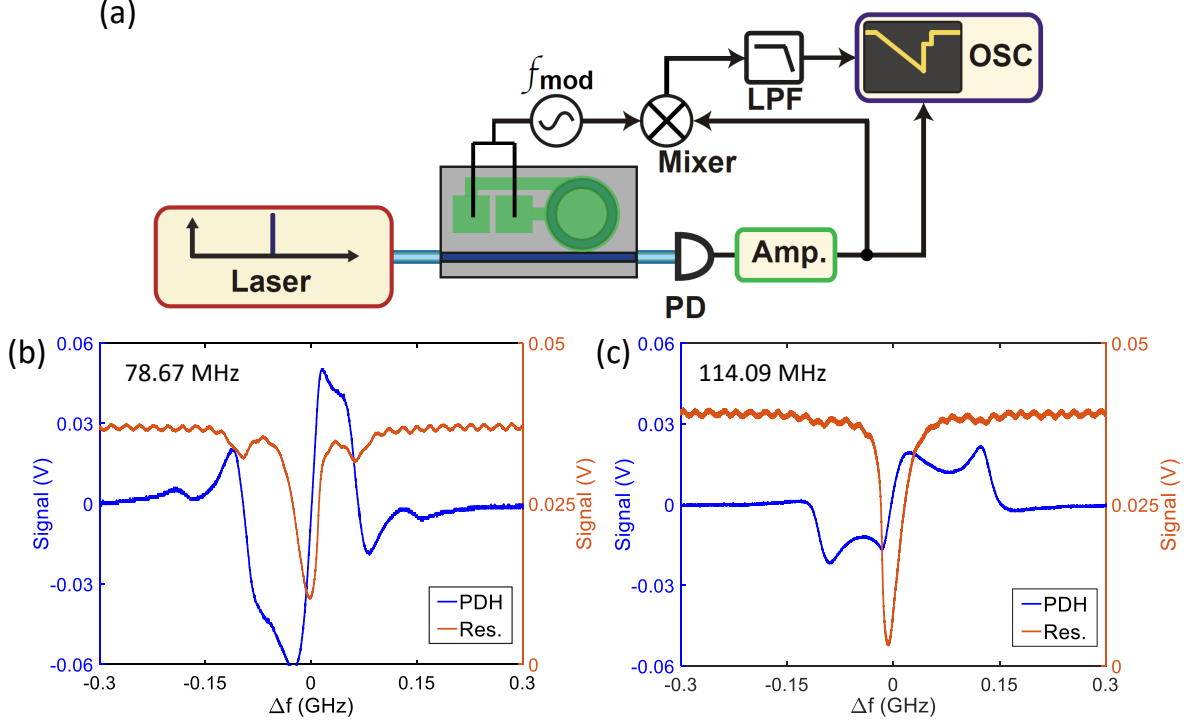


**Figure 3.5.** (a) Experimental set-up for On-chip generation of PDH error signals using the HBAR modes induced by AlN actuation. LPF: low-pass filter; Amp.: RF power amplifier. PDH error signal (blue) modulated at (b) 78.67 MHz and (c) 114.1 MHz HBAR modes. The optical resonance is shown as the orange curves.  $\Delta f$  is the relative detune between the laser and the optical resonance. Reprinted from Ref. [121].

which becomes the PDH error signal measured by the oscilloscope. This error signal gives precisely the information about the relative detune which be fed-back for stabilizing the laser frequency using a servo such as the proportional–integral–derivative (PID) controller.

Here, we demonstrated the generation of PDH error signal by acousto-optic modulating the optical microring resonator using the HBAR modes. Although narrow-band, HBAR modes offer an efficient way for modulating the optical resonator at a single frequency which is best suited for the PDH technique. Different modulation frequencies corresponding to different HBAR modes are investigated as shown in Fig. 3.5(b-c). It can be seen at the zero detune, the PDH error is zero due to the balance between the sidebands. As the laser deviates, the PDH error increases and shows different sign depending on the detuning direction. Thus, by adding a negative feedback gain in a closed loop, the laser frequency

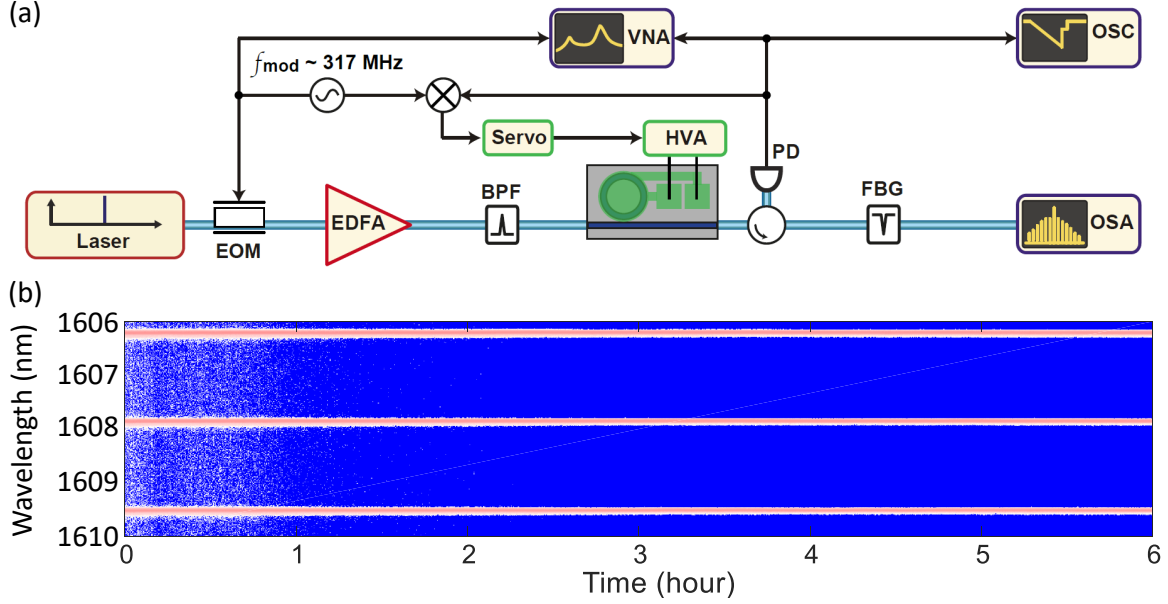


**Figure 3.6.** Stabilization of the frequency comb over a long period of time. (a) Experimental setup for locking the resonance to the laser and maintaining the soliton detuning. OSC: oscilloscope; BPF: bandpass filter; FBG: fiber Bragg grating. (b) Soliton stabilization over 5 hours. Three selected comb lines are shown here with stability over 5 h. Reprinted from Ref. [121].

can be quickly adjusted back to keep the PDH error zero, and therefore zero detuning. The response time of the feedback is ultimately limited by the bandwidth of the low pass filter which can be increased by driving higher frequency HBAR mode. In conclusion, the on-chip HBAR AOM provides an efficient and low-cost way to implement PDH locking, which will find useful in locking an integrated semiconductor laser to the  $\text{Si}_3\text{N}_4$  microring resonator [3]–[8].

### 3.4 Stabilization of the Kerr frequency comb

Not only for tuning the comb states by adjusting the detune between the laser and the optical resonance, the fast piezoelectric actuation also allows us to stabilize the detune over a long period of time. The setup for stabilization is shown in Fig. 3.6(a), where A feedback loop is applied to fix the soliton detuning at 317 MHz and eliminate the detuning fluctuation over the long term. Fig. 3.6(b) shows the evolution of three comb lines over 5 h. The final

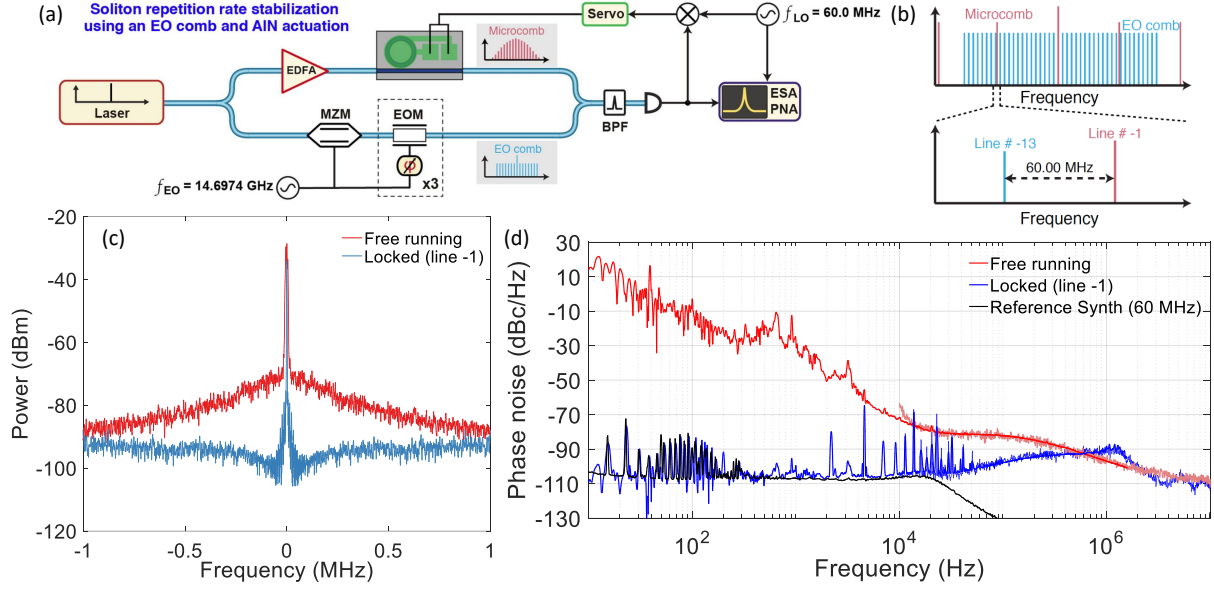


**Figure 3.7.** Stabilization of the repetition rate of the soliton. (a) Experimental setup used to lock the microcomb to an electro-optic (EO) comb, and characterize the in-loop phase noise of the beatnote signal between line no. -1 of the microcomb and line no. -13 of the EO comb. DSO, digital storage oscilloscope; MZM, Mach-Zehnder modulator; EOM, electro-optic modulator; ESA, electrical spectrum analyzer; PNA, phase noise analyser. (b) Schematic of soliton repetition rate stabilization using an EO comb with 14.6974 GHz line spacing. Line no. -1 of the microcomb and line no. -13 of the EO comb are locked and referenced to a 60.0 MHz signal. (c) Measured beat-note signal of line no. -1 of the microcomb and line no. -13 of the EO comb, in the cases of locked and free-running (unlocked) states. Resolution bandwidth (RBW) is 1 kHz. (d) Measured phase noise of the beat signal in the locked (blue) and free-running states (red), in comparison to the 60.0 MHz reference signal (black). The locking bandwidth of the AIN actuator is 0.6 MHz. Reprinted from Ref. [121].

soliton loss after 6 h is caused by the drift of the fiber-chip coupling using suspended lensed fibers, and can be mitigated by gluing the fibers to the chip [161], or via the photonic wire bonding [162], [163].

As mentioned in the introduction, for a stabilized frequency comb, it is required to lock the repetition rate to a standard frequency reference, which is implemented in the setup shown in Fig. 3.7(a). As the soliton repetition rate,  $f_{\text{rep}} = 191$  GHz, is not directly measurable, we use an electro-optic frequency comb (EO comb) of 14.6974 GHz line spacing, and measure the

beat signal between line number (no.) -1 of the microcomb and line no. -13 of the EO comb, as illustrated in Fig. 3.7(b). The EO comb is generated by cascading one MZM intensity modulator and three EO phase modulators which are driven with the same RF signal at 14.6974 GHz [164], [165]. Both microcomb and EO comb are generated with the same pump laser (Toptica CTL). The beat signal is compared to a reference signal of 60.0 MHz. The error signal is fed-back to the AlN actuator, such that the actuation on the microresonator stabilizes the soliton repetition rate to the EO comb line spacing.

The beat signal and the phase noise of it are measured for both free-running and locked cases as shown in Fig. 3.7(c-d). It can be seen clearly, after locking the linewidth of the beatnote and the phase noise are largely improved. The locking bandwidth, determined by the merging point of the two phase noise curves (red and blue), is 0.6 MHz. This bandwidth is wide compared to conventional lasers where the piezo response is typically limited to a few kilohertz (similar to integrated heaters). In addition, the 0.6 MHz bandwidth is limited by the chip contour and bulk modes of our sample. This bandwidth could be further extended to 10 MHz by eliminating the chip modes as outlined in Chapter 2.

### 3.5 Summary

In summary, we demonstrate the piezoelectric control of soliton microcombs, by monolithically integrating AlN actuators on ultralow-loss  $\text{Si}_3\text{N}_4$  waveguides. We show electrically controlled soliton initiation, tuning and megahertz-bandwidth locking. This novel approach of microcomb actuation not only benefits existing applications, but also allows synchronous scanning of the pump laser and microresonator, as required to build parallel FMCW LiDAR engines [83], [121]. The unprecedented bandwidth and low cross-talk offered by these piezoelectric actuators enable the suppression of parasitic line power fluctuations and Raman self-frequency shifts for LiDAR applications. By co-integration with CMOS microelectronic circuits and heterogeneously integrated semiconductor laser [7], compactly packaged microcombs with rapid electronic initiation, actuation, and stabilization are attainable, which will pave the paths for portable LiDAR and spectroscope in the future.

## 4. RELEASED PIEZOELECTRIC ACTUATION

In this chapter, the Si substrate beneath the piezoelectric actuator is removed to suspend the SiO<sub>2</sub> membrane such that it will have larger degree of freedom for mechanical bending. This will lead to more deformation of the optical microring than the unreleased device, and thus larger optical resonance tuning can be expected. As will be shown later, this larger deformation is at the expense of smaller tuning bandwidth due to the low frequency mechanical vibration modes of the SiO<sub>2</sub> membrane. These modes are measured and analyzed in more details. On the other hand, at the microwave frequency, HBAR can also be excited which will be tightly confined in the SiO<sub>2</sub> membrane. The AOM efficiency will be increased by 100 times compared with the unreleased device due to smaller acoustic mode volume and larger optomechanical interaction strength.

### 4.1 Design of the released piezoelectric actuator

Based on the resonance condition of optical ring resonator:  $Ln_{eff} = m\lambda$ , where  $L$  is the the cavity length  $2\pi R$ ,  $n_{eff}$  is the effective refractive index,  $m$  is the azimuthal order, there will be mainly two ways to tune the resonance wavelength  $\lambda$ : one is to change the cavity length  $L$  and the other will be to modify the effective refractive index. According to this idea, we designed released membrane structure, combining with piezoelectric actuator, which can be bent as we apply voltage. As shown in Fig. 4.1(a-c), the Si<sub>3</sub>N<sub>4</sub> waveguide is embedded in 5.8  $\mu\text{m}$  silica membrane which is 1.8  $\mu\text{m}$  wide and 800 nm thick. This guarantees most of optical mode is confined within low loss Si<sub>3</sub>N<sub>4</sub> waveguide, which helps to generate high optical quality factor. The optical ring resonator is constructed with the same waveguide dimensions with radius of 118  $\mu\text{m}$ . Depending on the relative position of the ring resonator within the membrane, three different structures are designed, with ring resonator 6  $\mu\text{m}$  (Fig. 4.1(a), Device Edge 1) and 12  $\mu\text{m}$  (Fig. 4.1(b), Device Edge 2) away from tip edge of the membrane, as well as at the anchor of the released membrane (Fig. 4.1(c), Device Anchor). Depending on the placement of the resonator, the devices will show distinct performance as demonstrated in the following sections.

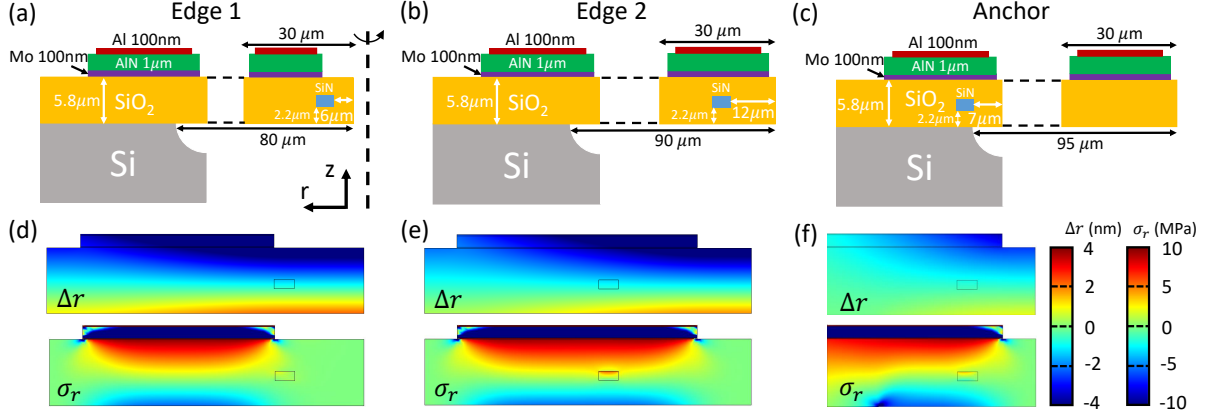


**Figure 4.1.** Schematics of cross-section of the devices with different relative positions of  $\text{Si}_3\text{N}_4$  ring resonator for (a)  $6 \mu\text{m}$  from tip edge, (b)  $12 \mu\text{m}$  from tip edge, and (c) right at the anchor. The thickness of each layer is labeled in each figure, while the dimensions of the waveguide is  $1.8 \times 0.8 \mu\text{m}^2$ . The relative position of rotational axis of the device is shown as in (a), and the cylindrical coordinate is employed. AlN sandwiched between Al and Mo serves as piezo-electric actuator which will bend the membrane when we apply voltage. (d-f) shows the FEM simulation of  $r$  direction displacement (top) and horizontal stress distribution (bottom) around the waveguide for (a-c), respectively. As positive  $60 \text{ V}$  is applied, the membrane will bend downwards, and tune the resonant wavelength by shrinking the ring mechanically and perturbing the refractive index through the stress-optical effect.

As illustrated in Fig. 4.1(a-c), the piezoelectric actuator is composed of AlN ( $1 \mu\text{m}$ ) which is sandwiched between Aluminum top electrode ( $100 \text{ nm}$ ) and Molybdenum bottom electrode ( $100 \text{ nm}$ ). The bottom electrode always serves as ground while voltage is applied to the top electrode across this work. As we apply positive voltage to the actuator, the AlN will expand and bend the membrane downwards. This actuation introduces  $r$  direction displacement, which is simulated for each structure as shown in the upper half of Fig. 4.1(d-f). As it bends down, upper part of the membrane experiences movement inwards the ring (negative  $\Delta r$  displacement), while the lower boundary moves outwards (positive  $\Delta r$  displacement). From the simulation, it can be seen that the waveguide undergoes negative horizontal displacement which means the optical ring will shrink. As the ring changes position gradually from the tip edge to the anchor, it experiences less and less horizontal displacement.

As expected, besides the mechanical displacement, there will be stress inside the membrane as it bends, which is also simulated and shown in the lower half of Fig. 4.1(d-f). Bending downwards generates extensional (positive) stress at the upper half of the membrane, while compressive (negative) stress is generated for the lower part. Interestingly, the area beneath the actuator shows enhanced stress and the stress around the waveguide is mainly determined by the relative position between ring and actuator, irregardless of the position of ring inside the membrane. Accordingly, as ring resonator gradually moves from the edge to the anchor, mechanical displacement will play less role, while stress-optical effect dominates. As the optical mode is mostly confined inside the  $\text{Si}_3\text{N}_4$  core, the change of effective refractive index is mainly determined by the change of index of  $\text{Si}_3\text{N}_4$  due to the stress-optical effect, which is different from previous work where the mode is less confined and inside the  $\text{SiO}_2$  cladding [71].

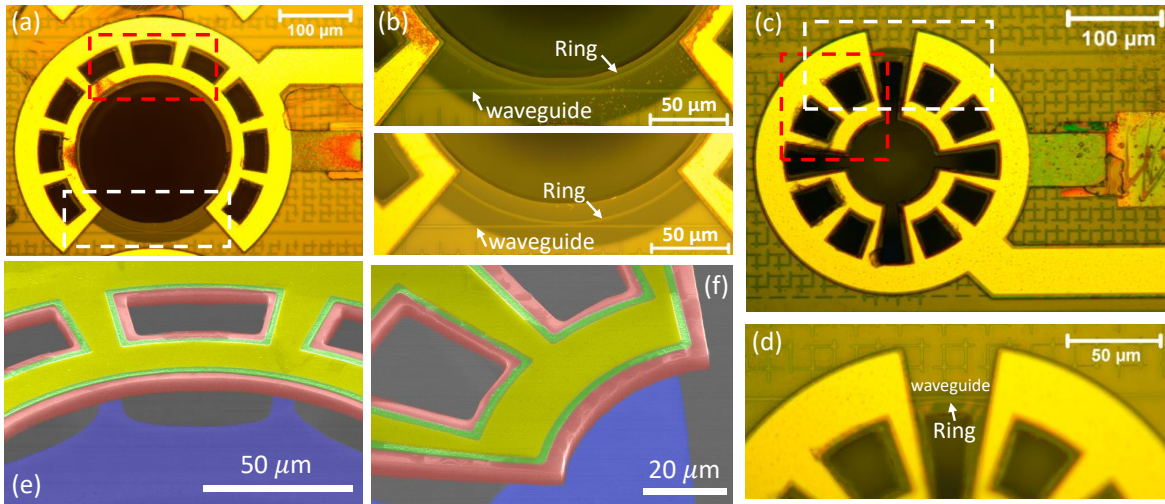


**Figure 4.2.** (a) Optical microscope of Device Edge 2. (b) Zoom-in optical microscope images around waveguide coupling region for Device Edge 1 (top) and Device Edge 2 (bottom), which corresponds to the white dashed rectangle in (a). The relative position of ring resonator inside membrane is clearly shown. (c) and (d) illustrate the optical microscope image of the whole device and zoom-in near waveguide coupling region (white dashed region in (c)) for Device Anchor, respectively. (e) and (f) show the false color SEM near red dashed rectangle in (a) and (c) respectively. Yellow region is top Al electrode with AlN (green) beneath it. Red is for released  $\text{SiO}_2$  membrane while blue is Si substrate.



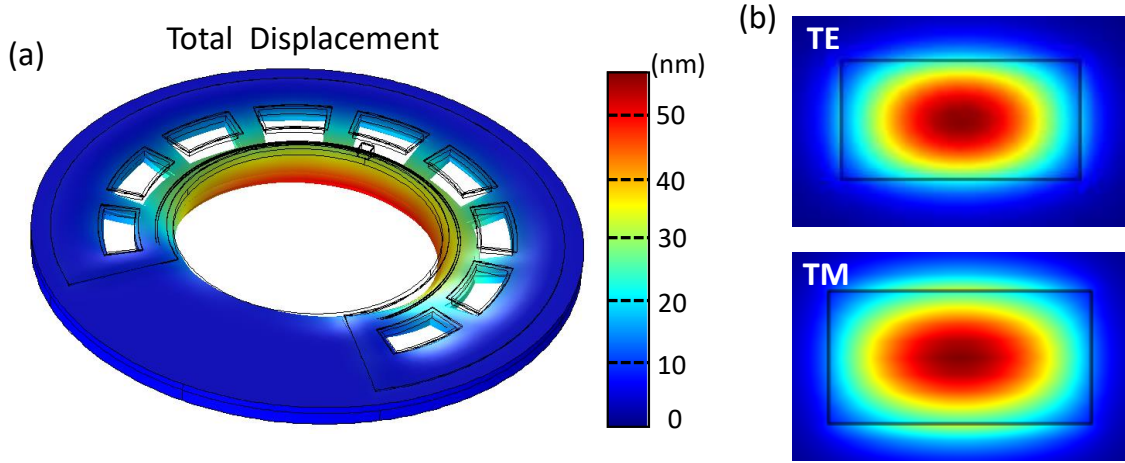


**Figure 4.3.** (a) COMSOL simulation of total displacement distribution of device Edge 2 under 60 V DC voltage. COMSOL optical mode simulation for (b) TE (upper) and TM (lower) modes respectively.

One of the optical microscope images of the final fabricated samples for device Edge 2 is shown in Fig. 4.2(a), while device Edge 1 shows much similar structure except for the relative position of ring resonator as illustrated in Fig. 4.2(b), which shows the zoom-in around the bus waveguide side coupling region. As expected, the ring of device Edge 1 is closer to the membrane edge than Edge 2. Inside the membrane, there are 9 rectangle holes that are defined for releasing the membrane uniformly, namely the releasing holes. To protect coupling between waveguide and ring from being perturbed by piezoelectric actuation, there is an intact region around the coupling area without any metal and piezoelectric material (Fig. 4.2(b)). Fig. 4.2(e) illustrates the skewed false-color SEM image of device Edge 2 of the red dashed region in Fig. 4.2(a), which shows the freely moving  $\text{SiO}_2$  membrane (red) together with the top AlN piezoelectric actuator (green).

Similarly, the optical image of device Anchor is shown in Fig. 4.2(c), with the zoom-in near coupling region in Fig. 4.2(d). One can see that the optical ring resonator locates at the anchor of the released membrane. The skewed SEM of device Anchor is also as presented in Fig. 4.2(f). Based on the SEMs, no significant buckling of the membrane after releasing is observable, demonstrating low residual stress inside the  $\text{SiO}_2$  membrane after the deposition.



The mechanical simulation of the device Edge 2 is provided in Fig. 4.3(a), which shows the total displacement under 60 V. The released membrane bends downwards for positive voltage with maximum displacement of 56 nm. Due to the lack of AlN near the waveguide coupling region, the displacement distribution is not cylindrically symmetric, which makes the simulation of optical resonance tuning challenging. The optical mode distribution of TE and TM modes are simulated as shown in Fig. 4.3(b). It can be seen that TE mode is more confined within  $\text{Si}_3\text{N}_4$  waveguide core than TM mode. This helps to reduce the waveguide surface scattering loss of TE mode. On the other hand, the TM mode extends more outside the waveguide in the vertical direction, which increases its absorption loss from metal on top of the cladding. From these simulations, TE mode shows lower losses and thus higher optical Q than TM mode as observed in the experimental results.

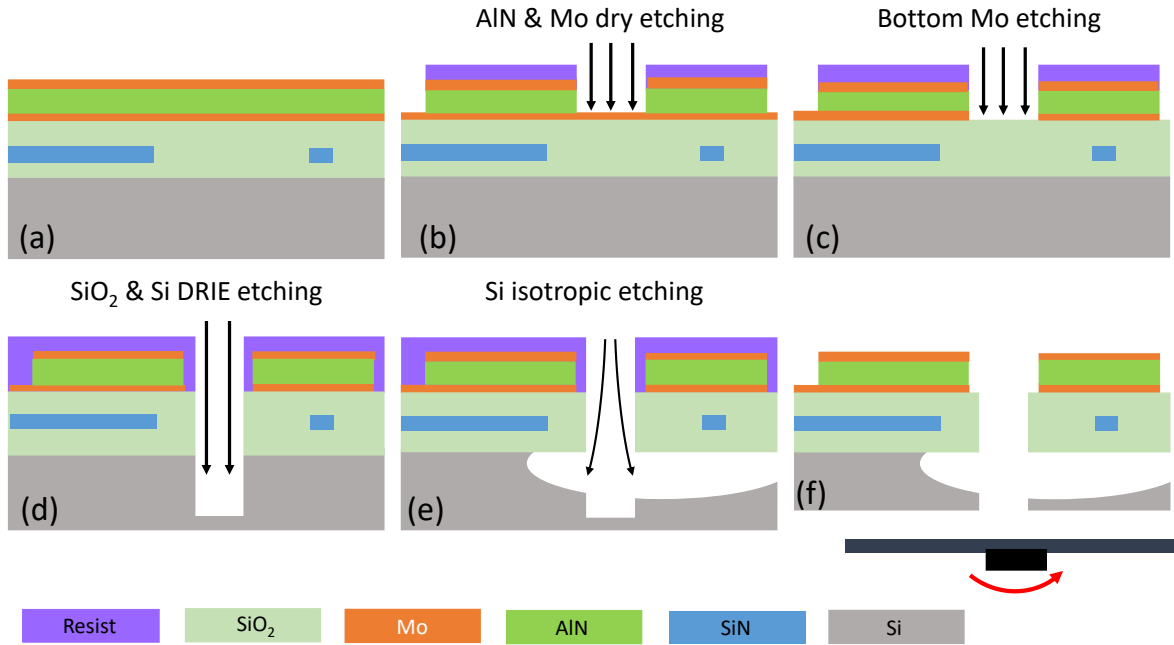


**Figure 4.4.** Schematics of fabrication flow for the released piezoelectric actuator. (a) Cross-section of the device after fabrication of the  $\text{Si}_3\text{N}_4$  ring resonator using the Damascene process. (b) Mo and AlN are RIE etched to define the shape of the actuator. (c) Etching the bottom Mo metal. (d) Release holes are defined by deep RIE etching of  $\text{SiO}_2$  and Si, followed by (e) isotropic dry etching of the Si substrate. (f) The wafer is finally mechanically polished to be diced into small chips.

## 4.2 Fabrication processes

To fabricate the released actuator, a novel releasing technique is proposed as illustrated in Fig. 4.4. The  $\text{Si}_3\text{N}_4$  photonic circuits is fabricated using the photonic Damascene process [24]. Films of 100 nm Mo and 1  $\mu\text{m}$  AlN are then sputtered on the wafer through foundry services (Plasma-Therm). The actuators are patterned by thick photoresist SPR220-4.5, and the top Mo is etched with Reactive Ion Etching (RIE) using  $\text{Cl}_2$  and the AlN is also RIE etched using  $\text{Cl}_2$  and  $\text{BCl}_3$  in the same Panasonic E620 Etcher. The bottom Mo electrode is patterned by photoresist AZ1518 and dry-etched using  $\text{Cl}_2$  in the same etcher. Note the device shown in Fig. 4.2 has Al top metal which is fabricated by lift-off process described in Chapter 2.

In the next step, the releasing holes are made by deep RIE (DRIE) etching of the  $\text{SiO}_2$  and Si, which is anisotropic and has good selectivity in the vertical direction as illustrated in Fig. 4.4(d). Note that the dicing lines between chips ( $5 \times 5 \text{ mm}^2$ ) are also etched in the same time, which helps to dice the wafer into individual chips in combination with the

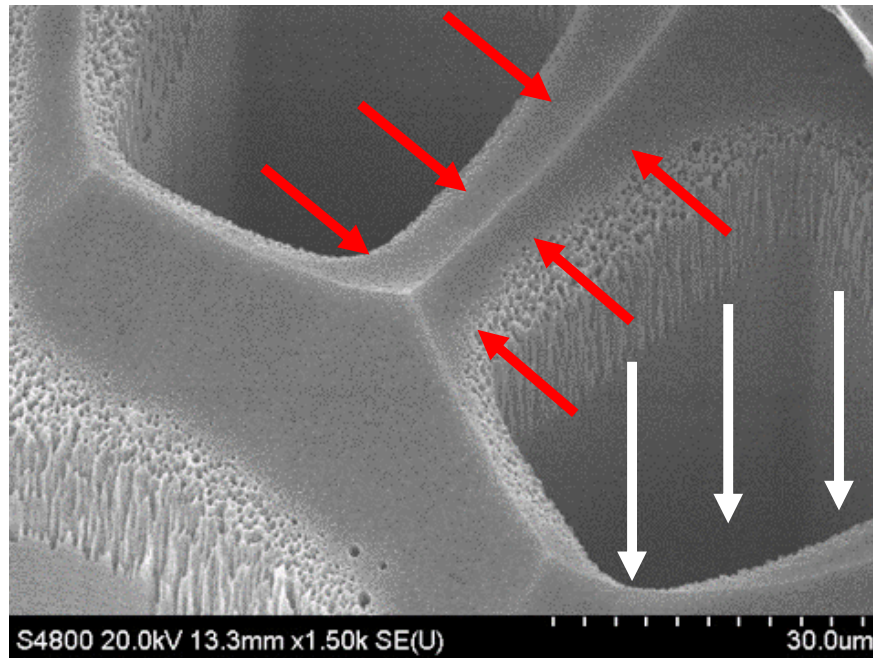


**Figure 4.5.** SEM image of the Si substrate of the device Anchor after vertical DRIE (white arrows) and Si lateral etching (red arrows).

mechanical polishing in the final step. Also, the DRIE makes sure smooth chip edge for good lensed fiber to chip edge coupling. In the following, Si isotropic dry etching using  $\text{SF}_6$  is performed to undercut and suspend the  $\text{SiO}_2$  membrane. The mechanical polishing serves as the final step to dice the wafer into chips. The SEM of the Si substrate of the device Anchor after the DRIE and Si lateral isotropic etching is shown in Fig. 4.5. DRIE first etched the Si vertically (white arrows) and defined releasing holes. The lateral Si isotropic dry etching (red arrows) is performed subsequently to release the remaining structures using the defined releasing holes. This leads to the curved surface and roughness at the corners.

### 4.3 DC optical resonance tuning

To demonstrate the tunability of the devices, we apply first DC voltages on the top electrode while grounding the bottom electrode, and then measure the corresponding spectrum using a tunable diode laser (New Focus TLB-6328). The results for the three kinds of devices are summarized in Fig. 4.6. Both TE and TM modes are measured which are identified by comparing the measured FSR of them with COMSOL mode simulation. For device Edge 1, where the ring is close to membrane edge, the resonant wavelengths of both TE and TM modes increase as we apply positive voltage, as shown in Fig. 4.6(a). As we switch the voltage to a negative value, the resonance shifts to lower wavelength, which means blue detune. This demonstrates bidirectional tuning ability, which is different from Ref [71], probably because the stress-optical effect plays a more important role rather than the purely mechanical deformation. One can see that, from Fig. 4.6(a), the tuning is achieved over one linewidth of the resonance under 60 V, which would be sufficient for applications like  $\text{Si}_3\text{N}_4$  micro-combs and optical modulator. The dependence of the tuning on DC voltage for device Edge 1 is shown in Fig. 4.6(d), which is highly linear with linear fitting  $R^2$  bigger than 0.99 (solid lines). Higher voltages are applied up to 100 V without breaking the AlN actuator, demonstrating AlN break down field higher than 100 V/ $\mu\text{m}$ . Both TE and TM modes show similar tuning efficiency of 0.4 pm/V (-50 MHz/V).

As the ring moves away from the edge, like Edge 2 (Fig. 4.6(b)), it shows similar bidirectional tuning performance as Edge 1, but now TE and TM modes have different tuning

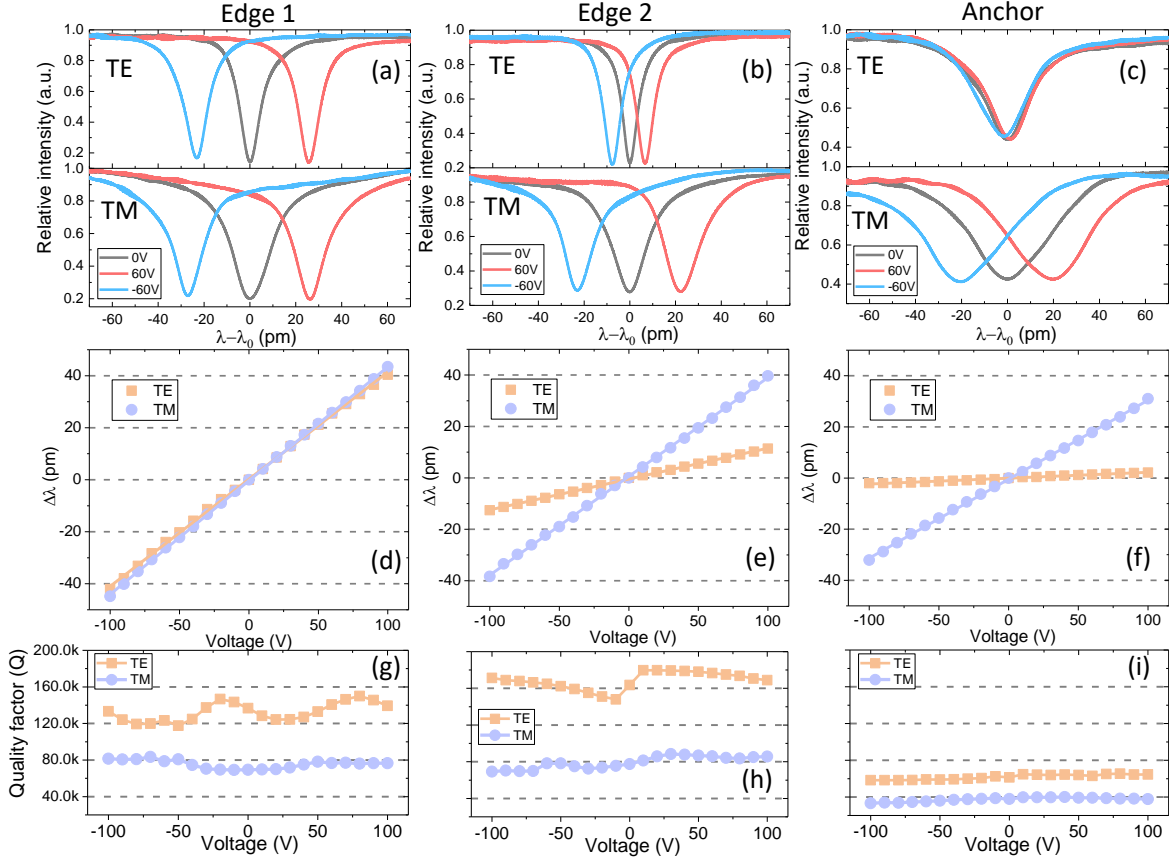


**Figure 4.6.** (a-c) DC tuning spectrum for TE (upper) and TM (lower) modes under 0 V (gray), 60 V (red), and -60 V (blue) for device Edge 1, Edge 2, and Anchor respectively. The x axis for each spectrum is relative to the center wavelength of each mode, with  $\lambda_0$  for Edge 1 TE mode 1548.4 nm and TM mode 1548.8 nm, and for Edge 2 TE mode 1549.6 nm and TM mode 1548.8 nm, and for Anchor TE mode 1549.1 nm and TM mode 1549.7 nm. All devices and modes show red detune (increasing resonant wavelength) for positive voltage and blue detune (decreasing resonant wavelength) under negative voltage, but with different tuning efficiency. (d-f) Dependence of the resonant wavelength tuning  $\Delta\lambda$  on DC voltage for devices Edge 1, Edge 2, and Anchor, respectively. Orange (purple) dots and lines are experiment points and linear fitting for TE (TM) mode, respectively. The tuning is highly linear ( $R^2 > 99\%$ ) and has positive slope with voltage, showing bidirectional tuning. (g-i) Dependence of the optical quality factor  $Q$  on voltages for TE (orange) and TM (purple) modes. TE modes show higher  $Q$  than TM mode in all cases.

efficiency, demonstrating the polarization dependency of the tuning due to stronger stress-optical effect. This is related with anisotropy of stress optical coefficients with large off diagonal elements in stress-optic tensor. Although TE mode shows smaller tuning efficiency of 0.12 pm/V (-15 MHz/V) than TM mode 0.4 pm/V (-50 MHz/V), it has much higher optical quality factor (narrower linewidth), probably because it is now far away from the edge with less scattering loss. The linearity of tuning is illustrated in Fig. 4.6(e), and the TE mode has smaller tuning slope than TM which is consistent with previous observation from the spectrum (Fig. 4.6(b)).

When the ring is located at the anchor (Fig. 4.6(c)), the mechanical deformation of ring radius is highly suppressed, with index perturbation mainly induced by the stress. Intriguingly, TE mode shows very little tuning of 0.02 pm/V (-2.5 MHz/V) while TM mode is less influenced with 0.3 pm/V (-37.5 MHz/V). It can be seen more clearly from Fig. 4.6(d-f), the slope of TE mode gradually decreases while the TM mode remains nearly unaffected as ring moves from edge to anchor. This tuning selectivity for TE and TM modes will be especially interesting for applications where the advanced tuning of the frequency separation between a pair of TE and TM modes is considered. Quantitatively speaking, from the FEM simulation of Fig. 4.1(d-f), the average radius change under 60 V is around -1.2 nm for device Edge 1, which corresponds to negative resonant wavelength detune around -16 pm. This is in stark contrast with the positive tuning from the experiment (Fig. 4.6(a)). One proposed hypothesis is the influence of stress-optical effect is large enough to overcome the change of radius effect and reverse the tuning sign. Also, the asymmetry of the structure requires fully 3D simulation model both optically and mechanically, which makes the problem difficult. In addition, the built-in stress inside the SiO<sub>2</sub> membrane and Si<sub>3</sub>N<sub>4</sub> after fabrication is ignored in the simulation, which worth further consideration in the future.

The optical quality factor  $Q$  is monitored as we change the voltage, as presented in Fig. 4.6(g-i). The  $Q$  shows little dependence on voltage and the fluctuation is mainly due to the measurement error. This demonstrates the membrane bending will not degrade the optical  $Q$  which is important for practical applications like micro-combs and tunable filters. In general, TM mode shows much smaller  $Q$  than TE mode for each device. This is because TE mode is more confined in the Si<sub>3</sub>N<sub>4</sub> waveguide core than TM mode, such that it has less scattering

loss from the waveguide surface due to the surface roughness. Also, the more confinement of TE in vertical direction helps to reduce the absorption from the metal electrode. As expected, device Edge 2 shows higher Q than device Edge 1 for both TE and TM modes, since optical ring in Edge 2 is farther away from the membrane edge, the roughness of which will further introduce scattering loss. Accordingly, Q as high as  $1.8 \times 10^5$  is observed for TE mode of Edge 2. Unfortunately, due to the presence of releasing holes, the ring in device Anchor is close to membrane etching edge (see Fig. 4.1(c)), which limits its Q to around  $5 \times 10^4$ . Finally, it is worth noting that, due to the low leaky current of AlN film, the DC current is kept below 1 nA as we increase the voltage up to 60 V, showing sub-100 nW power consumption tuning. The low power consumption and bidirectional tunability make this design stand out among similar works and thermal-optical method.

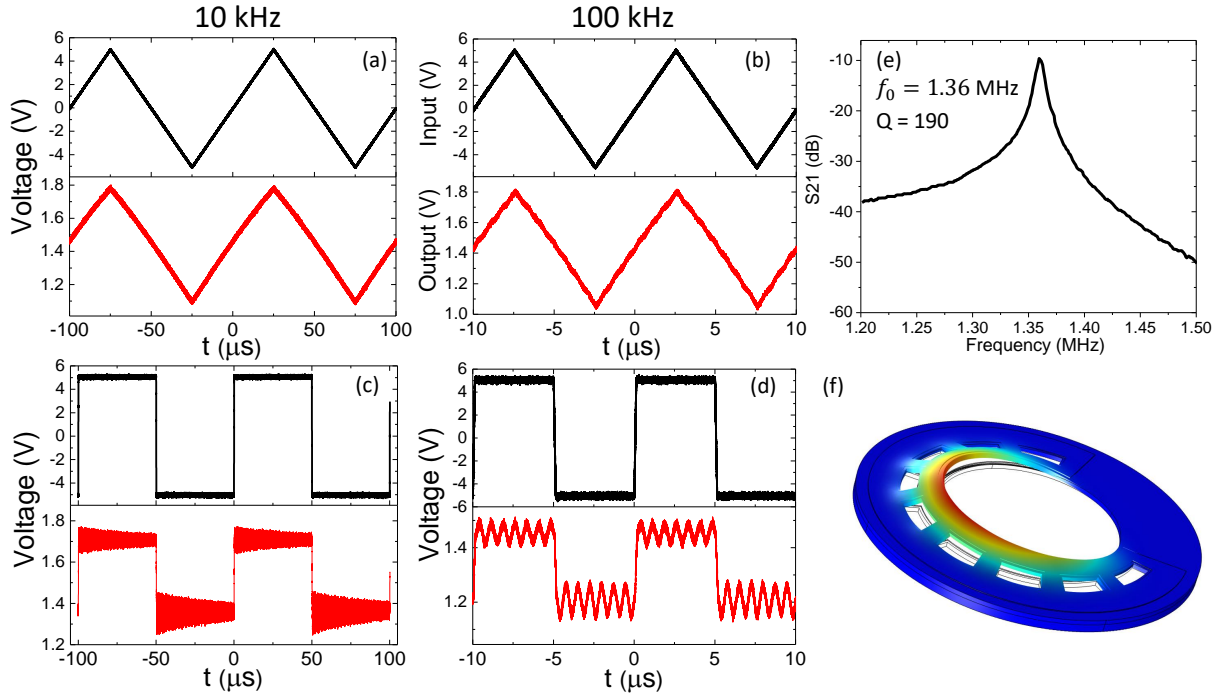


**Figure 4.7.** Time domain intensity modulation of device Edge 1 under triangle waves with (a) 10 kHz and (b) 100 kHz, as well as under square waves with 10 kHz (c) and 100 kHz (d). The top part (black) of each figure is the input RF signal while the lower part (red) is the output optical modulation. (e) Optomechanical  $S_{21}$  response to the input RF modulation, showing mechanical resonance at 1.36 MHz with 190 mechanical Q. (f) COMSOL simulation of the fundamental mechanical mode at 1.36 MHz.

#### 4.4 Tuning dynamics and speed

Besides the above mentioned advantages of the proposed design, this work also shows high tuning speed, which is mainly limited by the fundamental mechanical resonance. By properly designing mechanical structure, the resonant frequency of fundamental mechanical mode is around 1.3 MHz. To test the tuning speed of the device, time domain modulation is conducted with both triangle and square waves for different frequencies, as shown in Fig. 4.7, where device Edge 1 is first tested. For 10 kHz triangle wave (Fig. 4.7(a)), the output follows nearly with the input signal, and no hysteresis is observed. As we increase the frequency to 100 kHz (Fig. 4.7(b)), there appear ripples along the triangle which is induced by the mechanical ringing due to high frequency components from the sharp turning edge of the triangle wave. Therefore, for practical applications, we should avoid sharp features of the input signals to bypass the mechanical oscillation.

The influence of the mechanical resonance can be seen more easily from square wave drive as shown in Fig. 4.7(c-d). Due to the sharp edge of square, it contains frequency at the mechanical resonance which excites the oscillation after it switches from one state to the other. However, the edge of output is also sharp and follows the input, which shows that the tuning speed is mainly limited by the mechanical ringing. We can see clearly the ringing as it is switched in Fig. 4.7(c), and also the mechanical oscillation in Fig. 4.7(d). Furthermore, the ringing always exists although we reduce the repetition frequency of the square wave (from 100 kHz to 10 kHz), which is mainly related with the sharp edge.

The spectral response of the device around the fundamental mechanical mode is shown in Fig. 4.7(e). The resonant frequency shows up at 1.36 MHz with mechanical Q of 190. The high Q leads to long ring down time as in Fig. 4.7(c). The mode shape of the fundamental mechanical mode is simulated as shown in Fig. 4.7(f). To further increase the tuning speed, we can do preconditioning of the input signal by filtering the frequency components around mechanical resonances to suppress the mechanical oscillation. On the other hand, the mechanical oscillation can be suppressed by filling air with damping gases using commercial packaging techniques. These advanced strategies may reduce the influence of the mechanical resonance and worth more investigation in the future.



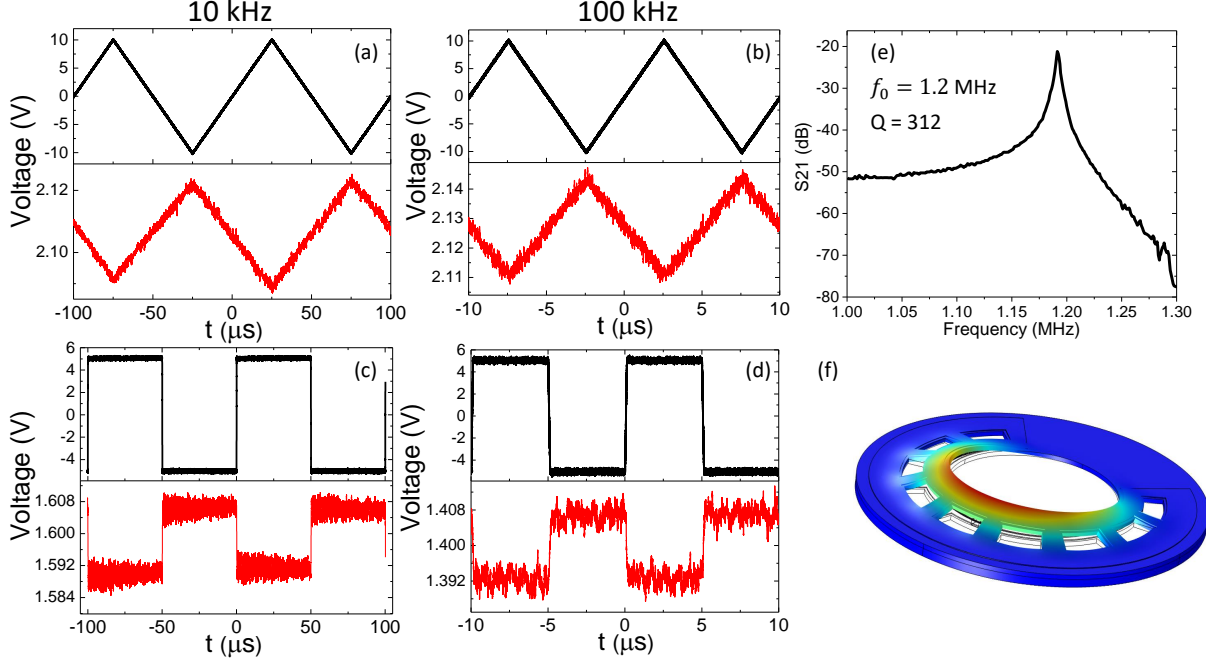


**Figure 4.8.** Time domain intensity modulation of device Edge 2 under triangle waves with (a) 10 kHz and (b) 100 kHz, as well as under square waves with 10 kHz (c) and 100 kHz (d). The top part (black) of each figure is the input RF signal while the lower part (red) is the output optical modulation. (e) Optomechanical  $S_{21}$  response to the input RF modulation, showing mechanical resonance at 1.2 MHz with 312 mechanical Q. (f) COMSOL simulation of fundamental mechanical mode at 1.2 MHz.

Similar testing is conducted for device Edge 2 as shown in Fig. 4.8, including time domain intensity modulation at different frequencies under both triangle and square waves, as well as spectral response. In this time, the laser is biased at the other slope of the resonance, such that the output has  $\pi$  phase shift with respect to the input. Other than that, it shows similar behavior as previous device. For example, it shows ringing effect when the input voltage switches from positive to negative, or vice versa. This is also caused by the mechanical resonance as shown in the spectral response (Fig. 4.8(e)), with fundamental mode at 1.2 MHz and Q of 312, which is simulated and illustrated in Fig. 4.8(f).

The dynamic modulation and response of device Anchor is studied following similar procedure as demonstrated in Fig. 4.9. Due to the different mechanical structure design, it shows four close mechanical modes around 1.35 MHz caused by four cantilevers that are only connected at the anchor. Since the waveguide coupling region is not covered by the



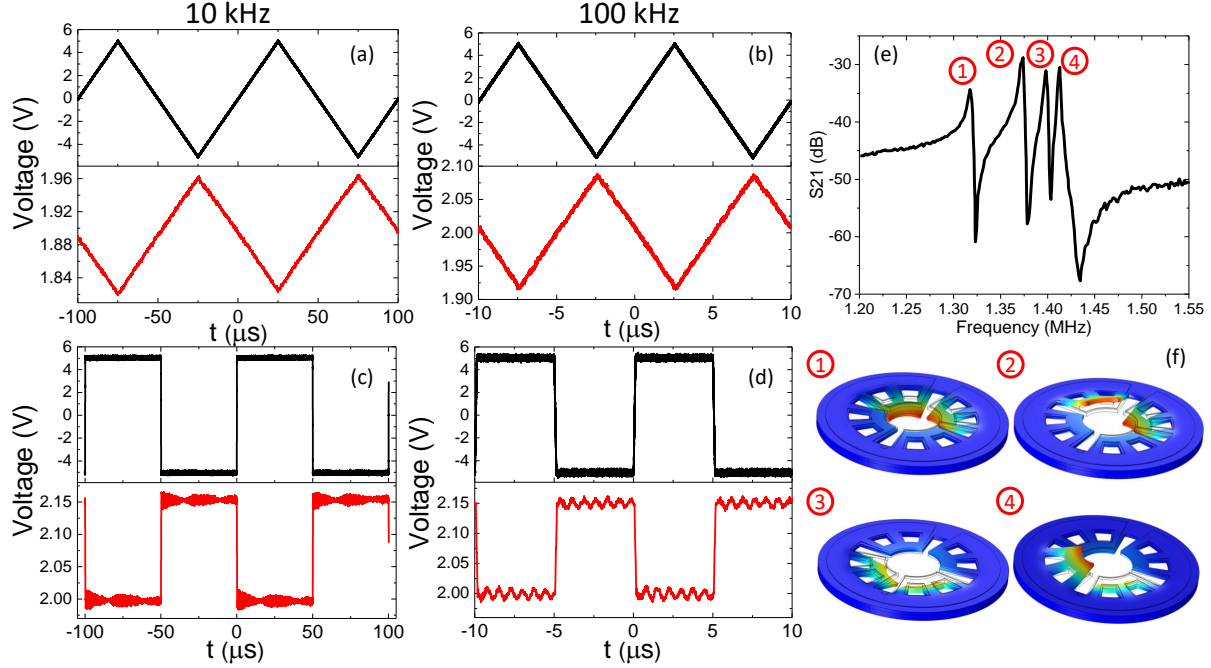


**Figure 4.9.** Time domain intensity modulation of device Anchor under triangle waves with (a) 10 kHz and (b) 100 kHz, as well as under square waves with 10 kHz (c) and 100 kHz (d). The top part (black) of each figure is the input RF signal while the lower part (red) is the output optical modulation. (e) Optomechanical  $S_{21}$  response to the input RF modulation, showing four closely located modes around 1.35 MHz. (f) COMSOL simulation of the four mechanical modes as labeled in (e).

actuator, it breaks the cylindrical symmetry and the cantilevers are grouped into two groups that have mirror symmetries. The upper two cantilevers form a group that generates the first two mechanical modes, as shown in Fig. 4.9(f). For mode 1, the two cantilever oscillate in phase, while for mode 2 they are out of phase. Similarly, for the lower two cantilevers, they form mode 3 and 4. Interestingly, the excitation of the four modes generates beating in the ringing for the square wave as can be seen in Fig. 4.9(c). The input and output show  $\pi$  phase difference depending on which slope the laser is biased at.

The mechanical modes of the device Edge 2 is further studied by by measuring the displacement of the cantilever using Laser Doppler Vibrometer (LDV), as shown in Fig. 4.10. From the displacement spectrum in Fig. 4.10(a), a series of flexural mode of the circular cantilever can be found with the mode order as labeled by the number. The displacement

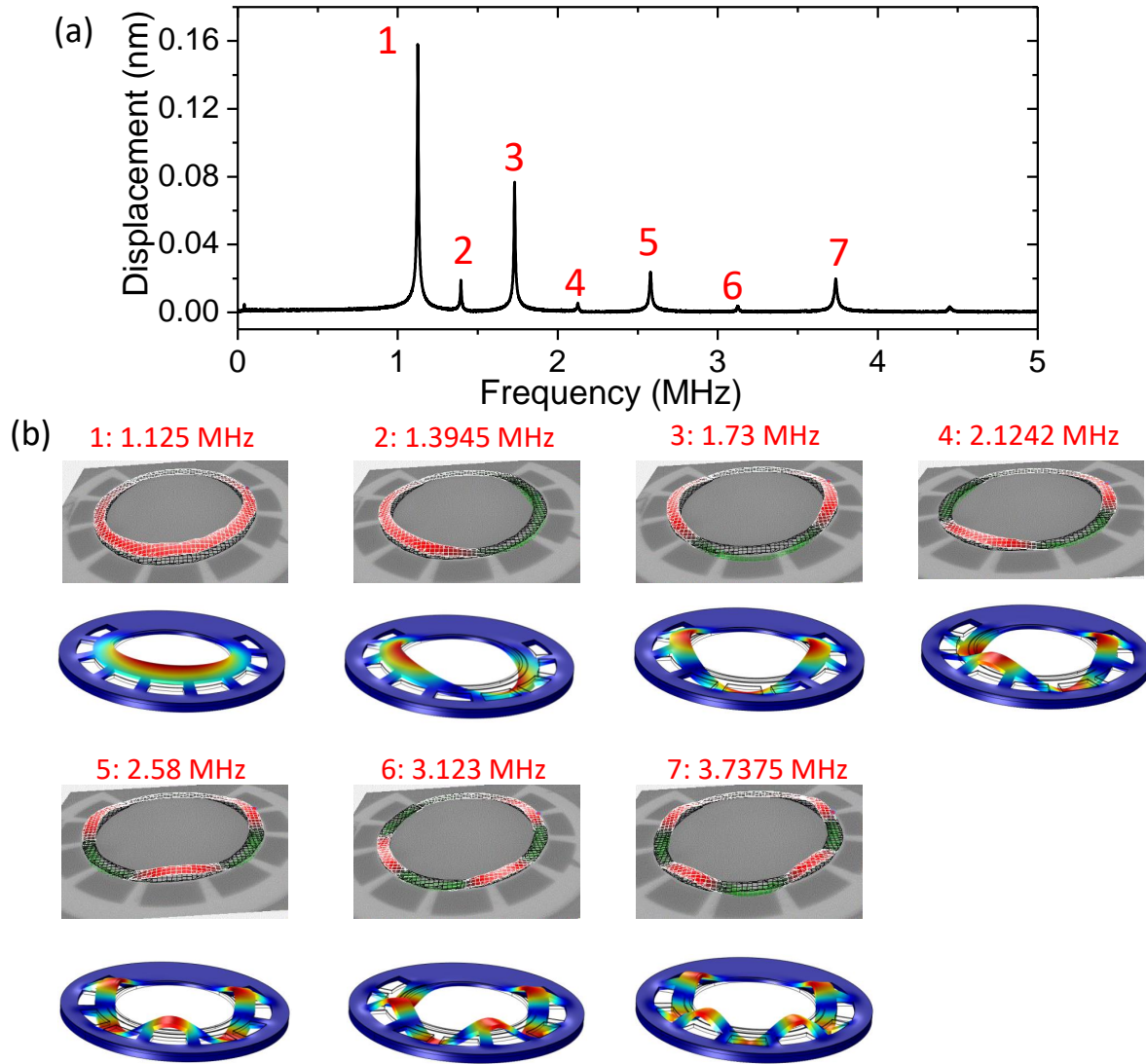


**Figure 4.10.** (a) Measured spectrum of the displacement at the tip of the cantilever using Laser Doppler Vibrometer (LDV). (b) Measured mechanical displacement distribution for each mode as labeled in (a). The COMSOL simulation is shown in the lower panel which matches well with the measurement.

distribution of each mode is measured in Fig. 4.10(b) together with the COMSOL simulation, which shows good agreement. It can be seen as the mode order increases, more nodes can be formed along the circle with smaller wavelength of the standing wave. This is similar as an optical ring resonator. It is interesting to observe that the peaks' amplitudes show alternative height as the mode order increases in Fig. 4.10(a). This is because the spectrum is measured at one point on the cantilever where it locates at the antinode and node for odd and even order mode, such that it experiences large and negligible displacement.

#### 4.5 GHz acousto-optic modulation via bulk acoustic resonance

In Chapter 2, I demonstrated the AOM of  $\text{Si}_3\text{N}_4$  microring using high-overtone bulk acoustic wave resonances (HBAR) [12], where the acoustic wave transmits vertically towards the substrate. This releases a degree of freedom for the design from the surface to out of the plane, where the waveguide can be buried deeply in a thick cladding layer. This largely preserves waveguide low-losses and large optical Q of the  $\text{Si}_3\text{N}_4$  ring resonator. Also, the acoustic resonances primarily rely on the material stack and thickness rather than lithography, which gives more lateral design freedoms regarding footprint, actuator shape, and fabrication cost, compared with SAW. Additionally, the high vertical acoustic mode confinement helps keep low cross-talk between two closely adjacent actuators, which is advantageous for compact spatiotemporal modulation [12].

However, the HBAR AOM is still suffering from low modulation efficiency which is mainly limited by the electromechanical and optomechanical coupling efficiency. In the previous study, the acoustic wave is evenly distributed over the whole 200  $\mu\text{m}$  Si substrate which lowers the acoustic excitation efficiency, and the large mode volume decreases optomechanical coupling rate  $g_0$  [12]. Here, by removing the Si substrate and forming a free-standing 5.5  $\mu\text{m}$   $\text{SiO}_2$  membrane, the bulk acoustic waves can be tightly confined in the acoustic cavity. The microwave frequency electromechanical and optomechanical responses of the device Edge 2 is studied in the following.

At first, the electromechanical  $S_{11}$  response is characterized by measuring the electrical reflection  $S_{11}$  using port 1 of the vector network analyzer (VNA), which shows up the en-

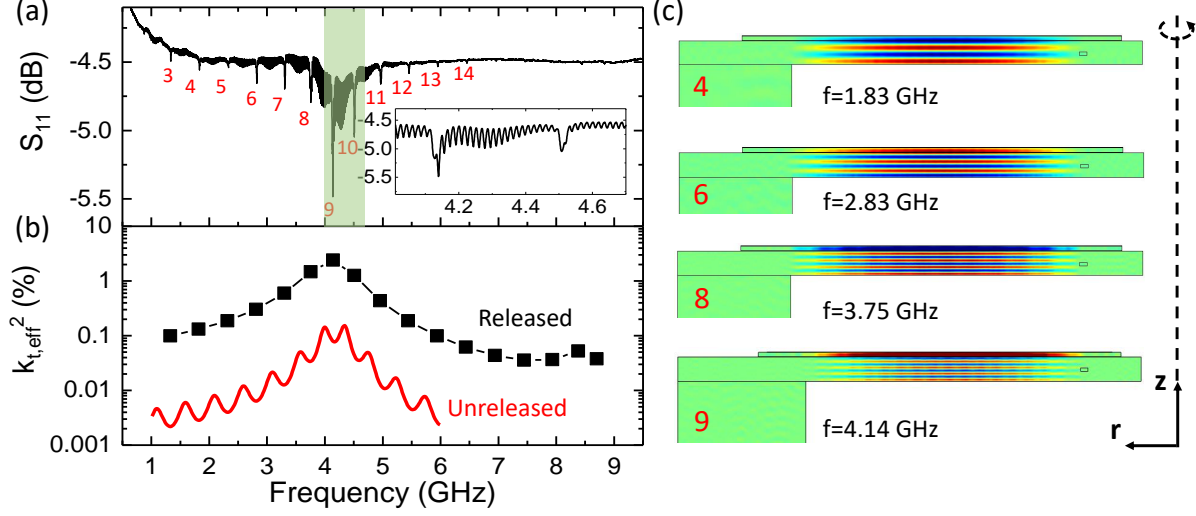


**Figure 4.11.** (a) Electromechanical  $S_{11}$  spectrum from 1 to 10 GHz with the mode order labeled for each visible acoustic resonance in oxide cavity. The inset shows the zoom-in of the green shaded region. (b) Calculated electromechanical coupling efficiency  $k_{t,eff}^2$  for each HBAR mode (black square). The  $k_{t,eff}^2$  of unreleased HBAR (red curve) is plotted for comparison. (c) Numerical simulation of the vertical stress distribution  $\sigma_z$  for typical modes. The mode order is as labeled in (a). The mode is axisymmetric which revolves around the vertical dashed line. Reprinted from Ref. [16].

ergy conversion from electrical to mechanical vibration as a dip. The result is shown in Fig. 4.11(a) where a series of periodic resonances can be observed with a free spectrum range (FSR) of 490 MHz. The mode order for each HBAR resonance is as labeled, which corresponds to the number of wavelengths in one round-trip inside the cavity similar as an optical Fabry-Pérot cavity. This can be seen more clearly from the Finite Element (COM-SOL) simulations of the stress distribution for typical modes in Fig. 4.11(c). Since the stress distributes uniformly over the whole oxide membrane, the optical waveguide can be buried deep inside the cladding without compromising the modulation efficiency.

Interestingly, the electromechanical response is enhanced (deeper resonance) around 4 GHz as in the green shaded region. This is because, at this frequency, the half acoustic wavelength in AlN equals the AlN thickness, approaching the fundamental (1st order) resonance of the AlN cavity (see mode simulation of order 9 in Fig. 4.11(c)). Besides the sharp resonances, there are small periodic dips overlapped at the background with a much

smaller FSR of 17 MHz (see the zoom-in shown in Fig. 4.11(a) inset). This comes from the HBAR resonances from the Si substrate as part of the contact pads and traces are not fully released and sits on the rigid substrate. By having a rough backside substrate surface, these resonances can be avoided in the future, which will prevent the energy leak into the substrate and increase the mechanical Q.

The electromechanical coupling efficiency  $k_{t,\text{eff}}^2$  for each mode is calculated using the traditional Mason model as shown in Fig. 4.11(b). The efficiency gradually increases as the frequency approaches the AlN fundamental resonance. A maximum of 2% can be achieved which is one order of magnitude improvement over previous HBAR modes with giant Si substrate (red curve in Fig. 4.11(b)). It can be seen that there is also an efficiency enhancement around 8.5 GHz which corresponds to the second order resonance of the AlN film. Theoretically, the second order AlN resonance can hardly be observed if the structure is symmetric

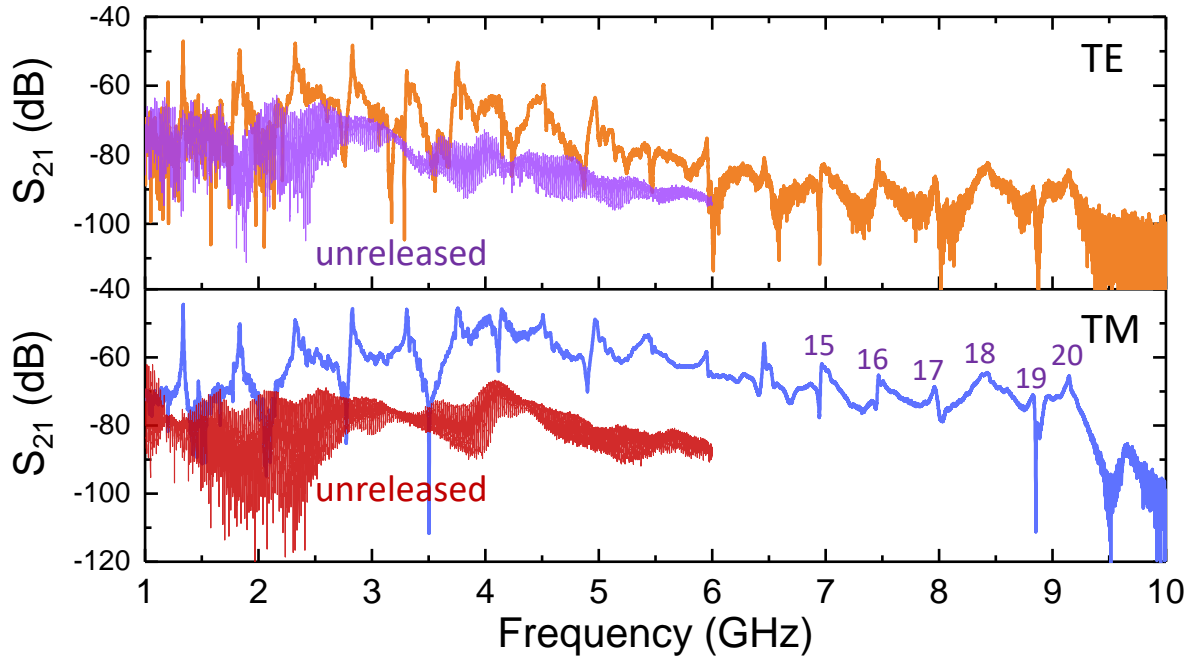


**Figure 4.12.** Acousto-optic modulation response  $S_{21}$  for TE (upper) and TM (lower) modes from 1 to 10 GHz. Periodic resonances can be observed corresponds to each of the dip from  $S_{11}$ . The orders for the resonances at high frequencies that can hardly be distinguished in  $S_{11}$  are as labeled. The  $S_{21}$  for unreleased devices for TE (purple) and TM (red) modes are overlapped for comparison.

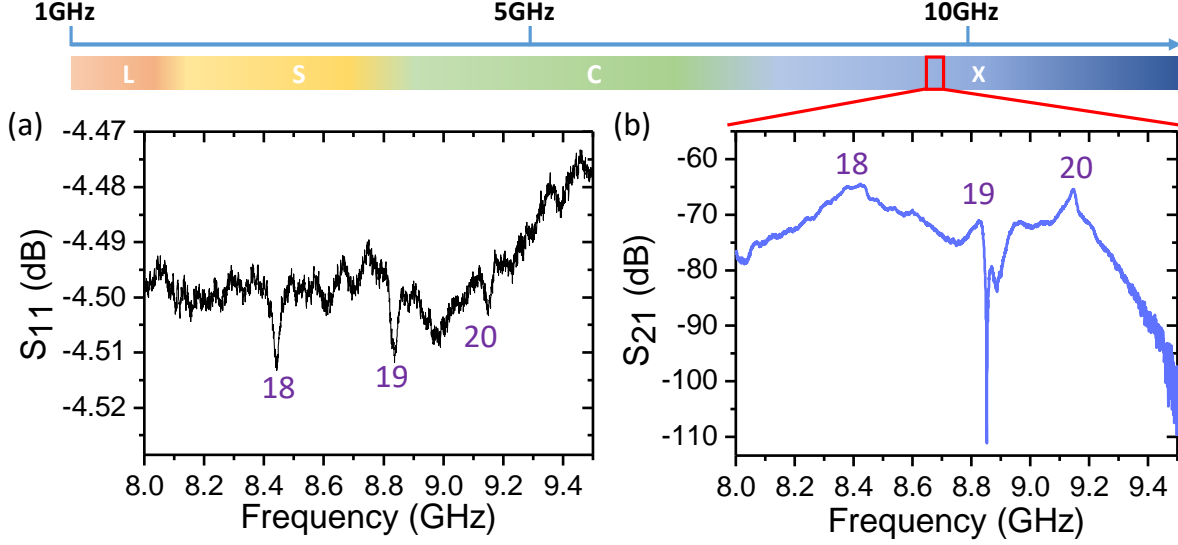


**Figure 4.13.** (a) Electromechanical  $S_{11}$  and (b) optomechanical  $S_{21}$  at the microwave X-band. The HBAR mode from 18 to 20 order can be clearly seen. The definition of different microwave bands is indicated at top.

with respect to the AlN film, since the net stress generated in the piezoelectric film is zero [166]. However, the symmetry is broken due to the choice of different materials as top and bottom metals and biasing of oxide layer. We will see below the second harmonic resonance will enhance the optical modulation at that high frequencies.

Each of the HBAR modes can be excited to modulate the optical refractive index via the stress-optical effect. This is measured by performing optomechanical  $S_{21}$  measurements, where, by setting the input laser frequency (1550 nm) at the slope of the optical resonance, the output modulated laser intensity is detected by a high-speed photodetector (PD) and sent to port 2 of the VNA, while a -5 dBm RF signal from port 1 of the VNA is launched on the AlN actuator. From Fig. 4.12 one can see the resonant modulation peaks corresponding to each of the oxide HBAR modes from  $S_{11}$ . The small resonances from the Si substrate HBAR as presented in  $S_{11}$  do not show up in optomechanical  $S_{21}$ , since the Si HBAR mainly locates at the outer anchor region which is far away from the inner  $\text{Si}_3\text{N}_4$  ring.

Intriguingly, resonances up to 9.15 GHz can be resolved, as shown in Fig. 4.13. Although the resonances of modes from 15 to 20 are very weak in  $S_{11}$  (Fig. 4.13(a)), the optomechanical response shows a larger signal to noise ratio (SNR) thanks to the high optical sensitivity.

This is true for both TE and TM modes, although TE shows lower level responses at high frequencies due to its higher optical Q and thus longer response time. The second-order resonance from AlN film helps to enhance the modulation efficiency at high frequencies around 9 GHz. It should be noted that this high frequency modulation falls into the microwave X-band, which will find widespread applications such as injection-locking of Kerr combs with 10 GHz FSR [49], atomic clocks that use Cesium's 9.19 GHz hyperfine transition frequency as a reference [167].

As high as -45 dB direct transduction efficiency from RF in to photo detector output at 4 GHz is achieved, which is two orders of magnitude increased compared with previous unreleased HBAR AOM under the similar input optical intensity ( $\sim 100 \mu\text{W}$ ). As mentioned earlier, one order of magnitude improvement comes from the electromechanical coupling efficiency. The other one order is from the enhancement of optomechanical coupling rate  $g_0$  due to the shrink of the mechanical mode volume.

GHz frequency acousto-optic modulation can find widespread applications, among which microwave to optical converter has attracted much attention recently for building a quantum computing network [168]. One important figure of merit is the quantum conversion efficiency  $\eta$  which measures the ratio of the number of photon scattered to the sideband over input microwave photons. It can be estimated from the  $S_{21}$  measurement as [15]:

$$\eta = \frac{2R_{\text{load}}}{IR_{\text{PD}}^2} \frac{\Omega_m}{\omega_0} S_{21} \quad (4.1)$$

where  $I$  is the pump optical power,  $R_{\text{load}}$  (50  $\Omega$ ) is the impedance of VNA,  $R_{\text{PD}}$  (800 V/W) is the responsivity of the photo-detector,  $\Omega_m$  and  $\omega_0$  is the resonant frequencies of mechanical and optical cavity, respectively. After plugging in the experimental numbers, the quantum efficiency  $\eta$  is  $8 \times 10^{-10}$ , which is still far from the ideal case. The dependence of  $\eta$  on device parameters is [106]:

$$\eta = \frac{\kappa_e}{\kappa} \frac{\Gamma_{\text{ex}}}{\Gamma} \frac{4C}{(1+C)^2} \quad (4.2)$$

where  $\kappa$  ( $\kappa_{\text{ex}}$ ) and  $\Gamma$  ( $\Gamma_{\text{ex}}$ ) are the total loss rate (external coupling rate) for optical and mechanical cavity, respectively.  $C = C_0 n_{\text{cav}}$  is the enhanced cooperativity with  $C_0 = 4g_0^2/\kappa\Gamma$



the single-photon cooperativity and  $n_{\text{cav}}$  the intra-cavity pump photon number. From the relations, there are many ways to increase the efficiency in the future: 1. Increasing the optical Q. The current device is fabricated using traditional subtractive process. With the recent Damascene reflow process, the Q can be increased further by 10 times [117]; 2. Increasing the mechanical Q ( $\sim 10\times$ ) by eliminating the Si HBAR modes through roughing the backside surface of Si substrate; 3. Increasing optomechanical coupling rate  $g_0$  by further shrinking the mode volume  $V$  (by  $\sim 100\times$ ) using THz  $\text{Si}_3\text{N}_4$  microring (22  $\mu\text{m}$  radius).  $g_0$  will increase by 10 times as it is proportional to  $1/\sqrt{V}$ ; 4. Increasing the intra-cavity pump photon number  $n_{\text{cav}}$  via triple-cavity scheme [106]. By aligning the pump light with a second optical cavity, the pump efficiency can be boosted by  $\sim 10^4\times$  especially with high optical Q. If these measures can be implemented successfully, we can achieve higher efficiency AOM on  $\text{Si}_3\text{N}_4$  ring resonator, which is not only useful for the converter but also spatiotemporal modulation for nonreciprocal devices in  $\text{Si}_3\text{N}_4$  circuit [169].

#### 4.6 Released HBAR with AlScN actuator

The excitation of released HBAR modes by an actuator made from Sc doped AlN (AlScN) is studied here as shown in Fig. 4.14. A 500-nm AlScN thin film is sandwiched between top and bottom electrodes made of Pt. The Si beneath the actuators is isotropically etched to form a freestanding oxide membrane that is 4  $\mu\text{m}$  thick. The electromechanical  $S_{11}$  of one of the actuator is measured as shown in Fig. 4.14(c), from where three oxide HBAR modes can be found around 5 GHz. The largest resonance is at 5.05 GHz with linewidth of 6.75 MHz and mechanical Q of 750. To extract the electromechanical coupling efficiency  $k_{\text{t,eff}}^2$ , the admittance  $Y_{11}$  is calculated from the  $S_{11}$  as shown in Fig. 4.14(d). The  $k_{\text{t,eff}}^2$  is estimated by fitting the  $Y_{11}$  using the Modified Butterworth-Van Dyke (MBVD) model [170], which is an equivalent circuit model that describes the piezoelectric interaction. From the fitting,  $k_{\text{t,eff}}^2$  is around 0.007%, which is smaller than the AlN actuator measured in the next chapter. One possible reason can be the relatively large signal pad's capacitance divides most of the current. Nonetheless, the excitation of HBAR modes by the AlScN actuator is first demonstrated with frequency as high as 5 GHz and high mechanical Q. More careful



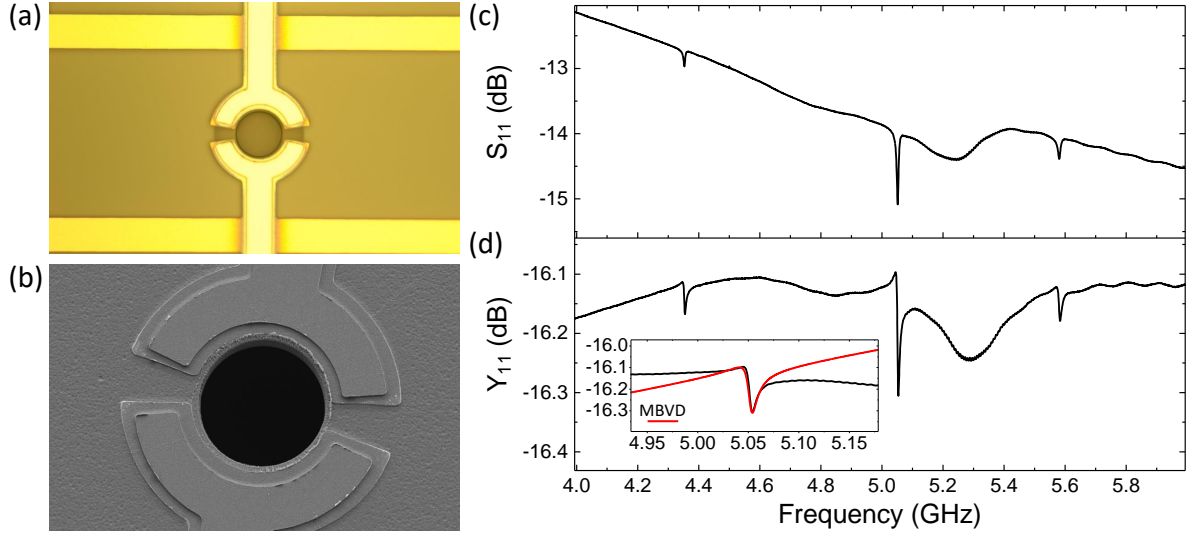


**Figure 4.14.** (a) Optical image of the fabrication released AlScN HBAR actuators. (b) Zoom-in SEM around the two actuators. (c) Electromechanical  $S_{11}$  and (d) admittance  $Y_{11}$  of one actuator. Inset in (d) shows the fitting of  $Y_{11}$  using the Modified Butterworth-Van Dyke model (MBVD, red line).

design and engineering can be done in the future to further increase the electromechanical coupling efficiency.

**Table 4.1.** Comparison of the piezoelectric tuning with different design parameters.

Device	Optical Mode	Tuning (MHz/V)	Mechanical resonance
Edge 1	TE	-50	1.36 MHz
Edge 1	TM	-50	
Edge 2	TE	-15	1.2 MHz
Edge 2	TM	-50	
Anchor	TE	-2.5	1.3 MHz
Anchor	TM	-37.5	

## 4.7 Summary

In summary, tuning of the  $\text{Si}_3\text{N}_4$  ring resonator is achieved by integrating AlN piezoelectric actuator on top of a free-standing  $\text{SiO}_2$  membrane that encapsulates the ring resonator. As applying the voltage, the membrane will bend which potentially changes the refractive index by enhanced stress and also the radius of ring by mechanical deformation. It is found

**Table 4.2.** Comparison with the piezoelectric tuning demonstrated in the literature. All the works here are released structure, and the optical waveguide is made from  $\text{Si}_3\text{N}_4$ . The FSR for each optical ring is as labeled.  $V_\pi \cdot L$  has unit of  $\text{V}\cdot\text{cm}$ , and is estimated from the resonance tuning for the microring structure. BW: bandwidth, which is also the frequency of the fundamental mechanical mode.

Ref.	Piezo	Structure	Tuning (MHz/V)	$V_\pi \cdot L$	BW (MHz)	Power
[73]	AlN	MZI		50	120	6 nW
[71]	PZT	Ring (52GHz)	3250	3.6	0.27	3 pW/MHz
[72]	AlN	Ring (1.2THz)	480	16	7.26	20 fW/MHz
This work	AlN	Ring (200GHz)	-50	141	1.3	20 pW/MHz

that the stress-optical effect dominates in all devices. Nevertheless, the tuning efficiency is improved compared with unreleased devices. The tuning shows good linearity up to 100 V for all devices and modes, while the high optical Q is preserved due to thick oxide cladding. While tuning, the leaky current is kept around or below 1 nA (1 nA at 60 V), demonstrating ultra-low power consumption compared with thermal technique. Limited by the mechanical ringing effect due to the first mechanical mode around 1.3 MHz, sub- $\mu\text{s}$  tuning speed is demonstrated experimentally, which can be further increased using advanced techniques, such as preconditioning of input signal and damping of the mechanical oscillation.

The tuning performance of the measured three kinds of devices is summarized in Table 4.1. It can be seen TE shows smaller tuning than TM mode, and TM is less dependent on the relative position of the optical waveguide. The results are further compared with other piezoelectric tuning with released structure in the literature in Table 4.2. Although Ref [71] demonstrated the highest efficiency which mainly relies on the mechanical bending, it suffers from low frequency mechanical resonance. The work in Ref. [72] works at 775 nm and shows the highest tuning efficiency with AlN actuator and the smallest power consumption.

At microwave frequencies, HBAR modes are excited and confined tightly in the  $\text{SiO}_2$  membrane, which increases the efficiency by two orders of magnitude compared with unreleased devices. Maximum 9.2 GHz AOM is achieved which lies in the microwave X-band. With further improvement in the future, the implementation of efficient AOM will bring novel features and functionalities into  $\text{Si}_3\text{N}_4$  photonics. By taking full advantages of  $\text{Si}_3\text{N}_4$ ,

new applications can be foreseen, such as quantum microwave to optical conversion [106],  $\text{Si}_3\text{N}_4$  topological devices [51], and injection locking of the  $\text{Si}_3\text{N}_4$  dissipative Kerr soliton [49].

I finally also demonstrated the first excitation of released HBAR modes with an AlScN actuator. Although the excitation efficiency is not as high as the AlN actuator, HBAR mode at 5 GHz is achieved with mechanical Q as high as 750.

## 5. MAGNETIC-FREE SILICON NITRIDE INTEGRATED OPTICAL ISOLATOR

### 5.1 Background

Integrated photonics [1] has enabled signal synthesis, modulation and conversion using photonic integrated circuits (PIC). Many materials have been developed, among which silicon nitride ( $\text{Si}_3\text{N}_4$ ) has emerged as a leading platform particularly for nonlinear photonics [27], [28]. Low-loss  $\text{Si}_3\text{N}_4$  PIC has been widely used for frequency comb generation [28], [29], narrow-linewidth lasers [5], [7], [171], microwave photonics [172], [173], photonic computing networks [174], [175], and even surface-electrode ion traps [176], [177]. Despite of these advances of  $\text{Si}_3\text{N}_4$  integrated photonics, non-reciprocal devices, such as isolators and circulators that are widely used in optical communications and data centers for signal routing, multiplexing, and protecting lasers from reflections, have not been improved via these developments.

Conventionally, optical non-reciprocity is realized in magneto-optic materials [178] where the Faraday effect induces non-reciprocal polarization rotation under external magnetic field. However, magneto-optic materials are not CMOS-compatible, posing challenges to integrate using standard CMOS techniques developed for silicon photonics. Besides, the magneto-optic effect is weak from the near-infrared to visible wavelength range, therefore requiring a strong external magnetic field applied at microscopic scale. Nevertheless, successful integration of cerium-substituted yttrium iron garnet (Ce:YIG) on PICs (e.g., on Si [179], [180] or  $\text{Si}_3\text{N}_4$  [181]) has been demonstrated via wafer bonding or deposition, though these efforts suffer from significant optical losses and external magnet. In addition, the requirement of large magnetic field bias makes it incompatible with superconducting qubits where optical isolation is needed for blocking reflected noises in optical interfaces for quantum interconnects [182].

To overcome these bottlenecks, magnetic-free schemes have been demonstrated to break Lorentz reciprocity and time reversal symmetry, through synthetic magnetic field [132], [183]–[185], optical nonlinearities [186]–[192], optomechanically induced transparency [193]–[196], and stimulated Brillouin scattering (SBS) [197]–[201]. In addition, optical non-reciprocity has also been demonstrated in atomic systems [202]–[204]. However, challenges remain in

all these approaches. For example, optomechanically induced non-reciprocity requires air-cladded, isolated microtoroids or microspheres that are difficult to integrate with PICs. In addition, the isolation bandwidth is primarily limited by the mechanical resonance linewidth that is typically within kilohertz to megahertz range. Separating the signal from the control pump laser using common multiplexing schemes is a formidable challenge, as they are spaced by the mechanical resonance that is below hundred megahertz. While nonlinear optics can work passively without active modulation, the main concern is the dynamic reciprocity that forbids light propagation in both directions with limited dynamic range of input optical power [205].

Spatio-temporal modulation [51], [92], [131], [206]–[209], which breaks reciprocity by coupling two optical modes and prescribing phase matching condition by active modulation, stands out in terms of integration and applicability on nearly all optical materials. Recently, schemes based on acousto-optic modulation (AOM) has been extensively developed due to their compatibility with low-loss PICs (e.g., AlN [131] and Si [92]). Thus far, only non-reciprocal sideband modulation is achieved, limited by the modulation efficiency and power handling capability of the interdigital transducers (IDT) for generating surface acoustic waves (SAW). In this chapter, I demonstrate the first AOM-based optical isolator for Si<sub>3</sub>N<sub>4</sub> integrated photonics. Three AlN piezoelectric actuators are equidistantly placed along a Si<sub>3</sub>N<sub>4</sub> microring resonator, and generate high-overtone bulk acoustic resonances (HBAR) [12] to create an effective rotating acoustic wave that couples two optical modes in the momentum-biased direction.

## 5.2 Design of the integrated optical isolator

### 5.2.1 Working principle and design

Our integrated optical isolator consists of three AlN piezoelectric actuators on top of a Si<sub>3</sub>N<sub>4</sub> microring resonator, as shown in Fig. 5.1(a). The Si<sub>3</sub>N<sub>4</sub> PIC (blue) fully cladded with silicon dioxide (SiO<sub>2</sub>) was fabricated using the photonic Damascene process [24], followed by monolithic integration of AlN actuators [12], [121]. The AlN thin film (green) with a piezoelectric coefficient of  $d_{33} = 3.9 \text{ pm V}^{-1}$  is sandwiched between top aluminum (Al, yellow) and

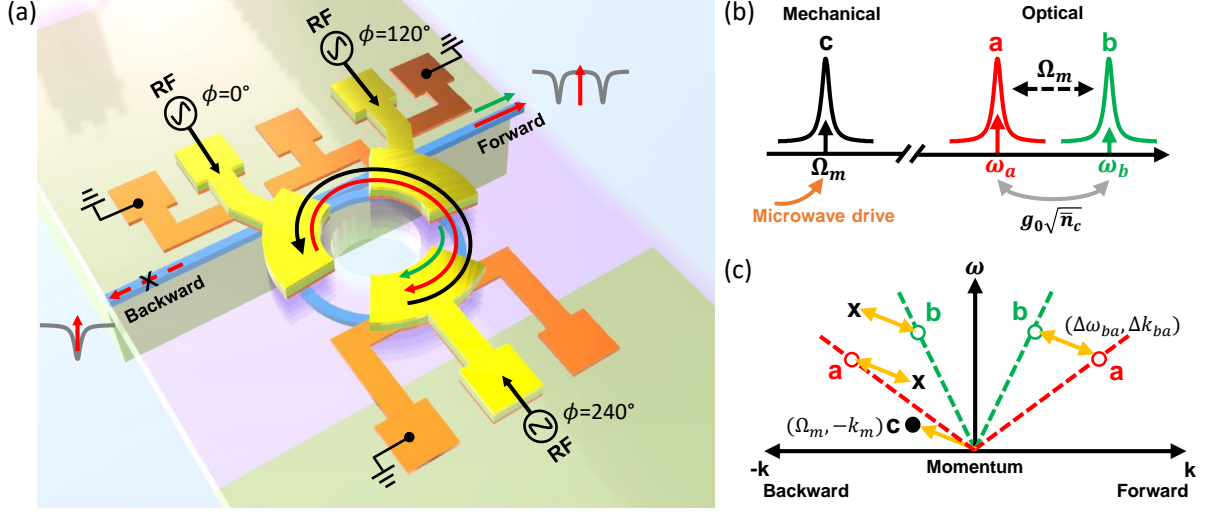


**Figure 5.1.** (a) Schematic and device rendering. Three discrete AlN piezoelectric actuators are equidistantly integrated on top of a Si<sub>3</sub>N<sub>4</sub> microring resonator (blue solid). Upon coherent driving these actuators with fixed relative phases  $(\phi_1, \phi_2, \phi_3) = (0^\circ, 120^\circ, 240^\circ)$ , a rotating acoustic wave (black arrow) is generated that spatio-temporally modulates the two co-propagating optical modes (red and green arrows), leading to indirect interband transition in only one direction where the phase matching condition is fulfilled. (b) Frequency domain representation illustrating the indirect interband transition. When the two optical modes,  $a$  and  $b$ , are spaced by the resonant frequency  $\Omega_m$  of the mechanical mode  $c$ , scattering among modes  $a$  and  $b$  happens with a scattering rate of  $g = g_0\sqrt{n_c}$  under a microwave drive at  $\Omega_m$ . (c) Schematic of  $\omega - k$  space showing the energy ( $\Delta\omega_{ba} = \Omega_m$ ) and momentum ( $\Delta k_{ba} = -k_m$ ) conservations. Interband transition that couples the two optical modes with the acoustic wave is only allowed in the direction where phase matching condition is fulfilled, giving rise to transparency on resonance in this direction (“forward”, as shown in **a**) and extinction in the other direction (“backward”). Reprinted from Ref. [169].

bottom molybdenum (Mo, orange) electrodes. When the electrodes are microwave-driven, bulk acoustic waves are formed vertically in the substrate (i.e. the HBAR mode) beneath the actuators. The Si substrate is removed to create a suspended SiO<sub>2</sub> membrane, which enables tight confinement of HBAR modes inside the Fabry-Pérot acoustic cavity formed by the top and bottom SiO<sub>2</sub>-air surfaces, and thus enhances the acousto-optic coupling through stress-optic effect [12].

The  $\text{Si}_3\text{N}_4$  microresonator is designed to support two optical eigenmodes,  $a$  and  $b$ , with frequency difference matching a mechanical/acoustic resonant frequency, as shown in Fig. 5.1(b). The design of the optical waveguide can be found in Appendix B. The microwave drives applied on the three AlN actuators create acoustic waves inside the mechanical cavity, which scatter light between modes  $a$  and  $b$  (i.e. indirect interband transition). Figure 5.1(c) illustrates the  $\omega-k$  space, where  $k = 2\pi/\lambda$  is wavenumber (the photon/phonon momentum is  $\hbar k$ , with the sign denoting the rotating direction along the microring, clockwise or counter-clockwise), and  $\omega$  is the angular frequency. To induce interband transition, energy and momentum conservations must be satisfied, known as the “phase matching condition”. With a nonzero phonon momentum  $k_m$ , phase matching requires  $\Delta\omega_{ba} = \omega_b - \omega_a = \Omega_m$  and  $\Delta k_{ba} = k_b - k_a = -k_m$ , where the minus sign of  $k_m$  indicates that the acoustic wave counter-propagates with the two co-propagating optical modes, as illustrated in Fig. 5.1(a). We denote this direction, where phase matching condition is fulfilled, as the “forward” direction in the following discussion.

While a single vertical HBAR mode from one AlN actuator carries zero in-plane momentum, an effective acoustic wave rotating along the microring is generated by driving three actuators coherently with phases of  $(0^\circ, 120^\circ, 240^\circ)$ , i.e.  $120^\circ$  phase difference between two adjacent actuators, as illustrated in Fig. 5.1(a). In the forward direction, the two optical modes can be coupled strongly and show Rabi mode splitting and transparency at the center. However, in the backward direction, the transmission will show a single resonance. If we work at critical coupling, most input light will sink into the resonator without transmission, as shown in Fig. 5.1(a). Next, the transmission in the forward and backward directions will be analyzed by the analytical Coupled Mode Theory (CMT).

### 5.2.2 Theoretical analysis via the coupled mode theory

In the forward direction, the two optical modes are coupled via the rotating acoustic wave, which can be quantum mechanically described by a three-wave mixing (two optical modes  $a$  and  $b$  and one mechanical mode  $c$ ) process, as shown in Fig. 5.2. The external

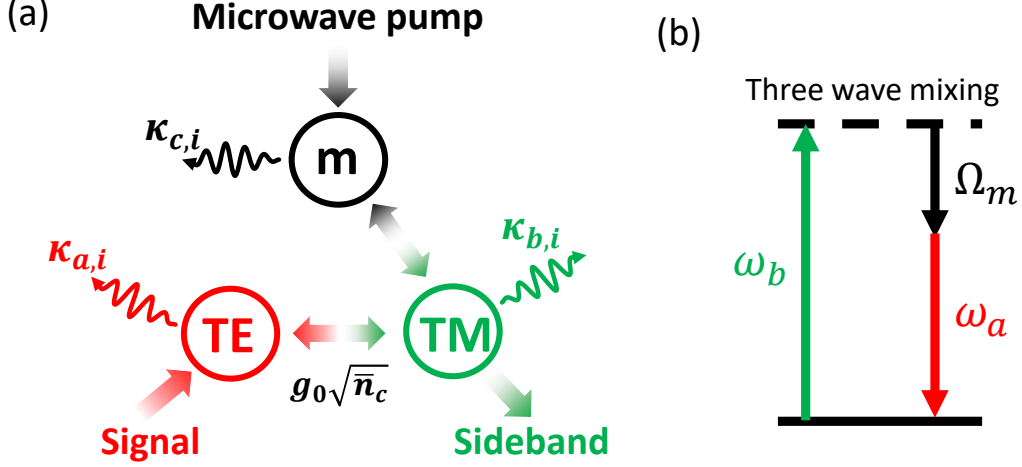


**Figure 5.2.** (a) Schematic for the coupling between the two optical modes and the mechanical mode. The system is pumped by the external microwave drive which couples strongly the two optical modes. (b) Energy level for the three wave mixing process. The microwave stimulates the energy exchange between the two optical modes.  $\kappa_{a,i}$ ,  $\kappa_{b,i}$ , and  $\kappa_{c,i}$  are the intrinsic losses for the two optical modes and the mechanical mode.

microwave pump assists the coupling and energy exchange between the two optical modes. The quantum interaction Hamiltonian of the system is:

$$H_I = \hbar g_0 (\hat{a} \hat{b}^\dagger \hat{c} + \hat{a}^\dagger \hat{b} \hat{c}^\dagger) \quad (5.1)$$

assuming that phase matching is fulfilled and  $\hat{a}$  has a smaller frequency than  $\hat{b}$ . Under these conditions, the optomechanical interaction can be understood as the combination of two processes: 1.  $\hat{a} \hat{b}^\dagger \hat{c}$ , annihilation of a photon  $\hat{a}$  and a phonon  $\hat{c}$  and generation of one higher-frequency photon  $\hat{b}$ ; 2.  $\hat{a}^\dagger \hat{b} \hat{c}^\dagger$ , annihilation of one photon  $\hat{b}$  and generation of a photon  $\hat{a}$  and a phonon  $\hat{c}$ . Following an approach similar to Ref. [106], the equations of motion for the



annihilation operators can be obtained by assuming resolved sidebands and rotating-wave approximation:

$$\frac{d}{dt}\hat{a} = -(\mathrm{i}\Delta_a + \frac{\kappa_a}{2})\hat{a} - \mathrm{i}g_0\hat{b}\hat{c}^\dagger + \sqrt{\kappa_{a,\mathrm{ex}}}\hat{a}_{\mathrm{in}} \quad (5.2)$$

$$\frac{d}{dt}\hat{b} = -(\mathrm{i}\Delta_b + \frac{\kappa_b}{2})\hat{b} - \mathrm{i}g_0\hat{a}\hat{c} \quad (5.3)$$

$$\frac{d}{dt}\hat{c} = -(\mathrm{i}\Omega_m + \frac{\Gamma_c}{2})\hat{c} - \mathrm{i}g_0\hat{a}^\dagger\hat{b} + \sqrt{\Gamma_{c,\mathrm{ex}}}\hat{c}_{\mathrm{in}}e^{-\mathrm{i}\Omega_d t} \quad (5.4)$$

$$\hat{a}_{\mathrm{out}} = \hat{a}_{\mathrm{in}} - \sqrt{\kappa_{a,\mathrm{ex}}}\hat{a} \quad (5.5)$$

$$\hat{b}_{\mathrm{out}} = -\sqrt{\kappa_{b,\mathrm{ex}}}\hat{b} \quad (5.6)$$

where  $\hat{a}$ ,  $\hat{b}$ , and  $\hat{c}$  are the intra-cavity amplitude of mode  $a$ ,  $b$ , and  $c$ . They normalized such that their square is the intra-cavity photon and phonon numbers.  $\kappa_a$  ( $\kappa_b$ ) are the total loss rate of mode  $a$  ( $b$ ), and  $\kappa_{a,\mathrm{ex}}$  and  $\kappa_{b,\mathrm{ex}}$  are the external coupling rate of each mode.  $g_0$  is the single photon-phonon coupling rate describing the optomechanical interaction strength. These equations of motion are transformed under the rotating-wave approximation (RWA) referenced to the input laser frequency  $\omega_L/2\pi$ , thus  $\Delta_a = \omega_a - \omega_L$  ( $\Delta_b = \omega_b - \omega_L$ ) is the relative detuning between the laser frequency and the optical resonant frequency of  $a$  ( $b$ ).  $\Omega_d/2\pi$  is the microwave drive frequency that can be slightly detuned from the mechanical resonant frequency  $\Omega_m/2\pi$ . Mode  $a$  is probed by the input light with amplitude  $\hat{a}_{\mathrm{in}}$ , and its optical transmission/isolation is studied in the following analysis.

$\Gamma_c/2\pi$  and  $\Gamma_{c,\mathrm{ex}}/2\pi$  are the total loss rate (11 MHz) of the mechanical mode and the external coupling rate (22 kHz) from the microwave line to the HBAR phonons, and  $\|\hat{c}_{\mathrm{in}}\| = \sqrt{P_{\mathrm{in}}/\hbar\Omega_d}$  is the input microwave amplitude [168]. Assuming that the optomechanical coupling (term  $g_0\hat{a}^\dagger\hat{b}$  in Eq. 5.4) has a much smaller contribution than the microwave drive, the mean intra-cavity amplitude of  $\bar{c}$  at steady state is:

$$\bar{c} = \sqrt{\bar{n}_c}e^{-\mathrm{i}\Omega_d t} \quad (5.7)$$

$$\bar{n}_c = \frac{\Gamma_{c,\mathrm{ex}}}{(\Omega_d - \Omega_m)^2 + \Gamma_c^2/4} \frac{P_{\mathrm{in}}}{\hbar\Omega_d} \quad (5.8)$$

By inserting Eq. 5.7 into Eqs. 5.2 and 5.3, we can obtain the simplified Coupled Mode Theory (CMT) equations:

$$\frac{d}{dt}\hat{a} = -(\mathrm{i}\Delta_a + \frac{\kappa_a}{2})\hat{a} - \mathrm{i}g\hat{b}e^{\mathrm{i}\Omega_d t} + \sqrt{\kappa_{a,\mathrm{ex}}}\hat{a}_{\mathrm{in}} \quad (5.9)$$

$$\frac{d}{dt}\hat{b} = -(\mathrm{i}\Delta_b + \frac{\kappa_b}{2})\hat{b} - \mathrm{i}g\hat{a}e^{-\mathrm{i}\Omega_d t} \quad (5.10)$$

where  $g = g_0\sqrt{\bar{n}_c}$  describes the scattering rate between the two optical modes. Due to the modulation, the frequency of mode  $\hat{b}$  is shifted by  $\Omega_d$  in the rotating frame of  $\omega_L$ . The slow amplitude and fast oscillation of mode  $\hat{b}$  can be separated by substituting  $\hat{b}$  with  $\tilde{b}e^{-\mathrm{i}\Omega_d t}$ .

At the steady state, Eqs. 5.9 and 5.10 can be solved by setting time derivatives to zero, and after some linear algebra [106] we obtain the general expressions for transmission  $T$  and sideband conversion efficiency  $\eta$ :

$$T = \left\| \frac{\hat{a}_{\mathrm{out}}}{\hat{a}_{\mathrm{in}}} \right\|^2 = \left\| 1 - \frac{\kappa_{a,\mathrm{ex}}}{\mathrm{i}\Delta_a + \frac{\kappa_a}{2} + \frac{g^2}{\mathrm{i}(\Delta_b - \Omega_d) + \frac{\kappa_b}{2}}} \right\|^2 \quad (5.11)$$

$$\eta = \left\| \frac{\hat{b}_{\mathrm{out}}}{\hat{a}_{\mathrm{in}}} \right\|^2 = \frac{\kappa_{a,\mathrm{ex}}}{\kappa_a} \frac{\kappa_{b,\mathrm{ex}}}{\kappa_b} \frac{4C}{\|C + (1 + \frac{2\mathrm{i}\Delta_a}{\kappa_a})(1 + \frac{2\mathrm{i}(\Delta_b - \Omega_d)}{\kappa_b})\|^2} \quad (5.12)$$

where  $\Delta_b - \Omega_d = \Delta_{ba} + \Delta_a - \Omega_d$ .  $C = 4g^2/\kappa_a\kappa_b$  is the optical-to-optical cooperativity, which measures the ratio of scattering rate to optical losses. It can be seen that at the optical resonance of mode  $a$  when  $\Delta_a = 0$  and  $\Delta_{ba} = \Omega_d$ , Eqs. 5.11 and 5.12 can be reduced to:

$$T = \left\| \frac{\hat{a}_{\mathrm{out}}}{\hat{a}_{\mathrm{in}}} \right\|_{\Delta_a=0}^2 = \left[ 1 - \frac{2\kappa_{a,\mathrm{ex}}}{\kappa_a(1+C)} \right]^2 \quad (5.13)$$

$$\eta = \left\| \frac{\hat{b}_{\mathrm{out}}}{\hat{a}_{\mathrm{in}}} \right\|_{\Delta_a=0}^2 = \frac{\kappa_{a,\mathrm{ex}}}{\kappa_a} \frac{\kappa_{b,\mathrm{ex}}}{\kappa_b} \frac{4C}{(1+C)^2} \quad (5.14)$$

In the forward direction, due to the efficient mode coupling, the scatter rate is much larger than the optical losses  $g \gg \kappa_{a,b}$ , such that  $C \gg 1$ . From Eq. 5.13, it can be seen  $T \rightarrow 1$ . This transparency can be understood intuitively as the impedance mismatch between the bus waveguide and the microresonator, resulted from the increasing effective intrinsic loss

due to the scattering to the other optical mode  $b$ . In the backward direction where the three-wave phase matching is not fulfilled, interband transition is prohibited, leading to  $C \approx 0$  and  $T = 0$  in the critical coupling regime ( $\kappa_{a,\text{ex}} = \kappa_{a,\text{i}}$ ). Consequently, the microresonator remains critically coupled and its light transmission is not affected by the presence of the acoustic wave. This non-reciprocal transmission between the forward ( $T = 1$ ) and backward directions ( $T = 0$ ) is the basic of our optical isolator.

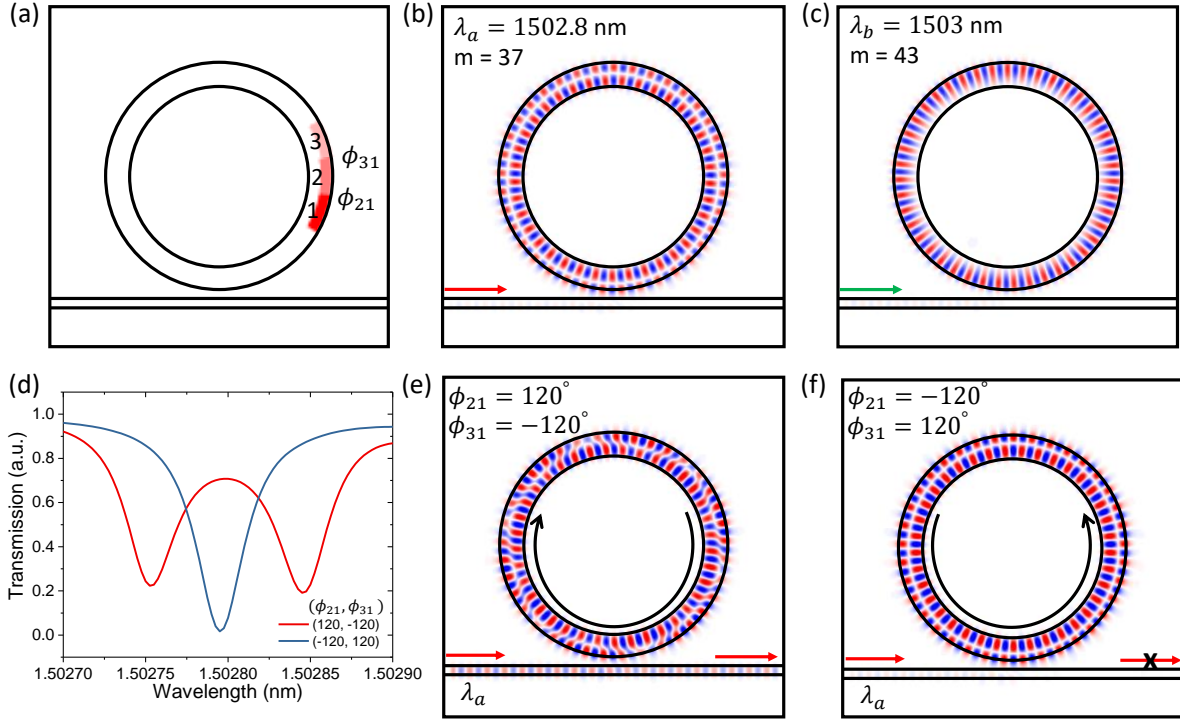


**Figure 5.3.** (a) 2D Schematic of the simulated optical ring resonator. The refractive index of three regions are modulated as labeled by the red area. The relative phases of the modulation between the adjacent area can be controlled in the simulation. Electric field ( $E_z$ , out of plane) distribution of (b) optical mode  $a$  and (c) mode  $b$ .  $m$  is the azimuthal order for each mode. (d) Optical transmission of mode  $a$  in the forward (red) and backward (blue) directions. Electric field ( $E_z$ , out of plane) distribution under reversed phases: (e)  $(\phi_{21}, \phi_{31}) = (120^\circ, -120^\circ)$  (perfect phase matching) and (f)  $(\phi_{21}, \phi_{31}) = (-120^\circ, 120^\circ)$  (largest phase mismatch). The input light wavelength is at the resonant wavelength of mode  $a$  ( $\lambda_a = 1502.8$  nm). As we change the rotation direction of the modulation wave, the light changes from (e) transmission to (f) isolation. Reprinted from Ref. [169].

### 5.2.3 Numerical simulation of the spatio-temporal modulation

The numerical simulation is conducted through a Finite Difference Frequency Domain (FDFD) algorithm developed by Y. Shi *et al.* in Ref. [210], [211]. As the optical microresonator used in the experiment is relatively large (118  $\mu\text{m}$  radius) which is time-consuming to simulate, a much smaller optical microring (3  $\mu\text{m}$  radius) is simulated following the same setting as Ref. [51], as shown in Fig. 5.3(a). Three regions are modulated with fixed relative phases to generate an effective in-plane modulation wave. The phases between them are studied in the simulation. Two optical modes are identified and the mode distribution of them are shown in Fig. 5.3(b-c). In the simulation, mode  $a$  is pumped and mode  $b$  is the generated sideband. Based on the relative position of the two optical modes in the  $\omega - k$  space (see Fig. 5.1(c)), a modulation wave that counter-propagates with the direction of the light is needed for the phase matching. This corresponds to an optimal modulation phases of  $(\phi_{21}, \phi_{31}) = (120^\circ, -120^\circ)$ .

With the optimal phases, mode  $a$  shows mode splitting and a transparent window opens at the center wavelength as shown in Fig. 5.3(d). However, if we reverse the modulation wave's direction by reversing the sign of the phases, mode  $a$  remains as single resonance as the two optical modes are not coupled efficiently. Note that in the simulation the input light direction is fixed while reversing the modulation direction, and this is equivalent to reversing the light direction with fixed modulation direction in practical application. The electric field distributions in the phase matching and phase mis-matching cases are shown in Fig. 5.3(e-f) with input light at the resonance of mode  $a$ . Under phase matching in Fig. 5.3(e), the light transmits through the bus waveguide, and the electric field in the optical microring is a mixture of modes  $a$  and  $b$  due to the mode coupling. If the modulation wave's direction is reversed in Fig. 5.3(f), the light is absorbed in the optical microring and the electric field shows the original distribution of mode  $a$ , indicating that no mode coupling is induced.

The phase  $(\phi_{21}, \phi_{31})$  are swept in the simulation, and the 2D plots of the spectra of the transmission of mode  $a$  and the conversion of mode  $b$  are shown in Fig. 5.4. It can be seen as the phase is close to the optimal phase matching, the mode splitting increases. However, for the reversed phases, single resonance is remained and the conversion to mode  $b$  is small. This

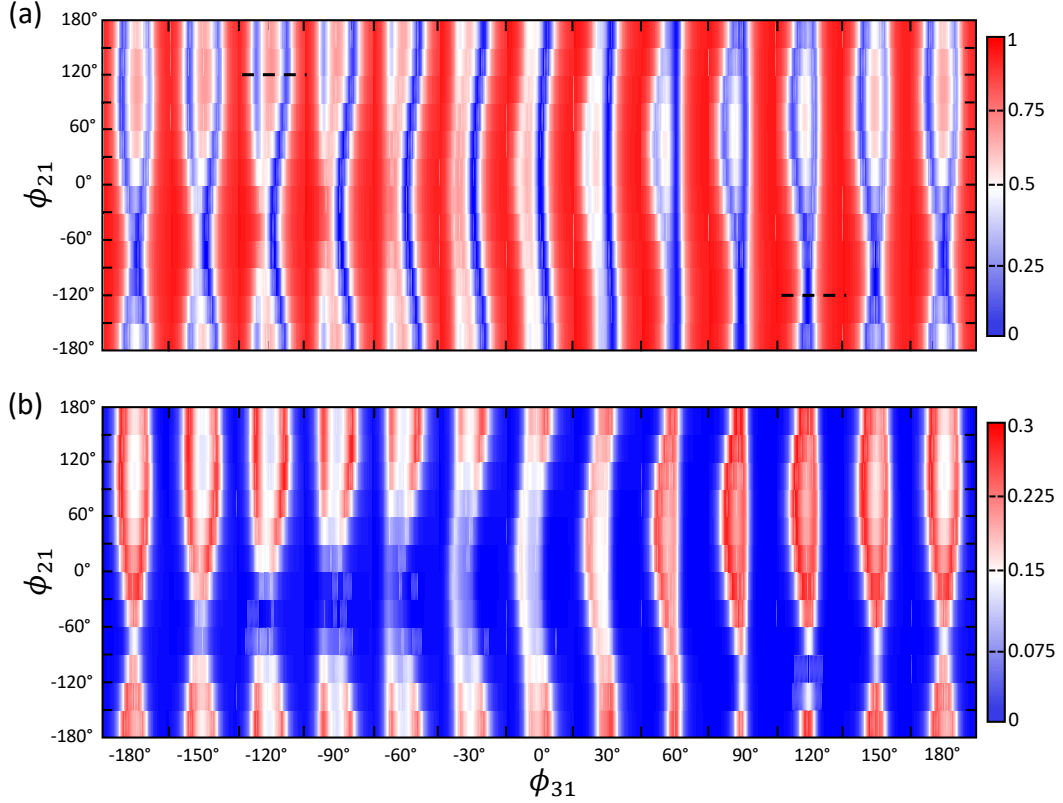


**Figure 5.4.** (a) Transmission spectra of mode *a* and (b) converted sideband in mode *b* under 2D sweep of the relative phase  $\phi_{21}$  and  $\phi_{31}$ . Each column corresponds to the spectrum under the same phase  $\phi_{31}$  and has a spectra span of (1.5027 nm, 1.5031nm). The spectra in Fig. 5.3(d) are the slices as labeled by the black dashed lines in (a). Reprinted from Ref. [169].

demonstrates the breaking of the spatial reciprocity. As can be seen later, the simulation explains very well the experimental data where detailed analysis will be given.

#### 5.2.4 Device fabrication and characterization

Figure 5.5(a) shows the false-colored, top-view scanning electron microscope (SEM) image of the fabricated device with three AlN actuators integrated on a released  $\text{Si}_3\text{N}_4$  microring resonator. The thickness of Al/AlN/ Mo is 100/1000/100 nm, respectively. The center hole is opened for Si-isotropic dry etching using a sulfur hexafluoride ( $\text{SF}_6$ ) Bosch process, to partially remove the Si substrate and to suspend the 5.4- $\mu\text{m}$ -thick  $\text{SiO}_2$  cladding. Figure 5.5(b) shows the optical microscope image highlighting the bus waveguide coupling region,

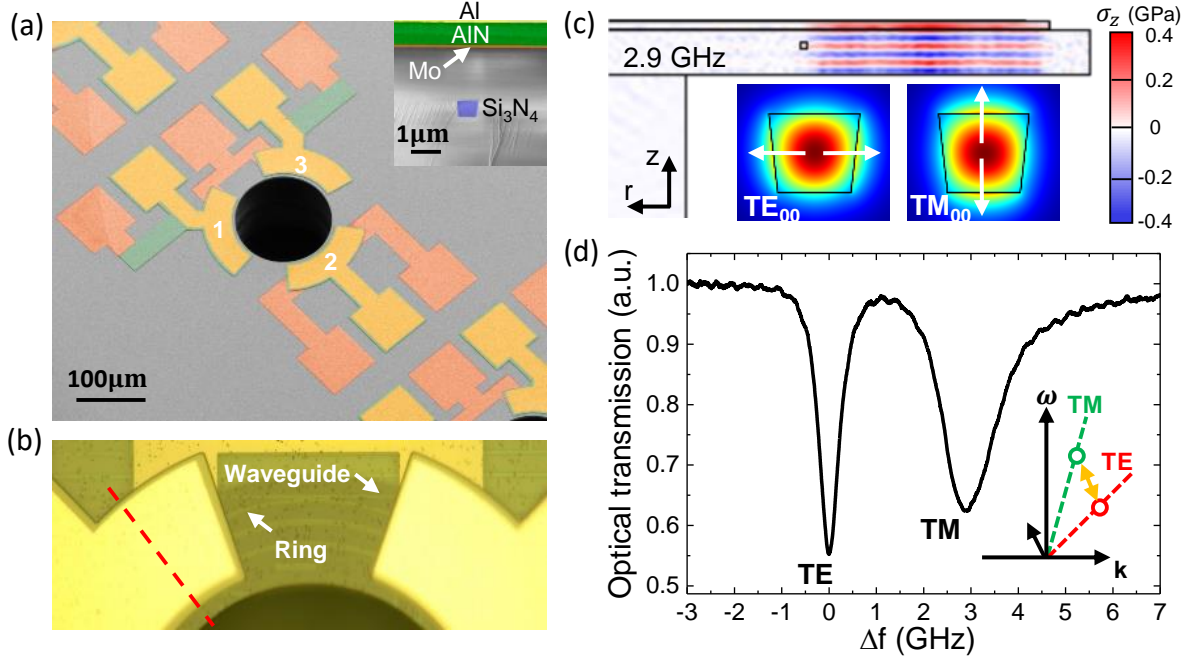


**Figure 5.5.** (a) False-colored top-view SEM image of the fabricated device. Inset: False-colored SEM image of the sample cross-section, showing the vertical structure of the piezoelectric actuator and quasi-square  $\text{Si}_3\text{N}_4$  photonic waveguide. (b) Optical microscope image highlighting the bus-microring coupling section, the released  $\text{SiO}_2$  area, and the relative positions of  $\text{Si}_3\text{N}_4$  waveguides (blue line) and two AlN actuators. (c) FEM numerical simulations of the vertical stress  $\sigma_z$  distribution of a typical HBAR mode at 2.9 GHz, which is conducted along the cross-section indicated by the red dashed line in (b). Insets: the optical profiles of the  $\text{TE}_{00}$  and  $\text{TM}_{00}$  modes of the quasi-square  $\text{Si}_3\text{N}_4$  waveguide. White arrows mark the optical polarization directions. (d) Optical transmission spectrum showing a pair of  $\text{TE}_{00}$  and  $\text{TM}_{00}$  modes with around 3 GHz frequency spacing. The x-axis is frequency-calibrated relative to the center frequency of the  $\text{TE}_{00}$  mode around 1546 nm. Inset shows the relative position of the two modes in the  $\omega - k$  space. Reprinted from Ref. [169].

the  $\text{Si}_3\text{N}_4$  microring with 118  $\mu\text{m}$  radius buried in the suspended  $\text{SiO}_2$  membrane, and two AlN actuators. Figure 5.5(c) shows the simulated stress distribution of one HBAR mode within the  $\text{SiO}_2$  membrane using Finite Element Method (FEM). It can be seen that the HBAR mode is uniformly distributed under the AlN actuator and tightly confined in the  $\text{SiO}_2$  membrane, allowing direct modulation of the optical mode propagating along the waveguide through photoelastic and moving boundary effects [212].

From the microring's resonant condition  $k = 2\pi/\lambda = m/r$ , the momentum is related to the azimuthal order  $m$  of the mode and the microring's radius  $r$ . As the three actuators cover the entire microring, the generated rotating acoustic wave has an effective wavelength of  $2\pi r$ , and thus the azimuthal order is  $m_c = 1$ . Therefore the phase matching condition requires the azimuthal order difference  $\Delta m_{ab} = m_a - m_b = m_c = 1$  between the  $\text{TE}_{00}$  and  $\text{TM}_{00}$  modes. As the  $\text{Si}_3\text{N}_4$  waveguide is fully cladded with  $\text{SiO}_2$ , a quasi-square waveguide cross-section ( $810 \times 820 \text{ nm}^2$ ), as shown in Fig. 5.5(a) inset, is designed to have slightly different effective refractive indices for the two optical modes (see Appendix B). Figure 5.5(c) shows the simulated  $\text{TE}_{00}$  and  $\text{TM}_{00}$  mode profiles, which also include the slanted waveguide sidewall. The transmission of polarization-tilted light through the optical microresonator, including a pair of  $\text{TE}_{00}$  and  $\text{TM}_{00}$  resonances, is shown in Fig. 5.5(d). The  $\text{TM}_{00}$  mode frequency is 3 GHz higher than that of the  $\text{TE}_{00}$  mode at around 1546 nm wavelength. The resonance linewidth (total loss  $\kappa_{a,b}/2\pi$ ) is 0.68 and 1.16 GHz for the  $\text{TE}_{00}$  and  $\text{TM}_{00}$  mode, respectively.

Figure 5.6 shows the microwave reflection  $S_{11}$ , where mechanical resonances are revealed. Only one actuator's  $S_{11}$  is shown as the others are similar. Three strong resonances are found around 3.0, 3.4 and 3.8 GHz, which are due to the  $\text{SiO}_2$  mechanical cavity with  $\sim 470$  MHz free spectral range (FSR, determined by the  $\text{SiO}_2$  cladding thickness). Besides, weak resonances with an FSR of  $\sim 19$  MHz are observed, due to the HBARs in thick Si substrate formed under square signal probe pads which were not undercut [12]. The  $\text{SiO}_2$  HBAR at 2.958 GHz is used in the following experiments to match the optical mode spacing at 3 GHz.

The HBAR can be analyzed using the well-known Modified Butterworth-Van Dyke model (MBVD) [170], which describes the HBAR resonance by an equivalent  $RLC$  circuit as shown in Fig. 5.7(a).  $L_m$  and  $C_m$  are motional inductance and capacitance which present kinetic and potential energy of the mechanical resonance, while the motional resistance  $R_m$  accounts for the intrinsic mechanical loss [168]. The mechanical  $R_m L_m C_m$  branch is parallel to a capacitance  $C_0$  that is the physical capacitance formed by the top and bottom electrodes

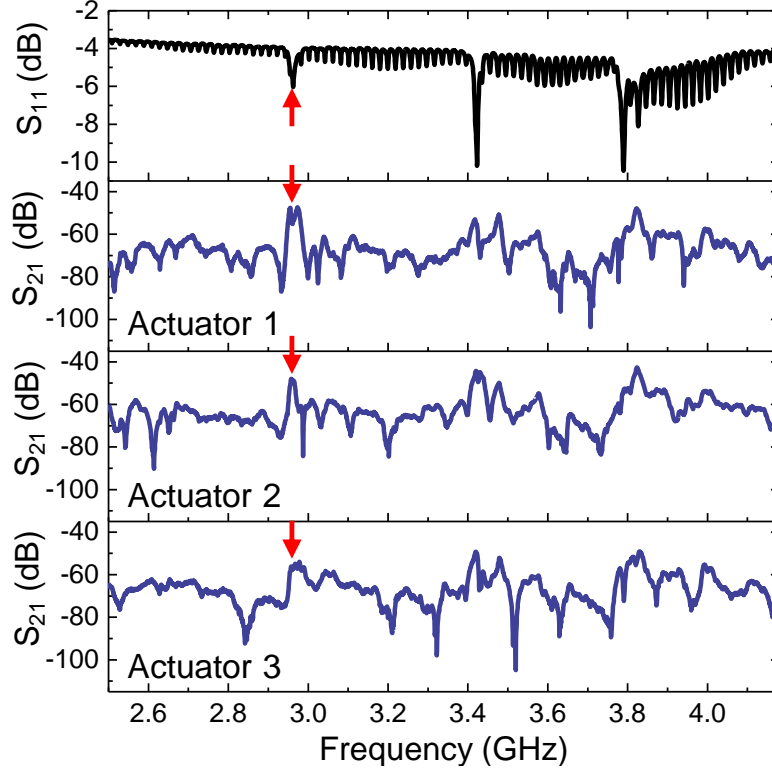


**Figure 5.6.** From top to bottom are microwave reflection  $S_{11}$ , and optomechanical response  $S_{21}$  of the actuator 1, 2, 3 (labeled in Fig. 5.5(a)), respectively. Red arrow marks the mechanical mode at 2.958 GHz that is used in the experiment. Reprinted from Ref. [169].

of our piezoelectric actuator.  $R_0$  is the capacitor loss and  $R_s$  is the series resistance. The admittance looking into the entire circuit can be calculated as [170]:

$$Y(\omega) = j\omega C_0 \frac{1 - (\frac{\omega}{\omega_p})^2 + j(\frac{\omega}{\omega_p})\frac{1}{Q_{p0}}}{1 - (\frac{\omega}{\omega_s})^2 + j(\frac{\omega}{\omega_s})\frac{1}{Q_{s0}}} \quad (5.15)$$

where  $\omega_s = 1/\sqrt{L_m C_m}$  is the series resonance of the  $R_m L_m C_m$  branch, which is also the mechanical resonance.  $\omega_p$  is the so-called parallel resonance, which is related with  $\omega_s$  by :

$$\left(\frac{\omega_p}{\omega_s}\right)^2 = 1 + \frac{C_m}{C_0} \quad (5.16)$$



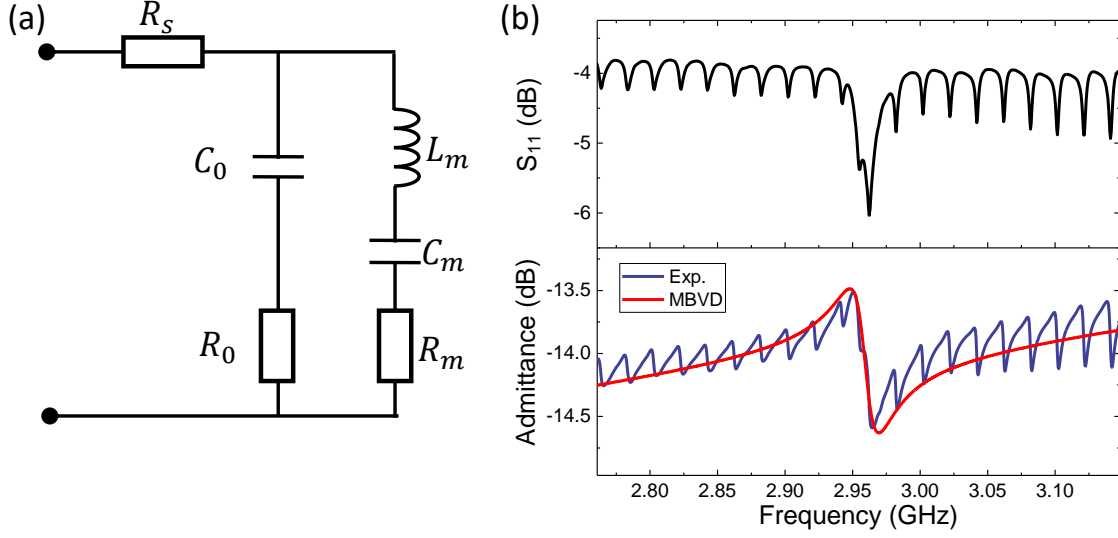


**Figure 5.7.** (a) Schematic of equivalent electrical circuit model representing one HBAR mode. (b) Upper panel: electro-mechanical  $S_{11}$  around the HBAR mode used in the experiment in the main text. Lower panel: Calculated admittance (blue) and MBVD fitting (red). Reprinted from Ref. [169].

$Q_{s0}$  and  $Q_{p0}$  are the  $Q$ s of each resonance:

$$\frac{1}{Q_{s0}} = \omega_s(R_m + R_s)C_m \quad (5.17)$$

$$\frac{1}{Q_{p0}} = \omega_p(R_0 + R_m)C_m \quad (5.18)$$

The  $S_{11}$  of the HBAR mode at 2.958 GHz is shown in Fig. 5.7(b), from which the admittance can be calculated as:

$$S_{11} = \frac{Z - Z_0}{Z + Z_0} \quad (5.19)$$

where  $Z_0$  is the impedance of the RF cable which is  $50 \, \Omega$ , and  $Z = 1/Y$  is the impedance of the device. The admittance obtained from the  $S_{11}$  measurement is then fitted using Eq. 5.15 as shown in Fig. 5.7(b). The fitting parameters are summarized in Table 5.1. The electro-mechanical coupling efficiency  $k_{t,\text{eff}}^2$  can be estimated by taking the ratio of capacitance [168]  $k_{t,\text{eff}}^2 = C_m/C_0$  which is around 0.2 % based on the fitting. The mechanical  $Q_m$  can be calculated by  $1/(\omega_m R_m C_m)$  which is 270.

**Table 5.1.** Fitting parameters of the MBVD model of HBAR at 2.958 GHz.

$C_0$	$C_m$	$L_m$	$R_m$	$R_0$	$R_s$	$k_{t,eff}^2$	$\omega_m/2\pi$	$Q_m$
2.137 pF	4.274 fF	0.677 $\mu$ H	46.8 $\Omega$	45 $\Omega$	47 $\Omega$	0.2 %	2.958 GHz	270

Only the HBARs confined in SiO<sub>2</sub> can efficiently modulate the optical mode because the HBARs in the Si substrate have negligible overlap with the Si<sub>3</sub>N<sub>4</sub> waveguide, which can be verified from the optomechanical  $S_{21}$  response shown in Fig. 5.6.  $S_{21}$  measures the ratio between the output light intensity modulation and the microwave drive power. Three actuators are measured individually. Since the HBARs are mainly determined by the thickness of each layer that is highly uniform over the device scale, the HBAR frequencies of the three actuators show only sub-megahertz misalignment. Maximum of  $-45$  dB  $S_{21}$  is achieved, providing 20 dB improvement over a previously reported unreleased Si HBAR AOM [12]. This is due to the significantly reduced mechanical mode volume and tighter HBAR confinement in the released SiO<sub>2</sub> membrane.

Additionally, maintaining small electrical signal cross-talk between adjacent actuators is important for keeping stable relative phases between them. The cross-talk is measured

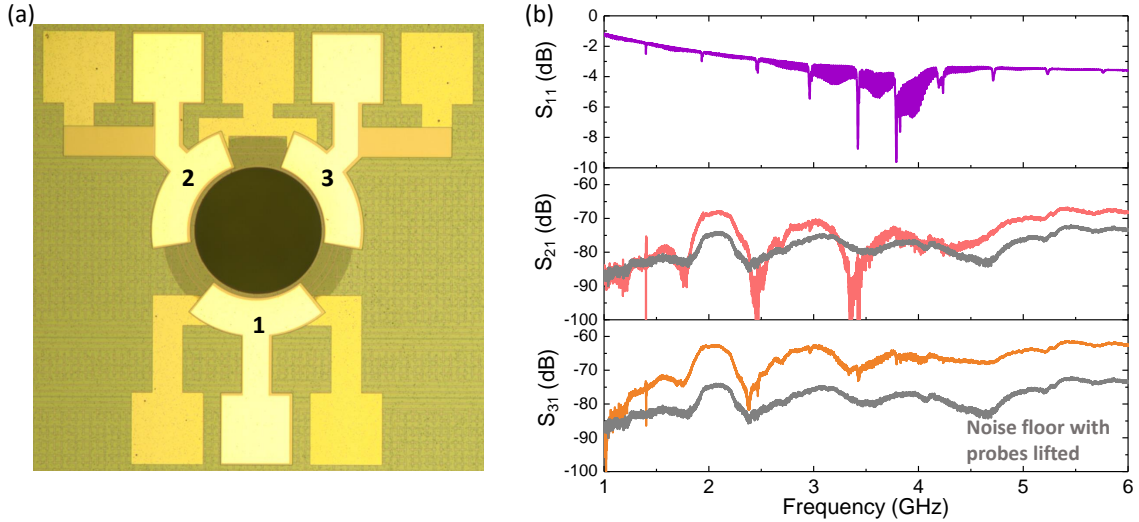


**Figure 5.8.** (a) Optical microscope image of the device. Three actuators are as labeled. (b) Electro-mechanical  $S_{11}$  (purple), electrical cross-talk between actuators 2 and 1  $S_{21}$  (pink), and 3 and 1  $S_{31}$  (yellow). The noise floor with probes lifted (gray) is shown for reference. Reprinted from Ref. [169].

by driving actuator 1 and detecting the output electrical signal from actuators 1 ( $S_{11}$ ), 2 ( $S_{21}$ ), and 3 ( $S_{31}$ ), as shown in Supplementary Fig. 5.8. Due to the rotational symmetry of the device, the cases for driving actuators 2 and 3 individually are similar. From the results, we can see that the cross-talk is well maintained below  $-60$  dB over the measured range of 1 to 6 GHz, which means that the cross-talk from adjacent actuators is 6 orders of magnitude smaller than the signal applied. The low cross-talk mainly comes from the tight acoustic wave confinement and the center release hole that prevents lateral acoustic waves from propagating. The variation of envelope is mainly from the background noise (gray) which is measured by lifting the probes.

### 5.3 Characterization of the on-chip optical isolation

#### 5.3.1 Measurement set-up for the isolator

The experimental setup is shown in Fig. 5.9(a). Three RF signal generators (Agilent E8257D) output RF drives that are amplified by three RF amplifiers (ZHL-5W-63-S+) before going into the device. The relative phases are controlled by their built-in phase controllers after synchronization by their internal 10 MHz clock. The CW laser's wavelength is continuously swept to probe the spectral response around the optical resonance. The input light polarization is controlled by fiber polarization controllers (FPC561). The light input direction is selected by a MEMS (micro-electro-mechanical system)  $2 \times 2$  optical switch (OSW22-1310E). The output TE and TM polarizations are separated by a fiber PBS (PBC1550SM-FC), which is a key reason why we use two modes of different polarizations. They are then measured by two photo-detectors (New Focus 1811) whose signals are recorded by an oscilloscope (MSO8104A). Note that the optical axis of the PBS is fixed, thus a polarization controller is needed to align correctly the TE and TM polarizations with respect to the optical axis of the PBS.

During the measurement, TE polarization is selected by rotating the polarization controller until that only TE mode resonances are observed. This process is repeated for both directions. It is worth noting that, although the polarization will change as we switch the MEMS optical switch, the polarization right before the PBS will be the same, since the

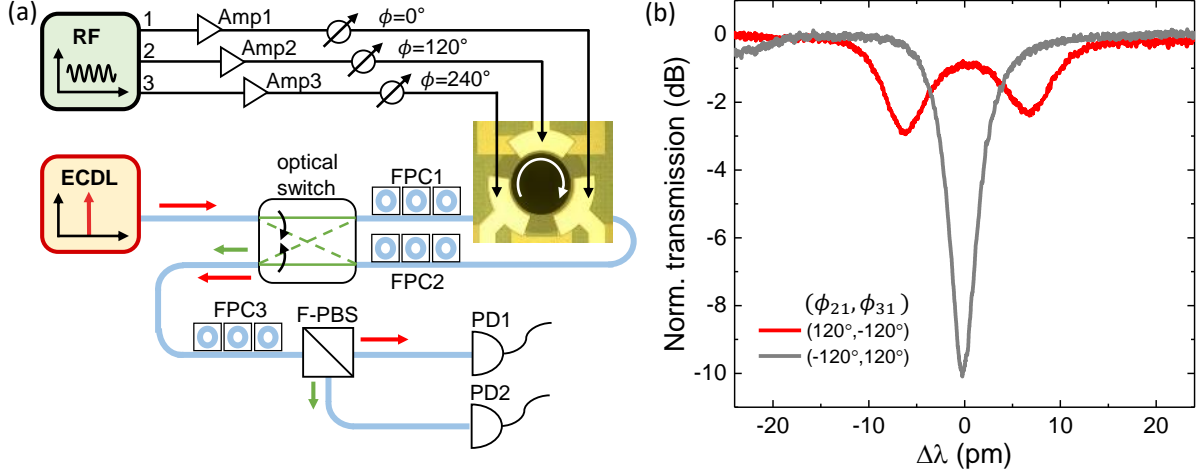


**Figure 5.9.** (a) Experimental setup. Three RF signals are amplified and applied to the AIN actuators with phases controlled individually. An optical switch is used to control the direction of input TE light (red arrows). The output TE light (red arrows) and the generated TM sideband (green arrows) are spatially separated and detected. The white arrow on the device denotes the clockwise rotation of the RF drive in the forward direction. Amp: RF amplifier. ECDL: external-cavity diode laser. FPC: fiber polarization controller. F-PBS: fiber polarization beam splitter. PD: photodetector. (b) Optical transmission spectra with  $(\phi_{21}, \phi_{31}) = (120^\circ, -120^\circ)$  (perfect phase matching, red) and  $(\phi_{21}, \phi_{31}) = (-120^\circ, 120^\circ)$  (largest phase mismatch, gray). Reprinted from Ref. [169].

optical switch itself is a reciprocal device. The RF phases are actively adjusted to compensate the drift of RF phases due to the thermal heating and HBAR resonance shift. The RF phases are calibrated by comparing the transmission spectrum with numerical simulations.

### 5.3.2 Dependency on the RF phases

The RF phases are critical for phase matching. Figure 5.10(a) shows the transmission spectrum of TE light by sweeping the RF phases of signals 2 and 3 relative to signal 1 ( $\phi_{21}$  and  $\phi_{31}$ ), while the output RF power (20 dBm for each actuator) and light input direction are fixed. Each pixel in the 2D plot is the spectrum by sweeping the laser wavelength across the resonance of the TE mode. Example of it is as shown in Fig. 5.9(b). The unit of the x-axis is the relative wavelength detune. The entire column is a stack of different spectrum with different phases of actuator 2 and corresponds to the same phase of actuator 3. Note

that reversing the sign of the RF phases changes the rotation direction of the acoustic wave. Non-reciprocity can be seen from the disparate transmission by reversing the RF phases with respect to the origin  $(0^\circ, 0^\circ)$ . As expected, strong mode splitting is induced under ideal phase setting  $(\phi_{21}, \phi_{31}) = (120^\circ, -120^\circ)$ , while the original single resonance is maintained at  $(\phi_{21}, \phi_{31}) = (-120^\circ, 120^\circ)$ , as shown in Fig. 5.9(b). When the RF phases deviate from the ideal values within  $\pm 30^\circ$ , non-reciprocity only slightly degrades, which allows large tolerance of phase fluctuations in practical applications. This behaviour and RF phase dependency matches well with the FDFD simulations, showing qualitative agreement with experimental data.

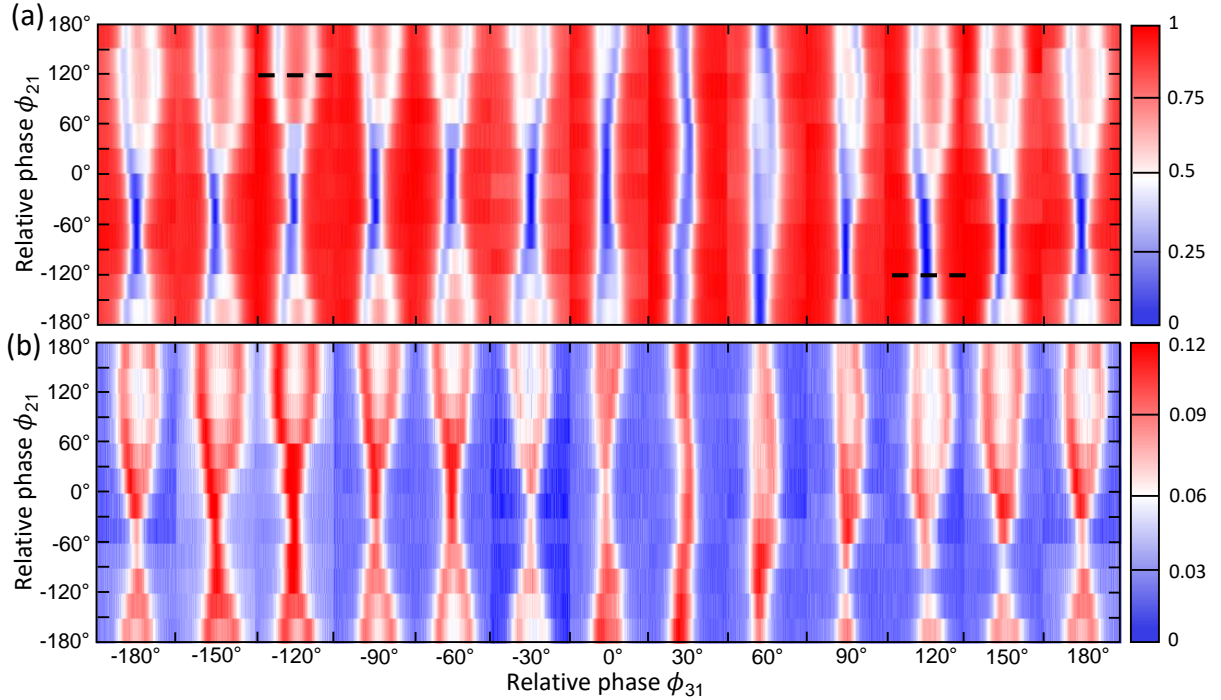


**Figure 5.10.** (a) Optical transmission and (b) converted sideband under phase sweep of signals 2 and 3 relative to signal 1, i.e. sweeping  $\phi_{21}$  and  $\phi_{31}$ . Each column is an experimentally measured spectrum under the same  $\phi_{31}$  with spectral span of  $\pm 16$  pm relative to the center wavelength  $\lambda_0$  (1542.6 nm) of the  $\text{TE}_{00}$  mode. Both **b** and **c** are normalized to the input TE light power on chip. The spectra in Fig. 5.9(b) are the slices as labeled by the black dashed lines in (a). Reprinted from Ref. [169].

Light transmission of the generated anti-Stokes TM sideband is simultaneously measured as shown in Fig. 5.10(b). It is normalized to the TE's input power, thus can be interpreted as conversion efficiency  $\eta$ . Figure 5.10(a) and (b) show similar pattern but with reversed color rendering. Prominent splitting and TE-TM conversion are found at  $(120^\circ, -120^\circ)$ , while TE-TM conversion is negligible at  $(-120^\circ, 120^\circ)$ . As the measured TM sideband is resulted from mode coupling and phase matching, it can be used as feedback signal for tuning and stabilizing the RF phases.

From Fig. 5.9(b), the optical isolation ratio between the clockwise (forward) and counter-clockwise (backward) directions is calculated as 9.3 dB, which is mainly limited by the level of critical coupling (-10.1 dB) of the optical microring (the current device is slightly under-coupled with 850 nm bus-microring gap). The isolation ratio can be improved in the future by fine tuning the bus-microring gap in the design and fabrication. 83% transmission is achieved on the resonance corresponding to 0.8 dB insertion loss in the forward direction.

I further note another device with 0.1 dB insertion loss (98% transmission) which shows higher modulation efficiency but less backward extinction due to the fact that the microring is more under-coupled with a wider gap with 950 nm. The results as shown in Fig. 5.11. The electro- and opto-mechanical properties are characterized in Fig. 5.11(a). It shows similar  $S_{11}$  as the device presented before, and the mechanical resonances of the actuators also align with each other. Since the optical mode spacing is around 4 GHz for this device, the HBAR at 3.833 GHz is chosen in the experiment.

Similar RF phase dependency measurement is conducted as shown in Fig. 5.11(b) under 20 dBm RF power applied on each actuator. This device shows larger mode splitting, and maximum of 3.3 GHz is achieved at phase matched case  $(\phi_{21}, \phi_{31}) = (-120^\circ, 120^\circ)$ . Intriguingly, for phase  $\phi_{31}$  between  $-150^\circ$  and  $-60^\circ$ , there is always mode splitting regardless of  $\phi_{21}$  because of its stronger mode coupling. The optical transmission under reversed phases is shown in Fig. 5.11(c). Due to the stronger mode coupling  $g/2\pi = 1.65$  GHz, and thus larger optical cooperativity  $C \sim 16$ , higher optical transmission at center wavelength can be reached around 98%, corresponding to 0.1 dB insertion loss. However, as this device has larger bus-microring coupling gap, the microring is undercoupled to the bus waveguide, leading to less extinction (6 dB) in the backward direction and thus smaller isolation ratio

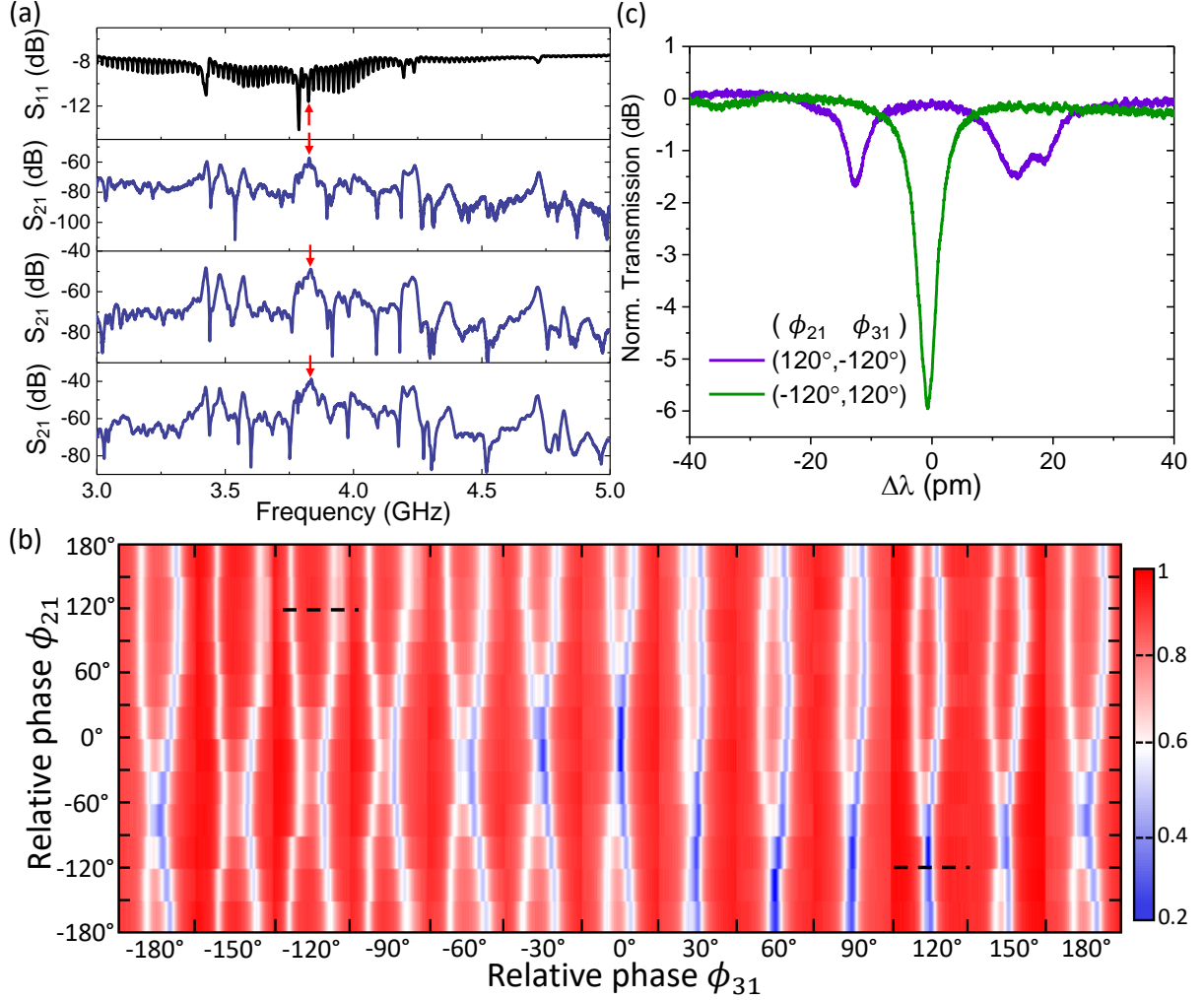


**Figure 5.11.** (a) From top to bottom are microwave reflection  $S_{11}$ , optomechanical response  $S_{21}$  of the three actuators 1, 2, and 3, respectively. Red arrows mark the mechanical mode at 3.833 GHz that is used in the experiment. (b) Normalized optical transmission of the  $TE_{00}$  mode under 2D sweep of phases of signals 2 and 3 relative to signal 1, i.e. sweeping  $\phi_{21}$  and  $\phi_{31}$ . Each column is the measured spectrum under the same  $\phi_{31}$  with spectral span of  $\pm 24$  pm relative to the center wavelength  $\lambda_0$  (1553 nm) of the  $TE_{00}$  mode. (c) Optical transmission spectra along black dashed lines in (b) with reversed phases:  $(\phi_{21}, \phi_{31}) = (120^\circ, -120^\circ)$  (purple, perfect phase matching) and  $(\phi_{21}, \phi_{31}) = (-120^\circ, 120^\circ)$  (green, largest phase mismatch). Reprinted from Ref. [169].

than the device in the main text. Nevertheless, this measurement shows that both low insertion loss (0.1 dB) and high isolation ( $>20$  dB) can be achieved if the bus-microring gap design is optimized in the future.

### 5.3.3 Dependency on the RF power

The evolution of optical isolation with varying applied RF power is studied in Fig. 5.12 with fixed RF phases of  $(\phi_{21}, \phi_{31}) = (120^\circ, -120^\circ)$  and drive frequency of 2.968 GHz. Figure 5.12(a) shows the measured forward and backward transmissions of the  $\text{TE}_{00}$  mode, with the RF power (applied to each actuator) increased from 15 to 20 dBm. In the forward direction, initially the resonance depth decreases and the linewidth broadens with increasing RF power up to 16 dBm, resulted from the increasing intrinsic loss caused by the scattering to the  $\text{TM}_{00}$  mode. Above 17 dBm, mode splitting appears, creating a transparency window at the original resonance frequency. In the backward direction, single-resonance profile remains, however with slightly increasing linewidth due to the weak mode coupling as predicted and described by the Floquet theorem [51]. Figure 5.12(c) shows the isolation ratio at zero laser detuning relative to the  $\text{TE}_{00}$  mode ( $\Delta\lambda = 0$ ) which increases exponentially with the applied RF power and is finally limited by the backward extinction.

The mode splitting rate, which is two times of the interband scattering rate  $g$ , is extracted by fitting the resonance profile using the generalized Eq. 5.13 from CMT, with  $g$  and  $\Delta\omega_{ba}$  being the fitting parameters. Figure 5.12(d) shows that  $g$  gradually increases with increasing RF power, and sharply increases to a higher value at 18 dBm RF power, above which  $g$  continuously increases and finally saturates at 20 dBm. This behaviour is caused by the blue shift of the  $\text{SiO}_2$  HBARs due to RF thermal heating, as  $\text{SiO}_2$  has a large positive temperature coefficient of elasticity of 188 ppm  $\text{K}^{-1}$  [213]. The RF drive frequency  $\Omega_d$  is initially blue-detuned from the HBAR frequency  $\Omega_m$  at room temperature, i.e.  $\Omega_d - \Omega_m > 0$ . As the RF power increases and the acoustic velocity in  $\text{SiO}_2$  increases,  $\Omega_m$  approaches  $\Omega_d$  (i.e.  $\Omega_d - \Omega_m \rightarrow 0$ ) and more phonons are pumped into the mechanical cavity. This in turn increases the temperature which further blue-shifts the HBAR. Thus, the thermal nonlinearity leads to an increase in  $g$  at approximately 18 dBm RF power.



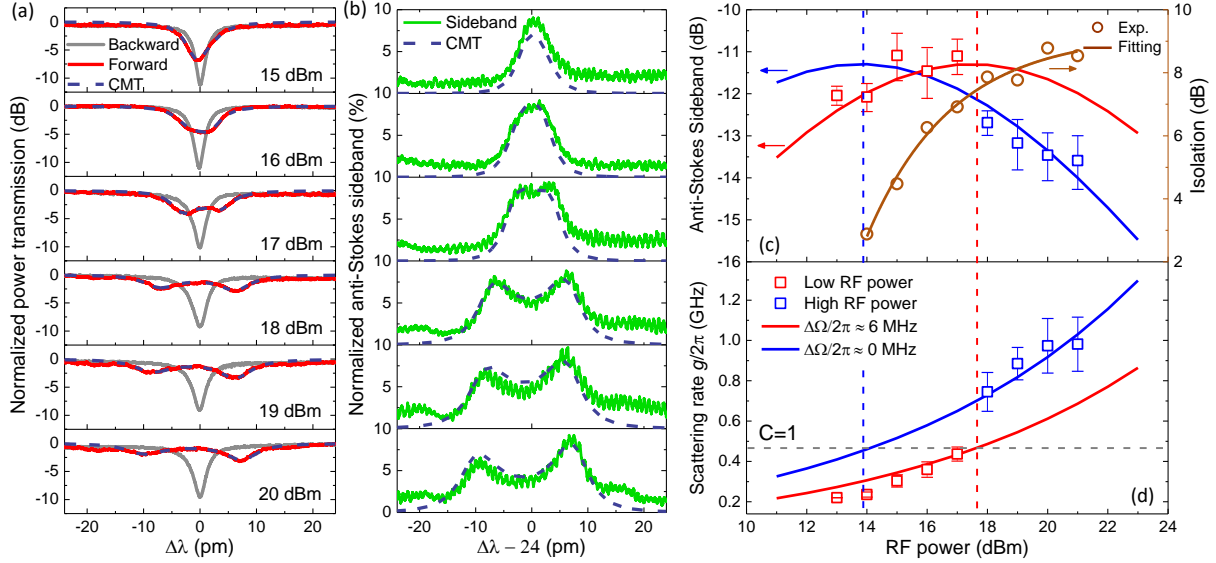


**Figure 5.12.** (a) Optical transmission spectra of the TE light in the forward (red solid) and backward (gray solid) directions, with increasing RF power from 15 to 20 dBm.  $\Delta\lambda$  is the wavelength detuning of the input laser relative to the  $\text{TE}_{00}$  mode  $\Delta\lambda = \lambda_L - \lambda_{\text{TE},0}$ , with  $\lambda_{\text{TE},0} = 1544.1$  nm. (b) Generated light of the anti-Stokes TM sideband in the forward direction, normalized by the input TE light power. The RF power increase is the same as (a). The anti-Stokes sideband is blue-shifted relative to the input laser by the modulation frequency 2.968 GHz ( $\sim 24$  pm,  $\lambda_{\text{TM}} - \lambda_{\text{TE},0} = \Delta\lambda - 24$ ). The fitted transmission using Coupled Mode Theory (CMT, blue dashed) is also shown in (a) and (b). (c) Conversion efficiency of the TM sideband at  $\Delta\lambda = 0$  and (d) Scattering rate  $g$  as a function of RF power. Experimental data (squares) are grouped as low RF power (red) and high RF power (blue), fitted individually with CMT (solid lines) with different microwave drive to mechanical resonance detuning  $\Delta\Omega = \Omega_d - \Omega_m$ . Horizontal gray dashed line in (d) marks the value of  $g/2\pi \sim 460$  MHz when cooperativity  $C = 1$ . Vertical red and blue dashed lines in (c) and (d) mark the maximum conversion at each detuning. The error bars of each data point represent the standard deviation (SD) from 5 individual measurements. The dependence of isolation on RF power is shown in (c) with experimental data (brown circle) and exponential fitting (brown solid line). Reprinted from Ref. [169].

With RF power above 20 dBm, the interband scattering rate  $g$  saturates, indicating that the efficiency of pumping phonons into the cavity starts dropping. This is likely because  $\Omega_d$  becomes red-detuned to  $\Omega_m$ , i.e.  $\Omega_d - \Omega_m < 0$ . Therefore, for RF power between 18 to 20 dBm, nearly zero detuning can be derived. In this regime, the single-phonon optomechanical coupling strength  $g_0/2\pi$  is calculated as 208 Hz, by fitting high RF power data (blue line) with  $g = g_0\sqrt{\bar{n}_c}$ , where  $\bar{n}_c$  is calculated by extracting the electro-mechanical coupling efficiency  $k_{t,\text{eff}}^2 = 0.2\%$  from  $S_{11}$  (see Supplementary Note 3). The low RF power region is fitted with  $(\Omega_d - \Omega_m)/2\pi \approx 6$  MHz blue-detuning (red line). Another consequence of the RF thermal effect is the drift of mode spacing  $\Delta\omega_{ba}$ . Figure 5.12(a) shows that the mode splitting evolves from symmetric (18 dBm) to asymmetric (20 dBm) with increasing RF power, and  $\Delta\omega_{ba}/2\pi$  is increased from 3 GHz to 3.3 GHz.

The spectrum of the TM anti-Stokes sideband is shown in Fig. 5.12(b). The conversion efficiency  $\eta$  at zero laser detuning to the  $\text{TE}_{00}$  mode ( $\Delta\lambda = 0$ ) is plotted in Fig. 5.12(c). Similarly, each data set with low and high RF power are fitted individually using Eq. 5.14 with the same detuning as used in Fig. 5.12(d). It can be derived from Eq. 5.14 that the maximum value of  $\eta$  is reached at  $C = 1$ . This can also be seen from Fig. 5.12(b) where the conversion starts to drop at center due to the mode splitting when  $C > 1$ . Maximum of 8% (−11 dB) of the  $\text{TE}_{00}$  mode power is converted to the  $\text{TM}_{00}$  sideband, which is mainly limited by the external coupling efficiency of the  $\text{TE}_{00}$  mode ( $\kappa_{a,\text{ex}}/\kappa_a = 0.34$ ) and  $\text{TM}_{00}$  mode ( $\kappa_{b,\text{ex}}/\kappa_b = 0.24$ ), see Eq. 5.14. At zero RF drive detuning (blue line),  $C = 1$  is achieved with 14 dBm RF power applied on each actuator (18.8 dBm in total), and the system operates in the strong coupling regime at 20 dBm. The detuning not only reduces  $g$  but increases the required RF power to achieve  $C = 1$ . In practice, the generated sideband can compromise the output signal purity. In our case, using optical modes with different polarizations enables the separation of different polarizations with high extinction ratio (>20 dB) using a PBS. Recently, an integrated PBS on  $\text{Si}_3\text{N}_4$  photonics has been demonstrated [214]. On the other hand, it is worth noting that the same device can work as a non-reciprocal frequency shifter and polarization rotator with 100% conversion achievable for strongly over-coupled devices (i.e.  $\kappa_{\text{ex}} \approx \kappa$ ). It could serve as a key building block in photonic quantum computing [215]–[217].

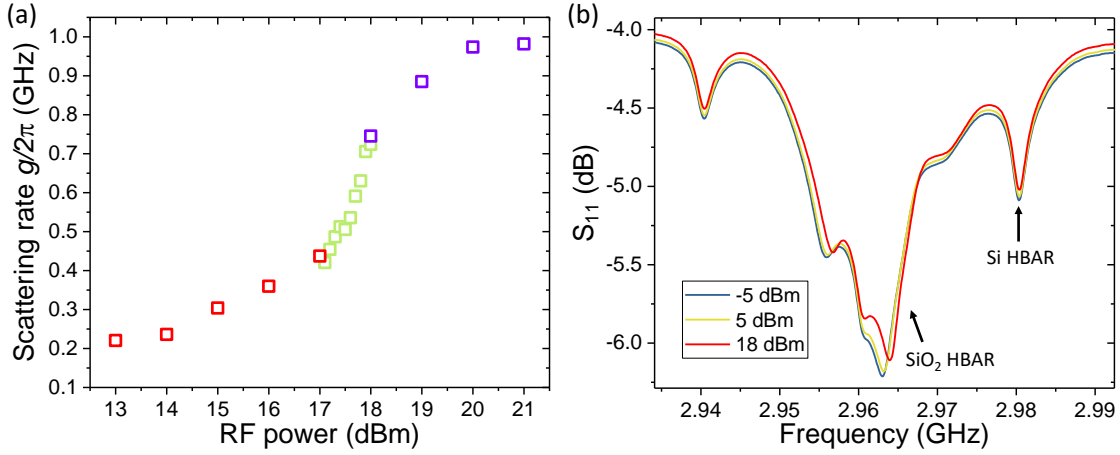


**Figure 5.13.** (a) Scattering rate  $g$  at different RF power. Green squares are fine sweep between 17 to 18 dBm with 0.1 dBm step. Red and purple squares correspond to the same data in the main text. (b) Electro-mechanical  $S_{11}$  under different RF power around the HBAR mode used in the main text. The resonances of SiO<sub>2</sub> and Si HBARs are as labeled. Reprinted from Ref. [169].

The fast transition from low  $g$  at 17 dBm to high  $g$  at 18 dBm is studied in details by fine RF power sweep with step of 0.1 dBm, as shown in Fig. 5.13(a). The fine sweep connects the low and high RF power data set. The sweep is conducted back and forth, and no obvious hysteresis is observed. To further explain the origin of the heating effects, electro-mechanical  $S_{11}$  is measured under different RF powers as shown in Fig. 5.13(b). It can be seen clearly that the SiO<sub>2</sub> HBAR is blue-shifted when the RF power increases from -5 dBm to 18 dBm. Intriguingly, due to the better thermal conductance of the Si substrate, the Si HBARs show no prominent shift, which also verifies that the blue shift of SiO<sub>2</sub> HBAR is not from measurement errors. The blue shift of the SiO<sub>2</sub> HBAR is mainly from the bad thermal conductance of the free-standing SiO<sub>2</sub> membrane and the large temperature coefficient of elasticity of SiO<sub>2</sub>. The shift of HBAR resonances will introduce phase shift on the modulation, which can be actively compensated by adjusting the RF signal phases experimentally.

The power handling capability of our piezoelectric actuators is also studied. For RF power under 27 dBm, the piezoelectric actuator can work continuously for several hours without degradation. However, for RF power higher than 30 dBm, there is gradual roughening of

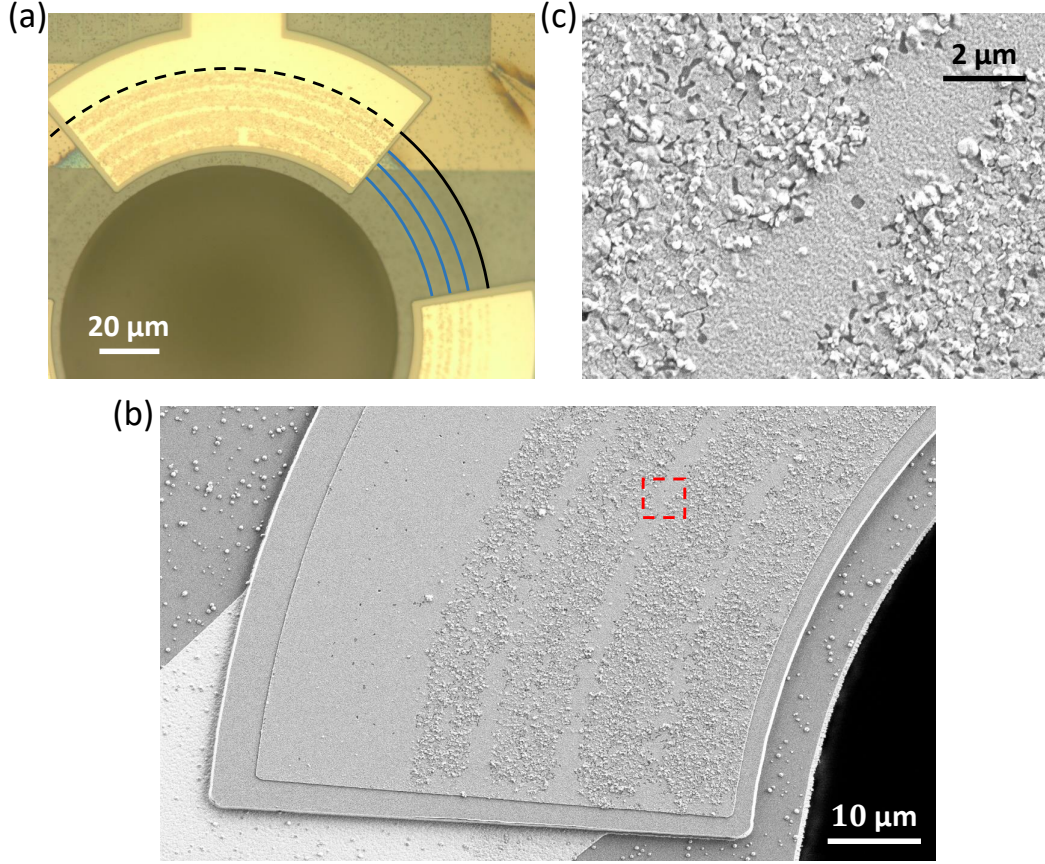


**Figure 5.14.** (a) Optical microscope image of the device undergoes 30 dBm RF power. Black line denotes the edge of the  $\text{SiO}_2$  undercut. Blue lines outlines the  $\text{Si}_3\text{N}_4$  microring waveguide and dummy waveguides. (b) SEM image showing the corrugated surface of the Al top electrode. (c) Zoom-in SEM of the region in the red dashed box in (b). Reprinted from Ref. [169].

the top electrode surface, as seen in Fig. 5.14(a). Also, there is burning at the sharp corners of the bottom electrode which is caused by the current crowding under high RF power. Interestingly, the outer edge of the rough region aligns with the edge of the undercut (black line), indicating that the degradation is mainly due to the low thermal conductivity of the suspended  $\text{SiO}_2$  membrane. Also, the degradation is split by three concentric circles into several regions which align with the underneath  $\text{Si}_3\text{N}_4$  microring waveguide and dummy ring structures (blue lines) designed for uniform chemical-mechanical polishing (CMP). This is likely due to that these  $\text{Si}_3\text{N}_4$  structures scatter the acoustic waves which reduces the energy density around these regions. The roughness is highlighted in the SEM images in

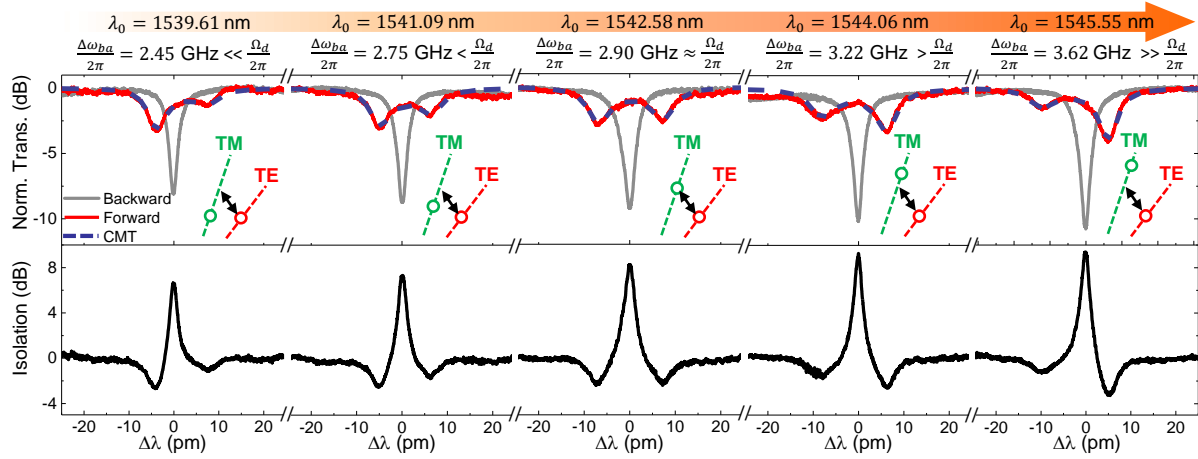


**Figure 5.15.** Top panel: Optical transmission spectra in the forward (red) and backward (gray) directions, with increasing center wavelength (left to right). The mode spacing ( $\Delta\omega_{ba}$ ) changes correspondingly due to the different FSRs of the  $\text{TE}_{00}$  and  $\text{TM}_{00}$  modes. Insets show the relative positions of the two modes in the  $\omega - k$  space (not to scale). Bottom panel: spectra of isolation ratios varying with the center wavelength. Reprinted from Ref. [169].

Fig. 5.14(b,c). The top Al layer is corrugated and detached from AlN. One possible reason for this detachment is that the large vertical displacement and vibration under high power loosen the adhesion of Al to AlN. This may explain why the  $\text{Si}_3\text{N}_4$  region is not influenced since the acoustic energy is dissipated by the scattering. So the corrugation of Al may “undesirably” maps the distribution of acoustic mode.

#### 5.3.4 Detuning of the optical mode spacing

Since there is 380 MHz difference in FSR between the  $\text{TE}_{00}$  and  $\text{TM}_{00}$  modes (see Appendix B), their frequency spacing  $\Delta\omega_{ba}$  varies from pair to pair for different center wavelengths. Here, the dependence of isolation performance on  $\Delta\omega_{ba}$  is studied in Fig. 5.15 under 20 dBm RF power. At  $\lambda_0 = 1542.58$  nm,  $\Delta\omega_{ba}$  is nearly equal to the driving frequency  $\Omega_d$ , and the mode splitting is symmetric. Because the optical resonance linewidths are around gigahertz level,  $\text{TE}_{00}$  and  $\text{TM}_{00}$  modes can still be coupled even with a frequency mismatch between  $\Delta\omega_{ba}/2\pi$  and  $\Omega_d/2\pi$  on the order of 0.5 GHz. The mismatch leads to asymmet-

ric mode splitting. Nevertheless, there is no prominent degradation of isolation within the measured range.

The decrease of maximum isolation for shorter wavelength is caused by the reduction of extinction in the backward direction. This is because that shorter wavelength has smaller mode size and thus a weaker bus-microring external coupling rate  $\kappa_{\text{ex}}$  that leads to under-coupling. Maximum of 9.5 dB isolation is achieved at 1545.55 nm, which is even larger than the matched symmetric case due to its better critical coupling. Therefore, the isolator can work simultaneously for multiple center wavelengths which is important for optical communication using wavelength multiplexing [218]. The wavelength range can be extended to cover the optical C-band by using pulley coupling scheme [219] to maintain critical coupling or slight over-coupling, and engineering the waveguide geometry to reach precise FSR match. On the other hand, thermal tuning to continuously shift the operating resonance can further increase the bandwidth.

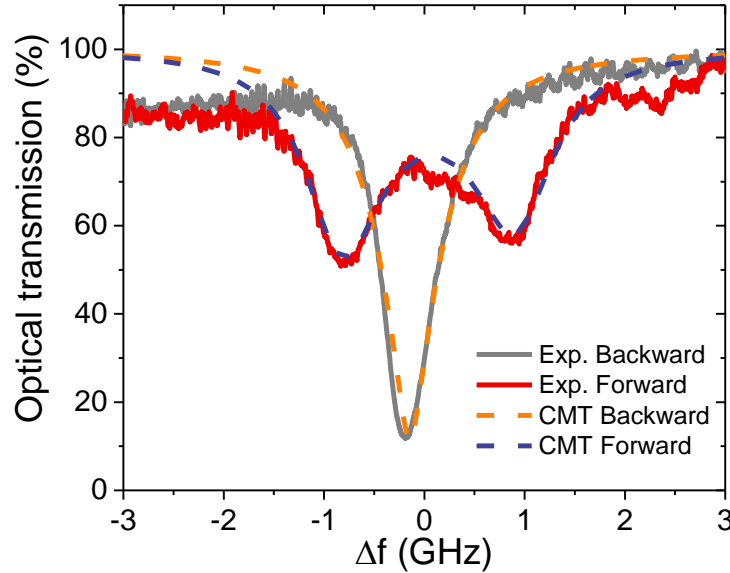


**Figure 5.16.** Comparison of one typical experimental result (the 18 dBm RF power case in Fig. 5.12(a)) with the temporal coupled mode theory based on the Floquet analysis from Ref. [51]. Here the backward direction transmission can also be predicted which shows good agreement with the experiment.



### 5.3.5 Comparison with the Floquet analysis

In the previous plots, the experimental results are compared with the simplified CMT developed in this thesis, which show good agreement. However, it cannot predict the behavior when there is phase mismatch in the backward direction. In the original paper by Y. Shi in Ref. [51], he derived a more rigorous temporal coupled mode theory to describe the direction-dependent dissipation based on the Floquet analysis. Following the equations in Ref. [51], one typical experiment result at 18 dBm RF power is fitted for both the forward and backward transmissions, as shown in Fig. 5.16. Good agreement can be found for both directions. From the fitting, the modulation-induced coupling strength between modes  $J$  is found to be  $0.3 \Omega_d$ . Other settings are similar as the simplified CMT before.

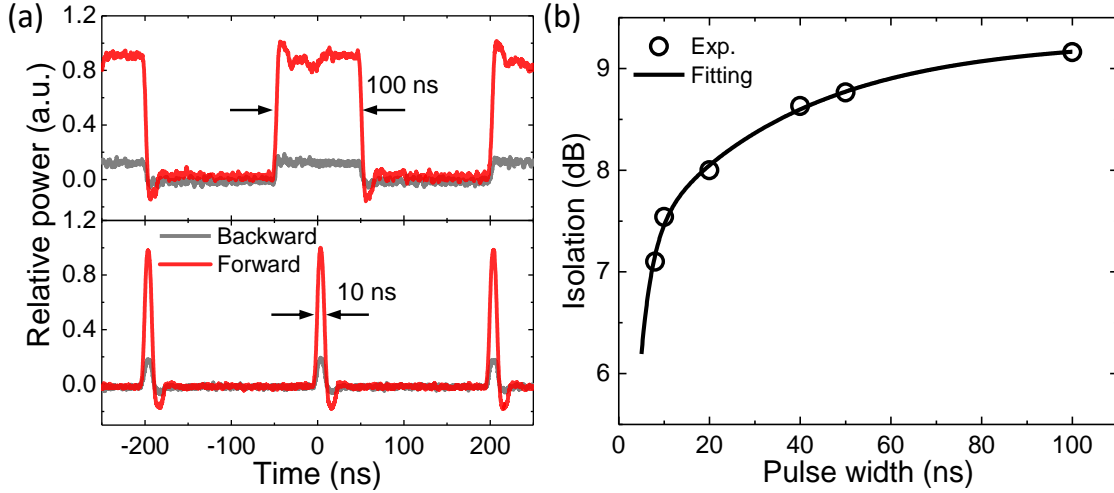


**Figure 5.17.** (a) Transmission of optical pulse trains in the forward (red) and backward (gray) directions for 100 ns (top panel) and 10 ns (bottom panel) pulse width. The power is normalized to the maximum power of the forward pulse in each case. (b) The isolation ratio decreases with narrower pulse width due to the finite photon lifetime ( $\sim 1.5$  ns) in the optical cavity. Experimental data (circle) are fitted with an exponential function (solid line). Reprinted from Ref. [169].

### 5.3.6 Time domain optical isolation

I further evaluate the optical isolator to demonstrate a unidirectional transmission of an optical pulse train to mimic (0, 1) data stream, as shown in Fig. 5.17(a). The 100-ns pulse shows the quasi-static response, where the backward reflection is only 11% of the forward transmission. The bump at the pulse edge is caused by the limited bandwidth ( $\sim 125$  MHz) of the photodetector. The dynamic response is tested with 10-ns pulses, illustrating a vast contrast in the two directions. The isolation bandwidth can be inferred from the decreasing isolation with decreasing pulse duration, as revealed in Fig. 5.17(b). A pulse of minimum 8 ns duration is measured, limited by the photodetector's bandwidth. Over 8 dB isolation is maintained for pulses longer than 20 ns. However, the isolation drops exponentially when the pulse duration is shorter than 20 ns, which is ultimately limited by the photon lifetime of  $\sim 1.5$  ns, corresponding to 680 MHz linewidth of the optical resonance.

### 5.3.7 Dependency on the optical power

Dynamic reciprocity has been a well-known limitation for most optical isolators relying on optical nonlinearity, where the isolation degrades dramatically when light transmits simultaneously in both directions and the optical power exceeds a certain threshold [191], [205]. In our work, with only electrical drives, the optical linearity is preserved as long as the intra-cavity photon number is smaller than the phonon number. Since phonon frequency is five orders of magnitude smaller than photon frequency, theoretically it suggests maximum of 6 kW optical power for 20 dBm RF power in the experiment. However, the optical linearity of our isolator is eventually limited to several Watts due to the Kerr nonlinearity of  $\text{Si}_3\text{N}_4$ . The quasi-square waveguide cross-section used here has a normal group velocity dispersion (GVD), and the optical microresonator has low optical  $Q < 5 \times 10^5$ , which suppress Kerr parametric oscillation [29].

The linearity is experimentally verified in microwatt to milliwatt range as shown in Fig. 5.18. The optical isolation remains nearly constant within the measurement range. The large variation at high optical power is mainly due to the optical thermal nonlinearity as the laser



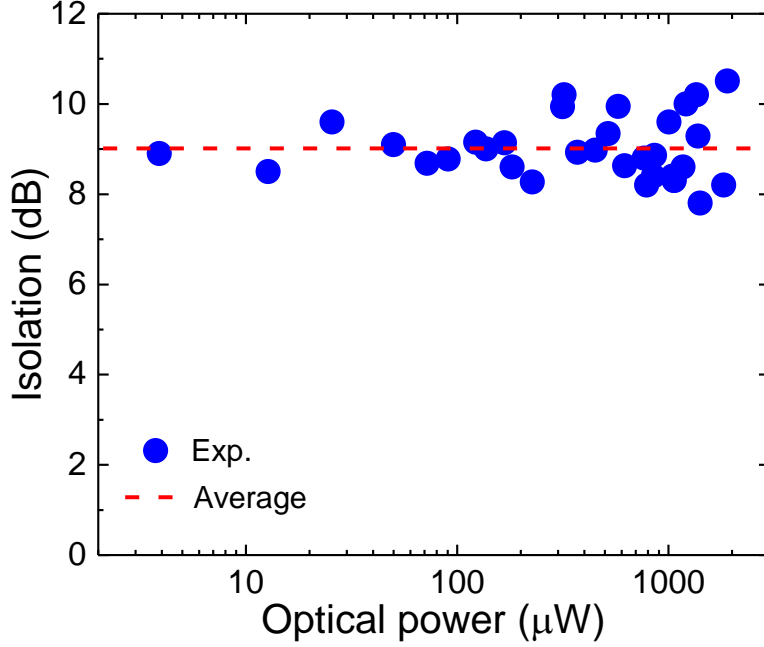


**Figure 5.18.** Measured data (blue circle) showing that the isolation remains nearly constant around 9 dB (red dashed line) over 30 dB dynamic range of the optical input power. Reprinted from Ref. [169].

is swept across the optical resonance. Theoretically there is no limit on the lower bound of the optical power, thus our device can work for photonic quantum computing [215]–[217].

### 5.3.8 Results of the over-coupled device

Most recently, Ref. [133] proposes a method to control the extinction of the optical mode by operating in the overcoupled regime. In this case, the device works in the opposite way: 1. As the device is overcoupled, it shows high transmission when there is no mode coupling induced in the phase-mismatched direction; 2. In the phase-matched direction, mode coupling converts the input light into the other auxiliary mode and finally gets filtered. The advantage of this approach is the amount of light converted into the other mode can be controlled by the RF power. This can also be understood intuitively that the conversion to the other mode effectively increases the microresonator intrinsic loss, and critical coupling can be achieved by matching the intrinsic loss with the external coupling rate. We can

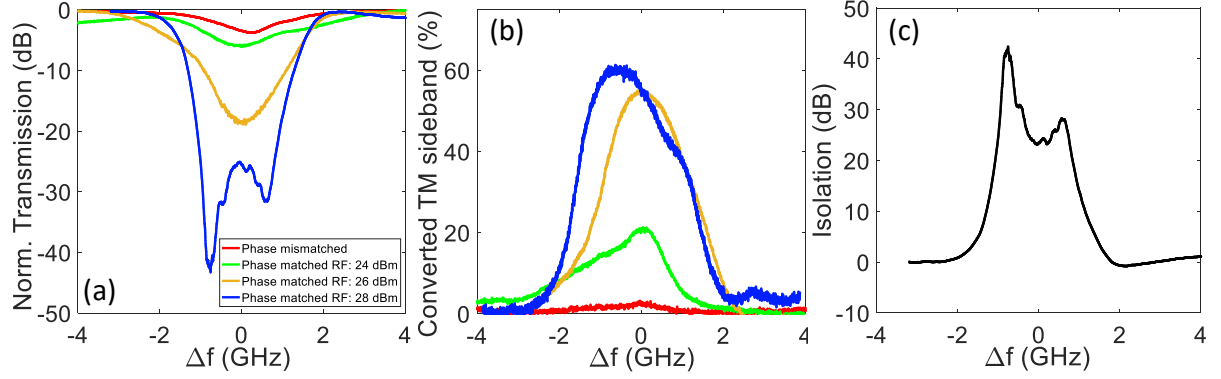


**Figure 5.19.** (a) Normalized optical transmission in the phase-mismatched case (red) and phase-matched cases with increasing RF power applied on each actuator (green, yellow, blue). (b) Conversion to the TM mode under each setting in (a). (c) Isolation ratio by taking difference between the phase-matched case under 28 dBm (blue) and mismatched case (red) in (a). Reprinted from Ref. [169].

imagine that the undercoupled device will not work as the external coupling rate would be always smaller than the intrinsic loss (since we can only increase intrinsic loss).

A device with 600 nm coupling gap is characterized as shown in Fig. 5.19. Maximum of 43.3 dB extinction is obtained at  $-0.75$  GHz laser detuning, with  $-1.86$  dB transmission at phase-mismatched case (red curve), corresponding to an isolation ratio of 41 dB. Due to the lower optical  $Q$  for over-coupled device, the modulation efficiency is reduced and the requires RF power is higher than that used for the under-coupled device in the main text. The extinction gradually increases with increasing RF power, and mode starts splitting over 28 dBm. Applying higher RF power is avoided as the AlN actuator starts to degrade. On the other hand, the lower optical  $Q$  helps to achieve larger isolation bandwidth as shown in Fig. 5.19(c). Isolation larger than 20 dB is obtained over 2 GHz bandwidth. Strategies to reduce RF power are discussed in the next section.

As mentioned previously, conversion to the TM sideband can have higher efficiency in over-coupled region, which is studied in Fig. 5.19(b). Maximum of 60% conversion is achieved which can be further increased in devices that are more over-coupled. This device integrates three features together: frequency shifting, polarization rotating, and non-reciprocity, which can find applications in frequency-encoded quantum optical computing [175], [220].

## 5.4 Frequency shifter and polarization rotator

Optical light has been the workhorse for today's telecommunication systems due to its flexible and versatile degree of freedom for encoding digital information. Most recently, encoding quantum information in optical photon has been widely studied because of its low thermal noise and losses at room temperature. For example, generation of entangled photons in vertical and horizontal polarization has been used for quantum key distribution [221], [222]. Another example is to encode the information in different optical paths. Photonic quantum computing and simulating have been demonstrated by building a mesh of Mach-Zehnder interferometer [175].

Most recently, encoding quantum information in frequency domain has enabled high dimensional quantum computing [215]. As shown in Fig. 5.20(a), light in  $\omega_0$  represents logical  $|0\rangle$ , whereas light in  $\omega_1$  is logic  $|1\rangle$ . Similar as a Mach-Zehnder interferometer in the spatial domain, the two basic operations can also be implemented in frequency domain by coupling the two optical mode as shown in Fig. 5.20(b-c). For example, for an ideal swap operation, light in one frequency is completely converted to the other frequency (this is also often called frequency shifter). In a beam-splitter operation, light is split equally into two frequency modes. The advantage of this encoding is that all the light can transmit in a single waveguide. Also, it works with discrete frequencies, such that we can use the optical resonators to enhance the interaction strength as shown in Fig. 5.20(d). In such a way, it will present good scalability, parallelism and compactness.

However, controlling the frequency in integrated photonic platforms has been difficult and is highly on demand as integrated photonic computing matures. Recently, the conversion between two optical modes in different frequencies is demonstrated by electro-optically modulating a coupled ring resonators, where light in the symmetric mode can be converted to the asymmetric mode in a different frequency, and vice versa [220]. The conversion efficiency can be controlled by RF powers, which can configure the device between frequency shifter and beam splitter. Non-reciprocal frequency shifting has been demonstrated with acousto-optic modulation on a suspended Si waveguide with maximum conversion efficiency of  $\sim 10^{-4}$  [223].

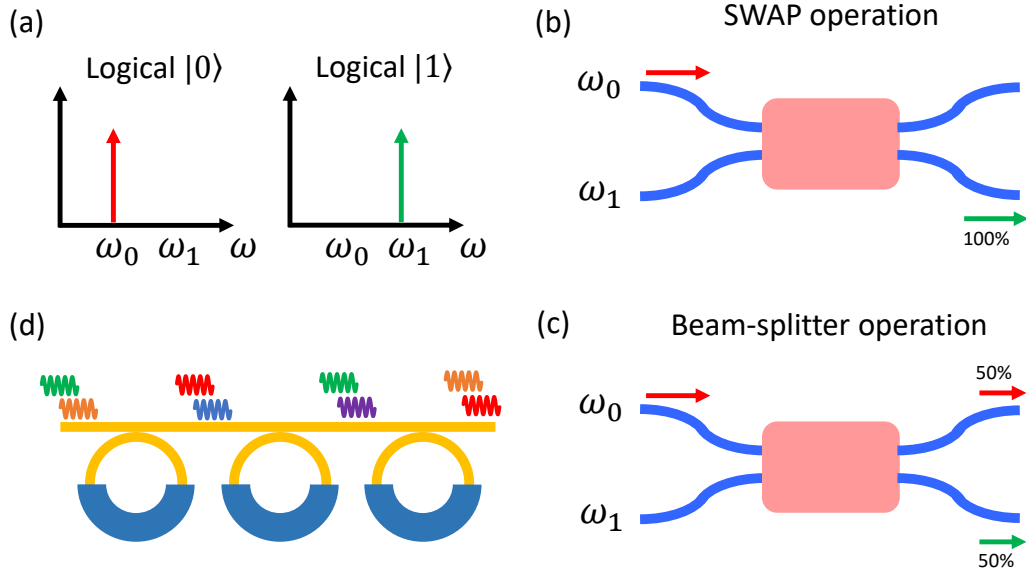


**Figure 5.20.** (a) Schematic showing encoding information (logical  $|0\rangle$  and  $|1\rangle$ ) in different frequencies of the optical modes ( $\omega_0$  and  $\omega_1$ ). Representations of (b) SWAP operation and (c) beam-splitter operation in analogy of a Mach-Zehnder interferometer in space. (d) Cascading of multiple microrings for compact integration.

From the demonstrations of the isolator discussed before, the coupling between TE and TM modes induces the energy conversion between them. Although in isolator, the generated sideband needs to be filtered out, it can be utilized to demonstrate the frequency shifter which also rotates the polarization of the light after shifting. From Fig. 5.12(b), it can be seen maximum of 9% conversion efficiency is achieved, which is mainly limited by the extraction efficiency to the bus waveguide as it's slightly under coupled with  $\kappa_{\text{ex}}/\kappa \sim 0.3$ .

To increase the efficiency, a device with 600 nm bus-ring gap is measured which is highly overcoupled with  $\kappa_{\text{ex}}/\kappa \gg 0.5$ . Initially, the beam-splitter operation is demonstrated as shown in Fig. 5.21. 10 dBm RF power is applied to each actuator. The transmission spectrum in Fig. 5.21(a) is measured by sweeping the laser frequency across the TE mode's resonance, and they are normalized by the off-resonance transmission of TE light. The generated TM light is separately measured which shows nearly equal transmission with the TE light at the zero detune ( $\Delta f = 0$ ). Next, the optical spectrum of the output light is measured by an optical spectrum analyzer (OSA) with laser biased at  $\Delta f = 0$ , as shown

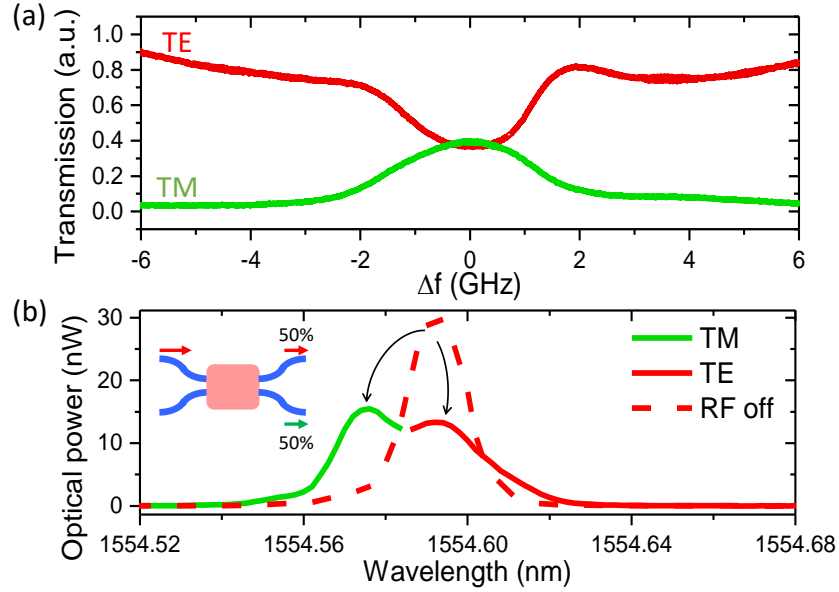


**Figure 5.21.** (a) Transmission spectrum for TE (red) and TM (green) modes under 10 dBm RF power applied to each actuator. x-axis the the relative detuning of the input laser to the resonance of TE mode. (b) Optical spectrum of the output light when RF power is off (red dashed line) and when RF power is on (solid line). Part of the energy is converted to the TM light (green) with shorter wavelength. The inset shows the beam-splitter operation diagram.

in 5.21(b). The broadening of the single frequency laser spectrum is mainly limited by the finite resolution of the OSA with 0.02 nm. When the RF drive is zero, there is a single peak (red dashed line). When the RF drive is turned on, there appear two peaks, with part of the light shifting to the lower wavelength, corresponding to the TM mode. Therefore, light injected into the TE will be split into TE and TM modes at the output with equal intensity. This corresponds to the beam-splitter operation in frequency domain.

The SWAP operation is further conducted by increasing the RF power to 20 dBm, as shown in Fig. 5.22. Note this was done on a different device with smaller optical Q. The optical spectrum before and after turning on the RF power is measured with fixed laser frequency at the resonance of TE mode. By comparing the optical spectrum, the output light shifts to the shorter wavelength (larger frequency) and the original input light is suppressed by 15.4 dB. The asymmetry between the two sidebands is 12 dB, which demonstrates a single sideband modulator with carrier frequency suppressed. The wavelength shifting can be seen

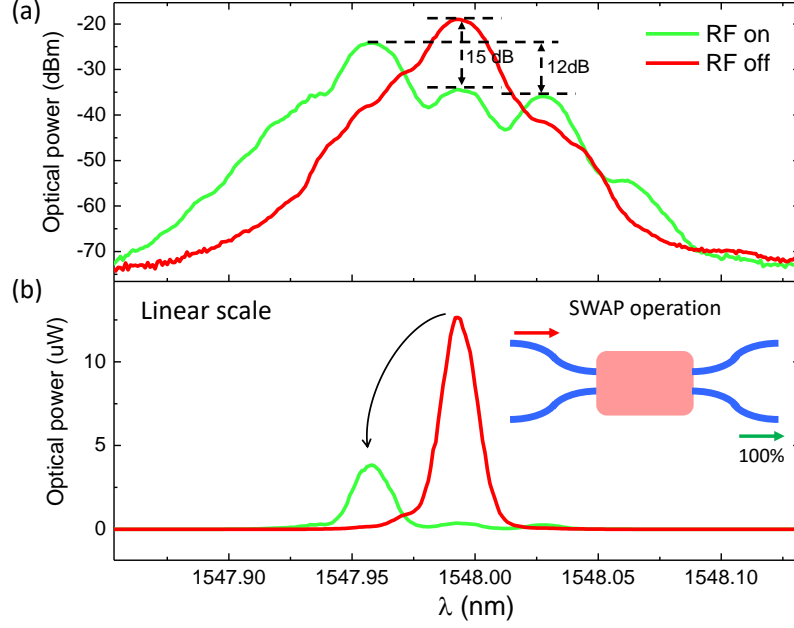


**Figure 5.22.** (a) Optical spectrum in log scale when RF power is on (green) and off (red) for fixed input laser frequency at the resonance of the TE mode. (b) Same optical spectrum as in (a) in linear scale. The inset shows the SWAP operation diagram.

more clearly in the linear scale in Fig. 5.22(b), where most light shifts to lower wavelength in the output.

The transmission spectrum for TE and TM modes when sweeping the laser across the TE resonance is shown in Fig. 5.23 upper panel. It can be seen at the center most TE is extinct which is converted to TM with 50% efficiency. Since this device is not in the strong over-coupled regime, the rest 50% TE light is lost as the intrinsic loss of the resonator. On the other hand, light can also be converted from TM to TE if TM mode is input as shown in the lower panel of Fig. 5.23. This demonstrates the bi-direction conversion between TE and TM modes. Also, the coupling between TE and TM modes also rotates the polarization after conversion. These novel features would help to pave the way for applications in photonic quantum computing.

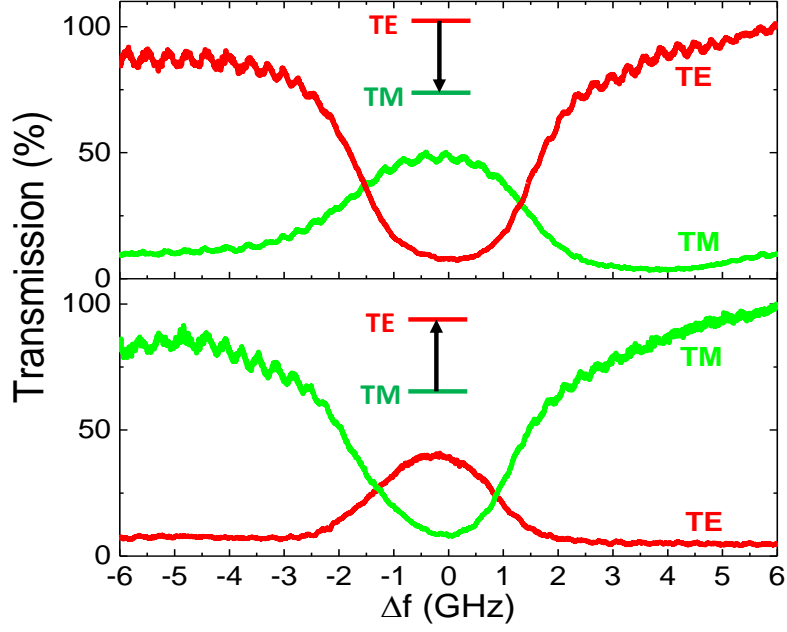


**Figure 5.23.** Transmission spectrum for TE (red) and TM (green) light when input light is aligned with the TM mode (upper) and TE mode (lower), which demonstrates the bi-directional conversion between TE and TM modes.

## 5.5 Comparison with the state of the art

This section reviews and summarizes most recent optical non-reciprocal devices realized using different schemes, and compares their performance with our work in Table 5.2. The isolation and insertion loss of these devices are summarized and plotted in Fig. 5.24 for better visualization. Optical non-reciprocal devices have long been realized using magneto-optic materials with the Faraday effect. However, it is challenging to integrate these materials as they are not compatible with most CMOS processes. Nevertheless, there have been advancements towards integrating cerium-substituted yttrium iron garnet (Ce:YIG) on Si photonic chips via wafer bonding [180]. Most recently, Ce:YIG has been grown on silicon nitride by pulsed laser deposition (PLD) [181]. However, it still needs bulky external magnet to generate the required magnetic field to break the Lorentz reciprocity. On the other hand, in the applications for building optical interfaces to connect distant superconducting circuits for quantum internet [182], the applied external magnetic field would unavoidably interfere

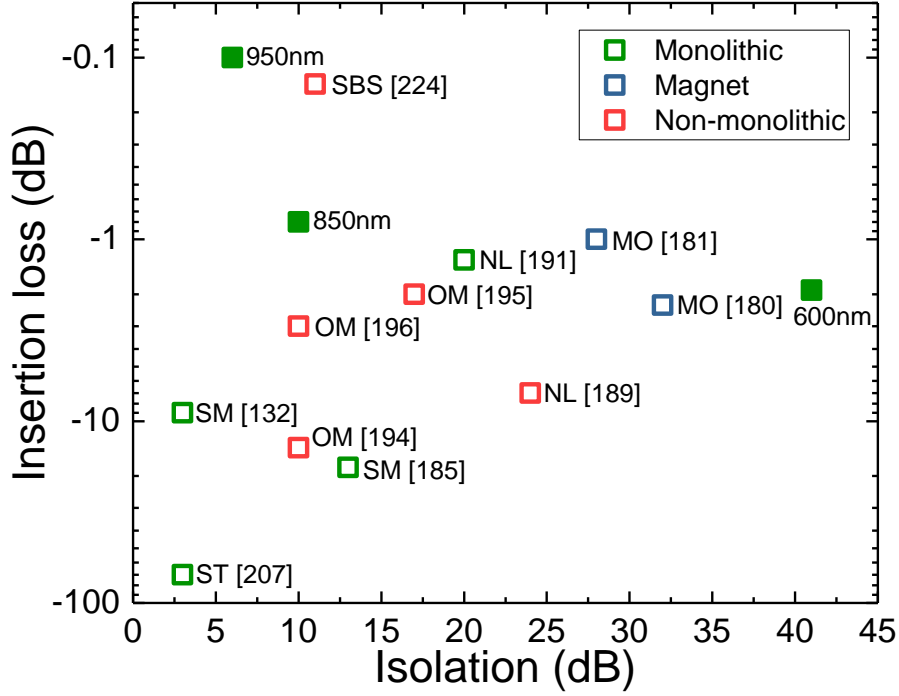


**Figure 5.24.** Comparison of insertion loss and isolation among several experimental realizations of optical isolators. These devices are classified by the level of integration into monolithic (green), and non-monolithic (red). Devices relying on magneto-optic material (blue) is separately listed while others are all magnetic-free. The three devices with 950, 850, and 600 nm gaps shown in this work are listed separately as solid green squares. The references are as labeled. Reprinted from Ref. [169].

the operation of superconducting qubits. Thus, magnetic-free optical isolators are especially desired in this case.

Optical non-reciprocity has been demonstrated in optomechanical systems through optomechanically induced transparency (OMIT) [193]–[196], where an optical pump in one optical mode excites and couples a mechanical resonance with another optical mode. However, most of these demonstrations are realized in a stand-alone optical microresonator (micro-toroid or microsphere) that supports both optical and mechanical whispering gallery modes (WGMs). This scheme is difficult to integrate with PICs in a convenient and reliable manner. Moreover, as it requires optical pump, the power of the probe light has to be much smaller than the pump light to maintain stable optomechanical interaction. This limits the dynamic range of the optical power that can be isolated. On the other hand, in OMIT the



**Table 5.2.** Comparison of optical non-reciprocal devices realized using different schemes: MO (magneto-optic), NL (nonlinear optics), OM (optomechanical), SBS (stimulated Brillouin scattering), SM (synthetic magnetic field), and ST (spatio-temporal modulation). IL: Insertion loss. The three devices with 950, 850, and 600 nm gaps shown in this work are listed separately. A commercial bulk optical isolator is listed for comparison. *a*: Non-reciprocal sideband modulation. *b*: Optical pump power.

Year	Scheme	Structure	Material	Isolation	IL (dB)	Bandwidth	Power	CMOS
2016[180]	MO	Ring	Si+Ce:YIG	32 dB	2.3	15 GHz	10 mW	No
2020[181]	MO	Ring	SiN+Ce:YIG	28 dB	1	15 GHz		No
2018[189]	NL	Toroid	SiO <sub>2</sub>	24 dB	7	1 MHz	No drive	No
2020[191]	NL	Ring	Si	20 dB	1.3	20 GHz	No drive	Yes
2016[194]	OM	Toroid	SiO <sub>2</sub>	10 dB	14	250 kHz	17 $\mu$ W <sup><i>b</i></sup>	No
2018[196]	OM	Toroid	SiO <sub>2</sub>	10 dB	3	60 kHz	60 $\mu$ W <sup><i>b</i></sup>	No
2018[195]	OM	Sphere	SiO <sub>2</sub>	17 dB	2	200 kHz	7.8 mW <sup><i>b</i></sup>	No
2017[224]	SBS	Sphere	SiO <sub>2</sub>	11 dB	0.14	400 kHz	235 $\mu$ W <sup><i>b</i></sup>	No
2014[184]	SM	MZI	Doped Si	2.4 dB		20 nm	34 dBm	Yes
2021[132]	SM	Ring	AlN	3 dB	9	4 GHz	16 dBm	Yes
2021[185]	SM	Ring	Doped Si	13 dB	18	2 GHz	-3 dBm	Yes
2012[207]	ST	MZI	Doped Si	3 dB	70	200 GHz	25 dBm	Yes
2018[209]	ST <sup><i>a</i></sup>	MZI	Si	39 dB	NA	125 GHz	90 mW <sup><i>b</i></sup>	Yes
2018[131]	ST <sup><i>a</i></sup>	Ring	AlN	15 dB	NA	1 GHz	18 dBm	Yes
2021[92]	ST <sup><i>a</i></sup>	MZI	Si+AlN	16 dB	NA	100 GHz	21 dBm	Yes
850 nm	ST	Ring	Si <sub>3</sub> N <sub>4</sub> +AlN	10 dB	0.8	0.7 GHz	25 dBm	Yes
950 nm	ST	Ring	Si <sub>3</sub> N <sub>4</sub> +AlN	6 dB	0.1	0.7 GHz	25 dBm	Yes
600 nm	ST	Ring	Si <sub>3</sub> N <sub>4</sub> +AlN	41 dB	1.9	2 GHz	33 dBm	Yes
Thorlab	IO-K-1550			35 dB	1.2	40 nm		No

bandwidth of the transparency window is limited by the mechanical linewidth, which limits the isolation bandwidth to below megahertz (see Table 5.2).

Other monolithic integrated optical non-reciprocal devices are realized either by optical nonlinearity or by dynamical modulation (spatio-temporal modulation and synthetic magnetic field), benefiting from the advanced integration of nonlinear components [34] and electro-optic and acousto-optic modulators [9]–[16]. The recent work [191] using the Si nonlinearity has achieved 20 dB isolation and 20 GHz bandwidth. However, the fact that it works for optical power within 4 to 8 dBm limits its applications. In contrast, dynamic modulation, especially with electrical driving, largely preserves the optical linearity by separating driving and sensing in two different domains. The early experiments [184], [207] are based on modulating doped-Si waveguides in a Mach-Zehnder interferometer (MZI).

However, the exaggerated loss of the doped-Si waveguides (70 dB insertion loss) limits the maximum isolation within 2.4 to 3 dB.

Recently, spatio-temporal modulation using AOM has been implemented [92], [131], [209]. Limited by either the modulation efficiency or the power handling capability of electrodes, complete mode conversion ( $C = 1$ ) has not been achieved, i.e. only non-reciprocal sideband modulation is demonstrated. Most recently, optical isolators are demonstrated by modulating coupled optical microrings through either synthetic Hall effect [132] or Aharonov-Bohm effect [185], but with limited isolation [132] and large insertion loss [185]. In comparison, our HBAR resonator shows better power handling capability because of its wide electrode area (and thus small resistance). Also, the tight confinement of acoustic energy in thin  $\text{SiO}_2$  membrane improves the modulation efficiency by 100 times compared with previous unreleased Si HBARs [12]. With these features, we demonstrate the lowest insertion loss among these works, and comparable isolation under reasonable amount of RF power applied.

## 5.6 Summary

In this chapter, I demonstrated an integrated optical isolator by spatio-temporal modulation of a  $\text{Si}_3\text{N}_4$  microring resonator via three AlN piezoelectric actuators. By carefully tuning the relative phases among these actuators, HBAR modes create an effective rotating acoustic wave that couples two optical modes in the momentum-biased direction. The device has been fully characterized in terms of RF phases, RF powers, optical spectra, and optical powers, showing agreement with theoretical models and numerical simulations. The device enters the mode splitting regime when RF drive power applied on each actuator is higher than 14 dBm, and maximum isolation of 10 dB and minimum insertion loss of 0.1 dB under 20 dBm RF power are achieved. An isolation bandwidth of 700 MHz is obtained, which is primarily determined by the optical resonance linewidth.

### 5.6.1 Outlook on future applications and improvements

In practical applications, the main figure of merit for an isolator is its insertion loss, isolation ratio and bandwidth. We summarize in Supplementary Table 5.2 the comparison

of our current devices with a commercial bulk isolator from Thorlab IO-K-1550. The critically coupled device (950 nm gap) have 0.1 dB insertion loss, while the isolation ratio is limited by the critical coupling level of the microring. In the current fabrication, we sweep the bus-microring gap distance coarsely with 50 nm step. In the future, finer gap sweep can be implemented for better critical coupling. Experimentally, 30 dB extinction can be achieved, which is comparable with most commercial isolators. On the other hand, due to the low insertion loss, cascading several isolators can increase isolation. For example, by cascading five 950-nm-gap devices, we can have 30 dB isolation and 0.5 dB insertion loss. The over-coupled 600-nm-gap device shows higher isolation and higher insertion loss than the commercial isolator.

The bandwidth is limited by the optical resonance linewidth. The isolator bandwidth can be increased by either increasing the microresonator's intrinsic loss, or increasing the external coupling rate by working in the over-coupling regime. This however increases the RF power consumption. Nevertheless, there are still ways to reduce the RF power in the future. The piezo-optomechanical coupling efficiency is mainly determined by the cooperativity  $C$ :

$$C = \frac{4g_0^2}{\kappa_a\kappa_b} \bar{n}_c \quad (5.20)$$

Based on the expression, there are some strategies to increase  $C$ :

- **Reducing the optical microring radius.** This is an effective way to increase the  $g_0$  by shrinking both of the optical and mechanical mode volume [168]. For optical microring with 22  $\mu\text{m}$  radius, the mechanical mode volume will be decreased by 25 times. As the  $g_0$  is inversely proportional to the square root of volume, this leads to 25 times decreasing of RF power to 12 mW.
- **Using scandium (Sc) doped AlN.** AlScN has 4 times larger piezoelectric coefficient than that of AlN [139]–[143]. If using AlScN, we anticipate at least 4 times increase of electro-mechanical coupling, leading to 4 times reduction of the RF power.
- **Increasing optical  $Q$ .** This can be achieved using our optimized photonic Damascene process [24]. We expect to achieve 100 MHz optical resonance linewidth ( $Q = 2 \times 10^6$ ).

This would lead to RF power reduction to 6 mW. However, there is a trade-off between isolation bandwidth and RF power. Additionally, if microresonators of  $Q > 10^7$  are used, the higher intra-cavity power boosted by higher  $Q$  will induce large resonance shift due to thermal-optic and Kerr nonlinearity. In this case, the resonance shift caused by high input power of the optical signal will be prominent, which will affect the device performance.

- **Increasing mechanical  $Q$ .** This will increase the intra-cavity phonon number under the same input microwave. Currently our mechanical  $Q$  is limited by the acoustic energy leakage into the HBAR mode within the substrate. In the future, the substrate HBAR can be eliminated by roughening the backside surface of the substrate as demonstrated in our previous work [12]. We anticipate at least two times improvement of mechanical  $Q$ .

We estimate that a combination of these strategies could reduce the required RF power to  $\sim 60 \mu\text{W}$ .

Isolators protect lasers from back-reflection and maintain unidirectional transmission of light signals. Recently, there are several demonstrations of self-injection locking of an integrated laser to a  $\text{Si}_3\text{N}_4$  microresonator [33], [225]. Laser self-injection locking enables direct interaction of the laser and the microresonator through back-scattered light from the microresonator, where an optical isolator is absent. However, an integrated optical isolator between the laser and the microresonator is still preferred in certain circumstances that full laser control is required. For example, Ref. [226] shows that an isolator between the semiconductor laser and the  $\text{Si}_3\text{N}_4$  microresonator is needed to increase the optical bandwidth of the generated soliton comb. In this case, an optical isolator of few hundreds of megahertz bandwidth (as our case) is sufficient to cover the laser tuning range for soliton comb generation.

Due to the resonant nature of the optical microresonator, the bandwidth is limited by the optical resonance linewidth. The current bandwidth of our device ( $\sim 700$  MHz) is sufficient for applications such as microwave to optical converters for quantum interconnects [182] and classical optical control and readout of superconducting qubits' states [227], [228], where the

qubit Rabi oscillation is usually on the order of tens of megahertz. The main limitation in these applications is the RF power consumption. In current commercial dilution fridges, the cooling power at 50 K and 4 K stages are 50 W and 1.5 W, respectively. The RF power consumption of our devices can be further reduced to meet the cooling power budget.

In summary, we believe that  $<1$  dB insertion loss and  $>30$  dB isolation can be achieved by optimizing our designs. Together with RF power of less than 1 mW, our integrated optical isolators can meet the requirements for many applications for nonlinear photonics and quantum engineering in the future.

## 6. QUANTUM MICROWAVE TO OPTICAL CONVERTER

### 6.1 Introduction

While superconducting qubits have shown powerful quantum computing and simulation abilities at cryogenic temperatures [229]–[233], the subsequent transporting of quantum information based on microwave carrier is prone to larger thermal noise at room temperature which is proportional to  $k_B T / \hbar \Omega_m$ , where  $k_B$  is the Boltzmann constant,  $T$  the temperature,  $\hbar$  the reduced Planck’s constant, and  $\Omega_m$  the microwave frequency. This largely restricts connecting distant quantum computers for distributed computing and quantum networks. On the other hand, the optical photon has 5 orders of magnitude larger frequency which leads to much less thermal noise at room temperature. Moreover, light has been the workhorse for today’s telecommunication system, and the main building blocks have been commercialized with low cost. Also, quantum key distribution (QKD) [221] via the optical telecommunication system has been well studied, and quantum information processing and simulation has been successfully implemented in an optical circuits all at room temperature [175], [234], [235].

In that sense, coherent microwave to optical conversion has been highly demanded for interfacing superconducting circuits with optical communication systems. While the former conducts high fidelity quantum information processing at cryogenic temperature, the latter enables transmitting quantum states at room temperature with ultra-low loss and thermal noise. This helps to take full advantage of each system for building a hybrid quantum network. To realize the frequency conversion from microwave to optical (or vice versa), optical nonlinear effects are required to induce three-wave-mixing. This is conventionally achieved in electro-optic materials with second order nonlinearity, such as LiNbO<sub>3</sub> [10], [19], [236], [237], LiTaO<sub>3</sub> [238], and AlN [124], [239]. However, since the metal electrodes have to be placed several microns away from the optical waveguide to have low optical losses, current electro-optic modulators show relatively low quantum efficiency due to low electric field confinement. Nevertheless, progressive efforts have been made, pushing the efficiency towards 1% [240] by increasing the pump efficiency via matching two optical modes [106],

[241] or coupling two optical ring resonators [240], [242]–[245], or with microwave-frequency-FSR optical resonator [246], [247].

Another approach that has been widely explored is to achieve the conversion between microwave and light mediated by a mechanical resonator. Strong coupling between superconducting qubit and different mechanical modes has been demonstrated including, SAW [248]–[250], BAW [97]–[99], [251], [252], and phononic crystal [253]–[255]. On the other hand, optomechanical interaction has been largely studied in the past decades [256], and achieved quantum sensing beyond the standard quantum limit. One famous example is the observation of the gravitational wave using LIGO [257]. The strong coupling of mechanics to both microwave and optical light makes it a good candidate for the quantum converter.

Similarly, different mechanical resonators have been investigated aiming at efficient transduction from microwave to mechanics and mechanics to optics. To date, the highest efficiency is achieved in an electro-optomechanical system [258], where a  $\text{Si}_3\text{N}_4$  membrane is capacitively coupled to a microwave  $LC$  cavity, and optomechanically coupled in a Fabry-Pérot optical cavity. Maximum of 10% conversion between microwave and optical is realized. However, the MHz frequency of the membrane resonator presents high thermal noise even at cryogenic temperature. Also, the low mechanical frequency limits the transduction bandwidth. The electro-mechanical excitation of a GHz frequency mechanical mode of an optomechanical crystal resonator has recently been demonstrated with maximum of 1.2% conversion efficiency [259].

Most recently, piezo-optomechanical transduction has drawn much attention, since it enables exciting mechanical resonances at GHz frequency, which can be cooled down to the ground state at cryogenic temperature, and matches with the working frequency with the superconducting qubit. One widely adopted structure is to use the optomechanical crystal (OMC) [260], where both the mechanical and optical modes are confined tightly in a defect of a co-designed 1D photonic and phononic crystal. Different material platforms have been explored in realizing efficient optomechanical coupling, including Si [261]–[263],  $\text{LiNbO}_3$  [264], [265],  $\text{Si}_3\text{N}_4$  [266], AlN [267]–[269], Gallium Phosphide (GaP) [270]–[272], and Gallium Arsenide (GaAs) [273]–[276]. Except for Si and  $\text{Si}_3\text{N}_4$ , others are all good piezoelectric materials. They both show their own advantages which will be discussed in details later. In

general, the mechanical mode is excited by launching surface acoustic waves [264], [265], or coupling to a 3D microwave cavity [275]. The advantage of OMC is the tight confinement of mechanical and optical modes. As can be seen from Eq. 1.22, the optomechanical coupling rate  $g_0$  is inversely proportional to the square root of the mechanical mode volume. OMC has achieved the highest coupling rate on the order of MHz. However, the tight confinement is at the expense of low optical Q on the order of GHz. Also, the small mode volume makes it challenging to impedance match with the external microwave channel [277], and the suspension of the 1D OMC beam in air compromises the thermal conductance.

Another well studied mechanical mode is to excite surface acoustic waves (SAW) by interdigital electrode transducer (IDT). The microwave to optical conversion has been realized and studied by modulating a photonic crystal [278] or an optical ring resonator [15]. IDT can be designed to better impedance match with the microwave transmission line for higher electromechanical conversion efficiency. Also, optical ring resonator usually shows higher optical Q than OMC, and it can support multiple optical modes to match with the pump and signal light.

In contrast, the application of HBAR in microwave to optical conversion is less studied, and the most recent studies couple HBAR with a free space Fabry-Pérot optical cavity [279]–[281]. The free space implementation presents difficulty in on-chip integration which prevents the high volume production, and the stability and robustness of the system is compromised which will be problematic once in the cryogenic chamber. In this thesis, I take advantage of the optical microring structure (high optical Q and triple-cavity design), and couple it with the HBAR mode excited by the AlN actuator as presented in the previous chapters. The advantage of using HBAR compared with SAW is the optical waveguide can be fully cladded which will reduce the influence of the stray light on the superconducting qubit [262]. Also, the HBAR can be immersed in superfluid Helium to have better thermal conductance and cooling. In the following I will present the theory and design of the HBAR based microwave to optical converter, and the first experimental results and future outlook.



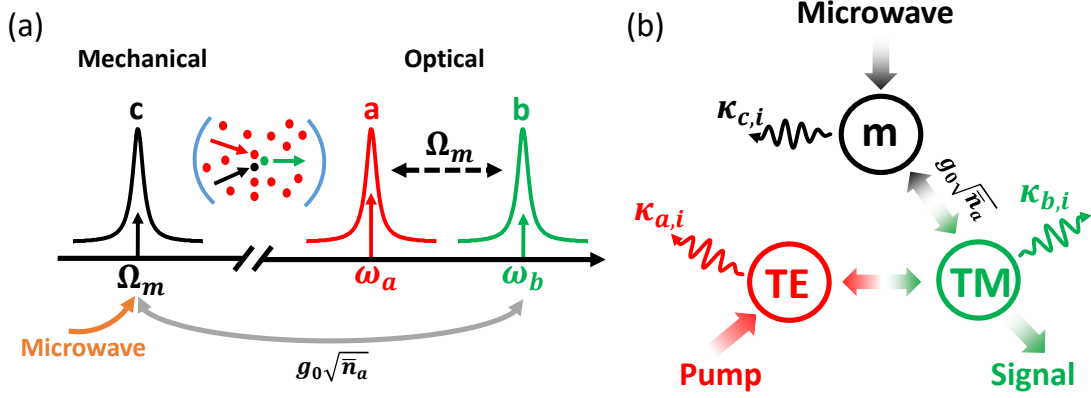


**Figure 6.1.** (a) Schematic showing the coupling between the mechanical mode and two optical modes. The vibration of mechanical resonator scatters pump light in mode  $a$  ( $\omega_a$ ) into higher frequency mode  $b$  ( $\omega_b$ ). The inset shows the quantum picture of the process where an incoming phonon scatters one pump photon into higher frequency signal photon. (b) Schematic for the triple-mode optomechanical system, where the TE mode is pumped which couples the mechanical and TM modes.

## 6.2 Theoretical analysis with Coupled Mode Theory

The theory that describes the system is provided in this section, as well as the figure of merits that guide the device design. I adopt the simplified CMT equations as presented in the last chapter [106], while more rigorous treatment can be found in Refs [168], [273], [282]. It is interesting to find that the converter can be described using the same scheme and equation set as the optical isolator presented in the last section, since they both rely on the three-wave-mixing between acoustic and optical modes.

As shown in Fig. 6.1, I assume there is one mechanical cavity at microwave frequency  $\Omega_m$  and two optical modes with spacing matching the mechanical mode. The two optical modes are also chosen to be TE and TM modes. This triple mode scheme is first proposed [241] and demonstrated [106] in electro-optical converter, which would large boost the pump efficiency of the light. The implementation in piezo-optomechanical converter has not been realized, and most OMC converters only support one optical mode. Different from the isolator, the light that is input into the lower frequency optical mode serves as the pump, while the mechanical and the other optical modes are coupled. The vibration of the mechanical res-

onator will modulate the pump light and generate the anti-Stokes sideband at mode  $b$ , which then carries the quantum information from the microwave channel and gets transmitted to another quantum processor.

From the stand point of quantum picture, as illustrated in the inset of Fig. 6.1, one incoming phonon will be absorbed and scattering one intra-cavity photon into one output higher frequency photon. The reverse process is theoretically possible where the high frequency photon can be split into a pair of photon and phonon. This reversible process also enables the detection of quantum information carried by optical photon for receiver. The scattering strength is characterized by the single-photon coupling strength  $g_0$ , which can be interpreted physically as the scattering rate between input phonon and the up-converted optical photon when there is one pump photon in the optical cavity.  $g_0$  is related with the mode overlap between mechanical and optical mode and is inversely proportional to the mode volume. Thus, by shrinking the device sizes and tightly confining the mechanical mode, we can increase the coupling strength. In an ideal case, we would like to work in the resolved sideband regime where the mechanical frequency is much larger than the optical linewidth. Otherwise, part of the pump photon will be scattered to the lower frequency Stokes sideband, which will become added noise as will be discussed later.

The dynamics of the process can be described by the same equations in Eq. 5.2-5.4. However, the roles of the modes  $a$  and  $c$  are exchanged. Assuming the optomechanical back-action on the property of mode  $a$  is negligible, we can ignore it and get a stationary solution for  $\hat{a}$ :

$$\hat{a} = \frac{\sqrt{\kappa_{a,\text{ex}}}\hat{a}_{\text{in}}}{i\Delta_a + \frac{\kappa_a}{2}} \quad (6.1)$$

And thus the intra-cavity pump photon number can be calculated as:

$$\bar{n}_a = \|\hat{a}\|^2 = \frac{\kappa_{a,\text{ex}}\|\hat{a}_{\text{in}}\|^2}{\Delta_a^2 + \frac{\kappa_a^2}{4}} \quad (6.2)$$

We can define a so-called enhanced optomechanical coupling  $g = g_0\sqrt{\bar{n}_a}$ , which can be understood as the increase of scattering possibility by having more pump photons in the cavity. The dynamic equations for  $\hat{b}$  and  $\hat{c}$  can then be reduced to:

$$-i\Omega_d\hat{b} = -(i\Delta_b + \frac{\kappa_b}{2})\hat{b} - ig\hat{c} \quad (6.3)$$

$$-i\Omega_d\hat{c} = -(i\Omega_m + \frac{\Gamma_c}{2})\hat{c} - ig\hat{b} + \sqrt{\Gamma_{c,\text{ex}}}\hat{c}_{\text{in}} \quad (6.4)$$

According to the input-output theorem in Eq. 5.6, the output of optical field  $\hat{b}$  can be calculated as:

$$\hat{b}_{\text{out}} = \frac{ig\sqrt{\kappa_{b,\text{ex}}\Gamma_{c,\text{ex}}}}{g^2 + [i\Delta_m + \Gamma/2][i(\Delta_b - \Omega_d) + \kappa_b/2]}\hat{c}_{\text{in}} \quad (6.5)$$

where  $\Delta_m = \Omega_m - \Omega_d$ . Finally, the overall quantum conversion efficiency can be calculated as:

$$\eta = \left\| \frac{\hat{b}_{\text{out}}}{\hat{c}_{\text{in}}} \right\|^2 = \frac{\kappa_{b,\text{ex}}}{\kappa_b} \frac{\Gamma_{c,\text{ex}}}{\Gamma_c} \frac{4C}{\|C + (1 + 2i(\Delta_b - \Omega_d)/\kappa_b)(1 + 2i\Delta_m/\Gamma_c)\|^2} \quad (6.6)$$

where  $C = C_0\bar{n}_a$  is the enhanced cooperativity, and  $C_0 = \frac{4g_0^2}{\kappa_b\Gamma_c}$  is the single photon cooperativity, that measures the coupling strength relative to the loss rate of mechanical and optical cavities. In practical application, we usually set the microwave drive at the mechanical resonant frequency:  $\Delta_m = \Omega_m - \Omega_d = 0$ , and the detuning of pump equals microwave frequency  $\Delta_b = \Omega_d$  such that field  $\hat{b}$  is on resonance. The efficiency can be reduced to:

$$\eta = \frac{\kappa_{b,\text{ex}}}{\kappa_b} \frac{\Gamma_{c,\text{ex}}}{\Gamma_c} \frac{4C}{(1 + C)^2} \quad (6.7)$$

From the above equation, the overall system efficiency can be divided into mainly three parts: the coupling efficiency from input microwave photon to phonon in the mechanical cavity,  $\eta_{\text{ex,m}} = \Gamma_{c,\text{ex}}/\Gamma_c$ ; the internal conversion efficiency from phonon to optical photon  $\eta_{\text{in}} = 4C/(1 + C)^2$ , occurring in the optical cavity; and the coupling efficiency from intra-cavity photon to output bus waveguide  $\eta_{\text{ex,opt}} = \kappa_{b,\text{ex}}/\kappa_b$ , which then connects to optical fiber for long distance communication. The dependence of internal conversion efficiency on system cooperativity is calculated and plotted in Fig. 6.2(b). It can be seen the internal

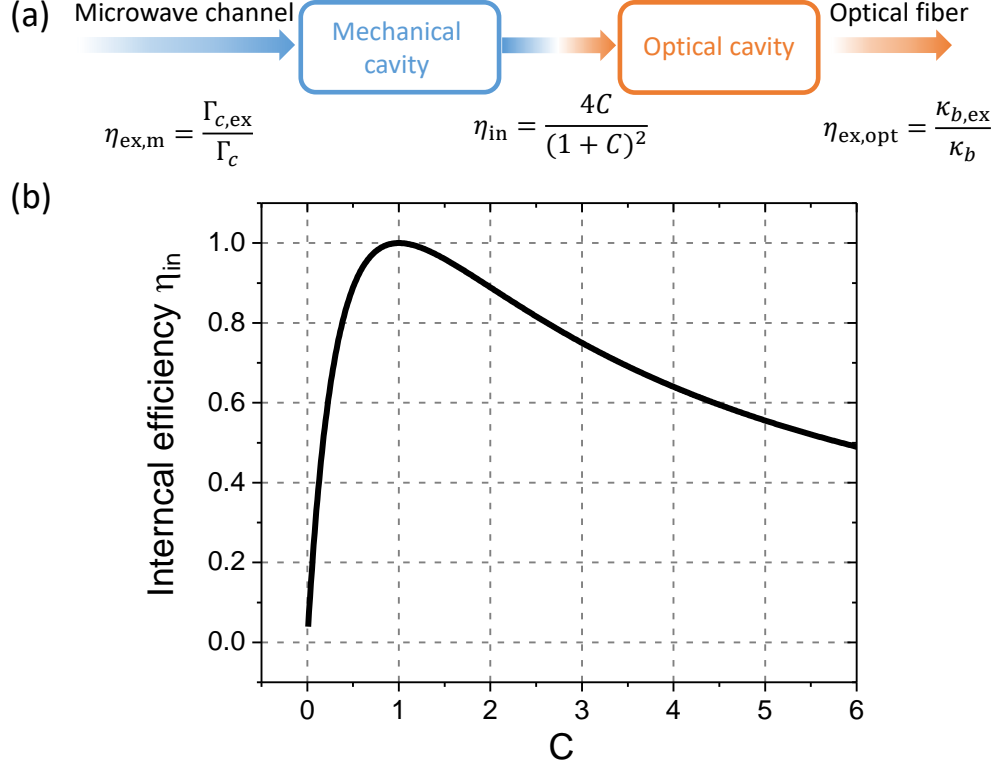


**Figure 6.2.** (a) Schematics showing the cascaded coupling efficiencies that determine overall system efficiency, including input coupling efficiency from microwave channel to mechanical cavity  $\eta_{\text{ex,m}}$ , intra-cavity conversion efficiency from mechanical phonon to photon  $\eta_{\text{in}}$ , and output coupling efficiency from optical cavity to fiber  $\eta_{\text{ex,opt}}$ . (b) The dependence of internal efficiency on enhanced cooperativity  $C$ .

efficiency reaches maximum 100% when  $C = 1$ . This can be understood qualitatively that, if the scattering rate  $g$  is much smaller than loss rate of mechanical and optical cavities, most of the intra-cavity phonon and photon are lost which leads to small efficiency. However, if  $g$  is much larger than the loss rate and thus the external coupling rate  $\kappa_{b,\text{ex}}$ , the generated photon will be converted back to phonon before being extracted to output waveguide. Therefore,  $g$  should be on the similar magnitude with the loss rate and thus  $C = 1$ . This is in contrast to the isolator case where  $C \gg 1$  is required for mode splitting.

To have high overall system efficiency, the external coupling efficiency is also important. Thus, it is preferred to have overcoupling for the mechanical and optical cavities,  $\kappa_{b,\text{ex}}/\kappa_b \sim 1$  and  $\Gamma_{c,\text{ex}}/\Gamma_c \sim 1$ . However, assuming intrinsic loss is fixed, this inevitably increases the total

loss and lowers the Q, and finally cooperativity  $C_0$ . To have  $C = 1$  we need to increase the pump power which in turn increases the thermal noise. Thus, there is a trade-off between efficiency and noise we need to consider in the real device design.

In most OMC structure, where only one optical mode is incorporated, the detuning of pump light makes it inefficient to pump into the optical cavity, especially when working deeply in resolved sideband regime ( $\Delta \gg \kappa$ ). This requires to increase the input pump power to have reasonable amount of intra-cavity photon for  $C = 1$ . However, the high power leads to larger thermal noise. To mitigate the high required power, it is proposed here to use a second optical resonance that aligns with the pump light to accumulate more pump photons inside the cavity, as shown in Fig. 6.1. When aligned with the resonance of mode  $a$ , the intra-cavity pump photon number can be calculated:

$$\bar{n}_a = \frac{4\kappa_{a,\text{ex}}}{\kappa_a^2} \frac{P_{\text{in,opt}}}{\hbar\omega_a} \quad (6.8)$$

where  $P_{\text{in,opt}}$  is the input pump power and  $\omega_a$  is the resonant frequency of mode  $a$ . As we increase the optical Q, we have more long lived photon in the cavity, which increases the possibility and rate for one phonon to be scattered into output photon.

### 6.2.1 Relation between $\eta$ and optomechanical $S_{21}$

The quantum conversion efficiency can be estimated from the optomechanical  $S_{21}$  measurement following the method in Ref. [15]. At first, the classical expression for the  $S_{21}$  is derived. To be consistent with the optomechanical  $S_{21}$  measurement performed for the unreleased and released devices before, I assume there is only one optical mode, and the cooperativity is low such that the back-action on the mechanical cavity can be ignored. In

that case, we can solve Eqs. 6.3-6.4 classically, and get the output electric field magnitude for the carrier  $A_{0,\text{out}}$  and anti-Stokes sideband  $A_{+,\text{out}}$ :

$$A_0 = \frac{\sqrt{\kappa_{\text{ex}}} A_{\text{in}}}{(i\Delta + \kappa/2)} \quad (6.9)$$

$$A_+ = -\frac{ig_0 B A_0}{i(\Delta - \Omega_d) + \kappa/2} \quad (6.10)$$

$$A_{0,\text{out}} = A_{\text{in}} - \sqrt{\kappa_{\text{ex}}} A_0 \quad (6.11)$$

$$A_{+,\text{out}} = -\sqrt{\kappa_{\text{ex}}} A_+ \quad (6.12)$$

where  $A_0$  and  $A_+$  are the magnitude of the intra-cavity optical field of the carrier and anti-Stokes sideband.  $A_{\text{in}}$  is the input electric field magnitude and its square is the input photon flux:  $A_{\text{in}}^2 = P_{\text{in,opt}}/\hbar\omega_L$ .  $\Delta = \omega_0 - \omega_L$  is the detuning of the laser relative to the optical cavity.  $B$  is the magnitude of the intra-cavity acoustic field, which is normalized such that its square is the intra-cavity phonon number as:

$$B^2 = \frac{4\Gamma_{\text{ex}}}{\Gamma^2} \frac{P_{\text{in},m}}{\hbar\Omega_d} \quad (6.13)$$

The output microwave voltage of the photodetector  $U$  can be calculated as:

$$U = R_{\text{PD}} \hbar\omega_L \|A_{+,\text{out}} A_{0,\text{out}}\| \quad (6.14)$$

$$= R_{\text{PD}} P_{\text{in,opt}} g_0 B \left\| \frac{\kappa_{\text{ex}}}{i(\Delta - \Omega_d) + \kappa/2} \frac{i\Delta + \kappa/2 - \kappa_{\text{ex}}}{(i\Delta + \kappa/2)^2} \right\| \quad (6.15)$$

$$= R_{\text{PD}} P_{\text{in,opt}} g_0 B \chi(\Omega_d, \Delta) \quad (6.16)$$

where  $R_{\text{PD}}$  is the responsivity of the photodetector in unit of V/W. The output microwave power of the photodetector measured by the VNA is:

$$P_{\text{out},m} = \frac{U^2}{2R_0} = \frac{R_{\text{PD}}^2 P_{\text{in,opt}}^2 g_0^2}{2R_0} \frac{4\Gamma_{\text{ex}}}{\Gamma^2} \frac{P_{\text{in},m}}{\hbar\Omega_d} \|\chi\|^2 \quad (6.17)$$

where  $R_0 = 50 \Omega$  is the impedance of the VNA. Therefore, the  $S_{21}$  can be calculated as:

$$S_{21} = \frac{P_{\text{out},m}}{P_{\text{in},m}} = \frac{2\Gamma_{\text{ex}}R_{\text{PD}}^2P_{\text{in,opt}}^2g_0^2}{\Gamma^2\hbar\Omega_dR_0}\|\chi\|^2 \quad (6.18)$$

When the laser detune equals the microwave drive and mechanical frequency,  $\Delta = \Omega_d = \Omega_m$ , and also the device works in the resolved sideband regime.  $S_{21}$  can be reduced to:

$$S_{21} = \frac{8\kappa_{\text{ex}}^2\Gamma_{\text{ex}}R_{\text{PD}}^2P_{\text{in,opt}}^2g_0^2}{\kappa^2\Gamma^2\hbar\Omega_d^3R_0} \quad (6.19)$$

The conversion efficiency can be related with the  $S_{21}$  if we find out their definitions as:

$$\eta = \frac{P_{+, \text{out}}/\hbar\omega_L}{P_{\text{in},m}/\hbar\Omega_d} \quad (6.20)$$

$$S_{21} = \frac{R_{\text{PD}}^2P_{+, \text{out}}P_{0, \text{out}}}{2R_0P_{\text{in},m}} \quad (6.21)$$

where  $P_{+, \text{out}}$  and  $P_{0, \text{out}}$  are the output optical power of the anti-Stokes sideband and the carrier. Therefore, the efficiency can be related with  $S_{21}$ :

$$\eta = \frac{2R_0}{R_{\text{PD}}^2P_{0, \text{out}}}\frac{\Omega_d}{\omega_L}S_{21} \quad (6.22)$$

The output power in the carrier  $P_{0, \text{out}}$  can be related with the input optical power as:

$$P_{0, \text{out}} = \left\| \frac{i\Delta + \kappa/2 - \kappa_{\text{ex}}}{i\Delta + \kappa/2} \right\|^2 P_{\text{in,opt}} \quad (6.23)$$

In the resolved sideband regime  $\Delta \gg \kappa$ ,  $P_{0, \text{out}} = P_{\text{in,opt}}$ . Note the above efficiency is off-chip efficiency which includes the coupling loss from the chip to the edge coupling optical lensed fiber.

### 6.2.2 Derivation of $V_\pi$ from $S_{21}$

The expression for the  $V_\pi$  of an AOM is derived in Ref. [264] as:

$$V_\pi = \frac{\Omega_m \pi \sqrt{2P_{\text{in},m} R_0}}{g_0 B} \quad (6.24)$$

By inserting Eq. 6.13 into the above expression, we can get:

$$V_\pi^2 = \frac{\hbar \Omega_m^3 \pi^2 R_0 \Gamma^2}{2g_0^2 \Gamma_{\text{ex}}} \quad (6.25)$$

By multiplying Eq. 6.19 and Eq. 6.25 and cancelling most of the terms in the numerator and denominator, we can get the following neat expression

$$S_{21} = \left( \frac{2\kappa_{\text{ex}}}{\kappa} \frac{\pi R_{\text{PD}} P_{\text{in,opt}}}{V_\pi} \right)^2 \quad (6.26)$$

If the optical mirroring is critically coupled, it can be further reduced to:

$$S_{21} = \left( \frac{\pi R_{\text{PD}} P_{\text{in,opt}}}{V_\pi} \right)^2 \quad (6.27)$$

Interestingly, this expression is the same as the one derived in Ref. [15] for Mach-Zehnder Interferometer (MZI).

### 6.2.3 Efficiency of the isolator device

From the above derived expressions, the AOM efficiency for the optical isolator from the last chapter can be estimated as a starting point. Figure 6.3 shows the measured  $S_{11}$  and  $S_{21}$  for one actuator of the isolator device. Here, only one optical mode is utilized. The pump power is 40  $\mu\text{W}$  and is detuned from the resonance. The  $S_{21}$  is -51.5 dB for the mode at 3.42 GHz as labeled by the red arrow. The quantum efficiency is thus calculated from Eq. 6.22 which is around  $5 \times 10^{-10}$ . Note the optical pump power is small (40  $\mu\text{W}$ ) and only one actuator is excited which covers one third of the ring. The efficiency can be increased by increasing the pump power. However, there is a limit of the maximum power that we can



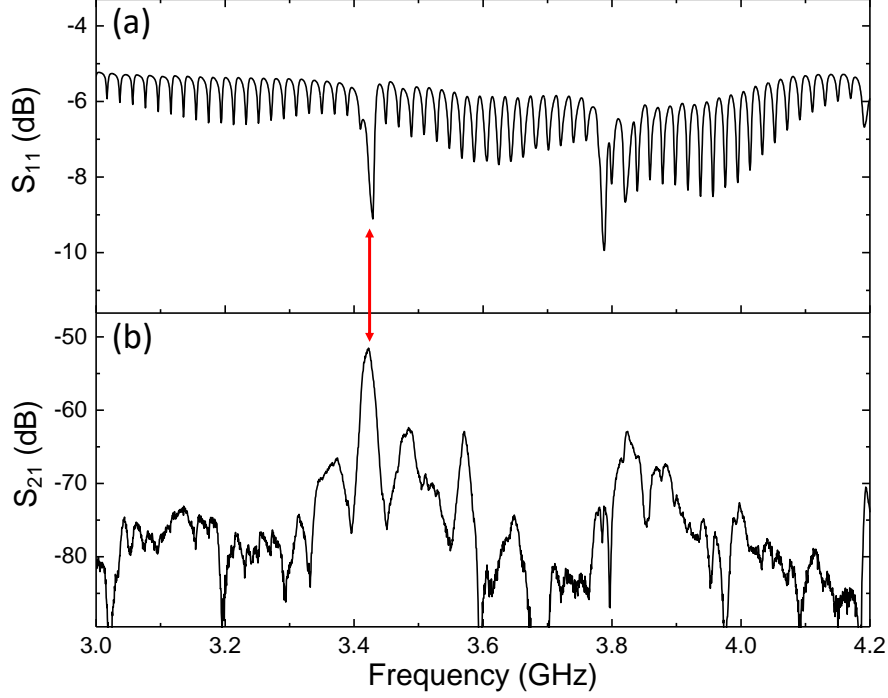


**Figure 6.3.** (a) Electromechanical  $S_{11}$  and (b) optomechanical  $S_{21}$  of one actuator of the isolator device. The red arrow denotes the mode that is analyzed.

apply in the dilution fridge, depending on the cooling power and thermal conductance. The  $V_\pi$  is calculated from Eq. 6.26 around 26 V. Other parameters of the device are summarized in Table 6.1. Therefore, to increase the efficiency, we need to design a new device with larger optomechanical coupling  $g_0$  and smaller optical and mechanical losses, as will be discussed below.

### 6.3 Device design

Based on the above analysis, there are several design goals for designing a converter with high efficiency and low added noise: 1. larger optical and mechanical Q; 2. large single photon scattering rate  $g_0$ . In practice, it is usually hard to meet the two requirement in the same time. To achieve large  $g_0$ , we need to confine optical mode into tight space, which in turn suffers large scattering losses due to fabrication. Nowadays, the state of art  $g_0$  has been achieved in optomechanical crystal (OMC) structures sub-micron confinement of optical and

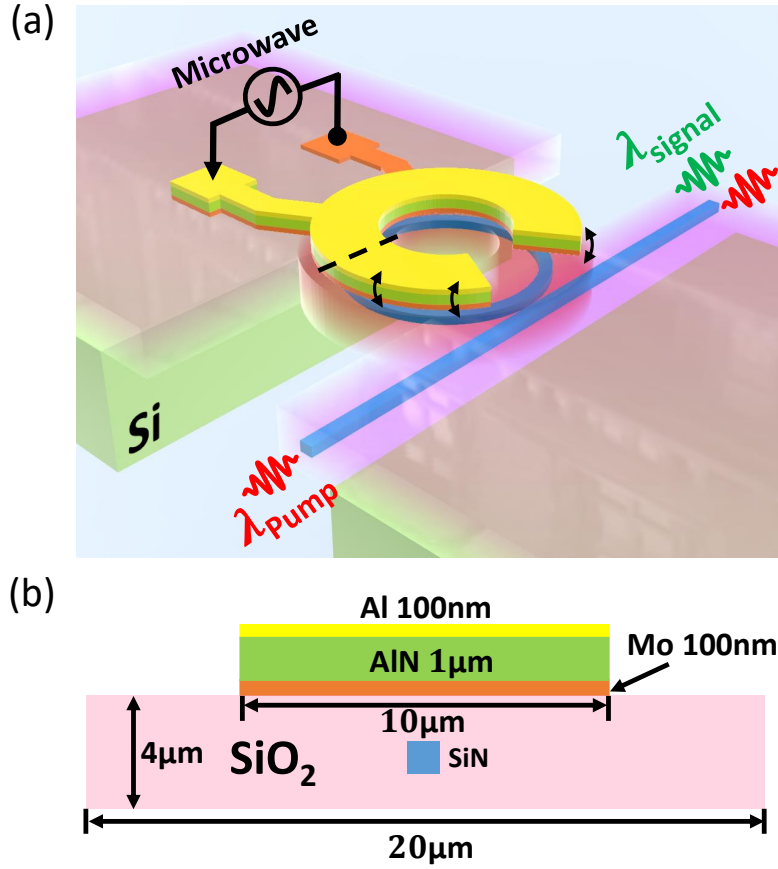


**Figure 6.4.** (a) Schematic showing the proposed piezo-optomechanical quantum converter. By driving the piezoelectric actuator with microwave signal, the input pump light is scattered to output signal photon with high quantum efficiency. (b) Cross-section along the black dashed line in (a).

mechanical modes [264]. However, limited by nano-fabrication, OMC usually shows low optical  $Q$  ( $\sim 10^5$ ) with linewidth on the order of GHz.

Higher optical  $Q$  ( $\sim 10^6 - 10^7$ ) can be achieved in optical ring resonators. Here, I propose to couple the HBAR mode with the  $\text{Si}_3\text{N}_4$  microring resonator to demonstrate an efficient microwave to optical converter. As shown in Fig. 6.4, HBAR is generated by an AlN piezoelectric actuator, which is overlaid on top of a  $\text{Si}_3\text{N}_4$  optical ring resonator that is buried inside a released  $\text{SiO}_2$  membrane. The full cladding of  $\text{Si}_3\text{N}_4$  waveguides helps isolate optical circuits from external environment and mechanical vibrations, making it robust compared with the OMC systems where there is an air gap between the OMC and bus waveguide. By

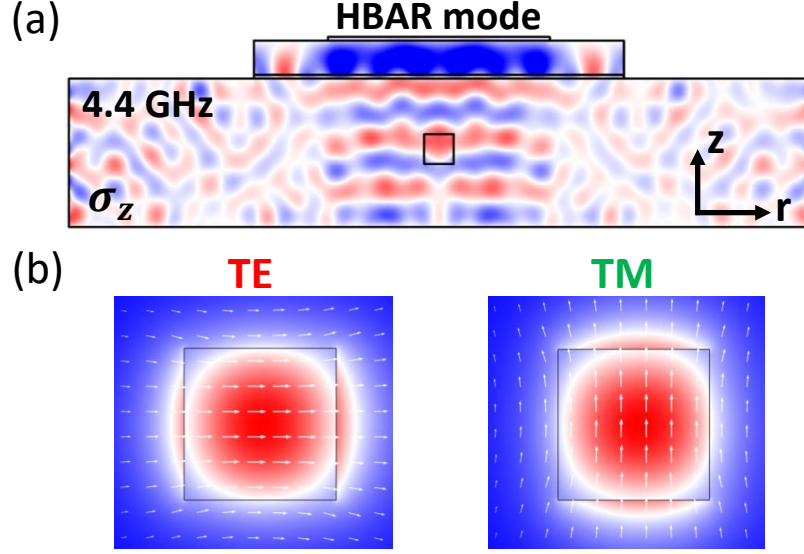


**Figure 6.5.** (a) Vertical stress distribution of one typical HBAR mode at 4.4 GHz. (b) Electric field distribution of TE and TM modes with close frequency spacing. The white arrows denote the magnitude and direction of the electric field.

applying a microwave signal, the AlN film starts vibrating and transmitting acoustic wave vertically which are tightly confined in the SiO<sub>2</sub> Fabry-Pérot acoustic cavity. To further shrink the optical and mechanical mode volume, the radius of the optical ring is reduced to 22  $\mu\text{m}$  while maintaining ultra-high optical  $Q$  ( $\sim 5 \times 10^5$ ) by using the reflow Damascene process for fabricating high  $Q$  Si<sub>3</sub>N<sub>4</sub> ring resonator [118].

The dimensions of vertical stacking are shown in Fig. 6.4(b). 1  $\mu\text{m}$  AlN is chosen which presents its fundamental resonance around 4 GHz. 4  $\mu\text{m}$  SiO<sub>2</sub> cavity forms a series of mechanical resonances with spacing of 500 MHz. By aligning AlN and SiO<sub>2</sub> resonances, one of the HBAR modes can be efficiently excited at 4.4 GHz as shown in the simulation of Fig. 6.5(a). Similar as the isolator, to efficiently convert one pump photon into signal photon, energy and momentum conservation of the process must be satisfied. Ideally, the pump and signal optical modes need to have the same azimuthal order  $m$ . However, it is experimentally hard to have TE and TM modes with the same  $m$  and in the same time have close frequency spacing, since the non-vertical sidewall of the waveguide inevitably strongly hybridizes the TE and TM modes [106]. Therefore, a quasi-square waveguide ( $800 \times 801 \text{ nm}^2$ ) is chosen for

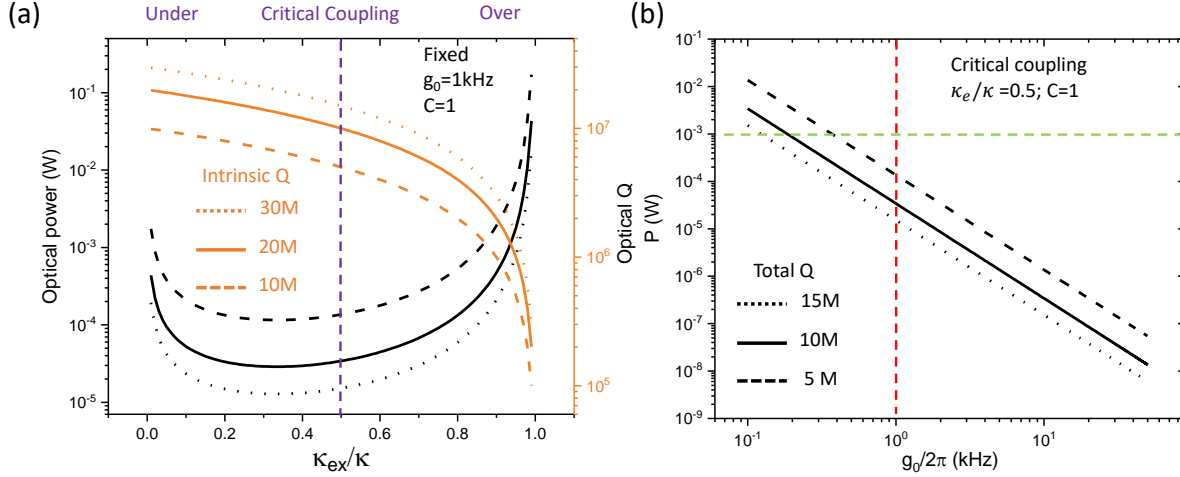


**Figure 6.6.** (a) Dependence of the required pump optical power to achieve  $C = 1$  (left Y axis) and total optical Q (right Y axis) on external coupling strength for fixed  $g_0 = 1$  kHz. Three different intrinsic Q are chosen that are experimentally realizable. M is short for Million. (b) Dependence of the required pump power on the optomechanical coupling strength  $g_0$  under critical coupling regime for three different optical Q. The green dashed line show the power level of 1 mW and red dashed line shows the position of 1 kHz  $g_0/2\pi$  as estimated in simulation.

TE and TM modes to have close effective refractive index and frequency spacing equal to the mechanical resonance  $\Omega_m$ . The mode shape of the two modes are simulated as in Fig. 6.5(b). The mode with lower frequency is chosen as pump to avoid phonon lasing and system instability. By doing mode overlap integral in COMSOL simulation, the coupling between mechanical and optical mode is estimated to be  $g_0/2\pi \sim 1$  kHz.

It is reasonable to examine the influence of the variation of device parameters on the performance. Since the ideal working condition is  $C = 1$ , the required pump optical power to achieve this condition can work as a figure of merit which leverages efficiency and added noise. The smaller the pump power, the better the device. As shown in Fig. 6.6 is the dependence of pump power on the external coupling strength  $\kappa_{\text{ex}}$  for fixed  $g_0$ . Three different regions can be found depending on the relative strength of  $\kappa_{\text{ex}}$  and  $\kappa$ : under-coupling region when  $\kappa_{\text{ex}}/\kappa < 0.5$ , critical coupling when  $\kappa_{\text{ex}}/\kappa = 0.5$ , and over-coupling when  $\kappa_{\text{ex}}/\kappa > 0.5$ . As pointed out in the last section, it is preferred to work at over-coupled region to increase the extraction efficiency of signal photon. However, from the calculation, the required pump

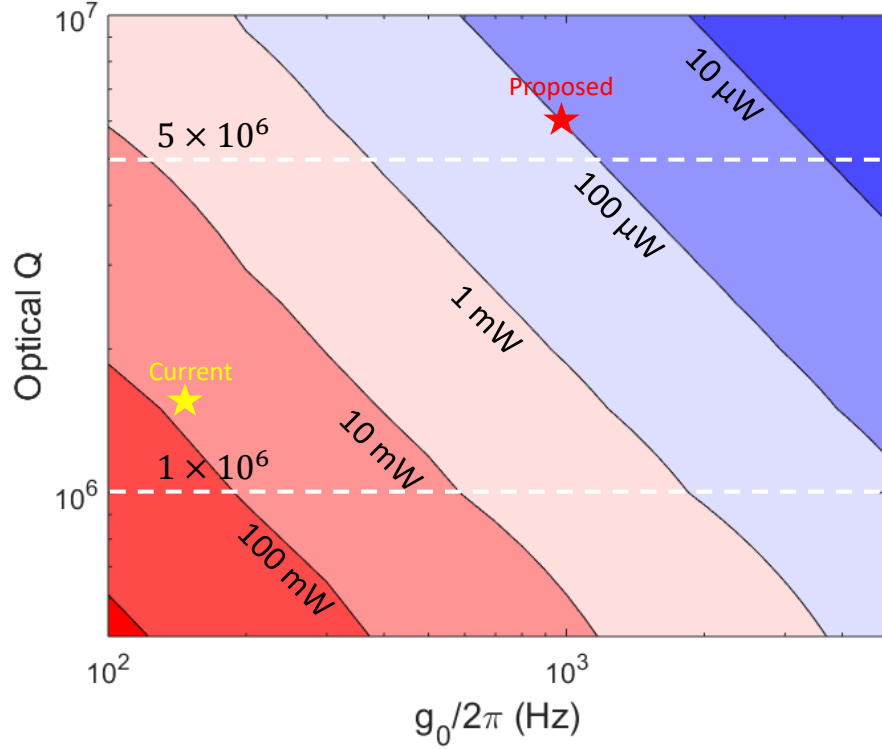


**Figure 6.7.** 2D contour plot of the required pump power for various optical  $Q$  and  $g_0$  under critical coupling. The mechanical loss rate is assumed to be 1 MHz. The red (yellow) star indicates the proposed (current measured) device parameters.

power will increase due to reduced quality factor. It is interesting to see that we will get the lowest power around critical coupling region rather than under-coupling. This is because at under-coupling, the coupling efficiency of pump into the cavity is decreased which reduces the intra-cavity photon. So we don't want to work at this region which not only has low extraction efficiency but requires higher pump power. Thus, the design goal is to push the system towards the bottom right corner of Fig. 6.6(a). By optimizing the fabrication process, the intrinsic  $Q$  can be increased which will lower the pump power in Fig. 6.6(a). Due to the maturity of fabricating ultra-low loss  $\text{Si}_3\text{N}_4$  waveguides, intrinsic optical  $Q$  of 10 million to 20 million can be achieved, indicating sub-100  $\mu\text{W}$  power can be achieved with 80% extracting efficiency.

The dependence of power on the optomechanical coupling strength  $g_0$  is also characterized in Fig. 6.6(b), where the power depends on the square of  $g_0$ . We can still have sub-mW pump

**Table 6.1.** Comparison with experimental demonstrations of microwave to optical converters in the literature using electro-optic (EO) or piezo-optomechanical (OM) methods. Note the “isolator” device is the same device presented in the last chapter and driven with a single optical mode. The proposed device is with two optical modes.

Ref.	[243]	[106]	[262]	[264]	Isolator	Proposed
Year	2020	2018	2020	2020		
Method	EO	EO	OM	OM	OM	OM
Material	LiNbO <sub>3</sub>	AlN	Si+AlN	LiNbO <sub>3</sub>	Si <sub>3</sub> N <sub>4</sub> +AlN	Si <sub>3</sub> N <sub>4</sub> +AlN
Structure	Ring	Ring	OMC	OMC	Ring	Ring
$g_0/2\pi$ (kHz)	1.2	0.3	420	80	0.07	1
$\kappa/2\pi$ (GHz)	0.6	0.285	1.6	1.2	0.377	0.03
$\kappa_{\text{ex}}/\kappa$	0.22	0.3	0.5	0.67	0.34	0.67
$\Gamma/2\pi$ (MHz)	21.6	0.5	0.45	2	14	1
$\Omega_m/2\pi$ (GHz)	6.8	8.3	5.16	2	3.42	4
$C_0$	$4.4 \times 10^{-10}$	$2.3 \times 10^{-9}$	$9.6 \times 10^{-4}$	$1.2 \times 10^{-5}$	$4 \times 10^{-12}$	$1.3 \times 10^{-7}$
$P_{\text{in,opt}}$ ( $\mu\text{W}$ )	100	5000	2	3.3	40	100
$C$	$3.6 \times 10^{-5}$	$7.5 \times 10^{-2}$	$4.2 \times 10^{-2}$	$6.5 \times 10^{-3}$	$2.17 \times 10^{-9}$	1
$\eta$	$6.6 \times 10^{-6}$	$2 \times 10^{-2}$	$1 \times 10^{-3}$	$1.7 \times 10^{-5}$	$5 \times 10^{-10}$	$1 \times 10^{-2}$

power when  $g_0/2\pi$  is around 200-300 Hz for the optical Q above 5 Million, which is achievable in the experiment. To better estimate the performance of the device, the dependence of the required power on optical Q and  $g_0$  is summarized in the 2D contour plot in Fig. 6.7. From our previous experiments, optical Q of 5-10 million is achievable with optimized fabrication. Around the estimated  $g_0/2\pi$  of 1 kHz, optical power as low as tens of microWatts is sufficient to achieve  $C = 1$  for 100% internal conversion efficiency. However, as the optical Q drops to 1 Million, the pump power increases to 10-100 mW for  $g_0/2\pi$  between 100-1000 Hz.

To put our design into perspective, I compare it with the most recently demonstrated converters using electro-optic (EO) [106], [243] or piezo-optomechanical crystal (OMC) [262], [264] methods, as shown in Table 6.1. While the OMC structure presents the highest  $g_0$ , optical microring has generally higher optical Q. Although OMC has higher single photon cooperativity, microring can pump more photon into the cavity because of the ability to have two optical modes and high optical Q, which helps it to achieve a similar order of the enhanced cooperativity. Although the current device is far from the best performance, there is still much room to improve in the future by increasing the optical Q and the  $g_0$ ,

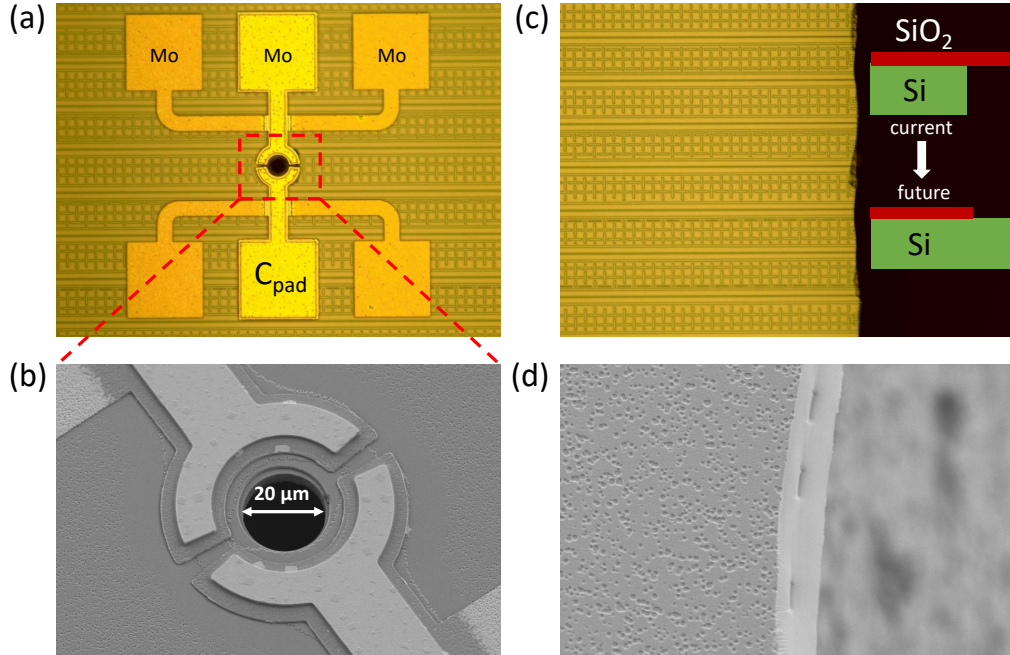


**Figure 6.8.** (a) Optical microscope image of the fabricated device with two AlN actuators fabricated on the same  $\text{Si}_3\text{N}_4$  microring resonator with  $22\ \mu\text{m}$  radius (THz FSR). (b) Zoom-in SEM of the device in the red dashed box in (a). (c) Optical image of the chip edge. The inset shows the pre-off of the Si at the chip edge to compensate for the etching during release in the future. (d) Zoom-in SEM of the chip edge after the breaking of the suspended oxide membrane.

as indicated by the proposed device. From these observations, the proposed microwave to optical converter based on the AlN-on-SiN platform can serve as an attractive quantum optical interface with high efficiency, low noise, and low cost (low power consumption and ease of fabrication). It is also compatible with cryogenic temperature and can be co-integrated with SC circuits for future hybrid integrated quantum system capable of quantum computing and communication.

#### 6.4 Experimental realization with $22\ \mu\text{m}$ radius device

Based on previous design, a new device with  $22\ \mu\text{m}$  radius (with THz FSR optical microring) is designed and fabricated as shown in Fig. 6.8(a). The zoom-in SEM of the device can be seen in Fig. 6.8(b). Due to the non-vertical sidewall of the waveguide, TE and TM



modes are coupled and hybridized, and sometimes the coupling is so strong that the spacing of them is too large to match with the mechanical resonances, especially when they have the same azimuthal order [106]. Thus, in the waveguide design, TE and TM are purposely designed to have slightly different azimuthal order. Two actuators are designed to match the momentum mismatch between TE and TM. Different than previous AlN actuators, the top and bottom metals are both made from Mo, which is especially important for small devices to avoid misalignment between the top metal and AlN. While testing the new devices, there appeared more challenges than expected. Each of them are presented in the followings.

#### 6.4.1 Challenge 1: releasing of the chip edge

As the scale of the device decreases, the size of the center releasing hole is also shrunk to 20  $\mu\text{m}$  in diameter as shown in Fig. 6.8(b). This undesirably extends the time required to fully release the actuators. This long time releasing inevitably etches the Si at the edge of the chip, which forms a suspended oxide membrane. The membrane in most case is too fragile and breaks as shown in Fig. 6.8(c). This increases the coupling loss from the chip edge to the lensed fiber to above 10 dB, which largely reduces the overall efficiency. Since the wafer is diced into pieces using a DRIE etching process and the releasing step is after that, a pre-offset of the Si at the chip edge during the DRIE can be applied to compensate for the etching of Si during releasing in the future, as illustrated in the inset of Fig. 6.8(c). With this modification of the fabrication, we can avoid releasing of the chip edge and preserve high edge coupling efficiency.

#### 6.4.2 Challenge 2: nonuniform releasing of the actuator

The other challenge of the fabrication is the nonuniform releasing of the oxide membrane where the optical microring resides in, as shown in Fig. 6.9(a). The Si beneath the oxide is isotropically etched with gas  $\text{XeF}_2$  which leads to an uneven edge at the released oxide membrane's anchor. It can be seen nearly half of the optical ring is not fully released which would reduces the AOM efficiency by half. It is found out that  $\text{SF}_6$  will isotropically etch Si in a more uniform way. As shown in Fig. 6.9(b), a uniform releasing circle and smooth



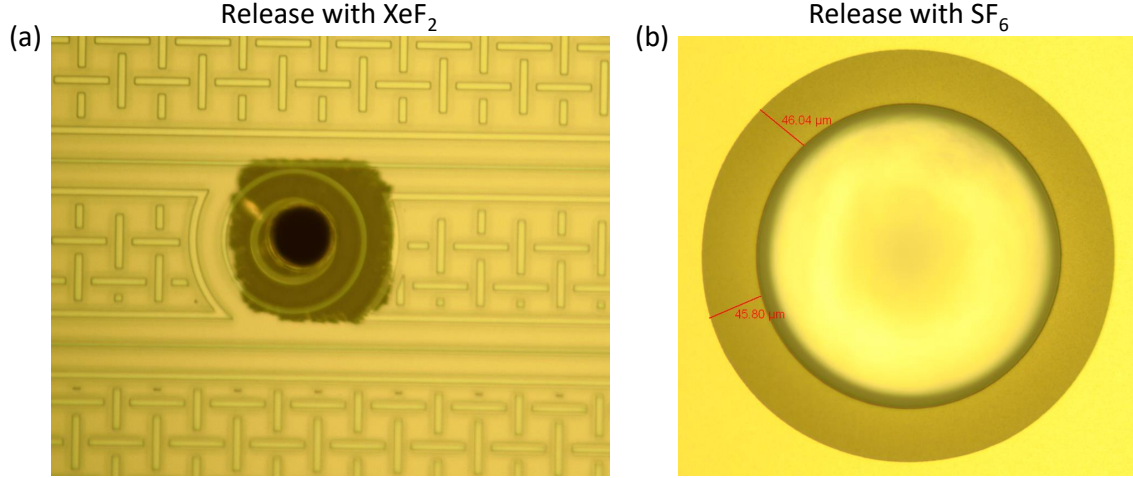


**Figure 6.9.** (a) Nonuniform releasing of the optical microring resonator with  $\text{XeF}_2$ . (b) Releasing of the oxide membrane with  $\text{SF}_6$  which generates a uniform circle.

edge can be achieved with  $\text{SF}_6$ . Therefore, in the future, by incorporating  $\text{SF}_6$ , we can have a more uniform releasing of the actuator, which will largely improve the mechanical Q and HBAR excitation efficiency.

### 6.4.3 Challenge 3: non-ideal optical modes

The typical optical transmission spectrum of different devices are shown in Fig. 6.10. It can be seen most of the optical resonances show triangle shape instead of Lorentz. Despite of that, the loaded optical Q is as high as 1.4 Million. For nearly half devices, there is a prominent mode splitting due to the back scattering with splitting as high as 500 MHz. This is typical for optical microring resonator with THz FSR, because as the bending radius decreases, more portion of the optical mode locates at the outer sidewall of the microring where the roughness of the sidewall will cause Rayleigh scattering (see Fig. 6.5(b) TE mode). The undesired back scattering will lose nearly half of the optical pump and signal and lower the quantum efficiency by four times (as both the pump and signal are halved). More severe problem is the smallest spacing between the TE and TM modes is found to be around 30 GHz which is much larger than the HBAR resonances, making the triple mode operation impossible. This is mainly because as the FSR increases, the difference of the FSR

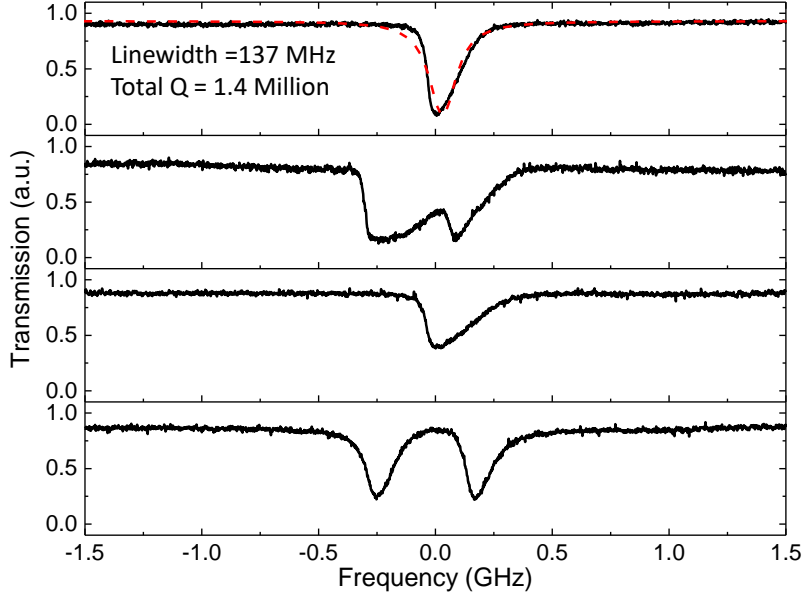


**Figure 6.10.** Optical transmission spectrum for different devices. The red dashed line is the Lorentz fitting with linewidth of 137 MHz, which indicates an optical Q of 1.4 Million.

between TE and TM modes also increases which exaggerates changing of the mode spacing over mode order. Furthermore, only few modes can be supported in the measurement range which lowers the possibility of finding the optimal mode spacing. In the future, we can decrease the FSR to 500 GHz with radius of 40  $\mu\text{m}$  to solve these problems and further increase the optical Q.

#### 6.4.4 Challenge 4: undesired HBAR beneath the signal pad

Since the bottom metal and AlN are deposited at the same time, there is bottom metal left beneath the signal pad as shown in Fig. 6.8(a). Therefore, the signal pad itself also forms a capacitor as part of the entire device, in parallel with the released actuator. Since the area of the signal pad is much larger than the actuator itself, it will dominate the electromechanical response of the whole device. Electrically, the large capacitance of the pad leads to small impedance which draws most of the current through it. Mechanically, the pad will also excite bulk acoustic waves into the Si substrate, as it is not released. It turns

out that these unreleased HBAR modes dominate the mechanical modes of the device, such that most of the input RF power is lost into the Si substrate without going into the released actuator. Consequently, the excitation efficiency of the released HBAR mode around the optical waveguide is quite small, as will be shown later. To circumvent the problem from the large signal pad, a novel so-called band-aid fabrication process will be developed in the future [283]. The purpose of the band-aid process is to remove the AlN and bottom metal beneath the signal pad, and route the top trace directly on top of the oxide cladding, which will get rid of the pad capacitance. This will also ease the wire bonding to the signal pad which is required for the application in the dilution fridge.

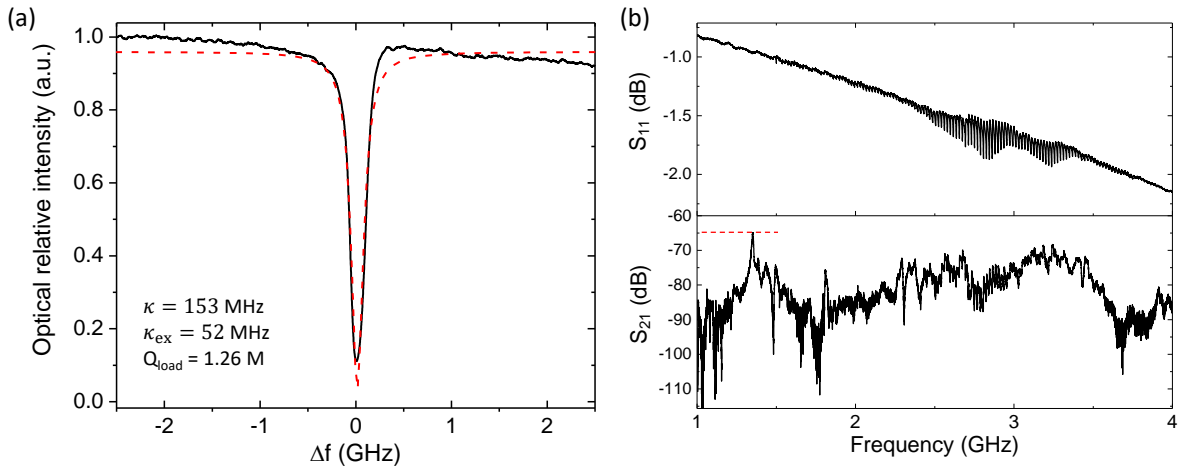


**Figure 6.11.** (a) Optical transmission spectrum of the TE mode. It is fitted with the Lorentz function (red dashed line), with linewidth of 153 MHz. (b) Electromechanical  $S_{11}$  and optomechanical  $S_{21}$  measured on one actuator.

## 6.5 Estimation of efficiency $\eta$ and $g_0$

Although it is hard to find the optimal spacing for the TE and TM modes, the measurement of AOM with one optical mode (here TE mode) can be conducted to estimate the AOM efficiency and the optomechanical coupling rate  $g_0$ , as shown in Fig. 6.11. The optical transmission spectrum of the TE mode is illustrated in Fig. 6.11(a), showing 153 MHz linewidth and loaded optical Q of 1.26 Million. Total of 583  $\mu\text{W}$  TE light is output from the laser, and only 106  $\mu\text{W}$  is coupled into the chip with around 7.3 dB loss per coupling facet. 19.7  $\mu\text{W}$

TE light is collected from the inverse taper and measured by the photodetector. From the  $S_{11}$  in Fig. 6.11(b), the HBAR resonances from the released oxide membrane can be hardly seen which are overwhelmed by the HBAR from the Si substrate beneath the signal pad as discussed in the last section. This largely reduces the coupling efficiency from the microwave to the oxide HBAR.

The single optical mode AOM is measured as shown in Fig. 6.11(b), with only one actuator is driven. Maximum of -65 dB is achieved for HBAR mode at 1.35 GHz. The mechanical linewidth is measured to be 10 MHz which corresponds to the mechanical Q of 135. During the measurement, the laser is biased 88 MHz off the optical resonance. The off-chip conversion efficiency can be estimated from Eq. 6.22 which is around  $2.7 \times 10^{-11}$ . The on-chip efficiency is thus  $1.48 \times 10^{-10}$ , which is on the similar order with the isolator device and mainly limited by the low electromechanical coupling efficiency. Since it is hard to find the oxide HBAR, the electromechanical efficiency is estimated by the Mason model (see Appendix A) which is 0.1%. The model takes into account the most ideal case which is overestimated compared with the real experiment. The enhanced cooperativity  $C$  can then be estimated from Eq. 6.6 to be  $2.98 \times 10^{-5}$ , and the signal photon cooperativity  $C_0$

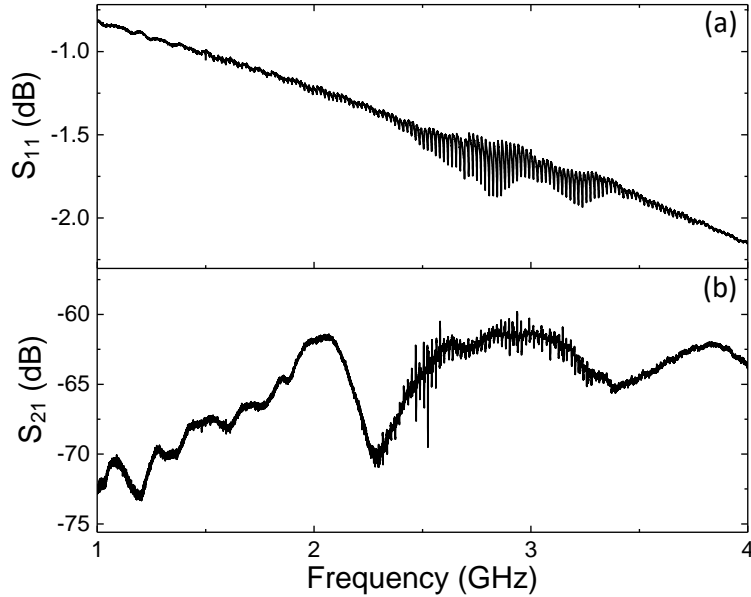


**Figure 6.12.** (a) Electromechanical  $S_{11}$  of one actuator. (b) Electromechanical  $S_{21}$  between the two actuators to measure the cross-talk between them.

**Table 6.2.** Summary of the parameters for the isolator device, current first-generation 22  $\mu\text{m}$ -radius device, and projected future goals.

Device	$g_0/2\pi$ (Hz)	$\kappa/2\pi$ (MHz)	$\Gamma/2\pi$ (MHz)	$C_0$	$C$	$\eta$
Isolator	70	377	14	$4 \times 10^{-12}$	$2.17 \times 10^{-9}$	$5 \times 10^{-10}$
Current	150	153	10	$5.9 \times 10^{-11}$	$2.98 \times 10^{-5}$	$1.48 \times 10^{-10}$
Future	1000	30	1	$1.3 \times 10^{-7}$	1	$1 \times 10^{-2}$

is  $5.92 \times 10^{-11}$ . The optomechanical coupling rate  $g_0$  can be estimated from the definition of  $C_0 = 4g_0^2/\kappa\Gamma$  which is  $2\pi \times 150$  Hz. This is underestimated because of the overestimation of the electromechanical efficiency. Nonetheless, it is much smaller than the expected value from the simulation of 1 kHz, because of the challenges presented in the last section.

The electromechanical cross-talk between the adjacent two actuators on the same optical microring is measured as shown in Fig. 6.12(b). The cross-talk between them is kept below -60 dB from 1 to 4 GHz, such that we can treat them as individual modulators. By driving them with differential phases, we can match the phase mismatch between the TE and TM modes in the future [106].

## 6.6 Summary

In this section, I proposed to demonstrate the quantum microwave to optical conversion using the efficient released HBAR formed in the oxide cladding. The results for the demonstrated conversion using the large isolator device and the new device with 22  $\mu\text{m}$ -radius are summarized in Table 6.2. By shrinking the size of the device, the  $g_0$  is increased by at least two times. Since the new device has thick oxide top cladding, the optical Q is improved by more than 2 times. These improvements lead to one order of magnitude higher single photon cooperativity  $C_0$ . However, the excitation efficiency of the HBAR mode in the new device is compromised by the loss into the Si substrate, which leads to similar overall efficiency as the isolator device.

In the future, by removing the HBAR in the Si substrate using the Bandaid process, the electromechanical coupling and mechanical quality factor can be largely improved by the better confinement of the oxide HBAR modes. Also, with uniform releasing profile using

$\text{SF}_6$ , the better mechanical and optical mode overlap will also increase the optomechanical coupling strength  $g_0$ . These two improvements (bandaid and uniform release) are critical and can be readily achieved in the near future. The increasing of optical Q with THz FSR optical ring resonator is more challenging. By increasing the radius to 40  $\mu\text{m}$  with 500 GHz FSR, the optical properties can be improved, including higher optical Q, little back scattering, and ease of matching TE and TM modes. With these procedures successfully implemented, the parameters of current device can be projected in the future as shown in Table 6.2, as well as in Fig. 6.7. Therefore, the proposed HBAR based microwave to optical converter will have the potential to perform efficiency quantum conversion in the future quantum networks. Furthermore, a new quantum protocol has been recently proposed to circumvent the requirement of the unit conversion efficiency by implementing quantum transportation with entangled microwave and optical photons generated by the converter [284]–[289].

## 7. OUTLOOK

In this thesis, a piezoelectric controllable photonic circuits is fully explored and its applications in versatile tuning of Kerr frequency comb [121], magnetic-free integrated optical isolator [169], and quantum microwave to optical converter are demonstrated and analyzed [168]. Piezoelectric transduction on a photonic chip has been widely studied in both quasi-DC tuning [67], [71]–[73] and microwave frequency modulation [14], [15]. The main innovation of this thesis is the incorporation of HBAR in the acousto-optic modulation [12] which paves paths for novel applications from photonic synthetic dimensions to hybrid quantum transduction. Compared with other mechanical resonators in the literature, such as SAW and OMC, the HBAR presents the advantages of ease of fabrication, high quality factor, a rich family of modes, and compact size. These unique features help HBAR stand out as a good candidate for future quantum applications. In the following, I will briefly outline the prospective applications in a hybrid quantum system.

### 7.1 Hybrid integrated quantum systems

Hybrid quantum systems have drawn intensive interest recently, as they leverage the advantages of different quantum objects for quantum applications with better performance [135]. For instance, while the nonlinearity of superconducting (SC) qubit makes it good at processing quantum information, the low thermal noise of optical photon advances in quantum information communication. On the other hand, the low speed of acoustic waves supports sub-micron wavelength at microwave frequency, which largely shrinks the device size compared with its electromagnetic counterpart. The long coherence time (low losses) of the mechanical resonator can help to store quantum information for a long time, and a hardware-efficient Quantum Random Access Memory (QRAM) has been theoretically proposed [290]. Moreover, phonon has been found to couple with most quantum objects, making it a good media for connecting different quantum platforms.

Figure 7.1 shows the diagram illustrating the direct or indirect coupling between three different quantum objects: photon, phonon, and SC qubit. The core material for the system is the piezoelectric material, such as AlN and LiNbO<sub>3</sub>, which are in the same time good

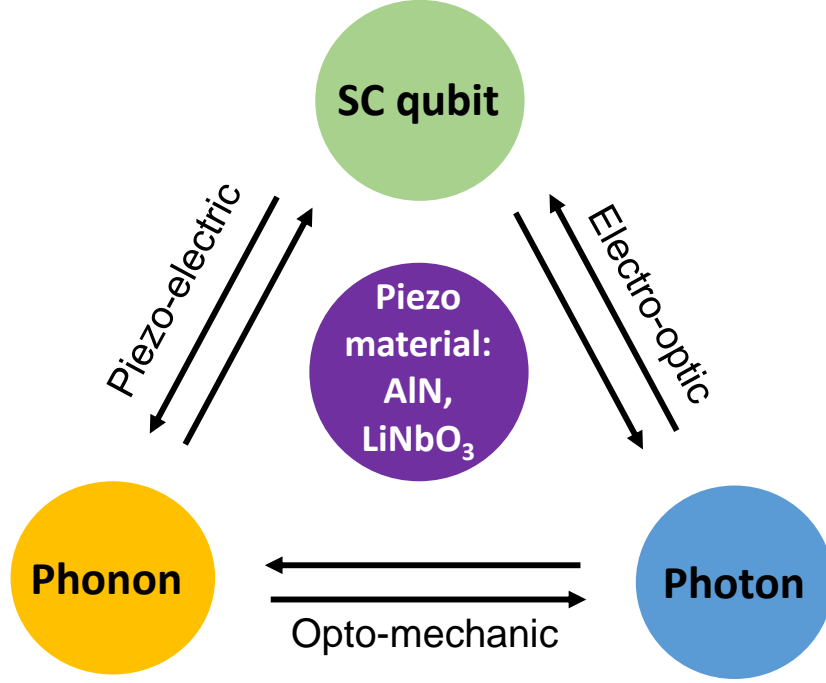


**Figure 7.1.** Diagram illustrating the interaction scheme between photon, phonon, and superconducting (SC) qubit. Piezoelectric material is the core for realization of this hybrid quantum system.

electro-optic materials. This makes it possible for the SC qubit to couple with photon and phonon through electro-optic and piezoelectric effects, respectively. The phonon and photon can interact through optomechanical effects (photoelastic and moving boundary) which closes the loop in a decent way. Note all the links are with double arrows which means the interactions are bi-directional, and the signal can transmit either clockwise or counter-clockwise. All the links have been experimentally demonstrated. For example, SC qubit is able to resolve different Fock state of phonon [99], [253], and phonon mediates the remote communication and entanglement between SC qubit [248], [250]. Photons have been used to classically control [228] and readout of SC qubit state [227]. However, the quantum interaction hasn't been demonstrated due to the currently low quantum efficiency of electro-optic modulators.

Thanks to the advances of nano-fabrication technologies, different mechanical and optical structures have been studied, and the coupling between them and the SC qubit has been



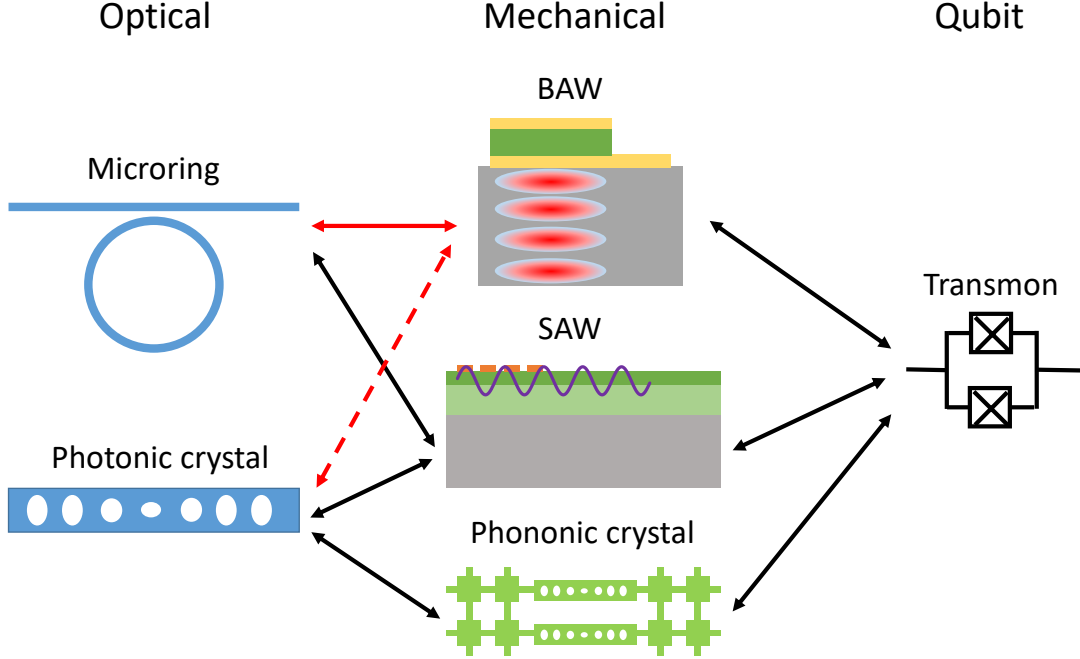


**Figure 7.2.** The coupling between optical, mechanical, and SC qubit devices with different structures has been studied and demonstrated. The black link shows the demonstrations from the literature. The red link is the work of this thesis. The red dashed link hasn't been achieved yet.

experimentally demonstrated in the literature as shown in Fig. 7.2. The coupling between mechanical resonator and the SC qubit has grown as a new field of so-called circuit quantum acousto-dynamics (cQAD) since its first demonstration of the coupling between an AlN BAW resonator with a Josephson phase qubit in 2010 by Andrew N Cleland *et al.* [251]. Although in its infancy, cQAD has brought new quantum resources, with the potential of being indispensable building blocks in future superconducting circuits design, due to its ultra-high  $Q$  ( $\sim 10^{10}$ ) and compact size. It has been demonstrated on different platforms, such as SAW [248]–[250], BAW [97], [98], and phononic crystal [253]–[255]. Advancements have been made in SC-qubit mediated preparation and control of mechanical resonators in different phononic Fock states [99], and phonon-number resolved readout [253]. On the optomechanical coupling side, SAW AOM of the optical microring resonator [14], [15] and the photonic crystal [278] has been demonstrated, and OMC combines together the photonic and phononic crystal for tight mode confinement [260]. In this thesis, I demonstrated the link

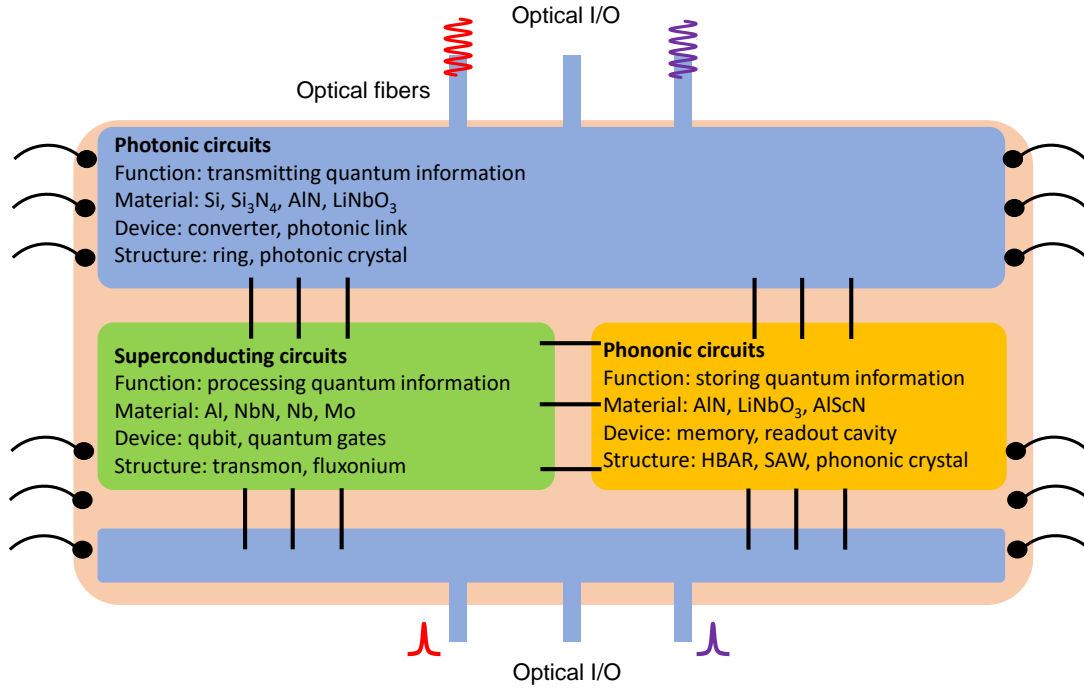


**Figure 7.3.** Layout for future hybrid quantum system that leverages different modules from photonic, phononic, and superconducting circuits. The function, material, devices, and structure for each module are listed. The optical input/output (I/O) ports serve to communicate the quantum information.

between HBAR and the optical ring resonator in both released and unreleased structure. It is interesting to note that the link between the HBAR and photonic crystal is still missing. The study of it in the future will provide a new way for realizing microwave to optical conversion with the advantages of better optical Q and thermal conductance than OMC (as it's cladded with SiO<sub>2</sub>), and smaller mode volume than the optical ring.

Figure 7.3 envisions the layout for future hybrid integrable quantum chip that includes different modules from the photonic, phononic, and superconducting circuits. Each of the module has their own functionalities. For example, after being processed by the superconducting qubit, the quantum information can be either stored by the phononic resonator or transmitted through the optical I/O to another dilution fridge. The advantages of each module will be fully utilized, and it has the potential to become the core for future quantum networks. More importantly, the materials that are required for each circuits are accessible at the foundry level and compatible with currently standard CMOS processes, especially for

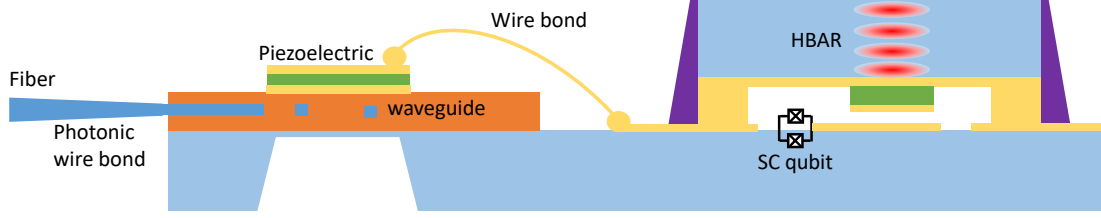


**Figure 7.4.** Schematic of a proposed fully packaged hybrid quantum chip. The SC qubit is protected from the stray light from the photonic circuits.

the Si,  $\text{Si}_3\text{N}_4$ , and AlN, which are the materials studied in this thesis. This enables to fully integrate them on the same chip with low cost.

To fully explore the potential of the hybrid quantum system where the advantages of each quantum component are treated well, it is desirable to integrate them on a single chip through novel fabrication technologies, such as flip-chip [98], [175], packaging, photonic wire bonding [162], as shown in Fig. 7.4. The HBAR resonator can be capacitively coupled with the SC qubit by flip-chip which encapsulates the SC qubit and protects it from the stray light scattered off the photonic circuits. The stray light otherwise will break the cooper pairs of the superconductor which generates decoherence of the SC qubit [262]. On the other hand, while photonics need to be cladded with  $\text{SiO}_2$ , the SC qubit needs to be fabricated directly on high resistivity Si substrate to preserve the coherence time and avoid the losses from Two-Level-System (TLS) [291]. This can be achieved by either etching away the  $\text{SiO}_2$  around the region of the SC circuits, or fabricating them on separate chips. The optical I/O serves to transmit the quantum information over long distance through low-loss optical fibers which can be connected with the on-chip waveguides through lensed fiber fixed with epoxy [292] or via photonic wire bonding [162]. This full package will also enhance the stability and robustness of the system once in the cryogenic chamber. Although HBAR and optical microring resonators are taken as an example in Fig. 7.4, other mechanical and optical structures can be incorporated such as OMC and SAW.

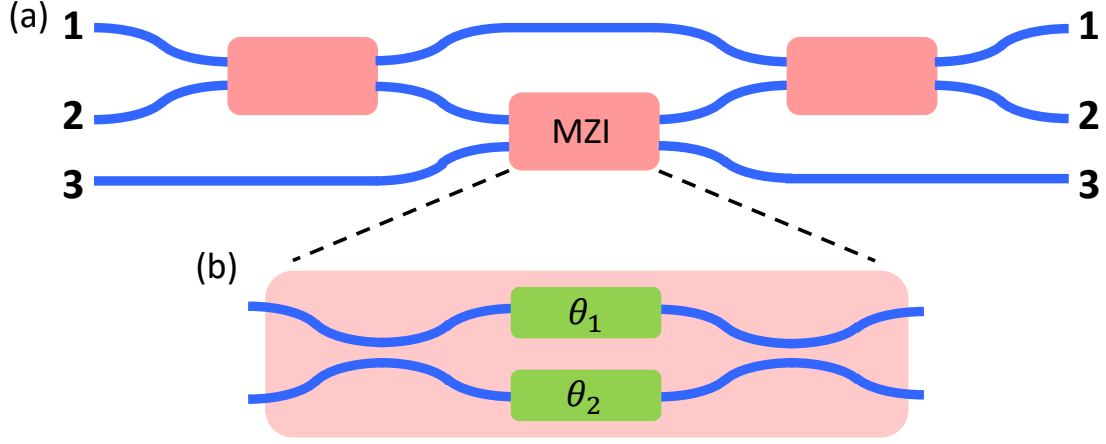


**Figure 7.5.** (a) Schematic for a programmable photonic circuits made from a mesh of Mach-Zehnder Interferometers (MZI). (b) Example of one MZI where the optical phases of the top and bottom arms will be actuated for controlling the path of photons.

### 7.1.1 Piezoelectric programmable photonic circuits

Programmable photonic circuits [293]–[295] has drawn much attention of being the core processor from photonic quantum computing and simulation [175] to optical neural networks (ONN) for deep learning [296]. It is in general made from a mesh of Mach-Zehnder Interferometers as shown in Fig. 7.5(a). The optical information is encoded in different channels (1, 2, 3, ...), and the interaction between adjacent channels is implemented by the MZI in Fig. 7.5(b). Depending on the phases that the light experiences when going through the top and bottom arms of the MZI, light can be either switched to the adjacent channel or remain in the original one. In that way, the light from the input channels can be programmatically mapped into the output channels. This arbitrary transformation is one of the key operation in advanced tasks in optical quantum information processing and machine learning, depending on whether quantum or classical light is input.

The key building block for the MZI is the optical phase shifter on each arm. Depending on the material of the waveguide, different ways for actuating the phase are studied. In the demonstration of the deep learning in Ref. [296], Si waveguide is thermally tuned which consumes a lot electrical power. Tuning of the Si waveguide through injection carriers is

also demonstrated [207] but shows much higher optical losses. In the most demonstration of implementing quantum algorithms (Gaussian Boson sampling, molecular vibronic spectra, graph similarity) on a  $\text{Si}_3\text{N}_4$  photonic circuits [175], thermo-optic tuning of the  $\text{Si}_3\text{N}_4$  waveguide is also employed. It is noteworthy that to achieve the universal transformation of  $N$  input ports, total of  $N(N - 1)/2$  MZI will be needed [294]. For example, 10 input ports would need 45 MZI. This grows on the order of  $O(N^2)$ , which will become problematic with thermal tuning especially with over 100 ports in practice. Also, both of the thermal tuning and injection carrier tuning have high cross-talk between adjacent actuators. In that sense, lower power consumption actuator, low optical loss MZI with low cross-talk will become essential for future programmable photonic circuits.

Piezoelectric tuning of the MZI photonic circuits has been recently demonstrated using the AlN piezoelectric actuator on a  $\text{Si}_3\text{N}_4$  MZI network [73]. Unitary transformation of 4 ports are implemented with 6 MZI. Dynamic and static power consumption of 200  $\mu\text{W}$  and 6 nW is achieved, and has been demonstrated to be compatible with cryogenic operation at 5 K. The figure of merit  $V_\pi \cdot L$  is of 50 V·cm. This preliminary result is promising for future large scale programmable photonic circuits. If we recall from eq. 1.18 that the stress-optical tuning is proportional to the  $n^2$  of the waveguide, it is time to revisit Si as the photonic waveguide in the Piezo-on-Photonics platform, thanks to its large refractive index  $n$  of 3.5. From our previous demonstration of PZT tuning of  $\text{Si}_3\text{N}_4$  waveguide,  $V_\pi \cdot L$  of 12 V·cm is within reach. By replacing  $\text{Si}_3\text{N}_4$  by Si, the  $V_\pi \cdot L$  can be further reduced to 4 V·cm which is on par with commercial electro-optical modulators. This means  $\pi$  phase shift can be achieved under 20 V for 1000  $\mu\text{m}$  Si waveguide in a push-pull MZI configuration. Therefore, piezoelectric programmable Si photonics could become one of the core processors for future optical quantum computer and machine learning.

### 7.1.2 Photonic synthetic dimension enabled by HBAR AOM

Optical light has been the pivot for today's telecommunication systems due to its flexible and versatile degree of freedom for encoding digital information. Most recently, encoding quantum information in optical photon has been widely studied because of its low thermal

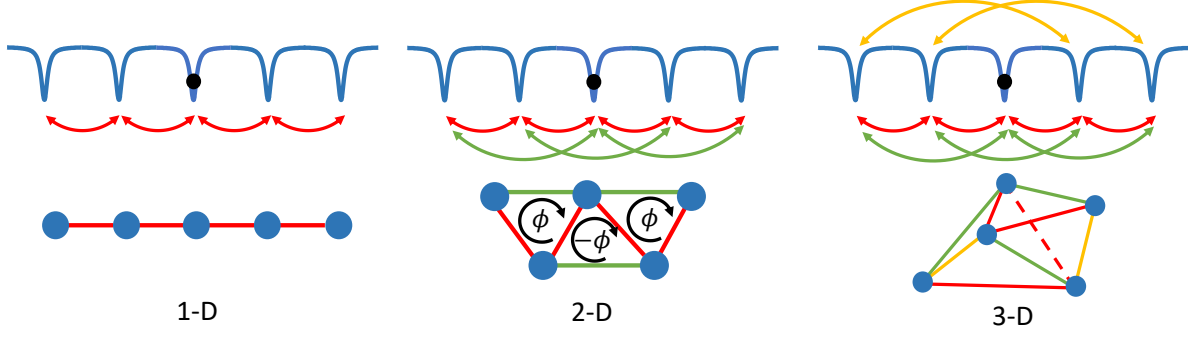


**Figure 7.6.** Top: The coupling between optical mode with its adjacent mode (red), the next-nearest neighbour (green), and the next-next-nearest neighbour (yellow). Bottom: equivalent synthetic frequency lattices in 1D, 2D, and 3D. The black dot indicates one photon.

noise and losses at room temperature. One famous example is by using the polarization of light. Quantum key distribution has been commercialized for quantum secure communication [221] based on photons encoded with different polarization states. Another example is to encode the information in different optical paths as discussed in the last section.

Encoding information in optical frequency has led to the concept of synthetic frequency dimensions [52], [297], where the dynamic modulation of the optical ring resonator induces coupling between adjacent optical modes as shown in Fig. 7.6. These modes are equally spaced, forming a lattice in the frequency domain. If the modulation frequency matches the FSR of the optical resonator, the optical mode can be coupled to its nearest neighbour. This naturally forms a tight-binding model for photon in a 1-D frequency lattice, mimicking the hopping of electrons in a crystal lattice. The Hamiltonian can be described as [52]:

$$H_{\text{TB}} = \sum_k \omega_k a_k^\dagger a_k + \sum_k g a_{(k+1)}^\dagger a_k e^{i\phi} + h.c. \quad (7.1)$$

where  $\omega_k$  is the frequency of each mode and here in the model it works as an on-site potential,  $\phi$  is the phase of the microwave drive.  $\hbar$  is omitted for simplicity. As the reciprocal space of frequency is time, the band structure can be directly measured by performing time-resolved reflection measurement [53]. By placing one photon into one lattice site, the coherent random walk of photon under continuous drive can be studied [298]. If instead the drive is detuned

from the resonant condition with  $\Delta = \Omega_d - \text{FSR}$ , an effective electric force can be generated on the photon, in the form of adding a constant potential to the Hamiltonian  $\sum_k k\Delta a_k^\dagger a_k$  allows us to study the 1D Bloch oscillation [299].

Long-range hopping term can be easily achieved by adding microwave drive at multiple of FSRs, which appears in the Hamiltonian as:  $\sum_k g_N a_{(k+N)}^\dagger a_k e^{i\phi_N}$ . This allows us to fold the 1D lattice into higher dimensions. For example, if the optical mode can in the same time be coupled with the next-nearest neighbor, a 2D lattice can be constructed (Fig. 7.6 2D). Depending of the relative phases between the microwave drives, an effective magnetic field and gauge potential can be generated threading the lattice [53], [300]. Similarly, a 3D lattice can be built by introducing the next-next-nearest hopping (Fig. 7.6 3D), and even higher dimensional physics can be studied which would be hard for real spaces [52]. Beyond that, more complex lattice can be constructed by coupling multiple optical resonators in physical dimension [301]. Very rich physical phenomena can be studied by engineering the magnitude and phase of each hopping term, such as topological band-structure [53], nonreciprocal frequency conversion (photon hops in one direction) [54], [302], [303], and synthetic quantum Hall effect [304].

Besides studying the topological physics, it is also proposed to implement the universal unitary transformation in the synthetic dimensions by engineering the coupling between modes [305]. It can fulfill similar tasks as the MZI network does in the last section, but in a very compact form in real space, since all the light can transmit in a single waveguide. Also, it works with discrete frequencies, such that we can use the optical resonators to enhance the interaction strength. In addition, by combining with the optical Kerr nonlinearity of the photonic waveguide, novel dynamics of the soliton generation has been theoretically predicted [306]. Therefore, the study of the synthetic frequency dimension will provide a vastly large spaces for investigating novel physics, and resources for classical and quantum computation.

Experimentally, synthetic frequency dimension in photonics has been demonstrated in different platforms, such as optical fiber loops [53], [54], electro-optic modulation of LiNbO<sub>3</sub> [298], [303], modulation Si racetrack resonator by p-n junction [307], and SAW AOM of AlN ring resonators [304]. The main challenge in the experiment is to match the modulation

with the FSR, especially for on-chip optical resonators with FSR from 10 GHz to THz range.  $\text{Si}_3\text{N}_4$  microring resonators with FSR as low as 2.5 GHz has been demonstrated with optical Q over 5 Million [84], which matches well with the HBAR resonances. Moreover, by matching HBAR resonances to multiple FSR such as 5 GHz, 7.5 GHz, higher dimensional lattices can be studied. Therefore, the HBAR AOM of microwave frequency FSR optical resonators would be of great interest for future research.

### 7.1.3 Classical readout and control of superconducting qubit

Superconducting qubit has become a leading platform for quantum computing, thanks to its scalability, high fidelity gate, and stability, with the quantum supremacy demonstrated recently [231]. However, current fault-tolerance algorithm requires millions of qubits which imposes challenge for signal routing and cabling. As each qubit requires at least three RF cables for qubit control and readout, this implies that millions of RF cables have to be connected into the dilution fridge, which is not only problematic for spacing but introduces large heat load for the fridge. Based on current experiments, 13 nW heat load is added for each RF coaxial cable. With 20  $\mu\text{W}$  cooling power for typical commercial dilution fridge, this suggests at most 500 qubits can be addressed, which is far from the ideal case [228].

Inspired by the traditional optical telecommunication, most recently, photonic link using optical fibers has been implemented successfully for both qubit control and readout with fidelity same as using coaxial cable [227], [228]. This method not only saves lots of spacing (0.1 mm fiber vs 2 mm cable), but also reduces the heat load. Thanks to the low thermal conductance of most silica optical fiber, 3 pW passive heat load is estimated, which increases ultimate number of qubits to 2 Million. Furthermore, by using frequency multiplexing, each fiber can address more than 10 qubits at the same time, which largely releases the wiring problem. Therefore, this approach paves a path towards scaling up number of qubits for fault-tolerance operation in the future.

In current photonic link demonstrations, microwave signals are generated by detecting incoming intensity modulated light through a photodiode [228]. The added noise of this photonic link is mainly limited by the shot noise which is intrinsic for photodiode, coming



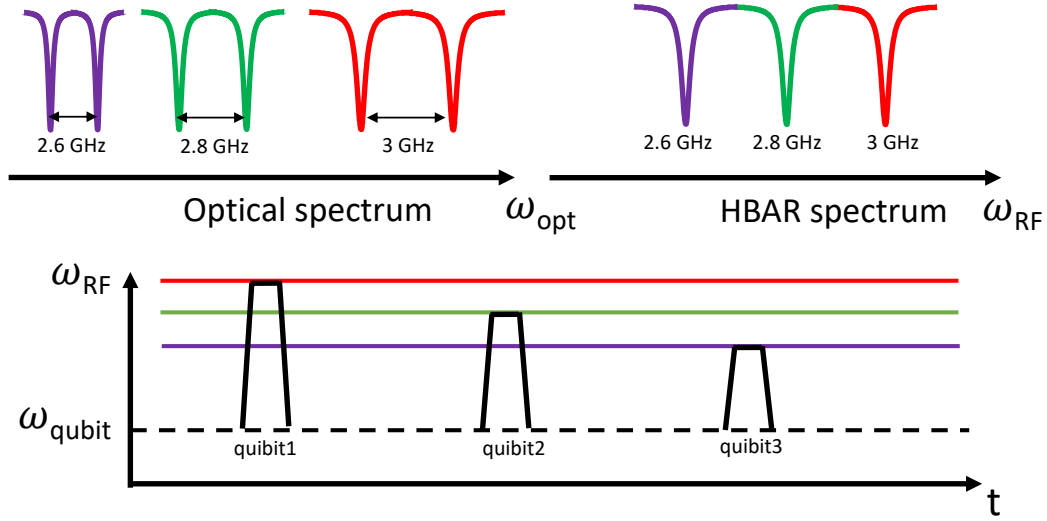


**Figure 7.7.** Schematic showing the multiplex of microwave tones for the control of multiple qubits with the same device. The spacing between the two optical modes are engineered by the FSR difference between them, where each pair can be coupled to HBAR modes with equidistant spacing. Each RF tone can be addressed to each qubit by flux tuning the qubit transition frequency.

from the fundamental quantum fluctuation of the electron-hole pair generation. On the other hand, although the efficiency of the microwave to optical converter demonstrated in the last section is still low for quantum applications, it can be used to generate classical microwaves for driving the SC qubit, where the beating between the pump and signal lights excites the HBAR mode which is then converted to the microwave through the piezoelectric actuator. By getting rid of the shot noise, the added noise is ultimately limited by the voltage noise at the electro-optical modulator (EOM), which is estimated to be one order of magnitude smaller than the shot noise [228]. The optical resonance used in the device intrinsically works as a filter that rejects the white noise outside of the resonance, which further suppresses the noise.

In terms of the heat load, the previous demonstration using photodiode is mainly limited by the active heating of the photodiode, despite of the ultra-low passive heat from the optical fiber. This heating is mainly from the non-radiative dissipation of the excess energy of the incoming photon above the bandgap of the semiconductor, which is intrinsic for the photodiode. However, for the optomechanical converter, by working at the over-coupling regime,

most pump light will transmit outside of the device and get recycled. Therefore, with the theoretically low added noise and heat load, the optomechanical approach may potentially be better suited for quantum applications than photodiode. As the optomechanical interaction is reversible, the device can not only work as photodetector but also optical modulator.

The device can be further engineered to multiplex microwave tones to drive multiple qubits at the same time, which fully utilizes the rich bandwidth of light and will largely reduce the number of fibers and converters required. The working scheme is as shown in Fig. 7.7, where the FSR difference between TE and TM modes can be engineered by the aspect ratio of the waveguide, such that the variation of mode spacing matches the frequencies of HBAR modes, whose FSR can be engineered easily by the oxide thickness. In this way, the same device can support multiple “triple cavity optomechanics” combinations working at different microwave frequencies. Each frequency can be addressed to each qubit by flux tuning the qubit’s transition frequency to align with the microwave drive. For example, with 5  $\mu\text{m}$  oxide, the HBAR’s FSR is around 500 MHz. With 2 GHz tuning range of current transmon qubit, at least four qubits can be multiplexed. It is worth mentioning that the use of optical microring structure makes it easy for engineering the optical FSR and dispersion compared with other optomechanical frequency converter such as OMC.

For an estimation of the required optical power in the application for qubit control, the power is calculated for inducing 10 MHz Rabi oscillation which is much larger than typical qubit’s relaxation rate ( 25 kHz). The Rabi frequency  $\Omega_R$  is related with the microwave photon flux as:

$$\Omega_R = 2\sqrt{n_{\text{MW}}\gamma_{\text{ex}}} \quad (7.2)$$

where  $\gamma_{\text{ex}}$  is the coupling rate of qubit to the microwave channel on the order of 1 kHz,  $n_{\text{MW}}$  is the microwave photon flux, which is related with the input optical photon flux via conversion efficiency  $\eta$ . With efficiency of  $1 \times 10^{-4}$ , 10  $\mu\text{W}$  is required for 10 MHz Rabi frequency under 100  $\mu\text{W}$  pump light.

## REFERENCES

- [1] D. Thomson, A. Zilkie, J. E. Bowers, T. Komljenovic, G. T. Reed, L. Vivien, D. Marris-Morini, E. Cassan, L. Viot, J.-M. Fédéli, J.-M. Hartmann, J. H. Schmid, D.-X. Xu, F. Boeuf, P. O'Brien, G. Z. Mashanovich, and M. Nedeljkovic, "Roadmap on silicon photonics," *Journal of Optics*, vol. 18, no. 7, p. 073 003, Jun. 2016.
- [2] E. Agrell, M. Karlsson, A. R. Chraplyvy, D. J. Richardson, P. M. Krummrich, P. Winzer, K. Roberts, J. K. Fischer, S. J. Savory, B. J. Eggleton, M. Secondini, F. R. Kschischang, A. Lord, J. Prat, I. Tomkos, J. E. Bowers, S. Srinivasan, M. Brandt-Pearce, and N. Gisin, "Roadmap of optical communications," *Journal of Optics*, vol. 18, no. 6, p. 063 002, 2016.
- [3] D. Huang, M. A. Tran, J. Guo, J. Peters, T. Komljenovic, A. Malik, P. A. Morton, and J. E. Bowers, "High-power sub-khz linewidth lasers fully integrated on silicon," *Optica*, vol. 6, no. 6, pp. 745–752, 2019.
- [4] C. Xiang, W. Jin, J. Guo, J. D. Peters, M. J. Kennedy, J. Selvidge, P. A. Morton, and J. E. Bowers, "Narrow-linewidth iii-v/si/si<sub>3</sub>n<sub>4</sub> laser using multilayer heterogeneous integration," *Optica*, vol. 7, no. 1, pp. 20–21, 2020.
- [5] W. Jin, Q.-F. Yang, L. Chang, B. Shen, H. Wang, M. A. Leal, L. Wu, M. Gao, A. Feshali, M. Paniccia, K. J. Vahala, and J. E. Bowers, "Hertz-linewidth semiconductor lasers using cmos-ready ultra-high-q microresonators," *Nature Photonics*, 2021.
- [6] K. A. McKinzie, C. Wang, A. A. Noman, D. L. Mathine, K. Han, D. E. Leaird, G. E. Hoefler, V. Lal, F. Kish, M. Qi, and A. M. Weiner, "Inp high power monolithically integrated widely tunable laser and soa array for hybrid integration," *Opt. Express*, vol. 29, no. 3, pp. 3490–3502, 2021.
- [7] C. Xiang, J. Liu, J. Guo, L. Chang, R. N. Wang, W. Weng, J. Peters, W. Xie, Z. Zhang, J. Riemensberger, *et al.*, "Laser soliton microcombs heterogeneously integrated on silicon," *Science*, vol. 373, no. 6550, pp. 99–103, 2021.
- [8] D. Liang and J. E. Bowers, "Recent progress in heterogeneous iii-v-on-silicon photonic integration," *Light: Advanced Manufacturing*, vol. 2, no. LAM2020070018, p. 1, 2021.
- [9] A. Melikyan, L. Alloatti, A. Muslija, D. Hillerkuss, P. C. Schindler, J. Li, R. Palmer, D. Korn, S. Muehlbrandt, D. Van Thourhout, B. Chen, R. Dinu, M. Sommer, C. Koos, M. Kohl, W. Freude, and J. Leuthold, "High-speed plasmonic phase modulators," *Nature Photonics*, vol. 8, no. 3, pp. 229–233, 2014.
- [10] C. Wang, M. Zhang, X. Chen, M. Bertrand, A. Shams-Ansari, S. Chandrasekhar, P. Winzer, and M. Lončar, "Integrated lithium niobate electro-optic modulators operating at cmos-compatible voltages," *Nature*, vol. 562, no. 7725, pp. 101–104, 2018.

- [11] M. He, M. Xu, Y. Ren, J. Jian, Z. Ruan, Y. Xu, S. Gao, S. Sun, X. Wen, L. Zhou, L. Liu, C. Guo, H. Chen, S. Yu, L. Liu, and X. Cai, “High-performance hybrid silicon and lithium niobate mach–zehnder modulators for 100 gbit s<sup>-1</sup> and beyond,” *Nature Photonics*, vol. 13, no. 5, pp. 359–364, 2019.
- [12] H. Tian, J. Liu, B. Dong, J. C. Skehan, M. Zervas, T. J. Kippenberg, and S. A. Bhave, “Hybrid integrated photonics using bulk acoustic resonators,” *Nature Communications*, vol. 11, no. 1, p. 3073, 2020.
- [13] L. Chen, Q. Xu, M. G. Wood, and R. M. Reano, “Hybrid silicon and lithium niobate electro-optical ring modulator,” *Optica*, vol. 1, no. 2, pp. 112–118, 2014.
- [14] S. A. Tadesse and M. Li, “Sub-optical wavelength acoustic wave modulation of integrated photonic resonators at microwave frequencies,” *Nature Communications*, vol. 5, no. 1, p. 5402, 2014.
- [15] L. Shao, M. Yu, S. Maity, N. Sinclair, L. Zheng, C. Chia, A. Shams-Ansari, C. Wang, M. Zhang, K. Lai, and M. Lončar, “Microwave-to-optical conversion using lithium niobate thin-film acoustic resonators,” *Optica*, vol. 6, no. 12, pp. 1498–1505, 2019.
- [16] H. Tian, J. Liu, A. Siddharth, T. Blésin, T. J. Kippenberg, and S. A. Bhave, “X-band aom on chip,” in *2021 IEEE 34th International Conference on Micro Electro Mechanical Systems (MEMS)*, 2021, pp. 210–213.
- [17] Y. Kang, H.-D. Liu, M. Morse, M. J. Paniccia, M. Zadka, S. Litski, G. Sarid, A. Pauchard, Y.-H. Kuo, H.-W. Chen, W. S. Zaoui, J. E. Bowers, A. Beling, D. C. McIntosh, X. Zheng, and J. C. Campbell, “Monolithic germanium/silicon avalanche photodiodes with 340 ghz gain–bandwidth product,” *Nature Photonics*, vol. 3, no. 1, pp. 59–63, 2009.
- [18] A. Beling, X. Xie, and J. C. Campbell, “High-power, high-linearity photodiodes,” *Optica*, vol. 3, no. 3, pp. 328–338, Mar. 2016.
- [19] M. Zhang, C. Wang, R. Cheng, A. Shams-Ansari, and M. Lončar, “Monolithic ultra-high-q lithium niobate microring resonator,” *Optica*, vol. 4, no. 12, pp. 1536–1537, Dec. 2017.
- [20] K. Y. Yang, D. Y. Oh, S. H. Lee, Q.-F. Yang, X. Yi, B. Shen, H. Wang, and K. Vahala, “Bridging ultrahigh-q devices and photonic circuits,” *Nature Photonics*, vol. 12, no. 5, pp. 297–302, 2018.
- [21] L. Chang, W. Xie, H. Shu, Q.-F. Yang, B. Shen, A. Boes, J. D. Peters, W. Jin, C. Xiang, S. Liu, G. Moille, S.-P. Yu, X. Wang, K. Srinivasan, S. B. Papp, K. Vahala, and J. E. Bowers, “Ultra-efficient frequency comb generation in algaas-on-insulator microresonators,” *Nature Communications*, vol. 11, no. 1, p. 1331, 2020.

- [22] Y. Xuan, Y. Liu, L. T. Varghese, A. J. Metcalf, X. Xue, P.-H. Wang, K. Han, J. A. Jaramillo-Villegas, A. A. Noman, C. Wang, S. Kim, M. Teng, Y. J. Lee, B. Niu, L. Fan, J. Wang, D. E. Leaird, A. M. Weiner, and M. Qi, “High-q silicon nitride microresonators exhibiting low-power frequency comb initiation,” *Optica*, vol. 3, no. 11, pp. 1171–1180, Nov. 2016.
- [23] X. Ji, F. A. S. Barbosa, S. P. Roberts, A. Dutt, J. Cardenas, Y. Okawachi, A. Bryant, A. L. Gaeta, and M. Lipson, “Ultra-low-loss on-chip resonators with sub-milliwatt parametric oscillation threshold,” *Optica*, vol. 4, no. 6, pp. 619–624, Jun. 2017.
- [24] J. Liu, G. Huang, R. N. Wang, J. He, A. S. Raja, T. Liu, N. J. Engelsen, and T. J. Kippenberg, “High-yield, wafer-scale fabrication of ultralow-loss, dispersion-engineered silicon nitride photonic circuits,” *Nature Communications*, vol. 12, no. 1, p. 2236, 2021.
- [25] Z. Ye, K. Twayana, P. A. Andrekson, and V. Torres-Company, “High-q si<sub>3</sub>n<sub>4</sub> microresonators based on a subtractive processing for kerr nonlinear optics,” *Opt. Express*, vol. 27, no. 24, pp. 35 719–35 727, Nov. 2019.
- [26] M. W. Puckett, K. Liu, N. Chauhan, Q. Zhao, N. Jin, H. Cheng, J. Wu, R. O. Behunin, P. T. Rakich, K. D. Nelson, and D. J. Blumenthal, “422 million intrinsic quality factor planar integrated all-waveguide resonator with sub-mhz linewidth,” *Nature Communications*, vol. 12, no. 1, p. 934, 2021.
- [27] D. J. Moss, R. Morandotti, A. L. Gaeta, and M. Lipson, “New cmos-compatible platforms based on silicon nitride and hydex for nonlinear optics,” *Nature Photonics*, vol. 7, p. 597, Jul. 2013.
- [28] A. L. Gaeta, M. Lipson, and T. J. Kippenberg, “Photonic-chip-based frequency combs,” *Nature Photonics*, vol. 13, no. 3, pp. 158–169, 2019.
- [29] T. J. Kippenberg, A. L. Gaeta, M. Lipson, and M. L. Gorodetsky, “Dissipative kerr solitons in optical microresonators,” *Science*, vol. 361, no. 6402, eaan8083, 2018, ISSN: 0036-8075.
- [30] T. Herr, V. Brasch, J. D. Jost, C. Y. Wang, N. M. Kondratiev, M. L. Gorodetsky, and T. J. Kippenberg, “Temporal solitons in optical microresonators,” *Nature Photonics*, vol. 8, p. 145, Dec. 2013.
- [31] B. Stern, X. Ji, Y. Okawachi, A. L. Gaeta, and M. Lipson, “Battery-operated integrated frequency comb generator,” *Nature*, vol. 562, no. 7727, pp. 401–405, 2018.

- [32] A. S. Raja, A. S. Voloshin, H. Guo, S. E. Agafonova, J. Liu, A. S. Gorodnitskiy, M. Karpov, N. G. Pavlov, E. Lucas, R. R. Galiev, A. E. Shitikov, J. D. Jost, M. L. Gorodetsky, and T. J. Kippenberg, “Electrically pumped photonic integrated soliton microcomb,” *Nature Communications*, vol. 10, no. 1, p. 680, 2019.
- [33] B. Shen, L. Chang, J. Liu, H. Wang, Q.-F. Yang, C. Xiang, R. N. Wang, J. He, T. Liu, W. Xie, J. Guo, D. Kinghorn, L. Wu, Q.-X. Ji, T. J. Kippenberg, K. Vahala, and J. E. Bowers, “Integrated turnkey soliton microcombs,” *Nature*, vol. 582, no. 7812, pp. 365–369, 2020.
- [34] A. Kovach, D. Chen, J. He, H. Choi, A. H. Dogan, M. Ghasemkhani, H. Taheri, and A. M. Armani, “Emerging material systems for integrated optical kerr frequency combs,” *Adv. Opt. Photon.*, vol. 12, no. 1, pp. 135–222, Mar. 2020.
- [35] C. Wang, M. Zhang, M. Yu, R. Zhu, H. Hu, and M. Loncar, “Monolithic lithium niobate photonic circuits for kerr frequency comb generation and modulation,” *Nature Communications*, vol. 10, no. 1, p. 978, 2019.
- [36] Y. He, Q.-F. Yang, J. Ling, R. Luo, H. Liang, M. Li, B. Shen, H. Wang, K. Vahala, and Q. Lin, “Self-starting bi-chromatic linbo3 soliton microcomb,” *Optica*, vol. 6, no. 9, pp. 1138–1144, Sep. 2019.
- [37] Z. Gong, X. Liu, Y. Xu, and H. X. Tang, “Near-octave lithium niobate soliton microcomb,” *Optica*, vol. 7, no. 10, pp. 1275–1278, Oct. 2020.
- [38] H. Jung, C. Xiong, K. Y. Fong, X. Zhang, and H. X. Tang, “Optical frequency comb generation from aluminum nitride microring resonator,” *Opt. Lett.*, vol. 38, no. 15, pp. 2810–2813, Aug. 2013.
- [39] X. Liu, C. Sun, B. Xiong, L. Wang, J. Wang, Y. Han, Z. Hao, H. Li, Y. Luo, J. Yan, T. Wei, Y. Zhang, and J. Wang, “Integrated high-q crystalline aln microresonators for broadband kerr and raman frequency combs,” *ACS Photonics*, vol. 5, no. 5, pp. 1943–1950, 2018.
- [40] M. Pu, L. Ottaviano, E. Semenova, and K. Yvind, “Efficient frequency comb generation in algaas-on-insulator,” *Optica*, vol. 3, no. 8, pp. 823–826, 2016.
- [41] V. Brasch, Q.-F. Chen, S. Schiller, and T. J. Kippenberg, “Radiation hardness of high-q silicon nitride microresonators for space compatible integrated optics,” *Optics express*, vol. 22, no. 25, pp. 30 786–30 794, 2014.
- [42] T. J. Kippenberg, R. Holzwarth, and S. A. Diddams, “Microresonator-based optical frequency combs,” *Science*, vol. 332, no. 6029, pp. 555–559, 2011, ISSN: 0036-8075.

- [43] T. Huffman, D. Baney, and D. J. Blumenthal, “High extinction ratio widely tunable low-loss integrated si<sub>3</sub>n<sub>4</sub> third-order filter,” *arXiv preprint arXiv:1708.06344*, 2017.
- [44] S. Gundavarapu, M. Belt, T. A. Huffman, M. A. Tran, T. Komljenovic, J. E. Bowers, and D. J. Blumenthal, “Interferometric optical gyroscope based on an integrated si<sub>3</sub>n<sub>4</sub> low-loss waveguide coil,” *Journal of Lightwave Technology*, vol. 36, no. 4, pp. 1185–1191, 2018.
- [45] Z. Yao, K. Wu, B. X. Tan, J. Wang, Y. Li, Y. Zhang, and A. W. Poon, “Integrated silicon photonic microresonators: Emerging technologies,” *IEEE Journal of Selected Topics in Quantum Electronics*, vol. 24, no. 6, pp. 1–24, 2018.
- [46] Q. Li, T. C. Briles, D. A. Westly, T. E. Drake, J. R. Stone, B. R. Ilic, S. A. Diddams, S. B. Papp, and K. Srinivasan, “Stably accessing octave-spanning microresonator frequency combs in the soliton regime,” *Optica*, vol. 4, no. 2, pp. 193–203, 2017.
- [47] M. H. P. Pfeiffer, C. Herkommer, J. Liu, H. Guo, M. Karpov, E. Lucas, M. Zervas, and T. J. Kippenberg, “Octave-spanning dissipative kerr soliton frequency combs in si<sub>3</sub>n<sub>4</sub> microresonators,” *Optica*, vol. 4, no. 7, pp. 684–691, 2017.
- [48] J. Liu, A. S. Raja, M. Karpov, B. Ghadiani, M. H. P. Pfeiffer, B. Du, N. J. Engelsen, H. Guo, M. Zervas, and T. J. Kippenberg, “Ultralow-power chip-based soliton microcombs for photonic integration,” *Optica*, vol. 5, no. 10, pp. 1347–1353, 2018.
- [49] J. Liu, E. Lucas, A. S. Raja, J. He, J. Riemensberger, R. N. Wang, M. Karpov, H. Guo, R. Bouchand, and T. J. Kippenberg, “Photonic microwave generation in the x- and k-band using integrated soliton microcombs,” *Nature Photonics*, vol. 14, no. 8, pp. 486–491, 2020.
- [50] D. T. Spencer, T. Drake, T. C. Briles, J. Stone, L. C. Sinclair, C. Fredrick, Q. Li, D. Westly, B. R. Ilic, A. Bluestone, N. Volet, T. Komljenovic, L. Chang, S. H. Lee, D. Y. Oh, M.-G. Suh, K. Y. Yang, M. H. P. Pfeiffer, T. J. Kippenberg, E. Norberg, L. Theogarajan, K. Vahala, N. R. Newbury, K. Srinivasan, J. E. Bowers, S. A. Diddams, and S. B. Papp, “An optical-frequency synthesizer using integrated photonics,” *Nature*, vol. 557, no. 7703, pp. 81–85, 2018.
- [51] Y. Shi, Q. Lin, M. Minkov, and S. Fan, “Nonreciprocal optical dissipation based on direction-dependent rabi splitting,” *IEEE J. Sel. Top. Quantum Electron.*, vol. 24, no. 6, pp. 1–7, 2018.
- [52] L. Yuan, A. Dutt, and S. Fan, “Synthetic frequency dimensions in dynamically modulated ring resonators,” *APL Photonics*, vol. 6, no. 7, p. 071 102, 2021.
- [53] A. Dutt, M. Minkov, Q. Lin, L. Yuan, D. A. Miller, and S. Fan, “Experimental band structure spectroscopy along a synthetic dimension,” *Nature communications*, vol. 10, no. 1, pp. 1–8, 2019.

- [54] A. Dutt, Q. Lin, L. Yuan, M. Minkov, M. Xiao, and S. Fan, “A single photonic cavity with two independent physical synthetic dimensions,” *Science*, vol. 367, no. 6473, pp. 59–64, 2020.
- [55] P. Dong, W. Qian, H. Liang, R. Shafiiha, D. Feng, G. Li, J. E. Cunningham, A. V. Krishnamoorthy, and M. Asghari, “Thermally tunable silicon racetrack resonators with ultralow tuning power,” *Optics express*, vol. 18, no. 19, pp. 20 298–20 304, 2010.
- [56] X. Xue, Y. Xuan, C. Wang, P.-H. Wang, Y. Liu, B. Niu, D. E. Leaird, M. Qi, and A. M. Weiner, “Thermal tuning of kerr frequency combs in silicon nitride microring resonators,” *Opt. Express*, vol. 24, no. 1, pp. 687–698, 2016.
- [57] C. Joshi, J. K. Jang, K. Luke, X. Ji, S. A. Miller, A. Klenner, Y. Okawachi, M. Lipson, and A. L. Gaeta, “Thermally controlled comb generation and soliton modelocking in microresonators,” *Opt. Lett.*, vol. 41, no. 11, pp. 2565–2568, 2016.
- [58] B. S. Lee, M. Zhang, F. A. Barbosa, S. A. Miller, A. Mohanty, R. St-Gelais, and M. Lipson, “On-chip thermo-optic tuning of suspended microresonators,” *Optics Express*, vol. 25, no. 11, pp. 12 109–12 120, 2017.
- [59] A. Dutt, C. Joshi, X. Ji, J. Cardenas, Y. Okawachi, K. Luke, A. L. Gaeta, and M. Lipson, “On-chip dual-comb source for spectroscopy,” *Science advances*, vol. 4, no. 3, e1701858, 2018.
- [60] G. Moille, X. Lu, A. Rao, Q. Li, D. A. Westly, L. Ranzani, S. B. Papp, M. Soltani, and K. Srinivasan, “Kerr-microresonator soliton frequency combs at cryogenic temperatures,” *Physical review applied*, vol. 12, no. 3, p. 034 057, 2019.
- [61] B. Yao, S.-W. Huang, Y. Liu, A. K. Vinod, C. Choi, M. Hoff, Y. Li, M. Yu, Z. Feng, D.-L. Kwong, *et al.*, “Gate-tunable frequency combs in graphene–nitride microresonators,” *Nature*, vol. 558, no. 7710, p. 410, 2018.
- [62] K. Alexander, J. P. George, J. Verbist, K. Neyts, B. Kuyken, D. Van Thourhout, and J. Beeckman, “Nanophotonic pockels modulators on a silicon nitride platform,” *Nature communications*, vol. 9, no. 1, p. 3444, 2018.
- [63] A. N. R. Ahmed, S. Shi, M. Zablocki, P. Yao, and D. W. Prather, “Tunable hybrid silicon nitride and thin-film lithium niobate electro-optic microresonator,” *Optics letters*, vol. 44, no. 3, pp. 618–621, 2019.
- [64] I. Datta, S. H. Chae, G. R. Bhatt, M. A. Tadayon, B. Li, Y. Yu, C. Park, J. Park, L. Cao, D. Basov, *et al.*, “Low-loss composite photonic platform based on 2d semiconductor monolayers,” *Nature Photonics*, vol. 14, no. 4, pp. 256–262, 2020.



- [65] M. Huang, “Stress effects on the performance of optical waveguides,” *International Journal of Solids and Structures*, vol. 40, no. 7, pp. 1615–1632, 2003.
- [66] P. J. Van Der Slot, M. A. Porcel, and K.-J. Boller, “Surface acoustic waves for acousto-optic modulation in buried silicon nitride waveguides,” *Optics express*, vol. 27, no. 2, pp. 1433–1452, 2019.
- [67] N. Hosseini, R. Dekker, M. Hoekman, M. Dekkers, J. Bos, A. Leinse, and R. Heideman, “Stress-optic modulator in triplex platform using a piezoelectric lead zirconate titanate (pzt) thin film,” *Optics express*, vol. 23, no. 11, pp. 14 018–14 026, 2015.
- [68] J. P. Epping, D. Marchenko, A. Leinse, R. Mateman, M. Hoekman, L. Wevers, E. J. Klein, C. G. Roeloffzen, M. Dekkers, and R. G. Heideman, “Ultra-low-power stress-optics modulator for microwave photonics,” in *Integrated Optics: Devices, Materials, and Technologies XXI*, International Society for Optics and Photonics, vol. 10106, 2017, 101060F.
- [69] J. Wang, K. Liu, Q. Zhao, A. Isichenko, R. Q. Rudy, and D. J. Blumenthal, “Fully symmetric controllable integrated three-resonator photonic molecule,” *arXiv preprint arXiv:2105.10815*, 2021.
- [70] A. Everhardt, T. Tran, C. Mitsolidou, T. Horner, R. Grootjans, *et al.*, “Ultra-low power stress-based phase actuation in triplex photonic circuits,” in *Proc. of SPIE Vol.*, vol. 12004, 2022, pp. 1 200 405–1.
- [71] W. Jin, R. G. Polcawich, P. A. Morton, and J. E. Bowers, “Piezoelectrically tuned silicon nitride ring resonator,” *Opt. Express*, vol. 26, no. 3, pp. 3174–3187, 2018.
- [72] P. Stanfield, A. Leenheer, C. Michael, R. Sims, and M. Eichenfield, “Cmos-compatible, piezo-optomechanically tunable photonics for visible wavelengths and cryogenic temperatures,” *Optics Express*, vol. 27, no. 20, pp. 28 588–28 605, 2019.
- [73] M. Dong, G. Clark, A. J. Leenheer, M. Zimmermann, D. Dominguez, A. J. Menssen, D. Heim, G. Gilbert, D. Englund, and M. Eichenfield, “High-speed programmable photonic circuits in a cryogenically compatible, visible–near-infrared 200 mm cmos architecture,” *Nature Photonics*, vol. 16, no. 1, pp. 59–65, 2022.
- [74] L. Midolo, A. Schliesser, and A. Fiore, “Nano-opto-electro-mechanical systems,” *Nature nanotechnology*, vol. 13, no. 1, p. 11, 2018.
- [75] C. Errando-Herranz, A. Y. Takabayashi, P. Edinger, H. Sattari, K. B. Gylfason, and N. Quack, “Mems for photonic integrated circuits,” *IEEE Journal of Selected Topics in Quantum Electronics*, vol. 26, no. 2, pp. 1–16, 2020.

- [76] C. Errando-Herranz, F. Niklaus, G. Stemme, and K. B. Gylfason, “A mems tunable photonic ring resonator with small footprint and large free spectral range,” in *2015 Transducers-2015 18th International Conference on Solid-State Sensors, Actuators and Microsystems (TRANSDUCERS)*, IEEE, 2015, pp. 1001–1004.
- [77] C. Bekker, C. G. Baker, R. Kalra, H.-H. Cheng, B.-B. Li, V. Prakash, and W. P. Bowen, “Free spectral range electrical tuning of a high quality on-chip microcavity,” *Optics express*, vol. 26, no. 26, pp. 33 649–33 670, 2018.
- [78] S. G. Johnson, M. Ibanescu, M. Skorobogatiy, O. Weisberg, J. Joannopoulos, and Y. Fink, “Perturbation theory for maxwell’s equations with shifting material boundaries,” *Physical review E*, vol. 65, no. 6, p. 066 611, 2002.
- [79] S. Gyger, J. Zichi, L. Schweickert, A. W. Elshaari, S. Steinhauer, S. F. Covre da Silva, A. Rastelli, V. Zwiller, K. D. Jöns, and C. Errando-Herranz, “Reconfigurable photonics with on-chip single-photon detectors,” *Nature communications*, vol. 12, no. 1, pp. 1–8, 2021.
- [80] C. Haffner, A. Joerg, M. Doderer, F. Mayor, D. Chelladurai, Y. Fedoryshyn, C. I. Roman, M. Mazur, M. Burla, H. J. Lezec, *et al.*, “Nano–opto-electro-mechanical switches operated at cmos-level voltages,” *Science*, vol. 366, no. 6467, pp. 860–864, 2019.
- [81] T. J. Seok, J. Luo, Z. Huang, K. Kwon, J. Henriksson, J. Jacobs, L. Ochikubo, R. S. Muller, and M. C. Wu, “Silicon photonic wavelength cross-connect with integrated mems switching,” *APL Photonics*, vol. 4, no. 10, p. 100 803, 2019.
- [82] P. Edinger, A. Y. Takabayashi, C. Errando-Herranz, U. Khan, H. Sattari, P. Verheyen, W. Bogaerts, N. Quack, and K. B. Gylfason, “Silicon photonic microelectromechanical phase shifters for scalable programmable photonics,” *Optics Letters*, vol. 46, no. 22, pp. 5671–5674, 2021.
- [83] J. Riemensberger, A. Lukashchuk, M. Karpov, W. Weng, E. Lucas, J. Liu, and T. J. Kippenberg, “Massively parallel coherent laser ranging using a soliton microcomb,” *Nature*, vol. 581, no. 7807, pp. 164–170, 2020.
- [84] G. Lihachev, J. Riemensberger, W. Weng, J. Liu, H. Tian, A. Siddharth, V. Snigirev, R. N. Wang, J. He, S. A. Bhave, *et al.*, “Ultralow-noise frequency-agile photonic integrated lasers,” *arXiv preprint arXiv:2104.02990*, 2021.
- [85] S. Ghosh and G. Piazza, “Laterally vibrating resonator based elasto-optic modulation in aluminum nitride,” *APL Photonics*, vol. 1, no. 3, p. 036 101, 2016.
- [86] H. Li, S. A. Tadesse, Q. Liu, and M. Li, “Nanophotonic cavity optomechanics with propagating acoustic waves at frequencies up to 12 ghz,” *Optica*, vol. 2, no. 9, pp. 826–831, 2015.

- [87] L. Cai, A. Mahmoud, M. Khan, M. Mahmoud, T. Mukherjee, J. Bain, and G. Piazza, “Acousto-optical modulation of thin film lithium niobate waveguide devices,” *Photonics Research*, vol. 7, no. 9, pp. 1003–1013, 2019.
- [88] Z. Yu and X. Sun, “Acousto-optic modulation of photonic bound state in the continuum,” *Light: Science & Applications*, vol. 9, no. 1, pp. 1–9, 2020.
- [89] C. J. Sarabalis, T. P. McKenna, R. N. Patel, R. Van Laer, and A. H. Safavi-Naeini, “Acousto-optic modulation in lithium niobate on sapphire,” *Appl Photonics*, vol. 5, no. 8, p. 086 104, 2020.
- [90] L. Shao, N. Sinclair, J. Leatham, Y. Hu, M. Yu, T. Turpin, D. Crowe, and M. Lončar, “Integrated microwave acousto-optic frequency shifter on thin-film lithium niobate,” *Optics Express*, vol. 28, no. 16, pp. 23 728–23 738, 2020.
- [91] A. E. Hassanien, S. Link, Y. Yang, E. Chow, L. L. Goddard, and S. Gong, “Efficient and wideband acousto-optic modulation on thin-film lithium niobate for microwave-to-photonic conversion,” *Photonics Research*, vol. 9, no. 7, pp. 1182–1190, 2021.
- [92] E. A. Kittlaus, W. M. Jones, P. T. Rakich, N. T. Otterstrom, R. E. Muller, and M. Rais-Zadeh, “Electrically driven acousto-optics and broadband non-reciprocity in silicon photonics,” *Nature Photonics*, vol. 15, no. 1, pp. 43–52, 2021.
- [93] F. Z. Bi and B. P. Barber, “Bulk acoustic wave rf technology,” *IEEE microwave magazine*, vol. 9, no. 5, pp. 65–80, 2008.
- [94] V. J. Gokhale, B. P. Downey, J. A. Roussos, D. S. Katzer, and D. J. Meyer, “Passive high power rf comb filters using epitaxial gan/nbn/sic hbars,” *IEEE Transactions on Ultrasonics, Ferroelectrics, and Frequency Control*, vol. 68, no. 11, pp. 3406–3414, 2021.
- [95] R. Boudot, G. Martin, J.-M. Friedt, and E. Rubiola, “Frequency flicker of 2.3 ghz aln-sapphire high-overtone bulk acoustic resonators,” *Journal of Applied Physics*, vol. 120, no. 22, p. 224 903, 2016.
- [96] T. Daugey, J.-M. Friedt, G. Martin, and R. Boudot, “A high-overtone bulk acoustic wave resonator-oscillator-based 4.596 ghz frequency source: Application to a coherent population trapping cs vapor cell atomic clock,” *Review of Scientific Instruments*, vol. 86, no. 11, p. 114 703, 2015.
- [97] Y. Chu, P. Kharel, W. H. Renninger, L. D. Burkhardt, L. Frunzio, P. T. Rakich, and R. J. Schoelkopf, “Quantum acoustics with superconducting qubits,” *Science*, vol. 358, no. 6360, pp. 199–202, 2017.

- [98] Y. Chu, P. Kharel, T. Yoon, L. Frunzio, P. T. Rakich, and R. J. Schoelkopf, “Creation and control of multi-phonon fock states in a bulk acoustic-wave resonator,” *Nature*, vol. 563, no. 7733, pp. 666–670, 2018.
- [99] U. von Lüpke, Y. Yang, M. Bild, L. Michaud, M. Fadel, and Y. Chu, “Parity measurement in the strong dispersive regime of circuit quantum acoustodynamics,” *arXiv preprint arXiv:2110.00263*, 2021.
- [100] E. MacQuarrie, T. Gosavi, N. Jungwirth, S. Bhave, and G. Fuchs, “Mechanical spin control of nitrogen-vacancy centers in diamond,” *Physical review letters*, vol. 111, no. 22, p. 227 602, 2013.
- [101] E. MacQuarrie, T. Gosavi, S. Bhave, and G. Fuchs, “Continuous dynamical decoupling of a single diamond nitrogen-vacancy center spin with a mechanical resonator,” *Physical Review B*, vol. 92, no. 22, p. 224 419, 2015.
- [102] D. Marpaung, J. Yao, and J. Capmany, “Integrated microwave photonics,” *Nature photonics*, vol. 13, no. 2, p. 80, 2019.
- [103] E. Obrzud, S. Lecomte, and T. Herr, “Temporal solitons in microresonators driven by optical pulses,” *Nature Photonics*, vol. 11, no. 9, p. 600, 2017.
- [104] L. Fan, C.-L. Zou, N. Zhu, and H. X. Tang, “Spectrotemporal shaping of itinerant photons via distributed nanomechanics,” *Nature Photonics*, p. 1, 2019.
- [105] V. Supradeepa, C. M. Long, R. Wu, F. Ferdous, E. Hamidi, D. E. Leaird, and A. M. Weiner, “Comb-based radiofrequency photonic filters with rapid tunability and high selectivity,” *Nature Photonics*, vol. 6, no. 3, p. 186, 2012.
- [106] L. Fan, C.-L. Zou, R. Cheng, X. Guo, X. Han, Z. Gong, S. Wang, and H. X. Tang, “Superconducting cavity electro-optics: A platform for coherent photon conversion between superconducting and photonic circuits,” *Science Advances*, vol. 4, no. 8, eaar4994, Aug. 2018.
- [107] M. Aspelmeyer, T. J. Kippenberg, and F. Marquardt, “Cavity optomechanics,” *Reviews of Modern Physics*, vol. 86, no. 4, p. 1391, 2014.
- [108] G. S. Wiederhecker, P. Dainese, and T. P. Mayer Alegre, “Brillouin optomechanics in nanophotonic structures,” *APL Photonics*, vol. 4, no. 7, p. 071 101, 2019.
- [109] J. Rosenberg, Q. Lin, and O. Painter, “Static and dynamic wavelength routing via the gradient optical force,” *Nature Photonics*, vol. 3, no. 8, pp. 478–483, 2009.
- [110] J. Xu and R. Stroud, *Acousto-optic devices: principles, design, and applications*. Wiley, 1992.

- [111] F. Gyger, J. Liu, F. Yang, J. He, A. S. Raja, R. N. Wang, S. A. Bhawe, T. J. Kippenberg, and L. Thévenaz, “Observation of stimulated brillouin scattering in silicon nitride integrated waveguides,” *Phys. Rev. Lett.*, vol. 124, p. 013 902, 1 2020.
- [112] T. Capelle, Y. Tsaturyan, A. Barg, and A. Schliesser, “Polarimetric analysis of stress anisotropy in nanomechanical silicon nitride resonators,” *Applied Physics Letters*, vol. 110, no. 18, p. 181 106, 2017.
- [113] J. Chan, A. H. Safavi-Naeini, J. T. Hill, S. Meenehan, and O. Painter, “Optimized optomechanical crystal cavity with acoustic radiation shield,” *Applied Physics Letters*, vol. 101, no. 8, p. 081 115, 2012.
- [114] M. Gorodetsky, A. Schliesser, G. Anetsberger, S. Deleglise, and T. J. Kippenberg, “Determination of the vacuum optomechanical coupling rate using frequency noise calibration,” *Optics express*, vol. 18, no. 22, pp. 23 236–23 246, 2010.
- [115] K. Luke, A. Dutt, C. B. Poitras, and M. Lipson, “Overcoming si<sub>3</sub>n<sub>4</sub> film stress limitations for high quality factor ring resonators,” *Opt. Express*, vol. 21, no. 19, pp. 22 829–22 833, 2013.
- [116] M. H. Pfeiffer, A. Kordts, V. Brasch, M. Zervas, M. Geiselmann, J. D. Jost, and T. J. Kippenberg, “Photonic damascene process for integrated high-q microresonator based nonlinear photonics,” *Optica*, vol. 3, no. 1, pp. 20–25, 2016.
- [117] M. H. P. Pfeiffer, C. Herkommer, J. Liu, T. Morais, M. Zervas, M. Geiselmann, and T. J. Kippenberg, “Photonic damascene process for low-loss, high-confinement silicon nitride waveguides,” *IEEE J. Sel. Top. Quantum Electron.*, vol. 24, no. 4, pp. 1–11, 2018.
- [118] M. H. Pfeiffer, J. Liu, A. S. Raja, T. Morais, B. Ghadiani, and T. J. Kippenberg, “Ultra-smooth silicon nitride waveguides based on the damascene reflow process: Fabrication and loss origins,” *Optica*, vol. 5, no. 7, pp. 884–892, 2018.
- [119] J. Yang, C. Si, G. Han, M. Zhang, L. Ma, Y. Zhao, and J. Ning, “Researching the aluminum nitride etching process for application in mems resonators,” *Micromachines*, vol. 6, no. 2, pp. 281–290, 2015.
- [120] D.-X. Xu, “Polarization control in silicon photonic waveguide components using cladding stress engineering,” in *Silicon Photonics II*, Springer, 2011, pp. 31–70.
- [121] J. Liu, H. Tian, E. Lucas, A. S. Raja, G. Lihachev, R. N. Wang, J. He, T. Liu, M. H. Anderson, W. Weng, S. A. Bhawe, and T. J. Kippenberg, “Monolithic piezoelectric control of soliton microcombs,” *Nature*, vol. 583, no. 7816, pp. 385–390, 2020.

- [122] C. Aardahl, J. Rogers Jr, H. Yun, Y. Ono, D. Tweet, and S.-T. Hsu, “Electrical properties of aln thin films deposited at low temperature on si (100),” *Thin Solid Films*, vol. 346, no. 1-2, pp. 174–180, 1999.
- [123] Z. L. Newman, V. Maurice, T. Drake, J. R. Stone, T. C. Briles, D. T. Spencer, C. Fredrick, Q. Li, D. Westly, B. R. Ilic, B. Shen, M.-G. Suh, K. Y. Yang, C. Johnson, D. M. S. Johnson, L. Hollberg, K. J. Vahala, K. Srinivasan, S. A. Diddams, J. Kitching, S. B. Papp, and M. T. Hummon, “Architecture for the photonic integration of an optical atomic clock,” *Optica*, vol. 6, no. 5, pp. 680–685, 2019.
- [124] C. Xiong, W. H. Pernice, X. Sun, C. Schuck, K. Y. Fong, and H. X. Tang, “Aluminum nitride as a new material for chip-scale optomechanics and nonlinear optics,” *New Journal of Physics*, vol. 14, no. 9, p. 095 014, 2012.
- [125] G. Wu, J. Xu, E. J. Ng, and W. Chen, “Mems resonators for frequency reference and timing applications,” *Journal of Microelectromechanical Systems*, vol. 29, no. 5, pp. 1137–1166, 2020.
- [126] I. Wilson-Rae, R. Barton, S. Verbridge, D. Southworth, B. Ilic, H. G. Craighead, and J. Parpia, “High-q nanomechanics via destructive interference of elastic waves,” *Physical review letters*, vol. 106, no. 4, p. 047 205, 2011.
- [127] Y. Zhang, Z. Wang, and J. D. N. Cheeke, “Resonant spectrum method to characterize piezoelectric films in composite resonators,” *ieee transactions on ultrasonics, ferroelectrics, and frequency control*, vol. 50, no. 3, pp. 321–333, 2003.
- [128] V. J. Gokhale, B. P. Downey, D. S. Katzer, and D. J. Meyer, “Temperature evolution of frequency and anharmonic phonon loss for multi-mode epitaxial hbars,” *Applied Physics Letters*, vol. 117, no. 12, p. 124 003, 2020.
- [129] V. J. Gokhale, B. P. Downey, D. S. Katzer, M. T. Hardy, N. Nepal, and D. J. Meyer, “Engineering efficient acoustic power transfer in hbars and other composite resonators,” *Journal of Microelectromechanical Systems*, vol. 29, no. 5, pp. 1014–1019, 2020.
- [130] V. J. Gokhale, B. P. Downey, D. S. Katzer, N. Nepal, A. C. Lang, R. M. Stroud, and D. J. Meyer, “Epitaxial bulk acoustic wave resonators as highly coherent multi-phonon sources for quantum acoustodynamics,” *Nature communications*, vol. 11, no. 1, pp. 1–9, 2020.
- [131] D. B. Sohn, S. Kim, and G. Bahl, “Time-reversal symmetry breaking with acoustic pumping of nanophotonic circuits,” *Nature Photonics*, vol. 12, no. 2, pp. 91–97, 2018.
- [132] S. Kim, D. B. Sohn, C. W. Peterson, and G. Bahl, “On-chip optical non-reciprocity through a synthetic hall effect for photons,” *APL Photonics*, vol. 6, no. 1, p. 011 301, 2021.

- [133] D. B. Sohn, O. E. Örsel, and G. Bahl, “Electrically driven optical isolation through phonon-mediated photonic autler–townes splitting,” *Nature Photonics*, vol. 15, no. 11, pp. 822–827, 2021.
- [134] V. Pinrod, B. Davaji, and A. Lal, “Coexisting surface and bulk gyroscopic effects,” in *2018 IEEE International Ultrasonics Symposium (IUS)*, IEEE, 2018, pp. 1–4.
- [135] G. Kurizki, P. Bertet, Y. Kubo, K. Mølmer, D. Petrosyan, P. Rabl, and J. Schmiedmayer, “Quantum technologies with hybrid systems,” *Proceedings of the National Academy of Sciences*, vol. 112, no. 13, pp. 3866–3873, 2015.
- [136] B. Jiang, N. Opondo, and S. A. Bhawe, “Semi-insulating 4h-sic lateral bulk acoustic wave resonators,” *Applied Physics Letters*, vol. 118, no. 11, p. 114002, 2021.
- [137] X. Zhu, Q. Wei, Y. Cheng, D. Wu, and X. Liu, “Perfect monochromatic acoustic anti-reflection: A first-principles study,” *Journal of Applied Physics*, vol. 121, no. 9, p. 094504, 2017.
- [138] M.-H. Lu, L. Feng, and Y.-F. Chen, “Phononic crystals and acoustic metamaterials,” *Materials today*, vol. 12, no. 12, pp. 34–42, 2009.
- [139] M. Pirro, B. Herrera, M. Assylbekova, G. Giribaldi, L. Colombo, and M. Rinaldi, “Characterization of dielectric and piezoelectric properties of ferroelectric alscn thin films,” in *2021 IEEE 34th International Conference on Micro Electro Mechanical Systems (MEMS)*, IEEE, 2021, pp. 646–649.
- [140] S. Fichtner, N. Wolff, G. Krishnamurthy, A. Petraru, S. Bohse, F. Lofink, S. Chemnitz, H. Kohlstedt, L. Kienle, and B. Wagner, “Identifying and overcoming the interface originating c-axis instability in highly sc enhanced aln for piezoelectric micro-electromechanical systems,” *Journal of Applied Physics*, vol. 122, no. 3, p. 035301, 2017.
- [141] C. Huang, H. Shi, L. Yu, K. Wang, M. Cheng, Q. Huang, W. Jiao, and J. Sun, “Acousto-optic modulation in silicon waveguides based on piezoelectric aluminum scandium nitride film,” *Advanced Optical Materials*, vol. 10, no. 6, p. 2102334, 2022.
- [142] G. Esteves, T. R. Young, Z. Tang, S. Yen, T. M. Bauer, M. D. Henry, and R. H. Olsson III, “Al<sub>0.68</sub>Sc<sub>0.32</sub>n lamb wave resonators with electromechanical coupling coefficients near 10.28%,” *Applied Physics Letters*, vol. 118, no. 17, p. 171902, 2021.
- [143] V. Yoshioka, J. Lu, Z. Tang, J. Jin, R. H. Olsson III, and B. Zhen, “Strongly enhanced second-order optical nonlinearity in cmos-compatible al<sub>1-x</sub>sc<sub>x</sub>n thin films,” *APL Materials*, vol. 9, no. 10, p. 101104, 2021.

- [144] T. Mikolajick, U. Schroeder, and S. Slesazeck, “The past, the present, and the future of ferroelectric memories,” *IEEE Transactions on Electron Devices*, vol. 67, no. 4, pp. 1434–1443, 2020.
- [145] E. D. Black, “An introduction to pound–drever–hall laser frequency stabilization,” *American journal of physics*, vol. 69, no. 1, pp. 79–87, 2001.
- [146] T. Udem, R. Holzwarth, and T. W. Hänsch, “Optical frequency metrology,” *Nature*, vol. 416, no. 6877, pp. 233–237, 2002.
- [147] I. Coddington, N. Newbury, and W. Swann, “Dual-comb spectroscopy,” *Optica*, vol. 3, no. 4, pp. 414–426, 2016.
- [148] S. T. Cundiff and J. Ye, “Colloquium: Femtosecond optical frequency combs,” *Reviews of Modern Physics*, vol. 75, no. 1, p. 325, 2003.
- [149] P. Del’Haye, A. Schliesser, O. Arcizet, T. Wilken, R. Holzwarth, and T. J. Kippenberg, “Optical frequency comb generation from a monolithic microresonator,” *Nature*, vol. 450, no. 7173, pp. 1214–1217, 2007.
- [150] T. Kippenberg, S. Spillane, and K. Vahala, “Kerr-nonlinearity optical parametric oscillation in an ultrahigh-q toroid microcavity,” *Physical review letters*, vol. 93, no. 8, p. 083 904, 2004.
- [151] Y. K. Chembo, “Kerr optical frequency combs: Theory, applications and perspectives,” *Nanophotonics*, vol. 5, no. 2, pp. 214–230, 2016.
- [152] J. S. Levy, A. Gondarenko, M. A. Foster, A. C. Turner-Foster, A. L. Gaeta, and M. Lipson, “Cmos-compatible multiple-wavelength oscillator for on-chip optical interconnects,” *Nature photonics*, vol. 4, no. 1, pp. 37–40, 2010.
- [153] A. A. Savchenkov, A. B. Matsko, V. S. Ilchenko, I. Solomatine, D. Seidel, and L. Maleki, “Tunable optical frequency comb with a crystalline whispering gallery mode resonator,” *Physical review letters*, vol. 101, no. 9, p. 093 902, 2008.
- [154] F. Riehle, *Frequency standards: basics and applications*. John Wiley & Sons, 2006.
- [155] R. J. Jones and J.-C. Diels, “Stabilization of femtosecond lasers for optical frequency metrology and direct optical to radio frequency synthesis,” *Physical review letters*, vol. 86, no. 15, p. 3288, 2001.
- [156] T. M. Fortier, M. S. Kirchner, F. Quinlan, J. Taylor, J. Bergquist, T. Rosenband, N. Lemke, A. Ludlow, Y. Jiang, C. Oates, *et al.*, “Generation of ultrastable microwaves via optical frequency division,” *Nature Photonics*, vol. 5, no. 7, pp. 425–429, 2011.



- [157] M. Takamoto, F.-L. Hong, R. Higashi, and H. Katori, “An optical lattice clock,” *Nature*, vol. 435, no. 7040, pp. 321–324, 2005.
- [158] T. Fortier and E. Baumann, “20 years of developments in optical frequency comb technology and applications,” *Communications Physics*, vol. 2, no. 1, pp. 1–16, 2019.
- [159] H. Guo, M. Karpov, E. Lucas, A. Kordts, M. H. Pfeiffer, V. Brasch, G. Lihachev, V. E. Lobanov, M. L. Gorodetsky, and T. J. Kippenberg, “Universal dynamics and deterministic switching of dissipative kerr solitons in optical microresonators,” *Nature Physics*, vol. 13, no. 1, pp. 94–102, 2017.
- [160] R. Drever, J. L. Hall, F. Kowalski, J. Hough, G. Ford, A. Munley, and H. Ward, “Laser phase and frequency stabilization using an optical resonator,” *Applied Physics B*, vol. 31, no. 2, pp. 97–105, 1983.
- [161] A. S. Raja, J. Liu, N. Volet, R. N. Wang, J. He, E. Lucas, R. Bouchandand, P. Morton, J. Bowers, and T. J. Kippenberg, “Chip-based soliton microcomb module using a hybrid semiconductor laser,” *Optics Express*, vol. 28, no. 3, pp. 2714–2721, 2020.
- [162] N. Lindenmann, G. Balthasar, D. Hillerkuss, R. Schmogrow, M. Jordan, J. Leuthold, W. Freude, and C. Koos, “Photonic wire bonding: A novel concept for chip-scale interconnects,” *Optics express*, vol. 20, no. 16, pp. 17 667–17 677, 2012.
- [163] N. Lindenmann, S. Dottermusch, M. L. Goedecke, T. Hoose, M. R. Billah, T. P. Onanuga, A. Hofmann, W. Freude, and C. Koos, “Connecting silicon photonic circuits to multicore fibers by photonic wire bonding,” *Journal of lightwave Technology*, vol. 33, no. 4, pp. 755–760, 2014.
- [164] R. Wu, C. M. Long, D. E. Leaird, and A. M. Weiner, “Directly generated gaussian-shaped optical frequency comb for microwave photonic filtering and picosecond pulse generation,” *IEEE Photonics Technology Letters*, vol. 24, no. 17, pp. 1484–1486, 2012.
- [165] Y. Dou, H. Zhang, and M. Yao, “Generation of flat optical-frequency comb using cascaded intensity and phase modulators,” *IEEE Photonics Technology Letters*, vol. 24, no. 9, pp. 727–729, 2012.
- [166] W. Pang, H. Zhang, R. C. Ruby, H. Yu, and E. S. Kim, “Analytical and experimental study on the second harmonic mode response of a bulk acoustic wave resonator,” *Journal of Micromechanics and Microengineering*, vol. 20, no. 11, p. 115 015, 2010.
- [167] C.-C. Nguyen and J. Kitching, “Towards chip-scale atomic clocks,” in *ISSCC. 2005 IEEE International Digest of Technical Papers. Solid-State Circuits Conference, 2005.*, IEEE, 2005, pp. 84–85.

- [168] T. Blésin, H. Tian, S. A. Bhave, and T. J. Kippenberg, “Quantum coherent microwave-optical transduction using high-overtone bulk acoustic resonances,” *Physical Review A*, vol. 104, no. 5, p. 052 601, 2021.
- [169] H. Tian, J. Liu, A. Siddharth, R. N. Wang, T. Blésin, J. He, T. J. Kippenberg, and S. A. Bhave, “Magnetic-free silicon nitride integrated optical isolator,” *Nature Photonics*, vol. 15, no. 11, pp. 828–836, 2021.
- [170] J. D. Larson, P. D. Bradley, S. Wartenberg, and R. C. Ruby, “Modified butterworth-van dyke circuit for fbar resonators and automated measurement system,” in *2000 IEEE Ultrasonics Symposium. Proceedings. An International Symposium (Cat. No. 00CH37121)*, IEEE, vol. 1, 2000, pp. 863–868.
- [171] S. Gundavarapu, G. M. Brodnik, M. Puckett, T. Huffman, D. Bose, R. Behunin, J. Wu, T. Qiu, C. Pinho, N. Chauhan, J. Nohava, P. T. Rakich, K. D. Nelson, M. Salit, and D. J. Blumenthal, “Sub-hertz fundamental linewidth photonic integrated brillouin laser,” *Nature Photonics*, vol. 13, no. 1, pp. 60–67, 2019.
- [172] C. G. H. Roeloffzen, L. Zhuang, C. Taddei, A. Leinse, R. G. Heideman, P. W. L. van Dijk, R. M. Oldenbeuving, D. A. I. Marpaung, M. Burla, and K. -J. Boller, “Silicon nitride microwave photonic circuits,” *Opt. Express*, vol. 21, no. 19, pp. 22 937–22 961, 2013.
- [173] J. Wu, X. Xu, T. G. Nguyen, S. T. Chu, B. E. Little, R. Morandotti, A. Mitchell, and D. J. Moss, “Rf photonics: An optical microcombs’perspective,” *IEEE J. Sel. Top. Quantum Electron.*, vol. 24, no. 4, pp. 1–20, 2018.
- [174] J. Feldmann, N. Youngblood, M. Karpov, H. Gehring, X. Li, M. Stappers, M. Le Gallo, X. Fu, A. Lukashchuk, A. S. Raja, J. Liu, C. D. Wright, A. Sebastian, T. J. Kippenberg, W. H. P. Pernice, and H. Bhaskaran, “Parallel convolutional processing using an integrated photonic tensor core,” *Nature*, vol. 589, no. 7840, pp. 52–58, 2021.
- [175] J. M. Arrazola, V. Bergholm, K. Brádler, T. R. Bromley, M. J. Collins, I. Dhand, A. Fumagalli, T. Gerrits, A. Goussev, L. G. Helt, J. Hundal, T. Isacson, R. B. Israel, J. Izaac, S. Jahangiri, R. Janik, N. Killoran, S. P. Kumar, J. Lavoie, A. E. Lita, D. H. Mahler, M. Menotti, B. Morrison, S. W. Nam, L. Neuhaus, H. Y. Qi, N. Quesada, A. Repeatingon, K. K. Sabapathy, M. Schuld, D. Su, J. Swinarton, A. Száva, K. Tan, P. Tan, V. D. Vaidya, Z. Vernon, Z. Zabaneh, and Y. Zhang, “Quantum circuits with many photons on a programmable nanophotonic chip,” *Nature*, vol. 591, no. 7848, pp. 54–60, 2021.
- [176] K. K. Mehta, C. Zhang, M. Malinowski, T.-L. Nguyen, M. Stadler, and J. P. Home, “Integrated optical multi-ion quantum logic,” *Nature*, vol. 586, no. 7830, pp. 533–537, 2020.

- [177] R. J. Niffenegger, J. Stuart, C. Sorace-Agaskar, D. Kharas, S. Bramhavar, C. D. Bruzewicz, W. Loh, R. T. Maxson, R. McConnell, D. Reens, G. N. West, J. M. Sage, and J. Chiaverini, “Integrated multi-wavelength control of an ion qubit,” *Nature*, vol. 586, no. 7830, pp. 538–542, 2020.
- [178] K. Srinivasan and B. J. H. Stadler, “Magneto-optical materials and designs for integrated te- and tm-mode planar waveguide isolators: A review,” *Opt. Mater. Express*, vol. 8, no. 11, pp. 3307–3318, 2018.
- [179] L. Bi, J. Hu, P. Jiang, D. H. Kim, G. F. Dionne, L. C. Kimerling, and C. A. Ross, “On-chip optical isolation in monolithically integrated non-reciprocal optical resonators,” *Nature Photonics*, vol. 5, no. 12, pp. 758–762, 2011.
- [180] D. Huang, P. Pintus, C. Zhang, Y. Shoji, T. Mizumoto, and J. E. Bowers, “Electrically driven and thermally tunable integrated optical isolators for silicon photonics,” *IEEE J. Sel. Top. Quantum Electron.*, vol. 22, no. 6, pp. 271–278, 2016, ISSN: 1558-4542.
- [181] W. Yan, Y. Yang, S. Liu, Y. Zhang, S. Xia, T. Kang, W. Yang, J. Qin, L. Deng, and L. Bi, “Waveguide-integrated high-performance magneto-optical isolators and circulators on silicon nitride platforms,” *Optica*, vol. 7, no. 11, pp. 1555–1562, 2020.
- [182] D. Awschalom, K. K. Berggren, H. Bernien, S. Bhave, L. D. Carr, P. Davids, S. E. Economou, D. Englund, A. Faraon, M. Fejer, S. Guha, M. V. Gustafsson, E. Hu, L. Jiang, J. Kim, B. Korzh, P. Kumar, P. G. Kwiat, M. Lončar, M. D. Lukin, D. A. Miller, C. Monroe, S. W. Nam, P. Narang, J. S. Orcutt, M. G. Raymer, A. H. Safavi-Naeini, M. Spiropulu, K. Srinivasan, S. Sun, J. Vučković, E. Waks, R. Walsworth, A. M. Weiner, and Z. Zhang, “Development of quantum interconnects (quics) for next-generation information technologies,” *PRX Quantum*, vol. 2, p. 017002, 1 2021.
- [183] K. Fang, Z. Yu, and S. Fan, “Realizing effective magnetic field for photons by controlling the phase of dynamic modulation,” *Nature Photonics*, vol. 6, no. 11, pp. 782–787, 2012.
- [184] L. D. Tzuang, K. Fang, P. Nussenzveig, S. Fan, and M. Lipson, “Non-reciprocal phase shift induced by an effective magnetic flux for light,” *Nature Photonics*, vol. 8, no. 9, pp. 701–705, 2014.
- [185] N. Dostart, H. Gevorgyan, D. Onural, and M. A. Popović, “Optical isolation using microring modulators,” *Opt. Lett.*, vol. 46, no. 3, pp. 460–463, 2021.
- [186] L. Fan, J. Wang, L. T. Varghese, H. Shen, B. Niu, Y. Xuan, A. M. Weiner, and M. Qi, “An all-silicon passive optical diode,” *Science*, vol. 335, no. 6067, pp. 447–450, 2012, ISSN: 0036-8075.

- [187] B. Peng, Ş. K. Özdemir, F. Lei, F. Monifi, M. Gianfreda, G. L. Long, S. Fan, F. Nori, C. M. Bender, and L. Yang, “Parity–time-symmetric whispering-gallery microcavities,” *Nature Physics*, vol. 10, no. 5, pp. 394–398, 2014.
- [188] L. Chang, X. Jiang, S. Hua, C. Yang, J. Wen, L. Jiang, G. Li, G. Wang, and M. Xiao, “Parity–time symmetry and variable optical isolation in active–passive-coupled microresonators,” *Nature Photonics*, vol. 8, no. 7, pp. 524–529, 2014.
- [189] L. D. Bino, J. M. Silver, M. T. M. Woodley, S. L. Stebbings, X. Zhao, and P. Del’Haye, “Microresonator isolators and circulators based on the intrinsic nonreciprocity of the kerr effect,” *Optica*, vol. 5, no. 3, pp. 279–282, 2018.
- [190] S. Hua, J. Wen, X. Jiang, Q. Hua, L. Jiang, and M. Xiao, “Demonstration of a chip-based optical isolator with parametric amplification,” *Nature Communications*, vol. 7, no. 1, p. 13 657, 2016.
- [191] K. Y. Yang, J. Skarda, M. Cotrufo, A. Dutt, G. H. Ahn, M. Sawaby, D. Vercruysse, A. Arbabian, S. Fan, A. Alù, and J. Vučković, “Inverse-designed non-reciprocal pulse router for chip-based lidar,” *Nature Photonics*, vol. 14, no. 6, pp. 369–374, 2020.
- [192] Q.-T. Cao, R. Liu, H. Wang, Y.-K. Lu, C.-W. Qiu, S. Rotter, Q. Gong, and Y.-F. Xiao, “Reconfigurable symmetry-broken laser in a symmetric microcavity,” *Nature Communications*, vol. 11, no. 1, p. 1136, 2020.
- [193] Z. Shen, Y.-L. Zhang, Y. Chen, C.-L. Zou, Y.-F. Xiao, X.-B. Zou, F.-W. Sun, G.-C. Guo, and C.-H. Dong, “Experimental realization of optomechanically induced non-reciprocity,” *Nature Photonics*, vol. 10, no. 10, pp. 657–661, 2016.
- [194] F. Ruesink, M.-A. Miri, A. Alù, and E. Verhagen, “Nonreciprocity and magnetic-free isolation based on optomechanical interactions,” *Nature Communications*, vol. 7, no. 1, p. 13 662, 2016.
- [195] Z. Shen, Y.-L. Zhang, Y. Chen, F.-W. Sun, X.-B. Zou, G.-C. Guo, C.-L. Zou, and C.-H. Dong, “Reconfigurable optomechanical circulator and directional amplifier,” *Nature Communications*, vol. 9, no. 1, p. 1797, 2018.
- [196] F. Ruesink, J. P. Mathew, M.-A. Miri, A. Alù, and E. Verhagen, “Optical circulation in a multimode optomechanical resonator,” *Nature Communications*, vol. 9, no. 1, p. 1798, 2018.
- [197] M. S. Kang, A. Butsch, and P. S. J. Russell, “Reconfigurable light-driven opto-acoustic isolators in photonic crystal fibre,” *Nature Photonics*, vol. 5, no. 9, pp. 549–553, 2011.

- [198] C. G. Poulton, R. Pant, A. Byrnes, S. Fan, M. J. Steel, and B. J. Eggleton, “Design for broadband on-chip isolator using stimulated brillouin scattering in dispersion-engineered chalcogenide waveguides,” *Opt. Express*, vol. 20, no. 19, pp. 21 235–21 246, 2012.
- [199] C.-H. Dong, Z. Shen, C.-L. Zou, Y.-L. Zhang, W. Fu, and G.-C. Guo, “Brillouin-scattering-induced transparency and non-reciprocal light storage,” *Nature Communications*, vol. 6, no. 1, p. 6193, 2015.
- [200] J. Kim, M. C. Kuzyk, K. Han, H. Wang, and G. Bahl, “Non-reciprocal brillouin scattering induced transparency,” *Nature Physics*, vol. 11, no. 3, pp. 275–280, 2015.
- [201] M. Merklein, B. Stiller, K. Vu, P. Ma, S. J. Madden, and B. J. Eggleton, “On-chip broadband nonreciprocal light storage,” *Nanophotonics*, vol. 10, no. 1, pp. 75–82, 2021.
- [202] M. Scheucher, A. Hilico, E. Will, J. Volz, and A. Rauschenbeutel, “Quantum optical circulator controlled by a single chirally coupled atom,” *Science*, vol. 354, no. 6319, pp. 1577–1580, 2016, ISSN: 0036-8075.
- [203] S. Zhang, Y. Hu, G. Lin, Y. Niu, K. Xia, J. Gong, and S. Gong, “Thermal-motion-induced non-reciprocal quantum optical system,” *Nature Photonics*, vol. 12, no. 12, pp. 744–748, 2018.
- [204] X.-X. Hu, Z.-B. Wang, P. Zhang, G.-J. Chen, Y.-L. Zhang, G. Li, X.-B. Zou, T. Zhang, H. X. Tang, C.-H. Dong, G.-C. Guo, and C.-L. Zou, “Noiseless photonic non-reciprocity via optically-induced magnetization,” *arXiv*, vol. 2009.09819, 2020.
- [205] Y. Shi, Z. Yu, and S. Fan, “Limitations of nonlinear optical isolators due to dynamic reciprocity,” *Nature Photonics*, vol. 9, no. 6, pp. 388–392, 2015.
- [206] Z. Yu and S. Fan, “Complete optical isolation created by indirect interband photonic transitions,” *Nature Photonics*, vol. 3, no. 2, pp. 91–94, 2009.
- [207] H. Lira, Z. Yu, S. Fan, and M. Lipson, “Electrically driven nonreciprocity induced by interband photonic transition on a silicon chip,” *Phys. Rev. Lett.*, vol. 109, p. 033 901, 3 2012.
- [208] D. L. Sounas and A. Alù, “Angular-momentum-biased nanorings to realize magnetic-free integrated optical isolation,” *ACS Photonics*, vol. 1, no. 3, pp. 198–204, 2014.
- [209] E. A. Kittlaus, N. T. Otterstrom, P. Kharel, S. Gertler, and P. T. Rakich, “Non-reciprocal interband brillouin modulation,” *Nature Photonics*, vol. 12, no. 10, pp. 613–619, 2018.

- [210] Y. Shi, W. Shin, and S. Fan, “Multi-frequency finite-difference frequency-domain algorithm for active nanophotonic device simulations,” *Optica*, vol. 3, no. 11, pp. 1256–1259, 2016.
- [211] Y. Shi, “Two-dimensional finite-difference frequency-domain (fdfd) programs,” 2018.
- [212] K. C. Balram, M. Davanço, J. Y. Lim, J. D. Song, and K. Srinivasan, “Moving boundary and photoelastic coupling in gaas optomechanical resonators,” *Optica*, vol. 1, no. 6, pp. 414–420, 2014.
- [213] M. Rais-Zadeh, V. A. Thakar, Z. Wu, and A. Peczalski, “Temperature compensated silicon resonators for space applications,” in *Reliability, Packaging, Testing, and Characterization of MOEMS/MEMS and Nanodevices XII*, International Society for Optics and Photonics, vol. 8614, 2013, 86140E.
- [214] K. Gallacher, P. F. Griffin, E. Riis, M. Sorel, and D. J. Paul, “Silicon nitride waveguide polarization rotator and polarization beam splitter for chip-scale atomic systems,” *APL Photonics*, vol. 7, no. 4, p. 046 101, 2022.
- [215] J. M. Lukens and P. Lougovski, “Frequency-encoded photonic qubits for scalable quantum information processing,” *Optica*, vol. 4, no. 1, pp. 8–16, 2017.
- [216] T. Kobayashi, R. Ikuta, S. Yasui, S. Miki, T. Yamashita, H. Terai, T. Yamamoto, M. Koashi, and N. Imoto, “Frequency-domain hong-ou-mandel interference,” *Nature Photonics*, vol. 10, no. 7, pp. 441–444, 2016.
- [217] C. Joshi, A. Farsi, A. Dutt, B. Y. Kim, X. Ji, Y. Zhao, A. M. Bishop, M. Lipson, and A. L. Gaeta, “Frequency-domain quantum interference with correlated photons from an integrated microresonator,” *Phys. Rev. Lett.*, vol. 124, p. 143 601, 14 2020.
- [218] P. Marin-Palomo, J. N. Kemal, M. Karpov, A. Kordts, J. Pfeifle, M. H. P. Pfeiffer, P. Trocha, S. Wolf, V. Brasch, M. H. Anderson, R. Rosenberger, K. Vijayan, W. Freude, T. J. Kippenberg, and C. Koos, “Microresonator-based solitons for massively parallel coherent optical communications,” *Nature*, vol. 546, p. 274, 2017.
- [219] G. Moille, Q. Li, T. C. Briles, S.-P. Yu, T. Drake, X. Lu, A. Rao, D. Westly, S. B. Papp, and K. Srinivasan, “Broadband resonator-waveguide coupling for efficient extraction of octave-spanning microcombs,” *Opt. Lett.*, vol. 44, no. 19, pp. 4737–4740, 2019.
- [220] Y. Hu, M. Yu, D. Zhu, N. Sinclair, A. Shams-Ansari, L. Shao, J. Holzgrafe, E. Puma, M. Zhang, and M. Lončar, “On-chip electro-optic frequency shifters and beam splitters,” *Nature*, vol. 599, no. 7886, pp. 587–593, 2021.

- [221] H.-K. Lo, M. Curty, and K. Tamaki, “Secure quantum key distribution,” *Nature Photonics*, vol. 8, no. 8, pp. 595–604, 2014.
- [222] V. Scarani, H. Bechmann-Pasquinucci, N. J. Cerf, M. Dušek, N. Lütkenhaus, and M. Peev, “The security of practical quantum key distribution,” *Reviews of modern physics*, vol. 81, no. 3, p. 1301, 2009.
- [223] N. T. Otterstrom, S. Gertler, E. A. Kittlaus, M. Gehl, A. L. Starbuck, C. M. Dallo, A. T. Pomerene, D. C. Trotter, P. T. Rakich, P. S. Davids, *et al.*, “Nonreciprocal frequency domain beam splitter,” *Physical review letters*, vol. 127, no. 25, p. 253 603, 2021.
- [224] J. Kim, S. Kim, and G. Bahl, “Complete linear optical isolation at the microscale with ultralow loss,” *Scientific Reports*, vol. 7, no. 1, p. 1647, 2017.
- [225] A. S. Voloshin, N. M. Kondratiev, G. V. Lihachev, J. Liu, V. E. Lobanov, N. Y. Dmitriev, W. Weng, T. J. Kippenberg, and I. A. Bilenko, “Dynamics of soliton self-injection locking in optical microresonators,” *Nature Communications*, vol. 12, no. 1, p. 235, 2021.
- [226] T. C. Briles, S.-P. Yu, L. Chang, C. Xiang, J. Guo, D. Kinghorn, G. Moille, K. Srinivasan, J. E. Bowers, and S. B. Papp, “Hybrid inp and sin integration of an octave-spanning frequency comb,” *APL Photonics*, vol. 6, no. 2, p. 026 102, 2021.
- [227] A. Youssefi, I. Shomroni, Y. J. Joshi, N. R. Bernier, A. Lukashchuk, P. Urich, L. Qiu, and T. J. Kippenberg, “A cryogenic electro-optic interconnect for superconducting devices,” *Nature Electronics*, vol. 4, no. 5, pp. 326–332, 2021.
- [228] F. Lecocq, F. Quinlan, K. Cicak, J. Aumentado, S. Diddams, and J. Teufel, “Control and readout of a superconducting qubit using a photonic link,” *Nature*, vol. 591, no. 7851, pp. 575–579, 2021.
- [229] Y. Y. Gao, M. A. Rol, S. Touzard, and C. Wang, “Practical guide for building superconducting quantum devices,” *PRX Quantum*, vol. 2, no. 4, p. 040 202, 2021.
- [230] A. Blais, A. L. Grimsmo, S. Girvin, and A. Wallraff, “Circuit quantum electrodynamics,” *Reviews of Modern Physics*, vol. 93, no. 2, p. 025 005, 2021.
- [231] F. Arute, K. Arya, R. Babbush, D. Bacon, J. C. Bardin, R. Barends, R. Biswas, S. Boixo, F. G. Brandao, D. A. Buell, *et al.*, “Quantum supremacy using a programmable superconducting processor,” *Nature*, vol. 574, no. 7779, pp. 505–510, 2019.
- [232] A. Blais, S. M. Girvin, and W. D. Oliver, “Quantum information processing and quantum optics with circuit quantum electrodynamics,” *Nature Physics*, vol. 16, no. 3, pp. 247–256, 2020.

- [233] J. Koch, M. Y. Terri, J. Gambetta, A. A. Houck, D. I. Schuster, J. Majer, A. Blais, M. H. Devoret, S. M. Girvin, and R. J. Schoelkopf, “Charge-insensitive qubit design derived from the cooper pair box,” *Physical Review A*, vol. 76, no. 4, p. 042319, 2007.
- [234] J. L. O’Brien, “Optical quantum computing,” *Science*, vol. 318, no. 5856, pp. 1567–1570, 2007.
- [235] H.-S. Zhong, H. Wang, Y.-H. Deng, M.-C. Chen, L.-C. Peng, Y.-H. Luo, J. Qin, D. Wu, X. Ding, Y. Hu, *et al.*, “Quantum computational advantage using photons,” *Science*, vol. 370, no. 6523, pp. 1460–1463, 2020.
- [236] M. Zhang, C. Wang, P. Kharel, D. Zhu, and M. Lončar, “Integrated lithium niobate electro-optic modulators: When performance meets scalability,” *Optica*, vol. 8, no. 5, pp. 652–667, 2021.
- [237] D. Zhu, L. Shao, M. Yu, R. Cheng, B. Desiatov, C. Xin, Y. Hu, J. Holzgrafe, S. Ghosh, A. Shams-Ansari, *et al.*, “Integrated photonics on thin-film lithium niobate,” *Advances in Optics and Photonics*, vol. 13, no. 2, pp. 242–352, 2021.
- [238] J. L. Casson, K. T. Gahagan, D. A. Scrymgeour, R. K. Jain, J. M. Robinson, V. Gopalan, and R. K. Sander, “Electro-optic coefficients of lithium tantalate at near-infrared wavelengths,” *JOSA B*, vol. 21, no. 11, pp. 1948–1952, 2004.
- [239] C. Xiong, W. H. Pernice, and H. X. Tang, “Low-loss, silicon integrated, aluminum nitride photonic circuits and their use for electro-optic signal processing,” *Nano letters*, vol. 12, no. 7, pp. 3562–3568, 2012.
- [240] Y. Xu, A. A. Sayem, L. Fan, C.-L. Zou, S. Wang, R. Cheng, W. Fu, L. Yang, M. Xu, and H. X. Tang, “Bidirectional interconversion of microwave and light with thin-film lithium niobate,” *Nature communications*, vol. 12, no. 1, pp. 1–7, 2021.
- [241] C. Javerzac-Galy, K. Plekhanov, N. Bernier, L. D. Toth, A. K. Feofanov, and T. J. Kippenberg, “On-chip microwave-to-optical quantum coherent converter based on a superconducting resonator coupled to an electro-optic microresonator,” *Physical Review A*, vol. 94, no. 5, p. 053815, 2016.
- [242] J. Holzgrafe, N. Sinclair, D. Zhu, A. Shams-Ansari, M. Colangelo, Y. Hu, M. Zhang, K. K. Berggren, and M. Lončar, “Cavity electro-optics in thin-film lithium niobate for efficient microwave-to-optical transduction,” *Optica*, vol. 7, no. 12, pp. 1714–1720, 2020.
- [243] T. P. McKenna, J. D. Witmer, R. N. Patel, W. Jiang, R. Van Laer, P. Arrangoiz-Arriola, E. A. Wollack, J. F. Herrmann, and A. H. Safavi-Naeini, “Cryogenic microwave-to-optical conversion using a triply resonant lithium-niobate-on-sapphire transducer,” *Optica*, vol. 7, no. 12, pp. 1737–1745, 2020.



- [244] M. Soltani, M. Zhang, C. Ryan, G. J. Ribeill, C. Wang, and M. Loncar, “Efficient quantum microwave-to-optical conversion using electro-optic nanophotonic coupled resonators,” *Physical Review A*, vol. 96, no. 4, p. 043 808, 2017.
- [245] W. Fu, M. Xu, X. Liu, C.-L. Zou, C. Zhong, X. Han, M. Shen, Y. Xu, R. Cheng, S. Wang, *et al.*, “Ground-state pulsed cavity electro-optics for microwave-to-optical conversion,” *arXiv preprint arXiv:2010.11392*, 2020.
- [246] W. Hease, A. Rueda, R. Sahu, M. Wulf, G. Arnold, H. G. Schwefel, and J. M. Fink, “Bidirectional electro-optic wavelength conversion in the quantum ground state,” *PRX Quantum*, vol. 1, no. 2, p. 020 315, 2020.
- [247] A. Rueda, F. Sedlmeir, M. C. Collodo, U. Vogl, B. Stiller, G. Schunk, D. V. Strekalov, C. Marquardt, J. M. Fink, O. Painter, *et al.*, “Efficient microwave to optical photon conversion: An electro-optical realization,” *Optica*, vol. 3, no. 6, pp. 597–604, 2016.
- [248] A. Bienfait, K. J. Satzinger, Y. Zhong, H.-S. Chang, M.-H. Chou, C. R. Conner, É. Dumur, J. Grebel, G. A. Peairs, R. G. Povey, *et al.*, “Phonon-mediated quantum state transfer and remote qubit entanglement,” *Science*, vol. 364, no. 6438, pp. 368–371, 2019.
- [249] L. R. Sletten, B. A. Moores, J. J. Viennot, and K. W. Lehnert, “Resolving phonon fock states in a multimode cavity with a double-slit qubit,” *Physical Review X*, vol. 9, no. 2, p. 021 056, 2019.
- [250] É. Dumur, K. Satzinger, G. Peairs, M.-H. Chou, A. Bienfait, H.-S. Chang, C. Conner, J. Grebel, R. Povey, Y. Zhong, *et al.*, “Quantum communication with itinerant surface acoustic wave phonons,” *npj Quantum Information*, vol. 7, no. 1, pp. 1–5, 2021.
- [251] A. D. O’Connell, M. Hofheinz, M. Ansmann, R. C. Bialczak, M. Lenander, E. Lucero, M. Neeley, D. Sank, H. Wang, M. Weides, *et al.*, “Quantum ground state and single-phonon control of a mechanical resonator,” *Nature*, vol. 464, no. 7289, pp. 697–703, 2010.
- [252] M. Kervinen, I. Rissanen, and M. Sillanpää, “Interfacing planar superconducting qubits with high overtone bulk acoustic phonons,” *Physical Review B*, vol. 97, no. 20, p. 205 443, 2018.
- [253] P. Arrangoiz-Arriola, E. A. Wollack, Z. Wang, M. Pechal, W. Jiang, T. P. McKenna, J. D. Witmer, R. Van Laer, and A. H. Safavi-Naeini, “Resolving the energy levels of a nanomechanical oscillator,” *Nature*, vol. 571, no. 7766, pp. 537–540, 2019.
- [254] P. Arrangoiz-Arriola, E. A. Wollack, M. Pechal, J. D. Witmer, J. T. Hill, and A. H. Safavi-Naeini, “Coupling a superconducting quantum circuit to a phononic crystal defect cavity,” *Physical Review X*, vol. 8, no. 3, p. 031 007, 2018.

- [255] E. A. Wollack, A. Y. Cleland, R. G. Gruenke, Z. Wang, P. Arrangoiz-Arriola, and A. H. Safavi-Naeini, “Quantum state preparation, tomography, and entanglement of mechanical oscillators,” *arXiv preprint arXiv:2110.07561*, 2021.
- [256] M. Aspelmeyer, T. J. Kippenberg, and F. Marquardt, “Cavity optomechanics,” *Reviews of Modern Physics*, vol. 86, no. 4, p. 1391, 2014.
- [257] B. P. Abbott, R. Abbott, T. Abbott, M. Abernathy, F. Acernese, K. Ackley, C. Adams, T. Adams, P. Addesso, R. Adhikari, *et al.*, “Observation of gravitational waves from a binary black hole merger,” *Physical review letters*, vol. 116, no. 6, p. 061 102, 2016.
- [258] R. W. Andrews, R. W. Peterson, T. P. Purdy, K. Cicak, R. W. Simmonds, C. A. Regal, and K. W. Lehnert, “Bidirectional and efficient conversion between microwave and optical light,” *Nature physics*, vol. 10, no. 4, pp. 321–326, 2014.
- [259] G. Arnold, M. Wulf, S. Barzanjeh, E. Redchenko, A. Rueda, W. J. Hease, F. Hassani, and J. M. Fink, “Converting microwave and telecom photons with a silicon photonic nanomechanical interface,” *Nature communications*, vol. 11, no. 1, pp. 1–7, 2020.
- [260] M. Eichenfield, J. Chan, R. M. Camacho, K. J. Vahala, and O. Painter, “Optomechanical crystals,” *Nature*, vol. 462, no. 7269, pp. 78–82, 2009.
- [261] J. T. Hill, A. H. Safavi-Naeini, J. Chan, and O. Painter, “Coherent optical wavelength conversion via cavity optomechanics,” *Nature communications*, vol. 3, no. 1, pp. 1–7, 2012.
- [262] M. Mirhosseini, A. Sipahigil, M. Kalaei, and O. Painter, “Superconducting qubit to optical photon transduction,” *Nature*, vol. 588, no. 7839, pp. 599–603, 2020.
- [263] G. Peairs, M.-H. Chou, A. Bienfait, H.-S. Chang, C. Conner, É. Dumur, J. Grebel, R. Povey, E. Şahin, K. Satzinger, *et al.*, “Continuous and time-domain coherent signal conversion between optical and microwave frequencies,” *Physical Review Applied*, vol. 14, no. 6, p. 061 001, 2020.
- [264] W. Jiang, C. J. Sarabalis, Y. D. Dahmani, R. N. Patel, F. M. Mayor, T. P. McKenna, R. Van Laer, and A. H. Safavi-Naeini, “Efficient bidirectional piezo-optomechanical transduction between microwave and optical frequency,” *Nature communications*, vol. 11, no. 1, pp. 1–7, 2020.
- [265] W. Jiang, R. N. Patel, F. M. Mayor, T. P. McKenna, P. Arrangoiz-Arriola, C. J. Sarabalis, J. D. Witmer, R. Van Laer, and A. H. Safavi-Naeini, “Lithium niobate piezo-optomechanical crystals,” *Optica*, vol. 6, no. 7, pp. 845–853, 2019.

- [266] K. E. Grutter, M. Davanco, and K. Srinivasan, “Si<sub>3</sub>N<sub>4</sub> nanobeam optomechanical crystals,” *IEEE Journal of Selected Topics in Quantum Electronics*, vol. 21, no. 4, pp. 61–71, 2014.
- [267] J. Bochmann, A. Vainsencher, D. D. Awschalom, and A. N. Cleland, “Nanomechanical coupling between microwave and optical photons,” *Nature Physics*, vol. 9, no. 11, pp. 712–716, 2013.
- [268] L. Fan, X. Sun, C. Xiong, C. Schuck, and H. X. Tang, “Aluminum nitride piezo-acousto-photonic crystal nanocavity with high quality factors,” *Applied Physics Letters*, vol. 102, no. 15, p. 153 507, 2013.
- [269] A. Vainsencher, K. Satzinger, G. Peairs, and A. Cleland, “Bi-directional conversion between microwave and optical frequencies in a piezoelectric optomechanical device,” *Applied Physics Letters*, vol. 109, no. 3, p. 033 107, 2016.
- [270] R. Stockill, M. Forsch, G. Beaudoin, K. Pantzas, I. Sagnes, R. Braive, and S. Gröblacher, “Gallium phosphide as a piezoelectric platform for quantum optomechanics,” *Physical review letters*, vol. 123, no. 16, p. 163 602, 2019.
- [271] R. Stockill, M. Forsch, F. Hijazi, G. Beaudoin, K. Pantzas, I. Sagnes, R. Braive, and S. Gröblacher, “Ultra-low-noise microwave to optics conversion in gallium phosphide,” *arXiv preprint arXiv:2107.04433*, 2021.
- [272] S. Hönl, Y. Popoff, D. Caimi, A. Beccari, T. J. Kippenberg, and P. Seidler, “Microwave-to-optical conversion with a gallium phosphide photonic crystal cavity,” *arXiv preprint arXiv:2105.13242*, 2021.
- [273] M. Wu, E. Zeuthen, K. C. Balram, and K. Srinivasan, “Microwave-to-optical transduction using a mechanical supermode for coupling piezoelectric and optomechanical resonators,” *Physical Review Applied*, vol. 13, no. 1, p. 014 027, 2020.
- [274] M. Forsch, R. Stockill, A. Wallucks, I. Marinković, C. Gärtner, R. A. Norte, F. van Otten, A. Fiore, K. Srinivasan, and S. Gröblacher, “Microwave-to-optics conversion using a mechanical oscillator in its quantum ground state,” *Nature Physics*, vol. 16, no. 1, pp. 69–74, 2020.
- [275] H. Ramp, T. Clark, B. Hauer, C. Doolin, K. C. Balram, K. Srinivasan, and J. Davis, “Wavelength transduction from a 3d microwave cavity to telecom using piezoelectric optomechanical crystals,” *Applied physics letters*, vol. 116, no. 17, p. 174 005, 2020.
- [276] K. C. Balram, M. I. Davanço, J. D. Song, and K. Srinivasan, “Coherent coupling between radiofrequency, optical and acoustic waves in piezo-optomechanical circuits,” *Nature photonics*, vol. 10, no. 5, pp. 346–352, 2016.

- [277] K. C. Balram and K. Srinivasan, “Piezoelectric optomechanical approaches for efficient quantum microwave-to-optical signal transduction: The need for co-design,” *Advanced Quantum Technologies*, p. 2100095, 2021.
- [278] I. Marinković, M. Drimmer, B. Hensen, and S. Gröblacher, “Hybrid integration of silicon photonic devices on lithium niobate for optomechanical wavelength conversion,” *Nano letters*, vol. 21, no. 1, pp. 529–535, 2021.
- [279] P. Kharel, G. I. Harris, E. A. Kittlaus, W. H. Renninger, N. T. Otterstrom, J. G. Harris, and P. T. Rakich, “High-frequency cavity optomechanics using bulk acoustic phonons,” *Science advances*, vol. 5, no. 4, eaav0582, 2019.
- [280] W. Renninger, P. Kharel, R. Behunin, and P. Rakich, “Bulk crystalline optomechanics,” *Nature Physics*, vol. 14, no. 6, pp. 601–607, 2018.
- [281] S. Valle and K. C. Balram, “Cryogenic operation of mems-based suspended high overtone bulk acoustic wave resonators for microwave to optical signal transduction,” *arXiv preprint arXiv:2109.11838*, 2021.
- [282] E. Zeuthen, A. Schliesser, J. M. Taylor, and A. S. Sørensen, “Electrooptomechanical equivalent circuits for quantum transduction,” *Physical Review Applied*, vol. 10, no. 4, p. 044036, 2018.
- [283] A. Kochhar, G. Vidal-Alvarez, L. Colombo, and G. Piazza, “Top electrode shaping for harnessing high coupling in thickness shear mode resonators in y-cut lithium niobate thin films,” in *2018 IEEE Micro Electro Mechanical Systems (MEMS)*, IEEE, 2018, pp. 71–74.
- [284] C. Zhong, Z. Wang, C. Zou, M. Zhang, X. Han, W. Fu, M. Xu, S. Shankar, M. H. Devoret, H. X. Tang, *et al.*, “Proposal for heralded generation and detection of entangled microwave–optical-photon pairs,” *Physical review letters*, vol. 124, no. 1, p. 010511, 2020.
- [285] C. Zhong, X. Han, H. X. Tang, and L. Jiang, “Entanglement of microwave-optical modes in a strongly coupled electro-optomechanical system,” *Physical Review A*, vol. 101, no. 3, p. 032345, 2020.
- [286] S. Krastanov, H. Raniwala, J. Holzgrafe, K. Jacobs, M. Lončar, M. J. Reagor, and D. R. Englund, “Optically heralded entanglement of superconducting systems in quantum networks,” *Physical Review Letters*, vol. 127, no. 4, p. 040503, 2021.
- [287] J. Wu, C. Cui, L. Fan, and Q. Zhuang, “Deterministic microwave-optical transduction based on quantum teleportation,” *Physical Review Applied*, vol. 16, no. 6, p. 064044, 2021.

- [288] A. Rueda, W. Hease, S. Barzanjeh, and J. M. Fink, “Electro-optic entanglement source for microwave to telecom quantum state transfer,” *npj Quantum Information*, vol. 5, no. 1, pp. 1–11, 2019.
- [289] N. Fiaschi, B. Hensen, A. Wallucks, R. Benevides, J. Li, T. P. M. Alegre, and S. Gröblacher, “Optomechanical quantum teleportation,” *Nature Photonics*, vol. 15, no. 11, pp. 817–821, 2021.
- [290] C. T. Hann, C.-L. Zou, Y. Zhang, Y. Chu, R. J. Schoelkopf, S. M. Girvin, and L. Jiang, “Hardware-efficient quantum random access memory with hybrid quantum acoustic systems,” *Physical Review Letters*, vol. 123, no. 25, p. 250 501, 2019.
- [291] C. Müller, J. H. Cole, and J. Lisenfeld, “Towards understanding two-level-systems in amorphous solids: Insights from quantum circuits,” *Reports on Progress in Physics*, vol. 82, no. 12, p. 124 501, 2019.
- [292] A. S. Raja, J. Liu, N. Volet, R. N. Wang, J. He, E. Lucas, R. Bouchand, P. Morton, J. Bowers, and T. J. Kippenberg, “Packaged photonic chip-based soliton microcomb using an ultralow-noise laser,” *arXiv preprint arXiv:1906.03194*, 2019.
- [293] W. Bogaerts, D. Pérez, J. Capmany, D. A. Miller, J. Poon, D. Englund, F. Morichetti, and A. Melloni, “Programmable photonic circuits,” *Nature*, vol. 586, no. 7828, pp. 207–216, 2020.
- [294] N. C. Harris, J. Carolan, D. Bunandar, M. Prabhu, M. Hochberg, T. Baehr-Jones, M. L. Fanto, A. M. Smith, C. C. Tison, P. M. Alsing, *et al.*, “Linear programmable nanophotonic processors,” *Optica*, vol. 5, no. 12, pp. 1623–1631, 2018.
- [295] N. C. Harris, D. Bunandar, M. Pant, G. R. Steinbrecher, J. Mower, M. Prabhu, T. Baehr-Jones, M. Hochberg, and D. Englund, “Large-scale quantum photonic circuits in silicon,” *Nanophotonics*, vol. 5, no. 3, pp. 456–468, 2016.
- [296] Y. Shen, N. C. Harris, S. Skirlo, M. Prabhu, T. Baehr-Jones, M. Hochberg, X. Sun, S. Zhao, H. Larochelle, D. Englund, *et al.*, “Deep learning with coherent nanophotonic circuits,” *Nature Photonics*, vol. 11, no. 7, pp. 441–446, 2017.
- [297] L. Yuan, Q. Lin, M. Xiao, and S. Fan, “Synthetic dimension in photonics,” *Optica*, vol. 5, no. 11, pp. 1396–1405, 2018.
- [298] Y. Hu, C. Reimer, A. Shams-Ansari, M. Zhang, and M. Loncar, “Realization of high-dimensional frequency crystals in electro-optic microcombs,” *Optica*, vol. 7, no. 9, pp. 1189–1194, 2020.

- [299] L. Yuan and S. Fan, “Bloch oscillation and unidirectional translation of frequency in a dynamically modulated ring resonator,” *Optica*, vol. 3, no. 9, pp. 1014–1018, 2016.
- [300] L. Yuan, Y. Shi, and S. Fan, “Photonic gauge potential in a system with a synthetic frequency dimension,” *Optics letters*, vol. 41, no. 4, pp. 741–744, 2016.
- [301] T. Ozawa, H. M. Price, N. Goldman, O. Zilberberg, and I. Carusotto, “Synthetic dimensions in integrated photonics: From optical isolation to four-dimensional quantum hall physics,” *Physical Review A*, vol. 93, no. 4, p. 043 827, 2016.
- [302] J. Wang, J. F. Herrmann, J. D. Witmer, A. H. Safavi-Naeini, and S. Fan, “Photonic modal circulator using temporal refractive-index modulation with spatial inversion symmetry,” *Physical Review Letters*, vol. 126, no. 19, p. 193 901, 2021.
- [303] J. F. Herrmann, V. Ansari, J. Wang, J. D. Witmer, S. Fan, and A. H. Safavi-Naeini, “Mirror symmetric on-chip frequency circulation of light,” *arXiv preprint arXiv:2109.13864*, 2021.
- [304] S. Kim, D. B. Sohn, C. W. Peterson, and G. Bahl, “On-chip optical non-reciprocity through a synthetic hall effect for photons,” *APL Photonics*, vol. 6, no. 1, p. 011 301, 2021.
- [305] S. Buddhiraju, A. Dutt, M. Minkov, I. A. Williamson, and S. Fan, “Arbitrary linear transformations for photons in the frequency synthetic dimension,” *Nature communications*, vol. 12, no. 1, pp. 1–9, 2021.
- [306] A. K. Tusnin, A. M. Tikan, and T. J. Kippenberg, “Nonlinear states and dynamics in a synthetic frequency dimension,” *Physical Review A*, vol. 102, no. 2, p. 023 518, 2020.
- [307] A. Balčytis, T. Ozawa, Y. Ota, S. Iwamoto, J. Maeda, and T. Baba, “Synthetic dimension band structures on a si cmos photonic platform,” *arXiv preprint arXiv:2105.13742*, 2021.
- [308] J. A. V. Tirado, “Bulk acoustic wave resonators and their application to microwave devices,” Ph.D. dissertation, Universitat Autònoma de Barcelona, 2010.
- [309] Q. Chen and Q.-m. Wang, “Characterization of mechanical and piezoelectric properties of the aln thin film in a composite resonator stuctrue,” in *2006 IEEE International Frequency Control Symposium and Exposition*, IEEE, 2006, pp. 104–110.
- [310] J. Li, M. Liu, and C. Wang, “Resonance spectrum characteristics of effective electromechanical coupling coefficient of high-overtone bulk acoustic resonator,” *Micromachines*, vol. 7, no. 9, p. 159, 2016.

## A. ANALYTIC ANALYSIS OF ELECTRO-OPTOMECHANICAL RESPONSE

### A.1 Electromechanical model of HBAR mode

To better explain the electromechanical S11 response and mechanical dispersion shown in the main text, a one-dimensional (1D) analytic electromechanical model is established by combining the well-known Mason model [127], [308] and the transfer matrix method [309], [310]. As shown in Fig. A.1(a), the acoustic wave is assumed to propagate bidirectionally along the  $z$  axis due to acoustic reflection at interfaces, such that the mechanical displacement  $u(z, t)$  can be expressed as [308]:

$$u(z, t) = A^+ e^{-j(kz - \omega t)} + A^- e^{j(kz + \omega t)} \quad (\text{A.1})$$

where,  $\omega$  and  $k = \omega/v_{ac}$  ( $v_{ac}$  is acoustic velocity) are the frequency and acoustic wave number respectively, and  $A^+$  and  $A^-$  are amplitudes for the bidirectional propagating waves. The wave is then related to the velocities  $v$  and forces  $F$  (or stress  $\sigma$ ) at the two surfaces at  $z_1$  and  $z_2$ , working as boundary conditions [308]:

$$v_1 = \frac{du(z_1)}{dt} = j\omega(A^+ e^{-jkz_1} + A^- e^{jkz_1}) \quad (\text{A.2})$$

$$v_2 = \frac{du(z_2)}{dt} = j\omega(A^+ e^{-jkz_2} + A^- e^{jkz_2}) \quad (\text{A.3})$$

$$F_1 = Sc^E \frac{du(z_1)}{dz} = -jScck(A^+ e^{-jkz_1} - A^- e^{jkz_1}) \quad (\text{A.4})$$

$$F_2 = Sc^E \frac{du(z_2)}{dz} = -jScck(A^+ e^{-jkz_2} - A^- e^{jkz_2}) \quad (\text{A.5})$$

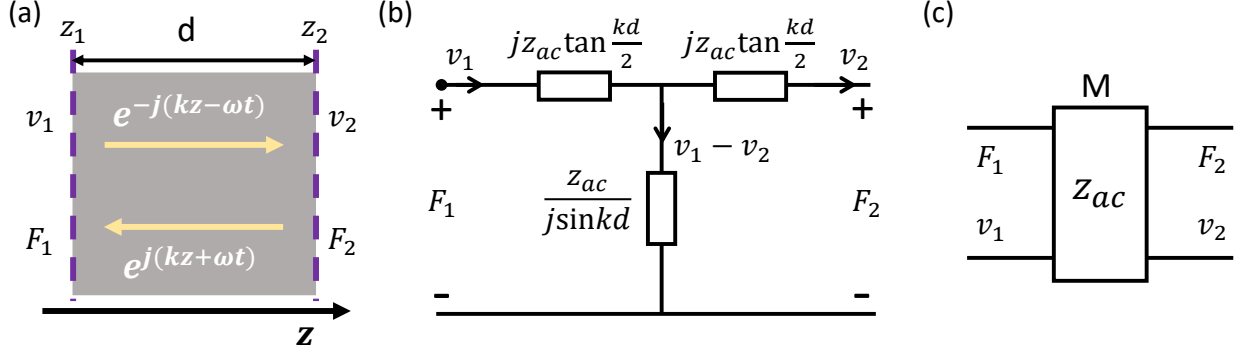


**Figure A.1.** Model of acoustic wave propagation in a non-piezoelectric material. (a) Acoustic wave propagates in forward and backward directions in a layer of non-piezoelectric material. The layer thickness is  $d$  with two boundaries located at  $z_1$  and  $z_2$ . The wave distribution is solely determined by the boundary conditions of force  $F$  and velocity  $v$ . (b) Equivalent circuit model describing acoustic wave transmission. (c) The two boundaries can be correlated by a transfer matrix  $M$  which is a function of the acoustic impedance and the propagation length. Reprinted from Ref. [12].

$S$  is the surface area, and  $c^E$  is the stiffness coefficient of the material. The prefactor related with time is omitted for simplicity. After some brief algebra, the forces can be expressed as the combination of velocities as:

$$F_1 = \frac{Z_{ac}}{j \sin(kd)}(v_1 - v_2) + jZ_{ac} \tan\left(\frac{kd}{2}\right)v_1 \quad (\text{A.6})$$

$$F_2 = \frac{Z_{ac}}{j \sin(kd)}(v_1 - v_2) - jZ_{ac} \tan\left(\frac{kd}{2}\right)v_2 \quad (\text{A.7})$$

where  $Z_{ac} (=S\rho v_{ac})$ , where  $\rho$  is the material density) is the acoustic impedance of the material, and  $d$  is the thickness. Interestingly, if we treat force and velocity as voltage and current, an equivalent circuit model can be built which satisfies Eq. A.6-A.7 according to the Kirchhoff's law, as shown in Fig. A.1(b). The circuit consists of three resistors with impedance as labeled in Fig. A.1(b). Since the force and velocity must be continuous at the boundary between two different layers, the circuit model makes it easy to cascade different layers by connecting their corresponding circuits.



From Eq. A.6-A.7, two adjacent boundaries can be related using a transfer matrix  $M$  as [309]:

$$\begin{bmatrix} F_1 \\ v_1 \end{bmatrix} = \begin{bmatrix} \cos(kd) & jZ_{ac}\sin(kd) \\ j\sin(kd)/Z_{ac} & \cos(kd) \end{bmatrix} \begin{bmatrix} F_2 \\ v_2 \end{bmatrix} = M \begin{bmatrix} F_2 \\ v_2 \end{bmatrix} \quad (\text{A.8})$$

In this way, each layer can be represented by its characteristic transfer matrix  $M$  [Fig. A.1(c)], and the relation between any two boundaries can be connected by multiplying the transfer matrix of each layer in between. The boundary condition at each interface can thus be determined from the very end boundaries of the entire stack structure which, for a general mechanical structure, satisfy the free boundary condition where the force is zero ( $F = 0$ ), or the fixed boundary condition where the velocity (or equivalently the displacement) is zero ( $v = 0$ ). After knowing the boundary conditions, the acoustic wave distribution in each layer can be determined from Eq. A.2-A.5 by solving for  $A^+$  and  $A^-$ . This is known as transfer matrix method for solving one-dimensional propagation of acoustic waves in multiple layer structures, which is suitable for our vertical stack structure of HBAR mode.

After the derivation of acoustic wave propagation, we are now ready for the model of acoustic wave excitation through a piezoelectric actuator. As we apply voltage to the piezoelectric material, the electric field will generate stress inside the film, which in turn builds up extra charges at the surfaces and change the electric field accordingly. The interplay between stress and electric field can be related as [308]:

$$\sigma = c^E \varepsilon + eE \quad (\text{A.9})$$

$$D = e\varepsilon + \epsilon E \quad (\text{A.10})$$

where  $c^E$  is the stiffness coefficient under constant  $E$ ,  $e$  is piezoelectric coefficient,  $\epsilon$  is dielectric constant,  $\varepsilon$  is strain,  $E$  is electric field, and  $D$  is electric displacement. In general, the coefficients are matrices which correlate the mechanical and electric field in different directions. In our case, we consider only the terms related to the  $z$  direction.

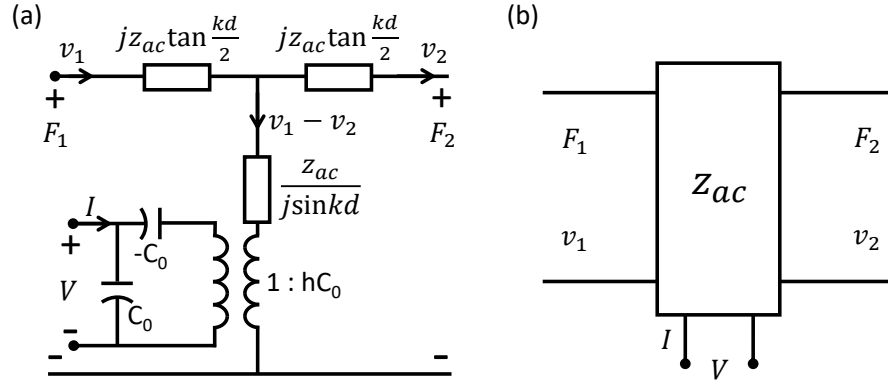


**Figure A.2.** Model of acoustic wave propagation in a piezoelectric material. (a) Equivalent circuit Mason model that describes the excitation and propagation of acoustic waves in the piezoelectric layer. The three resistors represent the propagation of acoustic waves, while the transformer represents energy conversion between electrical and mechanical domain. (c) Three ports representation of the piezoelectric actuator. Reprinted from Ref. [12].

By performing a similar procedure as before, the velocities and forces generated at the boundaries can be calculated from the applied external voltage and current through [308]:

$$F_1 = \frac{Z_{ac}}{j\sin(kd)}(v_1 - v_2) + jZ_{ac}\tan\left(\frac{kd}{2}\right)v_1 + \frac{h}{j\omega}I \quad (\text{A.11})$$

$$F_2 = \frac{Z_{ac}}{j\sin(kd)}(v_1 - v_2) - jZ_{ac}\tan\left(\frac{kd}{2}\right)v_2 + \frac{h}{j\omega}I \quad (\text{A.12})$$

$$V = \frac{1}{j\omega C_0}[I + hC_0(v_1 - v_2)] \quad (\text{A.13})$$

where  $C_0$  ( $= \epsilon S/d$ ) is the intrinsic capacitance of the piezoelectric actuator, and  $h = e/\epsilon$  is a constant related with the material properties. Based on these equations, an equivalent circuit model can be established as shown in Fig. A.2(a), which is the so-called Mason model [308]. Compared with the previous circuit in Fig. A.1(b) which does not consider the piezoelectric effect, a transformer is added to the middle branch with a ratio of  $1 : hC_0$ , which then connects to the external power source through series and parallel capacitances  $C_0$ . The series capacitance has a negative sign which indicates that its current will combine with the external current  $I$  and go through the parallel capacitance. This is to be consistent with Eq. A.13. The other resistors describe the acoustic wave propagation in the piezoelectric layer

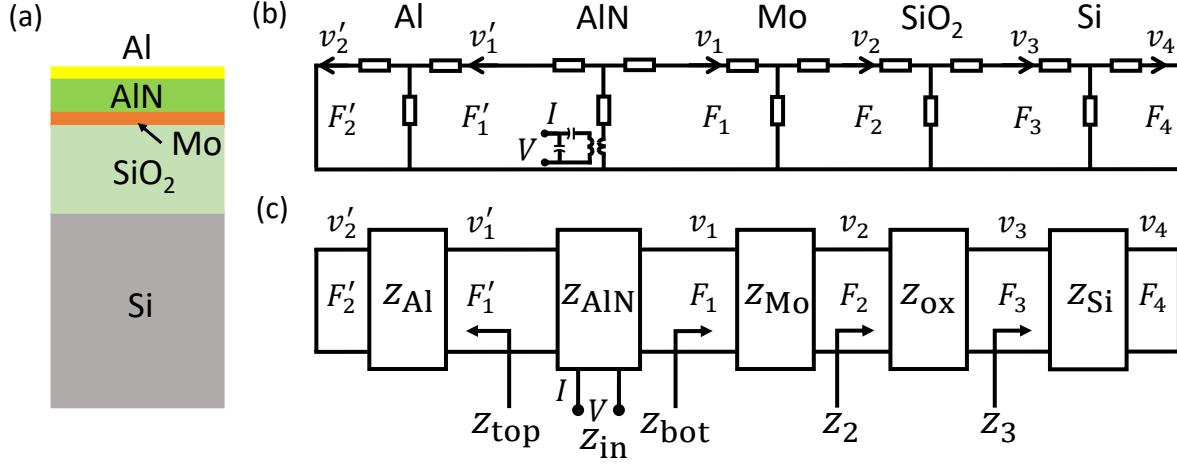


**Figure A.3.** Electromechanical model of the actual device in this work. (a) Vertical stacking structure of the whole device. (b) Equivalent circuit model by connecting adjacent layers. The end ports are shorted as required by the free boundary condition. (c) Transfer matrix chain that connects each interface. The input impedance at each port can be correlated and calculated by the multiplication of matrices in between. Reprinted from Ref. [12].

as before. The piezoelectric layer can be treated as a three port component as shown in Fig. A.2(b), where the mechanical ports are dependent on  $I$ - $V$  port. In transfer matrix method, this active component introduces additional boundary conditions through the electric port.

As we have the circuit model and transfer matrix of each layer, the actual device as described in the main text and shown in Fig. A.3(a) can be modeled by simply connecting each adjacent layer. Fig. A.3(b) shows the equivalent circuit of the whole device. Free boundary conditions at the top and bottom surfaces are employed such that the forces  $F'_2$  and  $F_4$  are zero, which correspond to an electric short in the circuit. The impedance looking into one interface can be defined as  $Z = F/v$ . By utilizing Eq. A.8, and assuming  $F'_2 = 0$  and  $F_4 = 0$ , the impedance at port 1' and 3 from the top Al electrode and bottom Si substrate can be calculated easily as:

$$Z_{\text{top}} = jZ_{\text{Al}}\tan(k_{\text{Al}}d_{\text{Al}}) \quad (\text{A.14})$$

$$Z_3 = jZ_{\text{Si}}\tan(k_{\text{Si}}d_{\text{Si}}) \quad (\text{A.15})$$

**Table A.1.** Material properties of each layer employed in the analytic model

Material	Density $\rho$ (kg/m <sup>3</sup> )	Velocity $v$ (m/s)	Thickness $d$ ( $\mu\text{m}$ )
Al	2700	6300	0.1
AlN	3300	11050	0.92
Mo	10200	6636	0.1
SiO <sub>2</sub>	2200	5640	5.44
Si	2329	8430	231.5

where  $Z_{\text{Al}}$  and  $Z_{\text{Si}}$  are the acoustic impedance of Al and Si respectively. Similarly, by multiplying matrices of cascaded layers, the impedance at ports 2 and 1 can be calculated:

$$Z_2 = j \frac{Z_{\text{Si}} \tan(k_{\text{Si}} d_{\text{Si}}) + Z_{\text{ox}} \tan(k_{\text{ox}} d_{\text{ox}})}{1 - (Z_{\text{Si}}/Z_{\text{ox}}) \tan(k_{\text{Si}} d_{\text{Si}}) \tan(k_{\text{ox}} d_{\text{ox}})} \quad (\text{A.16})$$

$$Z_{\text{bot}} = \frac{Z_2 + j Z_{\text{Mo}} \tan(k_{\text{Mo}} d_{\text{Mo}})}{1 + j (Z_2/Z_{\text{Mo}}) \tan(k_{\text{Mo}} d_{\text{Mo}})} \quad (\text{A.17})$$

where  $Z_{\text{ox}}$  and  $Z_{\text{Mo}}$  are the acoustic impedance of SiO<sub>2</sub> and Mo respectively. From Eq. A.11-A.13, the electrical impedance  $Z_{\text{in}}$  ( $= V/I$ ) can be obtained by [127], [308]:

$$Z_{\text{in}} = \frac{1}{j\omega C_0} \left\{ 1 - \frac{k_t^2}{k_{\text{AlN}} d_{\text{AlN}}} \frac{(z_{\text{top}} + z_{\text{bot}}) \sin(k_{\text{AlN}} d_{\text{AlN}}) + j2[1 - \cos(k_{\text{AlN}} d_{\text{AlN}})]}{(z_{\text{top}} + z_{\text{bot}}) \cos(k_{\text{AlN}} d_{\text{AlN}}) + j(1 + z_{\text{top}} z_{\text{bot}}) \sin(k_{\text{AlN}} d_{\text{AlN}})} \right\} \quad (\text{A.18})$$

where,  $k_t^2$  is the intrinsic electromechanical coupling coefficient of AlN which is 6.5%,  $z_{\text{top}}$  ( $= Z_{\text{top}}/Z_{\text{AlN}}$ ) and  $z_{\text{bot}}$  ( $= Z_{\text{bot}}/Z_{\text{AlN}}$ ) are the impedance from the top and bottom side of AlN which are normalized by the AlN acoustic impedance  $Z_{\text{AlN}}$ .

## A.2 Electromechanical $S_{11}$ reflection parameter

By applying actual material properties as summarized in Table A.1, the electrical input impedance can be calculated, from which the  $S_{11}$  response can be calculated as:

$$S_{11} = \frac{Z_0 - Z_{\text{in}}}{Z_0 + Z_{\text{in}}} \quad (\text{A.19})$$

where  $Z_0$  (50  $\Omega$ ) is the standard normalized impedance of the network analyzer. The results are shown in Fig. A.4 which demonstrates similarity between measurements and calculations

from the electromechanical model. The difference in magnitude is mainly introduced by the calibration and parasitic capacitance from the probe landing during the electrical experiments. The variation of envelope caused by the coupling between Si, SiO<sub>2</sub> and AlN cavities is well captured by the model. As mentioned in the main text, the node of the envelope corresponds to a SiO<sub>2</sub> resonance. This is because, at the SiO<sub>2</sub> resonance, more acoustic energy is confined in SiO<sub>2</sub> which is softer and has smaller acoustic impedance as compared to Si.

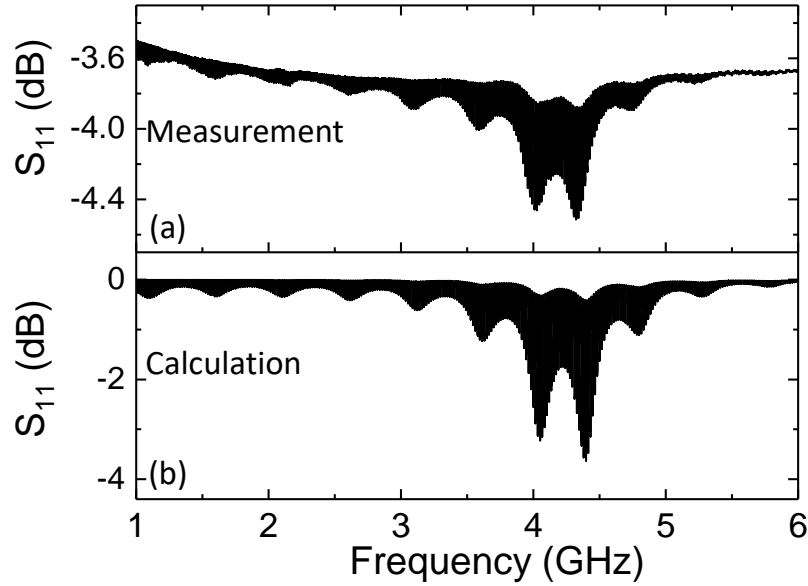


**Figure A.4.** Measured (a) and calculated (b)  $S_{11}$  reflection parameter, showing much similarity in terms of varied envelope and its period. Reprinted from Ref. [12].

### A.3 Mechanical dispersion analysis

Provided the precision of the model demonstrated in last section, we can rely on the model and analyze the mechanical dispersion by calculating resonant frequencies. By letting the denominator in Eq. A.18 equal zero, we retrieve the parallel resonant frequencies corresponding to the maximum resistance [127]:

$$(z_{\text{top}} + z_{\text{bot}})\cos(k_{\text{AlN}}d_{\text{AlN}}) + j(1 + z_{\text{top}}z_{\text{bot}})\sin(k_{\text{AlN}}d_{\text{AlN}}) = 0 \quad (\text{A.20})$$

The dispersion equation is transcendental and can be solved numerically. The FSR variation and higher order dispersion can thus be calculated from resonant frequencies as shown in the main text. To get a feeling of why and how the FSR varies, an analytic expression of FSR can be derived under simplified assumptions. Specifically, we can assume the metal thickness is much smaller than the acoustic wavelength, such that their impedance is nearly zero. Under this assumption, the dispersion equation Eq. A.20 can be simplified to:

$$Z_{\text{Si}} \tan(k_{\text{Si}} d_{\text{Si}}) + \frac{Z_{\text{ox}} \tan(k_{\text{ox}} d_{\text{ox}}) + Z_{\text{AlN}} \tan(k_{\text{AlN}} d_{\text{AlN}})}{1 - \frac{Z_{\text{AlN}}}{Z_{\text{ox}}} \tan(k_{\text{AlN}} d_{\text{AlN}}) \tan(k_{\text{ox}} d_{\text{ox}})} = 0 \quad (\text{A.21})$$

The equation is arranged in the way that SiO<sub>2</sub> and AlN are combined and work together as an external cavity coupled to the Si cavity. The FSR can be divided into four regions in terms of resonance and anti-resonance of SiO<sub>2</sub> and AlN cavities (see Table A.2 and Fig. A.5).

Firstly, let's consider frequencies around AlN resonance, where  $k_{\text{AlN}} d_{\text{AlN}} = p\pi + \delta_{\text{AlN}}$ , with  $p$  an integer number and  $\delta_{\text{AlN}}$  denoting a small deviation. When the SiO<sub>2</sub> is at resonance such that the second term in Eq. A.21 is near zero,  $k_{\text{ox}} d_{\text{ox}} = n\pi + \delta_{\text{ox}}$ . In this case, Si cavity must satisfy  $k_{\text{Si}} d_{\text{Si}} = m\pi + \delta_{\text{Si}}$ , such that Eq. A.21 becomes [127]:

$$Z_{\text{Si}} \delta_{\text{Si}} + Z_{\text{ox}} \delta_{\text{ox}} + Z_{\text{AlN}} \delta_{\text{AlN}} = 0 \quad (\text{A.22})$$

From Eq. A.22 we derive the relation between the three cavities as:

$$k_{\text{Si}} d_{\text{Si}} = m\pi - \frac{Z_{\text{ox}}}{Z_{\text{Si}}} (k_{\text{ox}} d_{\text{ox}} - n\pi) - \frac{Z_{\text{AlN}}}{Z_{\text{Si}}} (k_{\text{AlN}} d_{\text{AlN}} - p\pi) \quad (\text{A.23})$$

where  $k_{\text{Si}} = 2\pi f_m / v_{\text{Si}}$ ,  $k_{\text{ox}} = 2\pi f_m / v_{\text{ox}}$ ,  $k_{\text{AlN}} = 2\pi f_m / v_{\text{AlN}}$ . This is also true for the  $m - 1$  mode. Note that the mode order  $p$  and  $n$  of AlN and SiO<sub>2</sub> will not change for the  $m$  and  $m - 1$  modes. By taking the frequency difference between the  $m$  and  $m - 1$  modes, we can get the local FSR after some algebra as:

$$\Delta f = \Delta f_0 \frac{d_{\text{Si}}}{d_{\text{Si}} + \frac{\rho_{\text{ox}}}{\rho_{\text{Si}}} d_{\text{ox}} + \frac{\rho_{\text{AlN}}}{\rho_{\text{Si}}} d_{\text{AlN}}} \quad (\text{A.24})$$

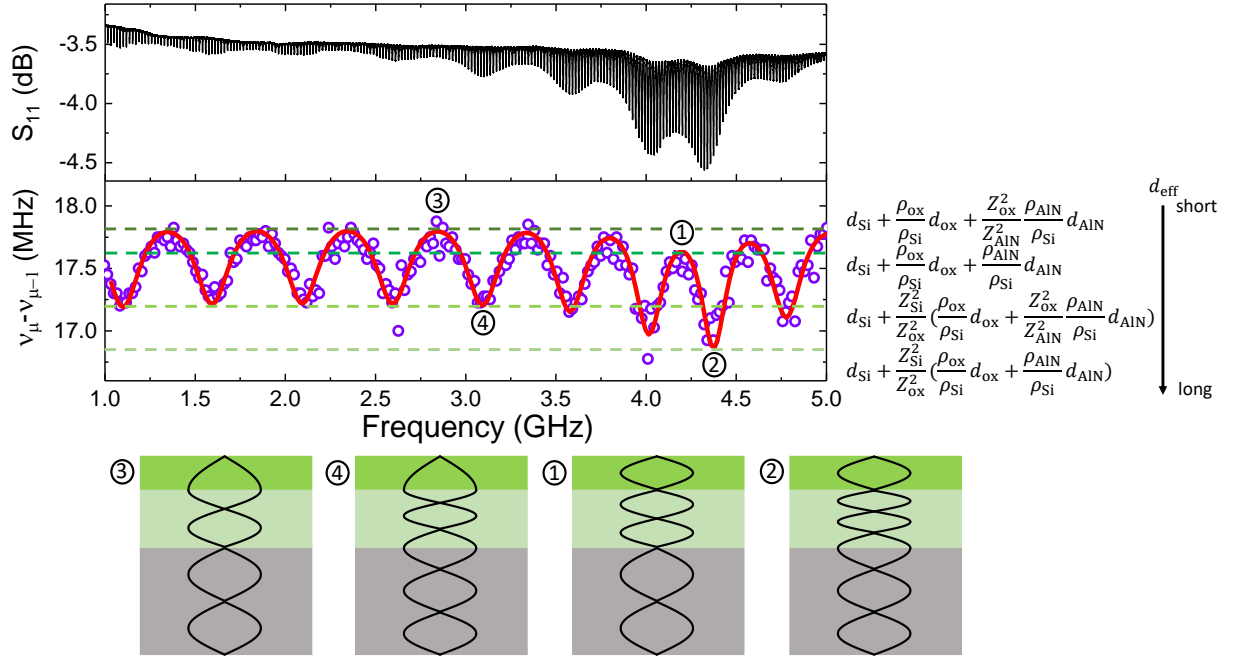


**Figure A.5.** Four different regions are labeled by number in the order from top to bottom corresponding to Table A.2. The green dashed lines denote the FSR of each region and the corresponding effective length  $d_{\text{eff}}$  is labeled on the right. The bottom insets show the schematics of the acoustic stress wave distribution for each region, illustrating the locations of interfaces relative to the stress wave. Reprinted from Ref. [12].

where  $\Delta f_0 = v_{\text{Si}}/(2d_{\text{Si}})$  is the original FSR of the Si cavity. This new FSR is smaller than the original FSR since the  $\text{SiO}_2$  and AlN extends the effective cavity length. It is interesting to note that this extension is not simply the physical length of each layer but the effective length weighted by its density relative to Si.

Following a similar procedure, the FSR at  $\text{SiO}_2$ 's anti-resonance and around AlN's resonance can be obtained. In this time, the three cavities satisfy:

$$k_{\text{AlN}}d_{\text{AlN}} = p\pi + \delta_{\text{AlN}} \quad (\text{A.25})$$

$$k_{\text{ox}}d_{\text{ox}} = n\pi + \pi/2 + \delta_{\text{ox}} \quad (\text{A.26})$$

$$k_{\text{Si}}d_{\text{Si}} = m\pi + \pi/2 + \delta_{\text{Si}} \quad (\text{A.27})$$

**Table A.2.** Effective cavity length at different resonant conditions. The effective boundary condition at each interface is compared.

$k_{\text{AlN}}d_{\text{AlN}}$	$k_{\text{ox}}d_{\text{ox}}$	$k_{\text{Si}}d_{\text{Si}}$	AlN-SiO <sub>2</sub>	SiO <sub>2</sub> -Si	Effective length
$p\pi$	$n\pi$	$m\pi$	Free	Free	$d_{\text{Si}} + \frac{\rho_{\text{ox}}}{\rho_{\text{Si}}}d_{\text{ox}} + \frac{\rho_{\text{AlN}}}{\rho_{\text{Si}}}d_{\text{AlN}}$
$p\pi$	$n\pi + \frac{\pi}{2}$	$m\pi + \frac{\pi}{2}$	Free	Fixed	$d_{\text{Si}} + \frac{Z_{\text{Si}}^2}{Z_{\text{ox}}^2} \left( \frac{\rho_{\text{ox}}}{\rho_{\text{Si}}}d_{\text{ox}} + \frac{\rho_{\text{AlN}}}{\rho_{\text{Si}}}d_{\text{AlN}} \right)$
$p\pi + \frac{\pi}{2}$	$n\pi + \frac{\pi}{2}$	$m\pi$	Fixed	Free	$d_{\text{Si}} + \frac{\rho_{\text{ox}}}{\rho_{\text{Si}}}d_{\text{ox}} + \frac{Z_{\text{ox}}^2}{Z_{\text{AlN}}^2} \frac{\rho_{\text{AlN}}}{\rho_{\text{Si}}}d_{\text{AlN}}$
$p\pi + \frac{\pi}{2}$	$n\pi$	$m\pi + \frac{\pi}{2}$	Fixed	Fixed	$d_{\text{Si}} + \frac{Z_{\text{Si}}^2}{Z_{\text{ox}}^2} \left( \frac{\rho_{\text{ox}}}{\rho_{\text{Si}}}d_{\text{ox}} + \frac{Z_{\text{ox}}^2}{Z_{\text{AlN}}^2} \frac{\rho_{\text{AlN}}}{\rho_{\text{Si}}}d_{\text{AlN}} \right)$

By inserting them into Eq. A.21, it becomes [127]:

$$-\frac{Z_{\text{Si}}}{\delta_{\text{Si}}} + \frac{-\frac{Z_{\text{ox}}}{\delta_{\text{ox}}} + Z_{\text{AlN}}\delta_{\text{AlN}}}{1 + \frac{Z_{\text{AlN}}\delta_{\text{AlN}}}{Z_{\text{ox}}\delta_{\text{ox}}}} = 0 \quad (\text{A.28})$$

Since  $Z_{\text{AlN}}\delta_{\text{AlN}}$  is a very small term, we can ignore it and get:

$$\delta_{\text{Si}} = -\frac{Z_{\text{Si}}}{Z_{\text{ox}}}\delta_{\text{ox}} - \frac{Z_{\text{Si}}Z_{\text{AlN}}}{Z_{\text{ox}}^2}\delta_{\text{AlN}} \quad (\text{A.29})$$

We can then retrieve the relation between the three cavities as:

$$k_{\text{Si}}d_{\text{Si}} = m\pi + \pi/2 - \frac{Z_{\text{Si}}}{Z_{\text{ox}}}(k_{\text{ox}}d_{\text{ox}} - n\pi - \pi/2) - \frac{Z_{\text{Si}}Z_{\text{AlN}}}{Z_{\text{ox}}^2}(k_{\text{AlN}}d_{\text{AlN}} - p\pi) \quad (\text{A.30})$$

By taking the frequency difference between  $f_m$  and  $f_{m-1}$ , we can find the local FSR as:

$$\Delta f = \Delta f_0 \frac{d_{\text{Si}}}{d_{\text{Si}} + \frac{Z_{\text{Si}}^2}{Z_{\text{ox}}^2} \left( \frac{\rho_{\text{ox}}}{\rho_{\text{Si}}}d_{\text{ox}} + \frac{\rho_{\text{AlN}}}{\rho_{\text{Si}}}d_{\text{AlN}} \right)} \quad (\text{A.31})$$

By comparing Eq. A.24 and A.31, it can be seen that the extra effective length due to SiO<sub>2</sub> and AlN is now multiplied by the square of the ratio between the acoustic impedance of Si and SiO<sub>2</sub>. Since SiO<sub>2</sub> has a smaller impedance than Si, the effective length is longer than before, and the FSR is thus smaller.

The cases where the AlN is near its anti-resonance condition  $k_{\text{AlN}}d_{\text{AlN}} = p\pi + \pi/2 + \delta_{\text{AlN}}$  can be calculated in a similar manner which are summarized in Table A.2. Note the SiO<sub>2</sub> resonance is defined as when there is no Si, and now its resonant condition becomes  $k_{\text{ox}}d_{\text{ox}} =$



$n\pi + \pi/2 + \delta_{\text{ox}}$  due to the  $\pi/2$  phase introduced from the AlN–SiO<sub>2</sub> interface. Similar as before, the length (FSR) is longer (smaller) around SiO<sub>2</sub>’s anti-resonance as compared to its resonance. By comparing cases between AlN resonance and anti-resonance regions, there is an additional factor of the ratio square between the impedance of oxide and AlN around AlN anti-resonance. Since AlN has a higher impedance than SiO<sub>2</sub>, the effective length (FSR) around AlN anti-resonance regions is shorter (larger) than the corresponding region around AlN resonance. Based on the effective length expressions, we can find that, for two coupled mechanical cavities, if the impedance of the small cavity is smaller (e.g., Si and SiO<sub>2</sub>), the effective length (FSR) is shorter (larger) around the small cavity resonance than its anti-resonance. This is also true for the reverse case (e.g., SiO<sub>2</sub> and AlN), where the small cavity has larger impedance, and the effective length (FSR) is longer (smaller) around AlN resonance [127].

The boundary conditions at the interfaces in each case are also summarized in Table A.2. The AlN–SiO<sub>2</sub> interface is free at the AlN resonance and fixed at anti-resonance. This is also true for the SiO<sub>2</sub>–Si interface. The four cases are numbered as 1-4 from top to bottom in Table A.2 and labeled and compared with experiments as shown in Fig. A.5. Around the AlN resonance, the FSR oscillates between 1 and 2, while at AlN’s anti-resonance it varies between 3 and 4, which is consistent with experiments. Finally, as a rule of thumb, since the envelope and FSR are both related with the matching of acoustic impedance, the node (anti-node) of the S<sub>11</sub> envelope corresponds to larger (smaller) local FSR.

#### A.4 Electromechanical coupling and acousto-optic overlap

The model can also be used to estimate the optomechanical S<sub>21</sub> response which is dependent on both electromechanical coupling efficiency and acousto-optic overlap. The stress field distribution in AlN will strongly influence the effective electromechanical coupling, which can be estimated by following the method, as found in the literature [127]:

$$k_{\text{t,eff}}^2 = \frac{\pi^2}{4} \frac{f_s}{f_p} \left(1 - \frac{f_s}{f_p}\right) \quad (\text{A.32})$$

where  $f_p$  is the parallel resonant frequency when the denominator of Eq. (18) equals zero, and  $f_s$  is the series resonant frequency when the numerator of Eq. (18) equals zero.  $k_{t,\text{eff}}^2$  is thus calculated as shown in Fig. A.6(a). A maximum value of 0.15% is reached around 4.3 GHz where the AIN resonance is located. It varies with a envelope similar as the  $S_{11}$  measurement.

In addition to the electromechanical conversion efficiency, the  $S_{21}$  also depends on acousto-optic overlap which determines the modulation of the optical resonant frequency. According to the perturbation theory, the relative change of resonant frequency can be related with the modulation of refractive index distribution as [14]:

$$\frac{\Delta\omega}{\omega} \approx -\frac{\iint \Delta n(x, y) \|\mathbf{E}(x, y)\|^2 dx dy}{\iint n(x, y) \|\mathbf{E}(x, y)\|^2 dx dy} \quad (\text{A.33})$$

where the perturbation of refractive index is caused by the induced stress through the stress-optical effect, and is proportional to the stress via the stress-optical coefficient. In our specific

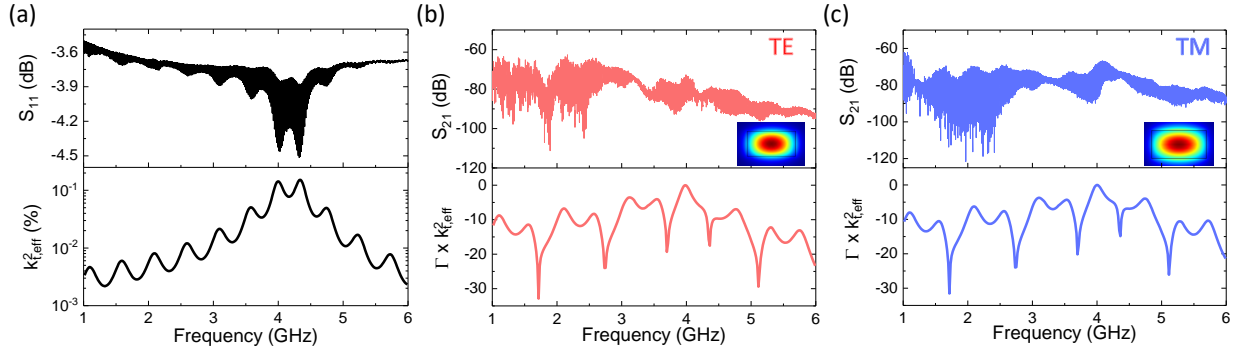


**Figure A.6.** (a) Measured  $S_{11}$  response (top) and calculated effective electromechanical coupling coefficient  $k_{t,\text{eff}}^2$  (bottom). The coupling reaches a maximum value of 0.15% around 4.3 GHz. (b-c) Measured  $S_{21}$  response of the TE and TM mode (top) and corresponding normalized product of acousto-optic overlap and  $k_{t,\text{eff}}^2$  (bottom). When the node of the acoustic stress wave is located at the center of the waveguide, the acousto-optic overlap integral  $\Gamma$  becomes zero and thus causes notches in the  $S_{21}$  response. Reprinted from Ref. [12].

case, the stress is dominated by the vertical stress  $\sigma_z$ . Therefore, the normalized acousto-optic overlap can be approximately estimated as [14]:

$$\Gamma = \frac{\iint \sigma_z(z) \|E(r, z)\|^2 dr dz}{\iint \|E(r, z)\|^2 dr dz} \quad (\text{A.34})$$

where  $\sigma_z$  is assumed to be dependent only on  $z$  and uniform in the  $r$  direction. In this way, the distribution of  $\sigma_z$  can be calculated from the aforementioned 1-D acoustic model. The electric field takes only the dominant component, that is  $E_r$  for TE mode and  $E_z$  for TM mode.

To better compare with the measured optomechanical  $S_{21}$  response, the normalized product of  $\Gamma$  and  $k_{t,\text{eff}}^2$  is plotted in Fig. A.6(b-c) for TE and TM modes. Their product can help us to explain the variation of  $S_{21}$  qualitatively. For instance, when the node of a stress wave locates at the center of the waveguide, the overlap integral approaches zero due to the vertical symmetry of the optical mode. This causes notches in the  $S_{21}$  response, such as the decreasing of  $S_{21}$  near 2 GHz of the TE mode. The nearly periodic variation of the envelope of  $S_{21}$  is due to the modulation of  $k_{t,\text{eff}}^2$ . Due to the high confinement of the optical mode in the waveguide, there exhibits only a small difference of the acousto-optic overlap between the TE and TM modes. On the other hand, the difference of the measured  $S_{21}$  response is mainly caused by the optical Q. Since TE mode shows nearly two times larger Q than TM mode, its response beyond 4 GHz is suppressed by entering into the resolved sideband regime. The perturbation of the local stress field due to the  $\text{Si}_3\text{N}_4$  waveguide is not taken into account which requires 2D numerical simulation. This may lead to the difference between measurement and calculation shown in Fig. A.6(b-c). Despite this, the analytic model can still give us a good qualitative estimation of the electro-optomechanical response

## B. DESIGNING THE OPTICAL WAVEGUIDE FOR TE-TM MODE COUPLING

### B.1 Design of quasi-square optical waveguide

As mentioned in the main text, phase matching is key for efficient mode coupling. This requires that the two optical modes have the frequency difference matching the mechanical frequency (below 5 GHz), and the azimuthal order difference equals to the effective azimuthal order of the modulation wave. Satisfying the frequency requirement is relatively easy since at the mode anti-crossing the two modes are closely spaced. It is more stringent for momentum. Since the three actuators cover the entire microring, the effective wavelength of the modulation wave is  $2\pi R$  indicating that the azimuthal order is 1. This requires the two optical modes to have very close effective refractive indices.

In the case of fully  $\text{SiO}_2$ -cladded  $\text{Si}_3\text{N}_4$ , an intuitive way is to design a quasi-square waveguide cross-section where the difference of effective refractive indices between  $\text{TE}_{00}$  and  $\text{TM}_{00}$  modes is determined by the aspect ratio of the waveguide's height  $h$  and width  $w_b$ , as shown in Fig. B.1(a). The sidewall angle  $\theta$  is also included in the design based on previous experiments [24], [48], [117]. As  $h$  depends on thin-film deposition and chemical-mechanical polishing,  $w_b$  depends on photolithography, and  $\theta$  depends on reactive ion etching (RIE), they all show variations over wafer scale due to fabrication, which should be taken into account in the waveguide design.

For specific waveguide geometry ( $h$ ,  $w_b$ , and  $\theta$ ), the resonant frequency and azimuthal order of the two modes are simulated using Finite Element Method (with COMSOL), where the frequency and azimuthal order difference  $\Delta m = m_{\text{TE}} - m_{\text{TM}}$  can be calculated. For fixed choice of  $\theta$  and  $\Delta m$ , there is a combination of  $h$  and  $w_b$  that will generate mode anti-crossing around 1550 nm wavelength (193.5 THz frequency), as seen in Fig. B.1(c). The initial design targets at  $\Delta m = 1$  with sidewall angle  $\theta = 89^\circ$  (red line with red filled square). As the waveguide height varies between 800 to 820 nm across the wafer, the waveguide width is designed to vary from 810 to 830 nm to take into account the height variations. The width is designed to be slightly larger than the height such that  $\text{TE}_{00}$  has a higher effective refractive index than that of  $\text{TM}_{00}$ , and thus a slightly higher azimuthal order. To maintain

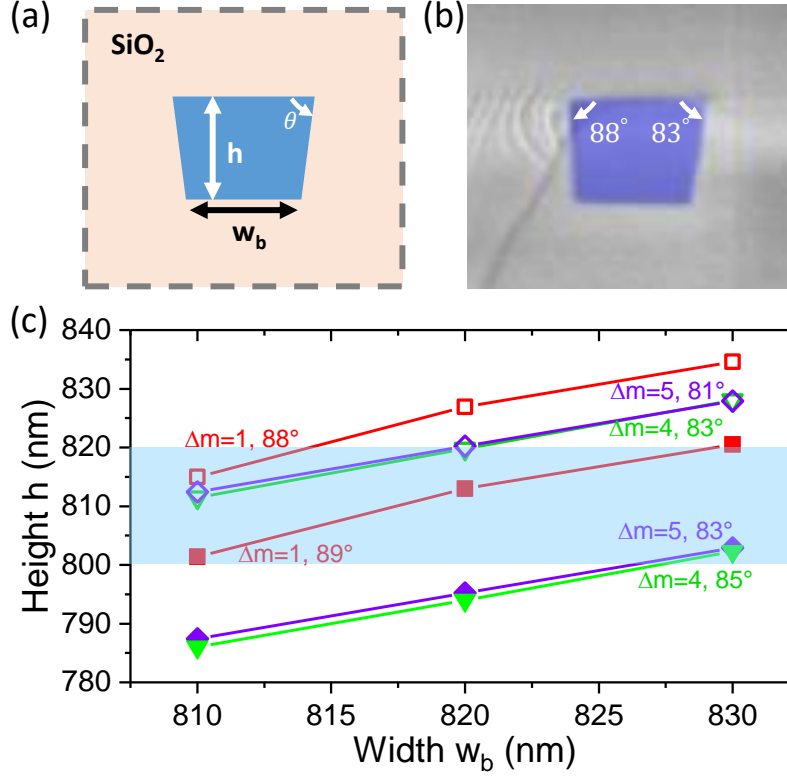


**Figure B.1.** (a) Schematic of optical waveguide cross-section with  $\text{Si}_3\text{N}_4$  (blue) fully embedded in isotropic  $\text{SiO}_2$  cladding. The definition of height  $h$ , bottom width  $w_b$ , and sidewall angle  $\theta$  are as labeled. (b) False colored SEM showing the cross-section of the fabricated optical waveguide. The sidewall angles are as labeled. (c) Simulations suggests that the required  $h$  and  $w_b$  combination produces close  $\text{TE}_{00}$  and  $\text{TM}_{00}$  modes around 1550 nm with  $\Delta m = 1$  (red),  $\Delta m = 4$  (green),  $\Delta m = 5$  (purple). Different sidewall angles are studied and labeled. The blue shaded area indicates the variation of waveguide height in the fabrication. Reprinted from Ref. [169].

$\Delta m$ , the width and height need to increase (or decrease) together to keep the aspect ratio. As the sidewall angle decreases to  $88^\circ$ , the required height increases at the same width (red line with red unfilled square). Nevertheless, the curve still crosses the height variation (blue shaded area) at small width. In this case, the initial design is supposed to cover the variation of height, width and sidewall angle.

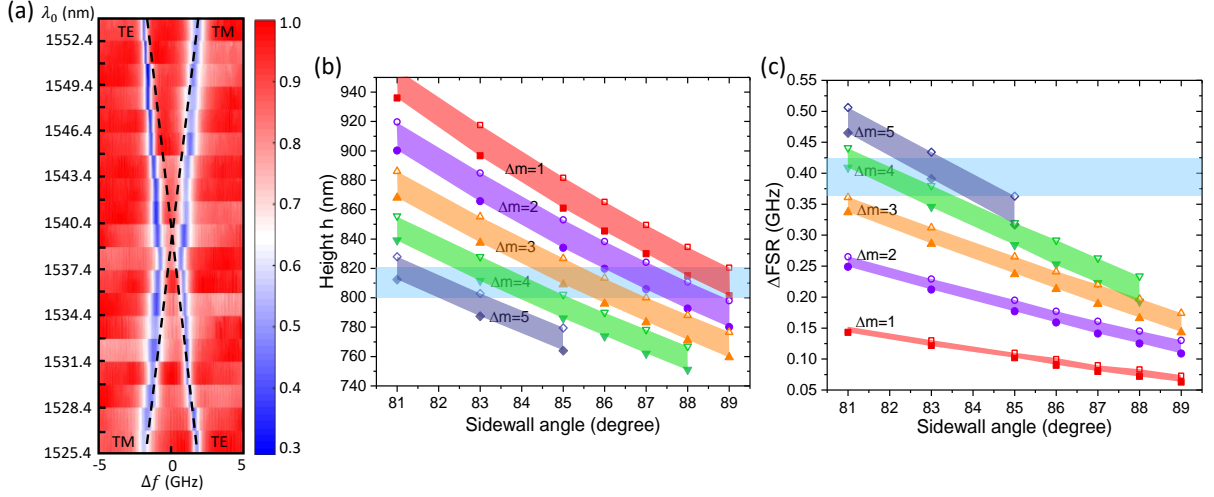


**Figure B.2.** (a) Measured TE<sub>00</sub> and TM<sub>00</sub> mode anti-crossing around 1540 nm. The wavelength  $\lambda_0$  is the center wavelength between TE<sub>00</sub> and TM<sub>00</sub>. (b) Simulated height  $h$  that generates close TE<sub>00</sub> and TM<sub>00</sub> modes, and (c) corresponding FSR difference  $\Delta FSR$  for different sidewall angles and  $\Delta m$ . The variation of width  $w_b$  is included as lower (810 nm) and higher (830 nm) bounds of each  $\Delta m$  plot. The blue shaded areas are experimental variations. Reprinted from Ref. [169].

## B.2 Calibration of the azimuthal order difference $\Delta m$

In this section, the azimuthal order difference  $\Delta m$  of the fabricated device is calibrated, showing deviation from the initial design in the previous section. The waveguide cross-section is shown in the SEM in Fig. B.1(b). The sidewall angles deviate from 89° with the smallest angle being 83°, which will be corrected in the following analysis. For the device shown in the main text, the spectra of TE<sub>00</sub> and TM<sub>00</sub> mode pairs are measured over a broad wavelength range, as shown in Fig. B.2(a). A mode anti-crossing is found around 1540 nm. At longer wavelength, TE mode has lower frequency than the TM mode ( $f_{TE} < f_{TM}$ ), while at shorter wavelength  $f_{TE} > f_{TM}$ . This shows that TE mode has a larger FSR than the TM mode, i.e.  $\Delta FSR = FSR_{TE} - FSR_{TM} \approx 380$  MHz. This FSR difference is used to find approximately the  $\Delta m$  of the measured device by comparing with numerical simulations (COMSOL), as illustrated in Fig. B.2(c).

Figure B.2(b) shows the simulation of the required  $h$  as a function of sidewall angle  $\theta$  for different  $\Delta m$ . The variation of width is also included in each  $\Delta m$  plot with the lower bound being  $w_b = 810$  nm and upper bound being  $w_b = 830$  nm. We find that, as the sidewall angle decreases, the required height increases, and it is higher for smaller  $\Delta m$ . For angle around  $83^\circ$ , the height achieved in the experiment overlaps with  $\Delta m = 4 \sim 5$ . In Fig. B.2(c), the change of  $\Delta\text{FSR}$  with sidewall angle is also plotted. It can be seen that  $\Delta\text{FSR}$  is smaller for small  $\Delta m$ , which means that the two optical modes has closer refractive indices.  $\Delta\text{FSR}$  also increases with decreasing sidewall angle. Based on the measured  $\Delta\text{FSR}$ ,  $\Delta m = 4$  shows better overlap with both height and  $\Delta m$ . Due to the discrete nature of the spatial modulation, there are higher-azimuthal-order Fourier components simultaneously excited that can fulfil phase matching at the expense of lower efficiency [208]. In the future,  $\Delta m$  can be precisely engineered to 1 with better estimation of the variations of waveguide height, width, and sidewall angles.

## VITA

Hao Tian is a Ph.D. student in the department of Electrical and Computer Engineering from Purdue University starting from 2017 Spring, under the supervision of Prof. Sunil Bhawe. His researches mainly focus on integrated optomechanical devices, piezoelectric transduction, acousto-optic modulation, and hybrid quantum systems. During his Ph.D. study, he demonstrated a piezoelectric controllable photonic system (Piezo-on-Photonics) that is multi-functional, foundry accessible, low power consumption, and low cost. He coupled the HBAR resonator with photonic circuits for the first time, and achieved efficient acousto-optic modulation up to microwave X-band. This technique enabled him to demonstrate a magnetic-free integrated optical isolator, eliminating the need for an external bulky magnet. He finally studied the quantum microwave to optical conversion based on HBAR, and the potential to establish a high-fidelity connection between superconducting qubit and photon for future quantum internets.

He was born in Jincheng, Shanxi from China. He received the Bachelor degree in Optoelectronic Technology and Science from Tianjin University, China in 2015 Fall. During the last semester of his undergraduate study in 2015, he worked as a visiting student in EMAT group of Department of Material Science and Engineering from MIT. He participated in the design of novel waveguide structure for optical manipulation of nanoparticles, and the research about novel ultra-fast Ge electro-absorption optical modulator under the supervision of Prof. Jurgen Michel and Dr. Lin Zhang. He received the Master degree in Electrical and Computer Engineering from Purdue University in 2016 December, under the supervision of Prof. Peter Bermel. During his study, he focused on the research of selective solar absorber and electromigration to increase the performance and lifetime of the solar thermal systems.

He was the recipient of 2022 Outstanding Graduate Student Research Award from College of Engineering of Purdue University, Bilsland Dissertation Fellowship, Outstanding Student Paper Award in IEEE MEMS conference in 2021, and NSF Quantum Information Science and Engineering Network (QISE-NET) award.



## LIST OF PUBLICATIONS

1. **Tian, Hao**, Junqiu Liu, Anat Siddharth, Rui Ning Wang, Terence Blésin, Jijun He, Tobias J. Kippenberg, and Sunil A. Bhave. “Magnetic-Free Silicon Nitride Integrated Optical Isolator.” *Nature Photonics* 15, 828–836 (2021).
2. Terrence Blésin, **Hao Tian**, Sunil A. Bhave, Tobias J. Kippenberg. “Quantum coherent microwave-optical transduction using high overtone bulk acoustic resonances.” *Physical Review A* 104, no. 5 (2021): 052601.
3. Lihachev, Grigory, Johann Riemensberger, Wenle Weng, Junqiu Liu, **Hao Tian**, Anat Siddharth, Viacheslav Snigirev et al. “Ultralow-noise frequency-agile photonic integrated lasers.” arXivpreprint arXiv:2104.02990 (2021).
4. Tong, Xin, **Hao Tian**, Yongjun Guo, Meng Zhang, and Lin Zhang. “Dynamic Nanoparticle Trapping by Cascaded Nanophotonic Traps in a Silicon Slot Waveguide.” *IEEE Journal of Selected Topics in Quantum Electronics* (2021) 27, no. 5 (2021): 1-8.
5. Liu, Junqiu\*, **Hao Tian\***, Erwan Lucas\*, Arslan S. Raja\*, Grigory Lihachev, Rui Ning Wang, Jijun He et al. “Monolithic piezoelectric control of soliton microcombs.” *Nature* 583, no. 7816 (2020): 385-390. (\* **joint first author**)
6. **Tian, Hao**, Junqiu Liu, Bin Dong, J. Connor Skehan, Michael Zervas, Tobias J. Kippenberg, and Sunil A. Bhave. “Hybrid integrated photonics using bulk acoustic resonators.” *Nature communications* 11, no. 1 (2020): 1-8.
7. Zhou, Zhiguang, **Hao Tian**, Thomas M. Hymel, Harsha Reddy, Vladimir M. Shalaev, Yi Cui, and Peter Bermel. “High-temperature, spectrally-selective, scalable, and flexible thin-film Si absorber and emitter.” *Optical Materials Express* 10, no. 1 (2020): 208-221.
8. **Tian, Hao**, Woojin Ahn, Kerry Maize, Mengwei Si, Peide Ye, Muhammad Ashraful Alam, Ali Shakouri, and Peter Bermel. “Thermoreflectance imaging of electromigration evolution in asymmetric aluminum constrictions.” *Journal of Applied Physics* 123, no. 3 (2018): 035107. (**Selected as top feature**)

9. **Tian, Hao**, Zhiguang Zhou, Tianran Liu, Cindy Karina, Urcan Guler, Vladimir Shalaev, and Peter Bermel. “High temperature efficient, stable Si wafer-based selective solar absorbers.” *Applied Physics Letters* 110, no. 14 (2017): 141101.
10. Yang, Fan, and **Hao Tian**. “Surface plasmon polaritons mode conversion via a coupled plasmonic system.” *Journal of Optics* 18, no. 5 (2016): 55005-55010.